DESORPTION OF AMMONIA-WATER MIXTURES IN MICROSCALE GEOMETRIES FOR MINIATURIZED ABSORPTION SYSTEMS

A Dissertation
Presented to
The Academic Faculty

by

Jared Carpenter Delahanty

In Partial Fulfillment
of the Requirements for the Degree
Doctor of Philosophy in Mechanical Engineering

Georgia Institute of Technology

December 2015

DESORPTION OF AMMONIA-WATER MIXTURES IN MICROSCALE GEOMETRIES FOR MINIATURIZED ABSORPTION SYSTEMS

Approved by:

Dr. Srinivas Garimella, Advisor
G. W. Woodruff School of Mechanical Engineering
Georgia Institute of Technology

Dr. Caroline Genzale
G. W. Woodruff School of Mechanical Engineering
Georgia Institute of Technology

Dr. Mostafa Ghiaasiaan
G. W. Woodruff School of Mechanical Engineering
Georgia Institute of Technology

Dr. Samuel Graham
G. W. Woodruff School of Mechanical Engineering
Georgia Institute of Technology

Dr. Thomas Fuller
School of Chemical and Biomolecular Engineering
Georgia Institute of Technology

Date Approved: October 28, 2015

To Marnie Lynn Levine

ACKNOWLEDGEMENTS

I would like to thank my advisor and mentor, Dr. Srinivas Garimella, for his continuous support and guidance, and for providing me with the opportunity to conduct my graduate research at the Sustainable Thermal Systems Laboratory. I am sure that the lessons I have learned through our mutual experiences will remain with me throughout my career. I also would like to thank the other members of my Ph.D. committee: Dr. Caroline Genzale, Dr. Mostafa Ghiaasiaan, Dr. Samuel Graham, and Dr. Thomas Fuller, who generously contributed their time, guidance, and thoughtful feedback during the course of this work.

I would like to thank Michael Garrabrant, of Stone Mountain Technologies, Inc. for providing his assistance and experience. His input and support were of great value to this work.

I also give my most sincere gratitude to the students of the Sustainable Thermal Systems Laboratory, past and present, who have been a constant source of inspiration and an invaluable resource. Specifically, I would like to thank Dr. Matthew Determan for his technical guidance during the early stages of this work, and Dr. Alex Rattner and Dr. Malcolm MacDonald, who provided their scientific counsel and comradery.

Finally, I wish to thank my family for preparing me for the challenges I have faced during this process, and providing me with the tools to overcome them.

TABLE OF CONTENTS

LIST OF TABLES

LIST OF FIGURES

Page

NOMENCLATURE

Symbols

A	Area (m^2), constant (-)
a_t	Length scale parameter (m^{-1})
B_0	Empirical parameter (-)
C	Flooding coefficient (-)
c_p	Specific heat (kJ kg^{-1} K^{-1})
C_T	Total molar concentration (kmol kg^{-1})
D_{aw}	Mass diffusivity (m^2 s^{-1})
D	Diameter (m)
D_h	Hydraulic diameter (m)
F	Empirical term (-)
g	Gravitational acceleration (m s^{-2})
h_{fg}	Enthalpy of vaporization/condensation (kJ kg^{-1})
h	Specific enthalpy (kJ kg^{-1})
j	Superficial vapor velocity (m s^{-1})
j^*	Dimensionless flooding parameter (-)
K	Binary fluid mixture correction factor (-)
k	Thermal conductivity (W m^{-1} K^{-1})
L	Length (m)
m	Empirical constant (-)
$\dot{m}$	Mass flow rate (kg s^{-1})
M	Molar mass (kg $kmol^{-1}$)
N, n	Number/quantity (-)
$\dot{n}''$	Molar flux (kmol m^{-2} s^{-1})

Nu	Nusselt number (-)
P	Pressure (kPa), perimeter (m)
P_r	Reduced pressure (-)
Pr	Prandtl number (-)
q	Fluid quality (-)
$\dot{Q}$	Heat transfer rate (W)
q''	Heat flux (W m^{-2})
R	Thermal resistance (K W^{-1}), radius (m), gas constant (kJ $kmol^{-1}$ K^{-1})
Re	Reynolds number (-)
Sc	Schmidt number (-)
t	Thickness (m)
T	Temperature (ºC)
U	Overall heat transfer coefficient (W m^{-2} K^{-1})
v	Specific volume (m^3 kg^{-1})
V, Vel	Velocity (m s^{-1})
$\dot{V\!\!\!-}$	Volumetric flow rate (m^3 s^{-1})
x	Mass fraction fluid concentration (-)
$\tilde{x}$	Mole fraction fluid concentration (-)
z	Concentration of vaporizing/condensing flux, mass fraction (-)
$\tilde{z}$	Concentration of vaporizing/condensing flux, mole fraction (-)
Z_{SBG}	Sensible heat ratio (-)

Greek Characters

α	Heat transfer coefficient (W m^{-2} K^{-1})
α'	Apparent heat transfer coefficient (W m^{-2} K^{-1})

β	Mass transfer coefficient (m s^{-1})
δ	Film thickness (m)
Δ	Numerical difference (-)
ε	Emissivity (-)
η	Fin efficiency (-)
ϕ	Angle of circular sector (rad), correction factor (-)
Γ	Mass flow rate per unit width (s^{-1})
μ	Dynamic viscosity (kg m^{-1} s^{-1})
ν	Kinematic viscosity (m^{2} s^{-1})
ρ	Density (kg m^{-3})
σ	Surface tension (N m^{-1})

Subscripts

1	More volatile component
2	Less volatile component
a	Ammonia property
amb	Ambient property
anlz	Analyzer section
atm	Atmospheric
avg	Average
aw	Ammonia-water
bp	Bubble point
bulk	Property of the bulk or average stream
c	Cross-sectional parameter, column
CF	Coupling-fluid parameter

ch	Channel
col	Column
comp	Component
cond	Conduction, condensation
conv	Convection
des	desorber section
f	Film
face	Parameter taken across the face of a channel
glide	Fluid glide parameter
H_2O	Water property
i	In, inlet
id	Ideal
in	Inlet
int	Phase interface
l	Liquid phase
NH_3	Ammonia
o	Out, outlet
out	Outlet
p	Packing
PC	Phase-change
rect	Rectifier section
S,V	Sensible vapor
sat	Saturation condition
sol, soln	Solution, liquid phase
T	Total

v	Vapor phase
w	Water
WF	Working fluid, ammonia-water

Abbreviations

COP	Coefficient of performance
LMTD	Log mean temperature difference
SBG	Silver, Bell and Ghaly method
VGU	Vapor generation unit

SUMMARY

A study of ammonia-water desorption in compact counter-flow geometries was conducted. Two novel vapor generation units, comprising integrated desorber, analyzer, and rectifier segments that use microchannel geometries, were conceptualized. The branched-tray concept features a desorber segment that uses predominantly pool-boiling mechanisms for desorption, while the vertical column desorber relies on falling-film evaporation and boiling mechanisms. Both concepts rely on falling-film heat and mass transfer mechanisms in the analyzer and rectifier sections. Segmented heat and mass transfer models, based on available correlations and modeling methodologies, were developed and used for the design of branched tray and vertical column test sections. An experimental facility was designed and constructed to evaluate desorption and rectification heat and mass transfer processes within these components, under realistic operating conditions. Data were analyzed to determine the boiling/evaporation (desorber) and condensation (rectifier) heat transfer coefficients, and to determine values of the desorber liquid and vapor mass transfer coefficients. Additionally, high-speed video and images were used to gain insights into the hydrodynamic phenomena and heat transfer mechanisms in these vapor generation units. Results of the heat and mass transfer analysis were compared with the predictions of correlations and modeling methods in the literature.

The vapor generation unit (VGU) test sections were evaluated across a range of concentrated solution mass fractions (0.400 – 0.550), desorber coupling-fluid inlet temperatures (170 – 190°C), and concentrated solution flow rates (0.70 – 1.3 g s^{-1}). Flow rates in this range correspond to desorber liquid Reynolds numbers of approximately 175 to 410 for the branched tray design, and desorber film Reynolds numbers of approximately 90 to 215 for the vertical column. Pressures observed within the VGU test sections ranged from approximately 1620 to 2840 kPa during testing. The novel VGUs were shown to achieve ideal cooling capacities as high as 432 and 323 W for the branched tray and vertical column, respectively. This parameter indicates the cooling capacity that would be achieved by an idealized cooling system using the refrigerant stream produced by the experimental VGU. Ideal COPs of 0.561 and 0.496 were demonstrated for the branched tray and vertical column, respectively.

Experimental heat transfer coefficients were found to range from approximately 1860 to 11690 W m^{-2} K^{-1} for the pool-boiling desorption of the branched tray VGU. A new correlation was proposed and shown to provide good agreement with the data, achieving average and average absolute deviation of -5.2 and 16.1%, respectively, across the range of conditions tested. Falling-film evaporation/boiling heat transfer coefficients, determined for the desorption process in the vertical column VGU, were found to range from approximately 1290 to 4310 W m^{-2} K^{-1}. Rectifier condensation heat transfer coefficients ranging from approximately 160 to 250 W m^{-2} K^{-1} were observed. Mass transfer coefficients for the desorbers of both concepts were also quantified. These results were used to develop revised heat and mass transfer models of the VGU concepts. The revised models were demonstrated to predict component-level performance with reasonable accuracy, and may be used in the design of future compact VGUs with similar geometries and operating conditions.

CHAPTER 1

INTRODUCTION

Vapor compression systems are widely used to provide space-conditioning in residential and commercial applications. However, these systems have several drawbacks, including the high-grade mechanical or electrical energy input required by the compression process. The high power consumption of these systems is a significant contributor to both electricity and fuel usage, which in turn results in significant greenhouse gas emissions and cost to users. Additionally, synthetic refrigerants commonly used in vapor compression systems have deleterious environmental effects such as the potential to cause climate change. Increasing interest in utilizing low-grade thermal resources and reducing the environmental and economic costs of the available space-conditioning technologies has resulted in a renewed interest in absorption systems. While sorption technology is promising for many space-conditioning applications, the adoption of such systems has been impeded by the lack of commercially available heat and mass exchangers capable of the high-flux performance necessary for producing compact, inexpensive systems for use in residential, light-commercial and mobile applications.

1.1 Applications for Compact Sorption Systems

Sorption systems have historically been most widely used in large-capacity applications, such as district heating and cooling, or industrial applications, where thermally-driven systems can make use of waste heat or underutilized, low-grade thermal resources. In these applications, the additional heat and mass exchange components required by sorption systems may be easily justified by cost savings realized from a reduction in primary energy usage.

Figure 1.1 shows a schematic of a vapor compression and an elementary absorption system. The driving energy input is electrical or mechanical work for the vapor compression system, while the absorption system eliminates the refrigerant compressor, reducing the required work input by several orders of magnitude and making use of a driving heat input provided by thermal resources. However, this requires the addition of the desorber and absorber components to the system and, in most applications, additional recuperative heat exchangers are used.

While sorption systems may be readily justified in large-scale applications with abundant thermal resources and limited constraints on component size and capital cost, significant low-grade thermal and waste-heat resources exist in much more disperse forms that are more difficult to utilize. These resources include solar thermal, geothermal, and engine exhaust heat from transportation and small-scale stationary power generation. As an example, Rattner and Garimella (2011) estimated that 5900×10^{6}

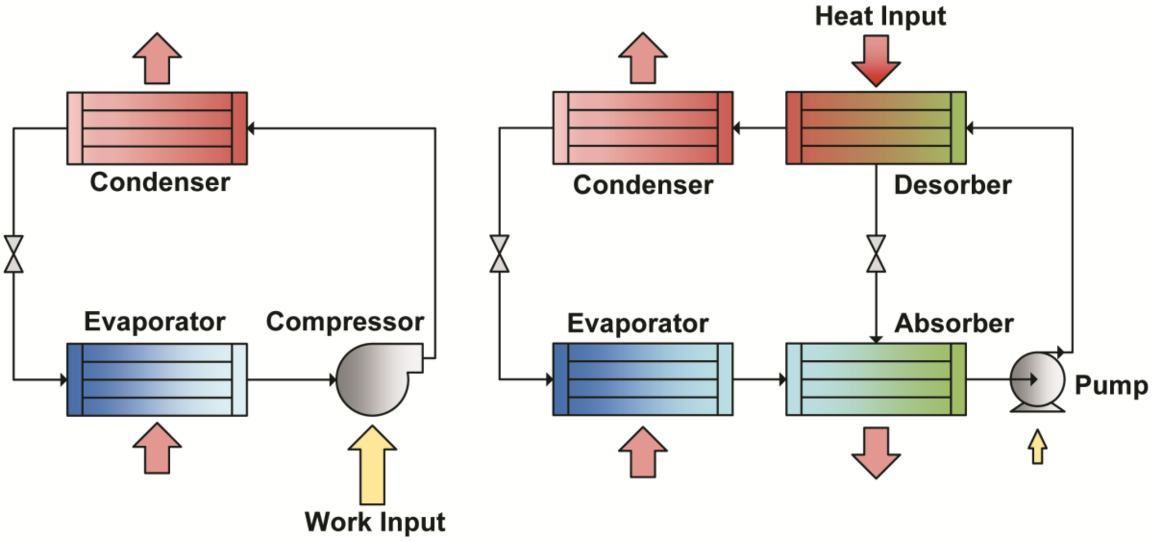

Figure 1.1: Compression (left) and absorption (right) cycles

GJ yr^{-1} of engine exhaust heat, at approximately 400°C, is available from the US transportation sector from highway vehicles alone. According to their estimates, this could be utilized by thermally-driven cooling systems to provide 920×10^6 GJ yr^{-1} of transportation air-conditioning needs, thereby dramatically reducing primary energy consumption and avoiding the emission of significant amounts of CO_2 and other environmentally harmful combustion products. These types of applications provide an excellent opportunity for compact thermally-driven absorption technologies.

Other significant applications of absorption technology include the recovery of waste heat from stationary power generation engines. This is a particularly attractive proposition in many military field applications, and in many developing countries. In both cases, power generation is often provided by relatively disperse use of small-capacity diesel or gasoline generators and much of the generated electricity is used for cooling and refrigeration applications. Keinath *et al.* (2012) demonstrated the feasibility and advantages of absorption-based ammonia-water waste heat recovery systems in these applications. A functioning prototype was later developed for the U.S. Army based on the study.

A final notable application of compact absorption systems is residential heating, cooling, and hot water heating. While this application requires the use of fossil fuel combustion to supply the driving heat input in many instances, a small-scale thermally-driven absorption system offers a versatile and cost-effective solution for residential space conditioning and water heating needs and provide higher efficiencies and reduced primary energy consumption relative to existing technologies. Recent studies (Garrabrant *et al.*, 2013a; Garrabrant *et al.*, 2013b), have shown this to be a viable application of ammonia-water absorption systems and have resulted in functional prototypes and early-stage field testing.

Recently, Determan and Garimella (2012) developed a modular microchannel-based absorption system for use in such applications. The unique monolithic sorption system achieved an extremely compact system size, with all heat and mass exchange components integrated into a single 200 × 200 × 34 mm envelope with a mass of only 7 kg. A functional prototype, using ammonia-water as the working fluid, was demonstrated in a laboratory setting and shown to produce a cooling capacity of 300 W with a maximum coefficient of performance (COP) of over 0.40. However, the relatively simple co-flow desorber design used in the prototype resulted in low refrigerant purities, requiring a large rectifier, used to increase the refrigerant concentration, and leading to system performance that was lower than desired. Compact ammonia-water absorption systems developed for other studies have faced similar issues (Nagavarapu, 2012), demonstrating that the desorber design is a critical factor in the development of miniaturized and small-scale absorption systems.

To illustrate the importance of achieving high refrigerant purity, representative evaporator temperature glides are shown in Figure 1.2 for a theoretical ammonia-water absorption cooling system. These plots show the increase in the saturation temperature of the refrigerant during evaporation for three different concentrations at a representative evaporator pressure of 500 kPa. Throughout the present study (including tables and figures), the fluid concentration is defined as the mass fraction of ammonia, unless otherwise noted to be a molar fraction. Unlike many conventional refrigerants, ammonia-water is a zeotropic mixture and therefore does not maintain a constant saturation temperature during a constant-pressure evaporation process. As the fluid quality increases, the saturation temperature also increases. For lower concentration refrigerant streams, such as the 96.0% ammonia case shown in Figure 1.2, this leads to a condition where the saturation temperature (indicated as 10°C in Figure 1.2) exceeds the desired chilled fluid temperature at relatively low qualities. Further evaporation leads to steep rises in the saturation temperature, which therefore cannot be used for cooling purposes. The inability to use the latter stages of the evaporation process effectively for cooling leads to a significant reduction in system efficiency and capacity. Figure 1.2 shows that ammonia-water absorption systems are particularly sensitive to the refrigerant concentration and purities above 99.0% must be maintained to avoid performance degradation. Achieving such high concentrations in an efficient process requires careful desorber design and, in small-scale applications, advanced desorber geometries.

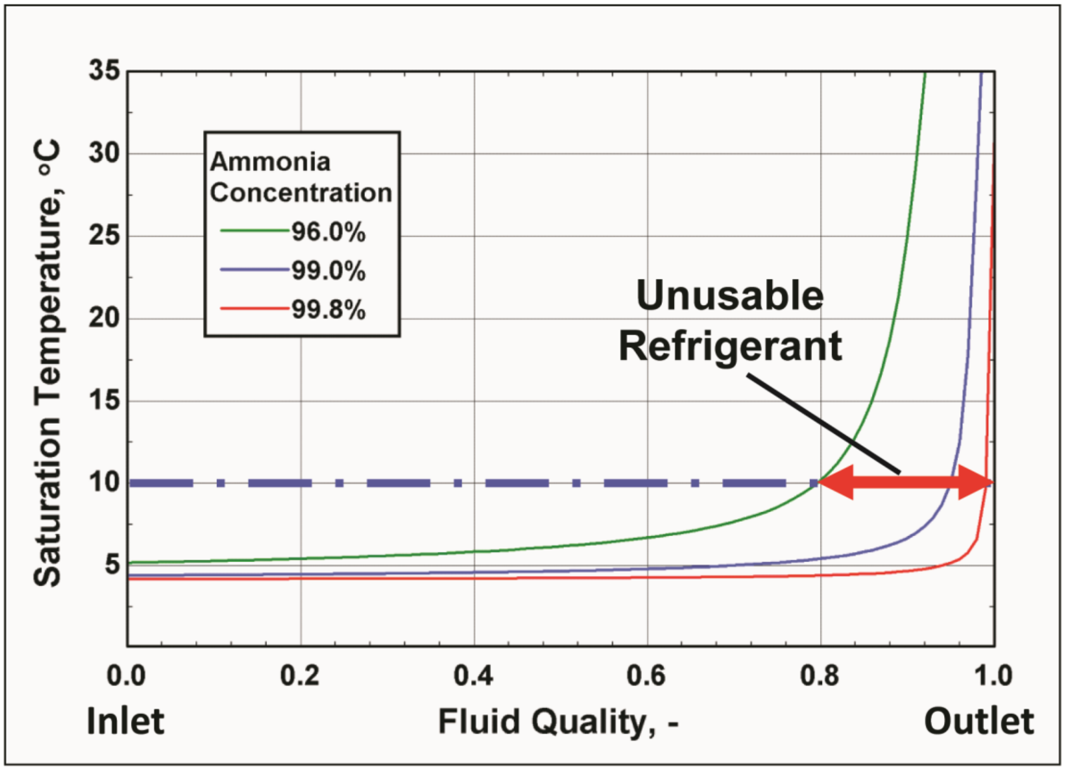

Figure 1.2: Temperature glide of evaporating ammonia-water refrigerant

Developing an effective, inexpensive and compact desorber is one of the main challenges for small-scale absorption systems. The desorber component functions as a multi-phase, multi-component, thermally driven separator, in which a concentrated liquid solution is heated, producing a refrigerant vapor and a dilute solution stream. To overcome the large heat and mass transfer resistances that are often observed during this process, careful design of the component is critical. Use of a fluid flow configuration in which the solution stream and generated vapor stream flow counter-current to each other, herein referred to as a counter-flow configuration, is an essential feature that can result in more beneficial temperature and concentration profiles within the component, thus allowing reduced size and increased refrigerant purity without adding to the rectifier load. Essentially, vapor exiting at close to equilibrium with the cooler incoming concentrated solution stream yields the necessary high vapor-phase ammonia concentrations. However, typical counter-flow desorbers utilize tube-bank, shell-an-tube, or similar designs. Even recently developed advanced components using microchannel tube bank geometries (Determan and Garimella, 2011) are not as compact and lightweight as desired for some applications, and therefore are not well-suited to small-scale, monolithic, or mobile systems.

In addition to the development of compact counter-flow desorbers, most small-scale absorption systems could achieve significant reductions in cost, size, complexity, and fluid inventories by shifting to integrated, rather than discrete, heat and mass exchangers, as demonstrated with the monolithic system of Determan and Garimella (2012). Additionally, the use of such compact, low-inventory components dramatically reduces the risk of significant exposure to ammonia in the event of a system leak, which one is the most commonly cited drawbacks of ammonia-water systems. As such, advanced desorber designs featuring integrated desorber, rectifier, and analyzer sections should be pursued. The rectifier increases refrigerant purity by partially condensing the refrigerant stream to remove excess water vapor. The analyzer is a recuperative section that reduces the desorber and rectifier loads by bringing the generated vapor and concentrated solution closer to thermal equilibrium and achieving some stripping of the water fraction from the vapor in an externally adiabatic section. These integrated elements yield an advanced vapor-generation unit (VGU), capable of providing high-purity refrigerant in a single compact and efficient component.

1.2 Scope of the Present Study

The primary objective of the present study is to characterize the dominant transport processes of two novel compact counter-flow vapor generation units for use in ammonia-water absorption systems. Ammonia-water was chosen as the working fluid due to the demonstrated need for more advanced desorbers in compact ammonia-water absorption systems. Additionally, the ammonia-water fluid pair provides excellent heat transfer and thermodynamic properties, such as high specific and latent heat, and is capable of operation in refrigeration systems, where the use of alternate fluid pairs such as Lithium Bromide-Water typically leads to freezing of the refrigerant (water) below 0°C and also to crystallization issues. In addition, the high specific volume of water vapor at low temperatures makes it difficult to package into small volumes without excessive pressure drops and saturation temperature drops. Both novel VGU configurations investigated here feature integrated desorber, rectification and recuperation, or analyzer, sections and are designed for use in small-scale single-effect ammonia-water absorption systems, particularly those utilizing a monolithic, micro-channel-based architecture. Microchannel passages are utilized for the heating and cooling fluids in the desorber and rectifier, respectively, thus taking advantage of the high heat transfer coefficients and substantial heat transfer area-to-volume ratios that can be achieved with microchannel geometries. The unique monolithic geometry used to integrate the desorber, rectifier, and analyzer sections also offers the advantages of being highly modular; scaling easily to a range of system capacities, and is conducive for vapor-liquid counter-flow configurations without requiring external separator tanks or extensive plumbing.

On the solution side, the first concept configuration operates primarily in a falling-film mode, while the second operates primarily in a pool-boiling mode. To study the details of the internal heat and mass transfer processes, instrumented test sections with visual access for simultaneous flow visualization are fabricated for both configurations and are evaluated under realistic conditions to quantify the heat transfer performance and observe the impact of hydrodynamic phenomena, such as component wetting, flooding, and inter-phase mixing, at a sub-component level. Based on the experimental investigations, improvements to the component models are made to more accurately predict the heat and mass transfer processes and the relevant hydrodynamic phenomena. Finally, the proposed study provides a comparison of the performance of the two configurations and recommendations for the refinement of the designs and modeling methods for use in next-generation absorption systems.

1.3 Thesis Organization

The organization of subsequent chapters is as follows:

- Chapter 2 provides a review of previous studies of compact absorption heat and mass exchangers as well as relevant studies of heat and mass transfer models and correlations applicable to the concepts under investigation here. The need for additional research and the detailed objectives of the present are also provided.
- Chapter 3 describes the initial modeling, design, and fabrication of the novel VGU test sections. Specifications of the experimental facility and instrumentation are provided along with the test matrix and operating conditions. Finally, the experimental procedures and safety considerations are described.
- Chapter 4 presents the data analysis methods and provides detailed sample calculations for the baseline experimental conditions.
- Chapter 5 provides the results of the heat and mass transfer experiments and analysis and compares the performance of the two concepts with other similar studies and with modeling methods and correlations available in the literature. Additionally, visualization images and flooding observations are discussed.
- Chapter 6 describes the implementation of improved heat and mass transfer models for the desorber, analyzer and rectifier sections, based on the results.
- Chapter 7 summarizes the major findings and conclusions of the present study and discusses areas of research that warrant additional investigation.

CHAPTER 2

PRIOR WORK

An overview of the literature pertaining to compact counter-flow geometries applicable to ammonia-water desorption and rectification and, more generally, to the underlying heat and mass transfer processes relevant to the present study, is discussed in this chapter.

2.1 Compact Desorption Studies

Widespread adoption of small-scale thermally driven absorption heating and cooling systems to mobile, residential and light-commercial applications has historically been difficult to achieve, in large part due to the significant mass, volume, and cost of the numerous heat and mass exchange components required. However, several miniaturized absorption heat and mass exchanger studies that aim to address these issues have been reported in the literature. A summary of the compact desorber studies available in the literature is provided in Table 2.1.

2.1.1 **General Absorber and Desorber Studies**

A microchannel falling-film heat and mass exchanger geometry was described by Garimella (1999, 2000, 2004) and was proposed for use in absorption systems. Their heat and mass exchanger consisted of an array of 1.575 mm outside-diameter tubes, with adjacent horizontal tube banks stacked in a crisscross pattern to form a vertical column of such tube banks. A prototype unit utilizing this geometry was studied experimentally as an absorber (Meacham and Garimella, 2002a) and an improved design (Meacham and

Table 2.1: Compact desorber studies in the literature

Study	Working Fluid	Counter-Flow Configuration	Integrated Rectifier	Notes
Fernández-Seara *et al.* (1998)	Ammonia-Water	Yes	No	Design and modeling study of kettle-type desorber
Ortega *et al.* (2008)	Ammonia-Water	No	No	Direct solar-fired desorber design study
Shi *et al.* (2010)	Lithium Bromide-Water	Yes	No	Experimental study of electrically heated falling-film desorber
Táboas *et al.* (2010); Táboas *et al.* (2012)	Ammonia-Water	No	No	Modeling study of flow boiling in plate-type desorber
Zacarías *et al.* (2010)	Ammonia-Lithium Nitrate	No	No	Experimental study of co-flow plate-type desorbers
Determan and Garimella (2011)	Ammonia-Water	Yes	No	Experimental investigation of tube-bank desorber
Sauceda *et al.* (2011)	Ammonia-Water	No	No	Direct solar-fired desorber design study
Determan and Garimella (2012)	Ammonia-Water	No	Yes	Experimental investigation of monolithic absorption system
Golden (2012)	Ammonia-Water	Yes	No	Experimental investigation of flooded-column desorber
Venegas *et al.* (2012)	Ammonia-Lithium Nitrate	No	No	Experimental study of co-flow plate-type desorbers

Garimella, 2004) that addressed earlier fluid distribution issues was developed and utilized for flow visualization as well as heat and mass transfer characterization studies. Determan *et al.* (2004) adapted this design for use as a desorber in an ammonia-water system and reported falling-film heat and mass transfer data and a component heat duty of 17.5 kW, typical of residential or light-commercial applications. The overall dimensions of the heat and mass exchange portion of the device were 178 × 178 × 508 mm (a larger shell-type pressure vessel around this tube array was required for operation). The unit demonstrated high local desorption rates, but performance could be improved further through better liquid distribution. Additionally, high cost and complexity of fabrication are expected, even in high-volume production.

More recently, Determan and Garimella (2012) developed a complete monolithic microchannel absorption system, which demonstrated a major reduction in system size, but utilized a simple co-flow, electrically heated desorber to reduce complexity. The system produced a nominal 300 W cooling capacity in laboratory demonstrations. All heat and mass exchange components were integrated into a single bonded unit with dimensions of 200 × 200 × 34 mm. However, the lack of a more advanced counter-flow desorber required the use of a large rectifier and contributed to a relatively low refrigerant concentration, limiting overall system performance.

Shi *et al.* (2010) also conducted an experimental investigation of a compact desorber design utilizing an electrically heated prototype, designed to simulate a flue-gas-heated desorber. The unit employed lithium bromide-water as the working pair and operated in the falling-film mode with the working fluid flowing through the inside of a vertical tube. An electrical resistance heater was positioned on the outer surface of the tube to provide the required heat input to the desorber. The results of the study indicated the potential for a significant reduction in component size over conventional flooded desorbers; however a full-scale or packaged prototype was not fabricated and tested.

Venegas *et al.* (2012) and Zacarías *et al.* (2010) presented experimental results for plate-type, co-flow desorbers for use in ammonia-lithium nitrate systems. These studies investigated the flow-boiling and nucleate-boiling phenomena that occurred during the desorption process and reported experimental heat transfer coefficients. They noted the advantages of the small size and low cost of such components. However, the co-flow configuration was again expected to require a large rectifier and limit system performance to some degree. In a pair of modeling studies, Táboas *et al*. (2010, 2012) also proposed the use of plate-type heat exchangers for flow-boiling desorption of ammonia-water with applications in absorption systems. Limited prior studies on the forced-convection boiling of ammonia-water mixtures posed significant challenges to the modeling effort.

A compact, microchannel-based desorber was experimentally demonstrated by Davis *et al.* (2010). Employing a co-flow arrangement and demonstrated with ammonia-water, the design has some similarities to the desorber used by Determan and Garimella (2012) in their monolithic system, but utilizes a fractal, branching design for the microchannel array. A heating oil was utilized to provide the energy input and this fluid also flows through a microchannel array adjacent to the ammonia-water channels. The device was found to be capable of heat duties in excess of 300 W. In addition to the co-flow limitations, a clear method for scaling the device to larger capacities, which may require an intricate header design, was not presented.

Other component and system-level studies have sought compact desorber designs for applications with specific constraints. Fernández-Seara *et al.* (1998) considered a heat recovery system, designed to power an ammonia-water chiller for fishing vessels, in which a kettle-type heat exchanger would be employed for use as a desorber with a plate heat exchanger used as an economizer. The system was designed to recover approximately 16.7 kW of thermal energy at 190°C from waste heat produced by the propulsion engine of the vessel. This waste heat was specified as the driving thermal input to an 11.1 kW desorber operating at 140°C, and designed to function as part of an absorption chiller with an 8.3 kW cooling capacity. While a counter-flow configuration may be possible with such a design, the proposed desorber design is more similar to a flooded desorber and does not appear to offer a particularly compact geometry, which would almost certainly be of great benefit given the application.

Exploration of solar-thermal absorption systems for residential applications has also led to the design and analysis of compact direct-generation desorbers using ammonia-water as the working fluid. Ortega *et al.* (2008) presented a design for an integrated desorber/solar-concentrator with the capacity to supply refrigerant vapor to a 3.8 kW absorption cooling system. The total length required for the desorber/collector was estimated at 35 m. A more recent design study of a similar system (Sauceda *et al.*, 2011) resulted in a direct-generation desorber/collector with dimensions of 7.18 × 3 m and was specified for use with a 10.6 kW air-cooled Generator-Absorber-Heat Exchange (GAX) cycle absorption system. Both systems were designed to be mounted on or near residential buildings.

Considering the need for compact, effective desorbers and rectifiers for use in absorption systems, Fernández-Seara and Sieres (2006) studied the influence of the desorption and rectification process on the overall performance of a single-effect ammonia-water absorption system. The impact of rectifier and desorber efficiencies on system COP was characterized. It was concluded that desorber and rectifier designs resulting in high-ammonia-purity refrigerant streams were critical to system performance for many common ammonia-water absorption system applications. Several specific designs for desorber and rectifier components, including different arrangements of multi-stage distillation columns as well as Pall-ring packed beds, aimed at increasing refrigerant purity and improving system performance, were also studied (Fernández-Seara *et al.*, 2003; Sieres *et al.*, 2008).

Flooded desorbers, operating in a pool-boiling mode, have been implemented previously in large-scale absorption systems and in design studies for more compact applications (Fernández-Seara *et al.*, 1998; Golden, 2012). Golden (2012) designed, fabricated and tested a 500 W flooded desorber using a method and facility similar to those of the present study. While high uncertainty was associated with many of the values reported by Golden (2012), feasibility of a compact desorber using falling-film or pool-boiling heat transfer modes was demonstrated.

2.1.2 **Compact VGU Component Studies**

The focus of the present study is the development and evaluation of compact absorption system components that feature integrated desorber, analyzer, and rectifier sections in a single vapor generation unit (VGU). The test sections developed in this study, and described in the following chapter (Section 3.1.2), are based on full-scale designs reported earlier by Delahanty *et al.* (2015).

In the study of Delahanty *et al.* (2015), coupled heat and mass transfer models were developed for use with novel counter-flow desorber, analyzer, and rectifier components. The desorber and analyzer models are based on the non-equilibrium method, which was pioneered by Colburn and Drew (1937) and subsequently applied to condensation of miscible binary mixtures by Price and Bell (1974). The rectifier models made use of the computationally simpler equilibrium method of Silver (1947), Bell and

Ghaly (1972), often referred to as the Silver-Bell-Ghaly, or SBG method. Details of these methods are discussed in subsequent chapters (Sections 3.1.1 and 5.3.5).

Delahanty *et al.* (2015) presented two compact VGU concepts intended for integration into small-scale thermally-driven absorption cooling systems. The two concepts were designed as components of a 3.5 kW cooling capacity absorption system, which required desorber duties of approximately 5.4 kW. Two distinct geometries were used. The first, referred to as the branched tray concept, features a desorber section with a number of liquid pools that facilitate pool-boiling heat transfer to generate the requisite refrigerant vapor. The second concept, referred to as the vertical column concept, uses internal desorber geometry with several vertical channels, or columns, that facilitate film evaporation. Both concepts include integrated analyzers, for direct-contact recuperative heat transfer between the vapor and ammonia-water solution streams. Additionally, integrated rectifiers are featured in both VGUs. The rectifiers both feature cooled vertical walls that promote partial falling-film mode condensation of the generated vapor to reduce water content and produce a high-purity ammonia refrigerant. The specific layout and features of the two concepts are presented here.

The vertical column VGU, shown in a partial exploded view in Figure 2.1, utilizes a vertical surface geometry in the desorber, analyzer, and rectifier sections and is designed to operate with the ammonia-water solution in a falling-film mode. The branched tray, shown in Figure 2.2, utilizes desorber geometry with a series of passages, which hold pools of ammonia-water solution while leaving a serpentine passage for flow of the generated vapor, and primarily operates in a pool-boiling mode. The rectifier section features falling-film mode condensation on a vertical wall with fin enhancement.

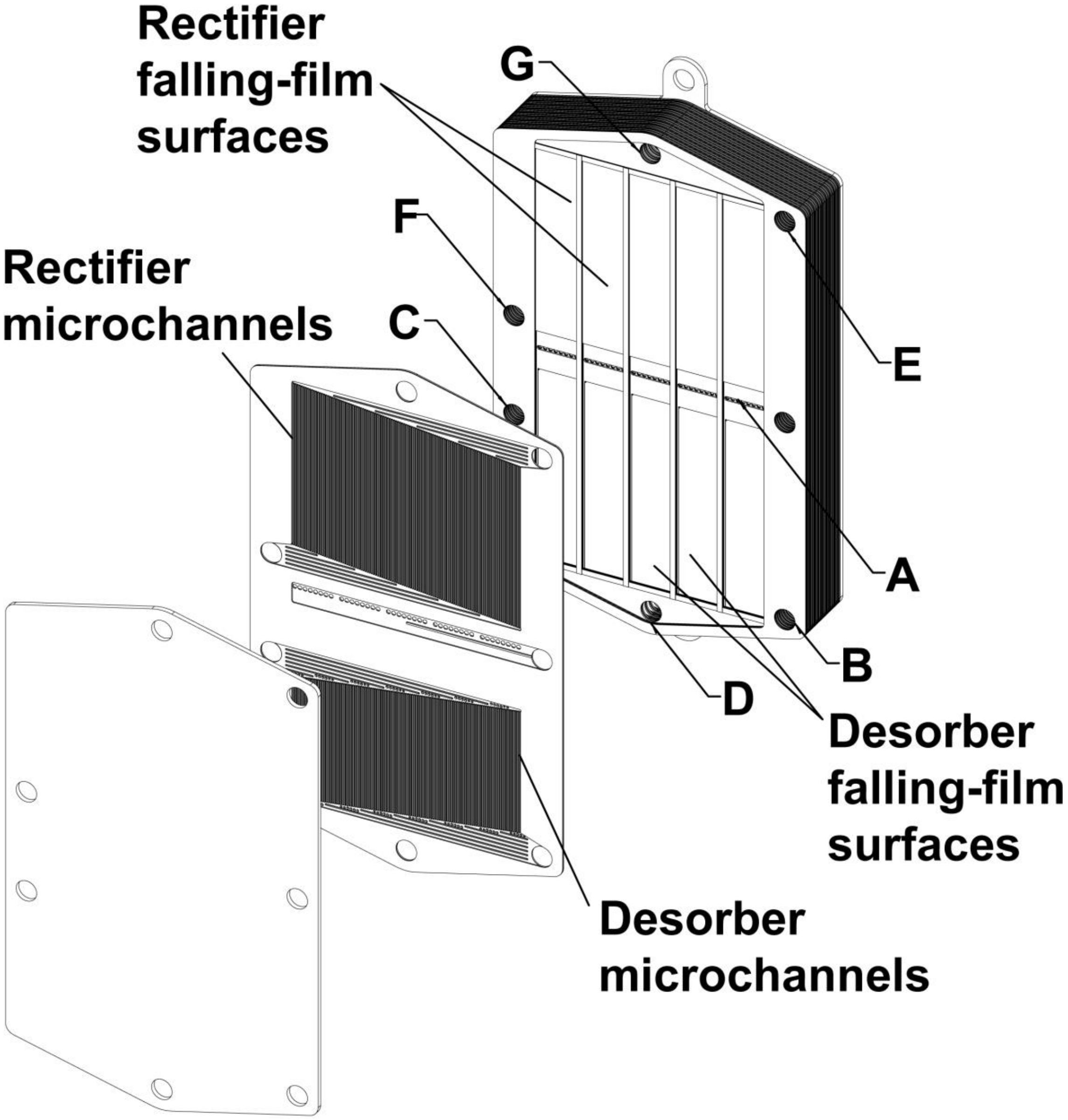

Figure 2.1: Vertical column assembly and fluid ports

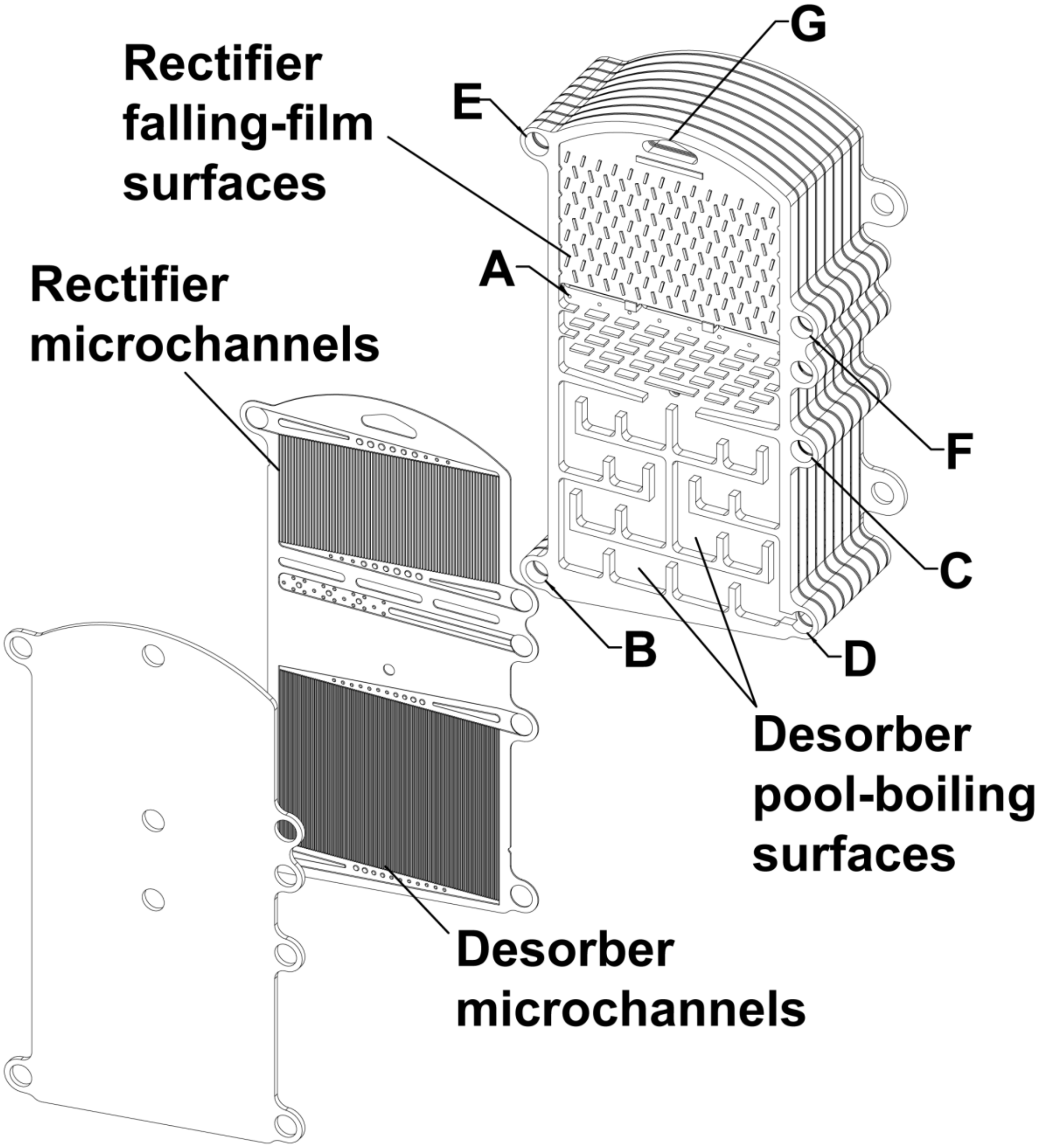

Figure 2.2: Branched tray assembly and fluid ports

Both concepts feature three distinct sections: desorber, analyzer and rectifier. The generated vapor and ammonia-water solution streams are arranged in a buoyancy-driven counter-flow configuration, in which the vapor rises past the downward-flowing solution. The coupling fluids in the desorber and rectification sections are also arranged in a counter-flow configuration relative to the solution and vapor streams, respectively.

As seen in Figure 2.1, the vertical column assembly is composed of front and back endplates, and a series of chemically-etched stainless steel shims. When assembled and sealed, via brazing, diffusion bonding, or other similar process, the assembly forms a series of vertical columns that contain the ammonia-water solution and generated vapor. Shims adjacent to these vertical columns feature arrays of vertical microchannels (442 μm hydraulic diameter), which contain the coupling fluids. The microchannels formed by the etching process are roughly semi- circular in cross-section. During operation, concentrated ammonia-water solution enters the assembly via a series of small injection ports (Point A) at the top of the analyzer section, having reached those ports through a header on the adjacent shim. The solution flows downward as a falling film, exchanging heat with the rising vapor, and then enters the desorption section. In this section, the walls of the vertical column are heated by the coupling fluid in the adjacent microchannel arrays. The coupling fluid flows counter to the solution, entering near the bottom of the component (Point B) and exiting at the top of the desorption section (Point C). As the solution film is heated, vapor is generated. At the bottom of the vertical columns, dilute solution is removed These two streams are in direct contact, allowing for heat and mass transfer, which increases the purity of the vapor stream and provides some recuperative heat transfer (from the hot vapor stream to the colder solution at the higher locations).

The vapor exits the desorption section, and then enters the analyzer section of the column, which is adiabatic, containing no coupling fluid channels. In the analyzer, the hot vapor stream continues to rise past the relatively cool solution stream providing additional area for recuperative heat transfer and beneficial mass transfer. After rising through the analyzer, the vapor enters the rectification section in which a chilled coupling fluid stream, flowing through adjacent microchannels, removes heat from the rising vapor leading to preferential condensation of the less volatile water vapor. The coupling fluid enters near the top of the component (Point E) and exits at the bottom of the rectification section (Point F), flowing counter-current to the rising vapor. The purified vapor stream exits the assembly through an external port at the top of the component (Point G). The rectifier condensate, or reflux, flows down the vertical column walls, is mixed with the solution stream, and ultimately removed from the assembly through the dilute solution exit port.

The branched tray VGU features similar flow paths for the fluid streams, but utilizes different geometry and flow regimes, changing the underlying heat and mass transfer mechanisms. As shown in Figure 2.2, the concentrated solution enters the component through a series of small injection ports (Point A) via an adjacent header and external port. The solution flows downward, entering the analyzer section, which is composed of a series of horizontal fins that distribute the solution and provide additional interface area between the falling solution and the generated vapor exiting the desorption section. The solution flows downward through the analyzer exchanging heat with the vapor stream and enters the desorber. The solution pools into a series of branched trays in the desorption section. The trays are heated via adjacent microchannel arrays and vapor is generated from the solution via pool-boiling. The hot coupling fluid enters the adjacent microchannel array at Point B and exits at Point C, flowing counter-current to the solution stream. During operation, the mass flow rate of solution entering the desorber is maintained at a level greater than the mass flow rate of generated vapor. This results in some solution spilling over the edges of the pools and flowing down to lower pools. Dilute solution is removed from the bottom-most tray via an external port (Point D). The generated vapor flows upwards from the trays and follows a serpentine path along the rows of trays. This counter-current flow between the vapor and solution provides beneficial temperature and concentration profiles and contact between the vapor stream and pooled solution enables recuperative heat transfer. The vapor leaves the top of the desorption section and flows upwards through the analyzer section. In this section, the vapor exchanges heat with the incoming solution providing additional heat recuperation and purifying the vapor stream. The vapor then enters the rectification section, composed of an offset fin array, where a cold coupling fluid flowing through adjacent microchannel arrays cools the vapor and partially condenses the water content, leading to a high-purity vapor stream. The cold coupling fluid enters the adjacent microchannel array near the top of the component (Point E) and exits at the bottom of the rectification section (Point F), flowing counter to the vapor. The vapor stream exits the assembly through an external port at the top of the component (Point G). The internal features of the branched tray desorber are designed to maximize the pool-boiling wall area per unit volume, while allowing sufficient flow area for the rising vapor to avoid flow reversal at the highest expected vapor generation rates. Additionally, the branched tray ribs are designed as structural members of the VGU, and bonding considerations played a role in the thickness and location of these features. This is the case for the fin structures in the analyzer and rectifier sections as well. Once the VGU plates are bonded, these features support the forces resulting for the appreciable pressure difference (as much as 3000 kPa in common applications) between the coupling- and working-fluid passages, and prevent the plates from rupturing or collapsing.

The rationale for using different rectifier designs in the vertical column and branched tray VGUs is two-fold. First, the vertical column geometry provides the necessary structural support in the rectifier through use of the vertical ribs that separate the falling-film surfaces (Figure 2.1), making the vertical wall a viable geometry. In the branched tray rectifier, structural features are required. Due to flexibility in the fabrication methods, the diagonal fin surfaces were designed to provide the required support as well as enhancement of the heat transfer process. In addition, the two different rectifier designs allow the exploration of alternate geometries.

The test sections developed for the present study are based on the full-scale vertical column and branched tray VGU concepts discussed above. Details of the modeling, design, and fabrication of the test sections are provided in the following chapter (Section 3.1).

Keinath *et al.* (2015) conducted an experimental investigation of component performance in the full-scale branched tray VGU, which was constructed based on the designs described above. The unit was tested as part of a single-pressure system on a breadboard test facility and was studied over a range of heat transfer fluid inlet temperatures and flow rates, and concentrated solution flow rates. Desorber performance was experimentally investigated over a wide range of test conditions to improve the understanding of performance at design and off-design conditions, and the potential for flow instabilities. The unit was found to achieve stable operation and was able to produce vapor generation rates commensurate with design conditions. The maximum vapor generation rate observed was in excess of 12 kg hr^{-1}, while the baseline design condition was approximately 11 kg hr^{-1}. However, required desorber heat duties were approximately 25% higher than expected to achieve baseline vapor generation rates. They suggested that this may have been due to over-rectification of the generated vapor. Additionally, some flow instabilities were observed at high source temperatures (190°C) and solution flow rates (above 32 kg hr^{-1}), which limited system performance at these conditions. This phenomenon was attributed to the onset of flooding. While the study served to demonstrate the feasibility of the branched tray concepts, additional investigation at the component and sub-component level, including more detailed investigation of the local heat and mass transfer processes and flow visualization, were recommended by them.

2.2 Absorption Heat and Mass Transfer Studies

To develop effective, high-flux heat and mass exchangers for compact ammonia-water absorption systems, it is critical to understand the governing coupled heat and mass transfer processes. The VGU configurations proposed for investigation in the present study are expected to operate primarily in the falling-film and pool-boiling modes. A brief review of some of the relevant literature for these two flow mechanisms follows.

2.2.1 Binary Pool-Boiling

While the study of boiling phenomena is well-established, literature on pool-boiling of ammonia-water mixtures is sparse, and agreement between available correlations and models for heat and mass transfer performance is poor (Inoue *et al.*, 2002a; Táboas *et al.*, 2007). This may be due to the fact that few data are available for the boiling of ammonia-water mixtures, and the majority of studies are conducted at idealized conditions that may not be representative of geometries typically used in ammonia-water desorbers. The development of widely applicable correlations for boiling of ammonia-water mixtures is made particularly difficult by the zeotropic nature of the mixture, resulting in large concentration differences between the phases and the resulting mass transfer resistances. Compared with those of the pure components, reported heat transfer coefficients for ammonia-water mixtures are typically far lower than the value that a molar- or mass-average value of the pure component coefficients would indicate (Inoue *et al.*, 2002a; Arima *et al.*, 2003). This suppression of heat transfer performance has proven difficult to predict over wide ranges of conditions and mixture compositions (Inoue *et al.*, 2002a; Táboas *et al.*, 2007).

Many binary fluid boiling correlations, developed for, or generally applicable to zeotropic fluids, are found in the literature. Available correlations attempt to account for the degradation in heat transfer coefficient, compared to the pure component values, which may be observed during the boiling of zeotropic mixtures. To do so, an ideal boiling heat transfer coefficient is defined, based on either the mixture properties, or a molar weighted average of the pure component heat transfer coefficients. In the present study, all binary fluid mixture boiling correlations considered use the molar average method.

To determine the pure component boiling heat transfer coefficients, suitable correlations must be used. Applicable pure ammonia correlations include the studies of

Gorenflo (1993), Stephan and Abdelsalam (1980), and Nishikawa and Fujita (1977). The correlation of Gorenflo (1993) was developed using a large body of experimental data and empirical constants specifically for ammonia, which is uncommon among boiling correlations. This correlation has been evaluated in several other ammonia boiling studies (Táboas *et al.*, 2007; Spindler, 2010; Golden, 2012) and was found to provide good agreement with experimental results for both pure ammonia boiling (Spindler, 2010) and when applied to binary fluid mixture boiling correlations (Golden, 2012). Notably, the studies of Spindler (2010) and Golden (2012) both consider cases with heat fluxes and saturation pressures that are similar in magnitude to those in the present study.

The correlation developed by Stephan and Abdelsalam (1980) has also been considered in other studies of ammonia pool-boiling (Táboas *et al.*, 2007; Spindler, 2010; Golden, 2012). This correlation has a specific formulation for refrigerants, which has been used in other studies to predict ammonia boiling coefficients. Golden (2012) found this correlation to give good agreement with data for pool-boiling of ammonia-water mixtures, and Táboas *et al.* (2007) reported good agreement with data from experimental studies that focused on lower heat fluxes. However, Spindler (2010) reported that the correlation under predicted experimental results due to a weak dependence on pressure.

Finally, the highly empirical correlation of Nishikawa and Fujita (1977) is useful in considering pool-boiling of pure ammonia. This correlation also has empirical constants available for ammonia, specifically, and has been reported to agree well with pure ammonia boiling data (Inoue *et al.*, 2002a; Arima *et al.*, 2003). This correlation has also been employed as a basis for binary fluid mixture boiling correlations in previous studies (Inoue *et al.*, 2002a; Arima *et al.*, 2003).

Considering correlations for the pool-boiling of pure water, several studies have investigated the applicability of numerous correlations to the binary fluid mixture boiling of ammonia-water solutions (Inoue *et al.*, 2002a; Táboas *et al.*, 2007; Golden, 2012) . The correlations of Gorenflo (1993) and Stephan and Abdelsalam (1980) were found by Táboas *et al.* (2007) to provide good agreement with data at heat fluxes similar to those of interest in the present study, specifically those of Kang (2000) and Borishanskii *et al.* (1964), who reported pool-boiling heat fluxes of 1.4-155 and 20 kW m^{-2}, respectively.

As discussed previously, corrected binary fluid mixture boiling heat transfer coefficients typically use an ideal binary fluid mixture boiling coefficient, which is based on pure component correlations, such as those discussed above. The ideal coefficient is corrected through the use of a correction factor that is typically a function of either the mixture temperature glide (difference in bubble- and dew-point temperatures), ΔT_{glide}, or the molar concentration difference between the liquid and vapor phases, $(\tilde{x}_v - \tilde{x}_l)$. Notable binary fluid mixture boiling correlations with correction factors that are based on the molar concentration difference include that of Thome (1981), Stephan and Körner (1969), and Schlunder (1982). Correlations that use the temperature glide in the correction factor include Thome and Shakir (1987), Inoue *et al.* (1998), and Fujita and Tsutsui (1997). Táboas *et al.* (2007) present a correlation that uses both the molar concentration difference and temperature glide, by combining the correction methods of Schlunder (1982) and Thome and Shakir (1987). The correlation of (Thome, 1981) is unique among the correlations mentioned here as it is purely analytical and does not rely on any empirical coefficients, although it does require knowledge of the liquid-phase mass diffusivity. Additional discussion of these correlations is given in relation to the experimental results of the present study in Section 5.3.3. The formulations for the pure and binary correlations discussed here are also provided in Section 5.3.3.

Táboas *et al.* (2007) conducted a comprehensive survey of published work in this area, which compiled much of the available experimental data on heat transfer coefficients for pool-boiling of ammonia and ammonia-water mixtures and presented a comparison with the predictions of the available correlations. Even for the relatively simple case of pure ammonia, significant variation was found in the pool-boiling heat transfer coefficients predicted by different correlations and some trends in the data were not captured effectively by any models. In the more complex case of ammonia-water mixtures, agreement between correlations was also poor and tended to under-predict the data originally presented by Inoue *et al.* (2002a) and Arima *et al.* (2003) by a significant margin, with errors of more than 100% for some conditions. They developed a new correlation for use with ammonia-water mixtures by combining the correlations of Schlunder (1982) and Thome and Shakir (1987) based on the bulk ammonia mass concentration of the fluid. The new correlation was reported to fit most data to within 40% error. They stressed that additional experimental work on boiling of ammonia-water mixtures is critically needed to supplement the available data and to help improve the understanding of the underlying phenomena.

Two of the most prominent experimental investigations of ammonia-water pool-boiling are by Inoue *et al.* (2002a) and Arima *et al.* (2003). Both studies utilize an idealized boiling surface that allows for careful measurement of heat input and control of surface features. Inoue *et al.* (2002a) utilized an electrically heated horizontal platinum wire, submerged in a pool of ammonia-water solution, as the nucleation surface. Heat transfer coefficients were reported over a range of heat fluxes, concentrations and pressures. The maximum pressure tested was 0.7 MPa. Cases with pure ammonia and pure water were also considered. They found that no existing correlation adequately predicted all trends observed in the ammonia-water mixture data, including the correlations of Stephan and Körner (1969) and Schlunder (1982). However, the single-component Nishikawa-Fujita correlation (Nishikawa and Fujita, 1977) was found to be in good agreement with pure ammonia and pure water data collected during the study, and was employed in calculating the heat transfer coefficients of the mixture. In the study by Arima *et al.* (2003), a horizontal polished sliver plate is used as the nucleation surface. The plate is electrically heated. Heat transfer coefficients were reported for a range of heat fluxes, concentrations and pressures, with maximum pressures of 1.5 MPa – closer to pressures typical of ammonia-water desorbers. Results were compared with the correlations of Inoue *et al.* (1998), which tended to under-predict values of the mixture heat transfer coefficient, and Stephan and Körner (1969), which tended to over-predict the values. They developed their own correlation to better match their data. Correlations by Stephan and Abdelsalam (1980) and Nishikawa and Fujita (1977) were employed for determining heat transfer coefficients for pure ammonia.

2.2.2 Binary Falling-Film Evaporation and Boiling

Falling-film absorption components are common in both ammonia-water and lithium bromide-water absorption systems. Such components typically employ a tube-bank design with a thin liquid film coating the external surfaces of the tube array and a heating (desorber) or cooling (absorber) fluid circulating through the tubes. The vertical column desorber, proposed for use in the present study, is also designed to operate in the falling-film mode, but rather than tube-bank geometry, a vertical wall with surface enhancement is employed.

Killion and Garimella (2001) presented a critical review of falling-film heat and mass transfer models for absorption heat pump components. Attention is given to modeling efforts based on the early modeling and design work of Price and Bell (1974) and the framework of Colburn and Drew (1937), in which a method for analyzing coupled heat and mass transfer during phase-change of binary fluids is proposed. Among the conclusions, they report that experimental validation is very limited for most of the modeling efforts and more thorough local measurements within components would be beneficial in improving understanding of the heat and mass transfer process and in validating modeling results. Additionally, it is concluded that many of the existing modeling approaches employ widely varying idealizations and assumptions about the hydrodynamics, such as assumptions concerning mixing of the liquid film, surface wetting, impact of film waviness, etc. There does not appear to be a consensus on which assumptions and simplifications can be reasonably applied to given geometries or conditions. As such, they recommend careful consideration of simplifying assumptions and experimental exploration of the proposed geometry and conditions along with experimental validation of models.

In a subsequent study, Killion and Garimella (2003) present a detailed review of experimental investigations of falling-films. The study focuses on the horizontal tube bank geometry and absorption of water, which is more applicable to water-lithium bromide systems, than ammonia-water systems. However, the study does offer some insight into the effect of a number of operating conditions, such as solution and coupling-fluid flow rates, on the performance of compact falling-film heat and mass exchangers, which is applicable to the present study. Additionally, Killion and Garimella (2003) emphasize that future investigations should examine both the heat and mass transfer processes of binary mixture falling-film absorption devices simultaneously, as consideration of either process independently fails to adequately predict component performance. They also suggest that any new investigations include parametric studies across a range of expected operating conditions, to allow for the optimization of system and component operation, and to facilitate the development of more widely applicable modeling methods and correlations.

Regardless of the framework and assumptions used to account for the effects of combined heat and mass transfer, an appropriate correlation must be used to determine the ideal film evaporation or boiling heat transfer coefficient. Several correlations are available in the literature that are applicable to falling-film evaporation in geometries similar to the vertical column desorber.

One of the most commonly-employed film evaporation correlations for downward flow along vertical surfaces is that of Chun and Seban (1971). In this correlation, an empirical enhancement factor is applied to the analytical Nusselt equation (Nusselt, 1916), originally developed for condensing films. Chun and Seban (1971) present formulations for both laminar and turbulent films. This correlation is recommended for use primarily with saturated films (Rohsenow, 1985). An earlier empirical correlation is presented by Wilke (1962) for downward flow along vertical surfaces, and is recommended for subcooled films (Rohsenow, 1985). Here, a curve-fit coefficient and exponent are applied to the film Reynolds number. Values of these empirical parameters are given for three ranges of film Reynolds number, corresponding approximately to laminar, transitional, and turbulent regimes. Different formulations of the film thickness are also recommended for the three regimes.

The case of combined falling-film evaporation and nucleate boiling for flow down vertical surfaces is not well-studied, but is expected to be a possible mode of heat transfer in the vertical column geometry. Few correlations are available in the literature for this case; however, Rohsenow (1985) does present the correlation of Damman (1973). This semi-empirical correlation is suggested for the case of fully-developed nucleate boiling of saturated films of water and aqueous solutions. Additionally, the range of film Reynolds numbers and heat fluxes used by Damman (1973) in the development of the correlation correspond well to the expected conditions for the vertical column VGU. Additional discussion of these correlations is given in connection with the experimental results of the present study in Section 5.3.5.

A review of primarily experimental studies of falling-film absorption by Fujita (1993) devotes much attention to the effects of film waviness, mixing, and instabilities on the performance of both absorber and desorber heat and mass exchangers. An overview of surface enhancement and roughness on vertical falling films is discussed, with analysis of several specific geometries presented. Published work on film breakdown and surface wetting is also reviewed. While the study considers, almost exclusively, the use of lithium bromide-water as the working fluid, the author notes that this is due to a lack of available published work on other fluids such as ammonia-water. It is also noted that, while horizontal tube-bank film heat exchangers dominate commercially available absorption components, vertically oriented components hold promise for future systems.

Experimental work focusing specifically on ammonia-water falling film absorption components, and desorbers specifically, is quite limited. As noted previously, Determan and Garimella (2011) successfully demonstrated a residential-scale tube-bank ammonia-water desorber. The design and modeling of the component was similar to that used in earlier studies by Kang and Christensen (1994), and based on the absorber studies of Meacham and Garimella (2002b, 2003, 2004). Sieres and Fernández-Seara (2007) developed a coupled heat-and mass transfer model for ammonia-water absorption and desorption. The modeling approach was again based on the framework of Colburn and Drew (1937), but considered heat and mass transfer resistances in both the liquid and vapor phases. The model was applied to the analysis of a packed-bed rectification column and the results were validated with experimental data. While the validation was limited to only the fluid inlet and outlet temperatures, the modeling results agreed well with the data. Additionally, the modeling work predicts that absorption of water and desorption of ammonia is possible at certain locations within the column, a result also reported by other investigators (Determan and Garimella, 2011).

2.2.3 Condensation

As in the vertical column desorber section, the rectifier sections of both concepts rely on phase-change heat transfer occurring on vertical surfaces. In the rectifier sections, this is a coupled heat and mass transfer problem involving the partial condensation of the ammonia-water refrigerant vapor. As mentioned previously, both equilibrium and non-equilibrium methods have been developed. However, use of an appropriate heat transfer correlation is required to determine the ideal heat transfer coefficient for the condensation process.

Again, many analytical models and correlations are available in the literature pertaining to condensation on a cooled, vertical surface. In the interest of capturing the range of condensation phenomena expected in the rectifier sections, both dropwise and film condensation correlations are considered in the present study.

Several analytical models have been developed for film condensation on vertical surfaces. The original model, developed by Nusselt (1916), is widely cited, and has served as a basis for the modeling of both condensation and evaporation in falling-film geometries. The model of Rohsenow *et al.* (1956) builds on this framework and includes the effects of vapor shear at the liquid-vapor interface. They provide an improved equation set for laminar films that can be used to determine the average Nusselt number and subsequently the average film heat transfer coefficient. Additionally, a criterion is developed for prediction of the transition from laminar to turbulent film flows, though the present study is only concerned with laminar films in the rectifier.

The semi-empirical correlation of Kutateladze (1982) was developed for falling-film condensation processes with wavy interfaces and film Reynolds numbers ranging from 0 to 400. The correlation is based on analytical models with several curve-fit parameters that were matched to a fairly extensive data set covering several fluids. The correlation has been found to agree well with data other than those for liquid metals (Carey, 2008).

Dropwise condensation could also occur in some regions of the rectifiers and it is important to consider these conditions, as heat transfer coefficients may be an order of magnitude greater than those for film condensation. While many dropwise condensation correlations have been developed for specific fluids, surfaces, and conditions, wide applicability to other cases is unsubstantiated (Carey, 2008). No dropwise condensation correlations applicable to ammonia-water mixtures were found in the literature. To provide some indication of the expected magnitude of the heat transfer coefficient at these conditions, the dropwise correlation of Rose *et al.* (1999) is considered during data analysis in subsequent chapters. The formulation, developed for the dropwise condensation of steam, is highly empirical, but has been shown to have good agreement with available data (Carey, 2008).

2.3 Research Needs

While some progress has been made in addressing the need for more effective, miniaturized absorption heat and mass exchangers, previous efforts have focused primarily on absorber design and analysis. Additionally, the majority of absorption heat and mass transfer studies consider lithium bromide-water working fluids, rather than ammonia-water. While some studies have been conducted on ammonia-water desorption and rectification components, they have either relied on designs that are still too large or expensive to be easily fabricated and integrated into compact residential or mobile systems, or have not incorporated a counter-flow arrangement between the solution and vapor streams within the desorber, resulting in the need for larger rectification components and potentially lower refrigerant concentration and a corresponding degradation of system performance.

Additionally, there is still a need for further studies of desorption and rectification heat and mass transfer for ammonia-water mixtures in practical, compact components. The literature on ammonia-water phase change focuses almost exclusively on idealized or large-scale geometries, and the component designs that have been studied typically employ tube-bank configurations, which are not particularly well suited to, or representative of, highly compact desorber-rectifiers. Even within these studies, there are wide discrepancies in predicted heat and mass transfer performance and little consideration of the impact of practical hydrodynamic phenomena such as component flooding, surface wetting, liquid-vapor shear, and fluid mixing.

2.4 Objectives of Present Study

While several studies in the literature have presented modeling methods and some limited experimental studies of compact counter-flow geometries for use in the desorption and rectification of ammonia-water, the understanding of the fluid-flow phenomena and heat and mass transfer processes within these components is quite limited. As such, it is difficult to predict the performance at the component-level and the overall impact on system operation. Additionally, selection of the correct methods and correlations for use in the modeling and design of these components is difficult, and is often based on unsubstantiated assumptions about the internal operating conditions of the components. Thus, a detailed investigation of the two proposed VGU concepts is required.

The objectives of this investigation are to:

1. Model, design, and develop two VGU concept test sections using the vertical column and branched tray desorber geometries.
2. Conduct heat and mass transfer experiments to evaluate the performance of the desorber and rectifier sections, including heat and mass transfer coefficients, and to investigate overall VGU performance over a range of realistic operating conditions.

3. Compare the experimental results with existing correlations and modeling methods available in the literature.
4. Develop refined models of the concept VGUs based on the results of the experimental investigations.

CHAPTER 3

EXPERIMENTAL APPROACH

To characterize performance of the novel desorber-rectifier test sections over a range of conditions representative of ammonia-water absorption heat pump operation, an experimental facility, as well as two VGU test sections, were designed and fabricated. The experimental facility is used to condition and supply the necessary working-fluid and coupling-fluid streams to the test sections. Performance of the test sections is evaluated over a range of ammonia-water solution flow rates, concentrations, and heating-fluid temperatures that are provided in the following sections. The instrumentation and data acquisition system installed on the facility provide local measurements of temperatures, pressures, and flow rates, which are used subsequently to evaluate the heat and mass transfer performance of the test sections. Details of the test section modeling and design, test facility specifications, instrumentation, and operating procedures, are provided in the following sections.

3.1 VGU Test Sections

3.1.1 Test Section Modeling

To estimate the required component sizes and optimize the geometry of the internal features, segmented heat and mass transfer models are developed for both the branched tray and vertical column desorber concepts described in Section 2.1.2. Both models have similar architecture, but utilize heat and mass transfer correlations that are appropriate for the internal geometries and expected flow regimes of each geometry. With these models, the variations in local heat and mass transfer resistances can be estimated throughout the component and the composition and properties of the various fluid streams may be calculated.

Similar models have been developed and documented in previous studies for the modeling of heat and mass exchangers, with Price and Bell (1974) pioneering a technique based on the film theory framework proposed by Colburn and Drew (1937) for the condensation of miscible binary mixtures. Many other studies have used this technique, including several specific to ammonia-water absorption system components (Kang and Christensen, 1994, 1995; Garrabrant and Christensen, 1997; Kang *et al.,* 1997; Kang *et al.,* 1998; Meacham and Garimella, 2003, 2004). Recently, Determan and Garimella (2011) applied this modeling technique to the development of a falling-film tube-bank desorber with some similarities to the present study. Nagavarapu and Garimella (2011) also applied a similar approach for the modeling of an ammonia-water absorber.

For both the branched tray and vertical column desorbers, the liquid solution is assumed to be well-mixed, such that negligible concentration profiles exist across any liquid film or pool. Desorption of vapor from the liquid phase is then governed by the mass transfer process from the two-phase interface to the vapor bulk. The molar flux of vapor being desorbed from liquid solution is given by:

$$\dot{n}''_T = -C_T \beta_v \ln\left[\frac{\tilde{z} - \tilde{x}_{v,int}}{\tilde{z} - \tilde{x}_{v,bulk}}\right] \tag{3.1}$$

In this equation, C_T represents the total molar concentration of the vapor. The parameters of the molar concentration gradient include the molar concentration of the condensing flux, $\tilde{z}$, the equilibrium molar concentration of the vapor at the interface, $\tilde{x}_{v,int}$, and the molar concentration of the vapor bulk, $\tilde{x}_{v,bulk}$. The vapor interface molar concentration is determined from the local quality (saturated vapor), pressure, and temperature. The vapor interface temperature is assumed to be equal to the liquid interface temperature, which is determined from the thermal resistance network described below. The vapor mass transfer coefficient, β_v, is determined from a heat and mass transfer analogy. In both concepts, the vapor flow is laminar, with maximum vapor Reynolds numbers for the branched tray and vertical column predicted to be 390 and 1500, respectively. As such, the corresponding vapor heat transfer coefficients are given by the constant Nusselt number solutions for rectangular channels presented in Kays *et al.* (2005). The rates of desorption for the ammonia and water components are determined individually from the following equations:

$$\dot{m}_{des,a} = M_a \dot{n}''_a A \tag{3.2}$$

$$\dot{m}_{des,w} = M_w \dot{n}''_w A \tag{3.3}$$

M_a and M_w are the molar masses of ammonia and water, respectively, and A is the interface area available for the mass transfer process, calculated for the given geometries of the two concepts. The outlet flow rates and concentrations for each segment may be determined by application of mass and species balances, assuming steady operation.

$$\dot{m}_{l,in} + \dot{m}_{v,in} = \dot{m}_{l,out} + \dot{m}_{v,out} \tag{3.4}$$

$$\dot{m}_{l,in} x_{l,in} + \dot{m}_{v,in} x_{v,in} = \dot{m}_{l,out} x_{l,out} + \dot{m}_{v,out} x_{v,out} \tag{3.5}$$

A value for $\tilde{z}$ is required to evaluate the desorption rate as outlined above. This may be determined by applying an energy balance on the solution-side of the component for each segment.

$$\dot{Q}_{seg} = \dot{m}_{l,out} h_{l,out} + \dot{m}_{v,out} h_{v,out} - \dot{m}_{l,in} h_{l,in} - \dot{m}_{v,in} h_{v,in} \tag{3.6}$$

This equation accounts for both the sensible heating of the solution stream as well as the latent heat of desorption. Coupled with the mass and species balances above, the mass flow rates may now be calculated. Solution inlet and outlet enthalpies are calculated from the corresponding equilibrium conditions assuming a saturated solution stream. Vapor inlet enthalpy is known from the output of the previous segment. Vapor outlet enthalpy is determined by evaluating the sensible heating of the vapor stream by the liquid. This heat transfer process may be described as follows:

$$\dot{Q}_v = \alpha_v \left(\frac{\phi}{1 - e^{-\phi}} \right) A \cdot LMTD_v \tag{3.7}$$

Where α_v is the vapor heat transfer coefficient and $LMTD_v$ is the logarithmic mean temperature difference between vapor and liquid streams. The Ackerman correction factor (the term in the parentheses) is applied to account for the influence of mass transfer on the process. The parameter, ϕ, used in this factor is given by:

$$\phi = \frac{\left(\dot{n}_a'' \tilde{C}_{p,a} \right) + \left(\dot{n}_w'' \tilde{C}_{p,w} \right)}{\alpha_v} \tag{3.8}$$

Here $\tilde{C}_{p,a}$ and $\tilde{C}_{p,w}$ are the molar specific heats of the ammonia vapor and water vapor, respectively. From these equations, the vapor outlet enthalpy may be determined.

To complete the model, the heat transfer from the coupling fluid to the solution must be considered. The heat duty on the coupling fluid side can be expressed by an energy balance:

$$\dot{Q}_{seg} = \dot{m}_{cf} c_{p,cf} \left(T_{cf,in} - T_{cf,out} \right) \tag{3.9}$$

The model segments are defined by equal heat duties, with the total heat duty for the component defined based on system design decisions. The coupling fluid flow rate is determined by consideration of pressure drop through the coupling fluid channels (described in more detail below), and the coupling fluid inlet temperature to the first segment is specified based on the available system heat source. Thus, the inlet and outlet temperatures for the coupling fluid are defined for all segments.

Finally, to calculate the required size of the component, the heat transfer process between the coupling fluid and solution must be considered:

$$\dot{Q}_{seg} = \left(\frac{1}{R_T} \right) \cdot LMTD_{cf,sol} \tag{3.10}$$

Here the driving temperature difference, $LMTD_{cf,sol}$, is the temperature difference between the coupling fluid and the ammonia-water solution. The thermal resistance to heat transfer between these fluids can be estimated as follows:

$$R_T = R_{cf} + R_{wall} + R_{sol} \tag{3.11}$$

Where R_{cf} is the thermal resistance from the coupling fluid bulk to the wall, R_{wall} is the conduction resistance through the microchannel wall separating the coupling fluid and solution streams, and R_{sol} is the thermal resistance from the wall to the bulk solution.

In both concepts, microchannel geometry is used for the coupling fluid stream. The thermal resistance R_{cf} is modeled by utilizing a fin-array approach described by Determan and Garimella (2012) for microchannel components and also utilized by Nagavarapu and Garimella (2011). This approach is discussed in further detail in Section 4.3.3, and a schematic of the geometry is shown in Figure 4.9. The convective heat transfer coefficient used in this approach is calculated using the single-phase analytical solution for semi-circular channels (Sparrow and Haji-Sheikh, 1965).

The thermal resistance on the solution side R_{sol} is modeled assuming a falling-film process in the vertical column geometry and a pool-boiling process in the branched tray geometry. For the falling-film process, the heat transfer coefficient is calculated using the correlation of Chun and Seban (1971). To determine the heat transfer coefficient for the binary-fluid pool-boiling process, first the single-component pool-boiling heat transfer coefficients for both pure ammonia and pure water are computed. The nucleate boiling correlation developed by Rohsenow (1952) is applied in these calculations. A molar average, ideal binary coefficient is then computed:

$$\alpha_{ideal} = \left[\frac{\tilde{x}_{a,sol}}{\alpha_a} + \frac{1-\tilde{x}_{a,sol}}{\alpha_w} \right]^{-1} \tag{3.12}$$

Here $\tilde{x}_{a,sol}$ is the mole fraction of ammonia in the solution stream, while α_a and α_w are the pure component heat transfer coefficients for ammonia and water, respectively. This ideal heat transfer coefficient is then corrected using a correlation that accounts for the mass transfer resistance inherent in the boiling of zeotropic mixtures. In this case, the correlation of Stephan and Korner (1969) is applied as suggested by Inoue *et al*. (2002a) in their survey of binary pool-boiling correlations. A value of 3.10 is used for the Stephan Korner constant, A_o, based on the more recent study of Thome (1983). This corrected, binary heat transfer coefficient can then be used to determine the thermal resistance R_{sol}. With the geometry for both concepts defined, the model may be closed by iterating on the segment length (heat transfer area) until the values of $\dot{Q}_{seg}$ given in Eq. (3.6), (3.9), and (3.10) are matched.

In addition to consideration of the desorption process described above, the models for both concepts also consider the heat and mass transfer processes in the analyzer and rectifier sections. The analyzer section is considered as an additional segment of the desorber models, but the overall heat duty for the segment is set to zero as the analyzer is an unheated section. As such, no heat is added to the solution stream from the coupling fluid in this segment, but heat and mass exchange does occur between the solution and vapor streams.

Consideration of the rectifier requires a somewhat different approach than that required for the desorber and analyzer. While the architecture is similar, with a segmented model tracking the fluid properties for vapor and liquid stream, and similar modeling of the heat transfer process to the coupling fluid, the rectifier is not well suited to the Colburn-Drew framework as the extremely high vapor concentrations and the resulting steep temperature gradients can cause computational instabilities. Instead, the vapor and liquid phases are both assumed to be at saturated equilibrium locally within the rectifier and the Silver-Bell-Ghaly (SBG) method (Silver, 1947; Bell and Ghaly, 1972) is applied. This eliminates the need to consider the mass transfer process explicitly and the heat transfer process is evaluated as in the desorber segments. In both concepts, the liquid condensate, or reflux, is expected to exist primarily in a falling-film regime and the correlation of Chun and Seban (1971) is again applied to determine the liquid heat transfer coefficient. The vapor heat transfer coefficient is determined as in the desorber segments. The SBG method is discussed in additional detail in Section 5.3.5.

The pressure drop for both heating and cooling fluids was estimated and utilized as a guide to determine the allowable or optimal coupling fluid flow rates, and the number of parallel channels in the microchannel arrays. In both the desorber and rectifier sections, the Sparrow and Haji-Sheikh (1965) friction factor correlation for semi-circular microchannels was applied to determine the pressure drop along the length of the microchannels. Additional terms accounting for pressure drop through the headers and minor losses were included in the analysis based on prior experimental evaluation of similar geometries. Total coupling fluid pressure drop through the desorbers of both concepts is predicted to be less than 30 kPa at the specified flow rates. Coupling fluid pressure drop on the rectifiers of both concepts is predicted to be less than 2 kPa at the specified flow rates. Desorber coupling fluid pressure drop is significantly higher than rectifier coupling fluid pressure drop due to the higher mass fluxes (approximately 360 kg m^{-2} s^{-1}) and higher viscosity (approximately 0.0010 kg m^{-1} s^{-1}, at 180°C baseline conditions) of the heating fluid. For comparison, the mass flux and viscosity of the rectifier coupling fluid are approximately 79 kg m^{-2} s^{-1} and 0.0005 kg m^{-1} s^{-1}, respectively, at the design conditions. Flow through the solution passages is designed to be gravity driven and pressure drop is considered negligible.

One additional consideration that can place constraints on the heat and mass transfer processes of compact counter-flow desorbers, such as the test sections considered here, is the potential for flooding. If the difference in velocities between the vapor and liquid phases becomes too large within the solution channels, momentum exchange can lead to liquid entrainment and ultimately to flooding of the component. Flooding dramatically reduces the effectiveness of the analyzer and rectifier. Performance of the condenser and evaporator can also be severely degraded if liquid becomes entrained in the rectifier vapor outlet. As such, care must be taken to ensure that sufficient cross-sectional area is present in the solution channels to limit vapor velocities to a manageable level. The method of Wallis (1969) was used to estimate flooding limits. While this method uses a one-dimensional model and was developed based on data from far simpler geometries, such as plain vertical tubes, it does capture the most important momentum-exchange parameters that lead to flooding. Additionally, no other correlations in the literature were found to address the complex geometries of interest in the present study. Wallis (1969) presents the following general equation to predict flooding in vertical tubes.

$$C = j_v^{*1/2} + m \cdot j_l^{*1/2} \tag{3.13}$$

Here, C, is the flooding coefficient, which corresponds to the onset of flooding. The parameters j_v^* and j_l^* are dimensionless groups that relate the momentum fluxes to the hydrostatic forces for the vapor and liquid phases, respectively.

Values of 0.70 and 1.0 were used for the empirical constants, C and m, respectively. These values were found to correspond reasonably well to the onset of flooding based on experimental flooding studies conducted with air and methanol-water solution in geometries similar to those utilized in these designs. For comparison, the method outlined by Kwon and Jeong (2004) was also employed to estimate the maximum allowable vapor velocity before the onset of flooding. The Wallis method was found to result in more conservative designs. For example, with all other conditions held at baseline values, the branched tray desorber is predicted by Wallis (1969) to flood at vapor velocities greater than 0.529 m s^{-1}, while the correlation of Kwon and Jeong (2004) predicts that flooding will not occur until vapor velocities exceed 0.605 m s^{-1}. Additionally, by using the experimentally validated value of the empirical constant, C = 0.70, with the Wallis (1969) method, adequate cross-sectional area for vapor flow is expected to be achieved.

This modeling method was used to determine the appropriate sizing for the VGU test sections. The details of the designs are given in the following section. In addition to providing sizing information for the test sections, the model is capable of predicting many of the fluid properties and segment parameters, such as heat duty or vapor generation rate. These parameters can be used to gain insight into the internal operation of the VGUs and an overview of the initial model results is provided here. A revised model based on an interpretation of the experimental results is presented and discussed in Chapter 6.

Predicted temperatures for the ammonia-water vapor and solution streams and coupling-fluids are shown in Figure 3.1. The predicted temperatures are very similar for both test sections; however, the vertical column is shown to have increased vapor-to-solution heat transfer in the desorber section, leading to lower vapor temperatures. The working-fluid flow rates and mass-basis concentrations are shown in Figures 3.2 and 3.3, respectively. Flow rates of the solution and vapor are predicted to be similar for both designs, although the branched tray reflux flow rate is appreciably higher than that of the vertical column. This is explained by examining the concentration profiles shown in Figure 3.3. Here, the vertical column is shown to produce significantly higher concentration vapor in the desorber and analyzer sections. This is due to higher average

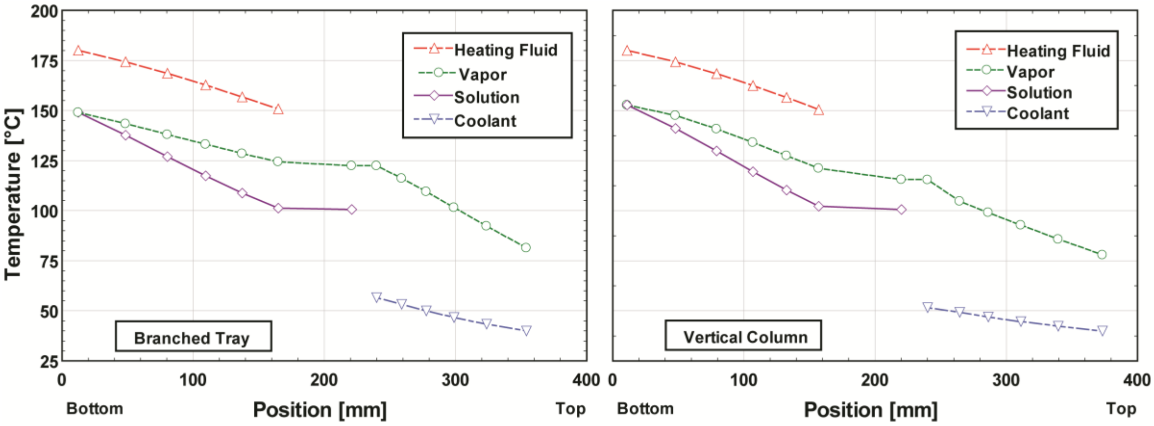

Figure 3.1 : Predicted test section temperatures

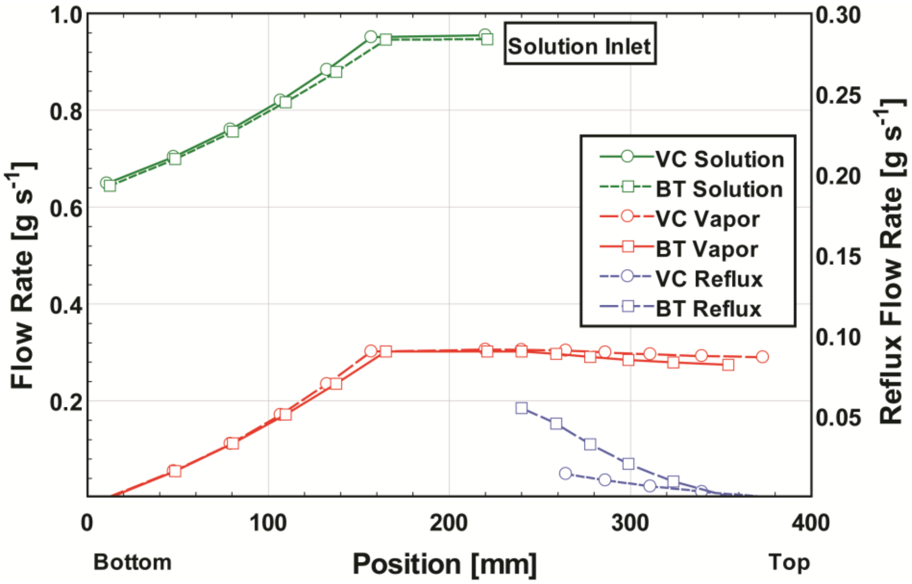

Figure 3.2 : Predicted test section mass flow rates; shown for vertical column (VC) and branched tray (BT)

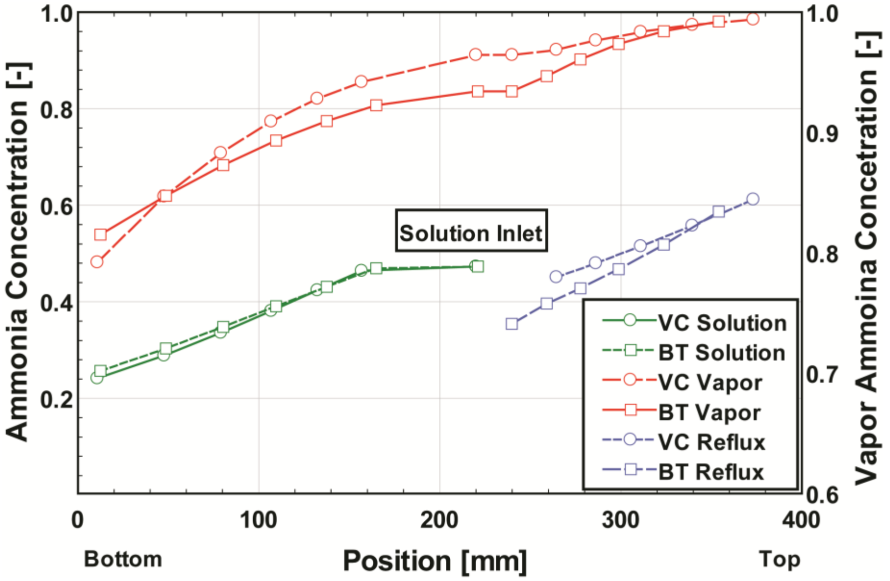

Figure 3.3: Predicted ammonia concentrations; shown for vertical column (VC) and branched tray (BT)

predicted vapor heat transfer coefficients in these sections of the vertical column (approximately 80 W m^{-2} K^{-1} and 20 W m^{-2} K^{-1}, in the vertical column and branched tray, respectively), which allow the hot, rising vapor to reject more heat back to the cooler solution. As a result, the vapor temperature exiting the analyzers was predicted to be

115.6°C and 122.4°C for the vertical column and branched tray, respectively. The resulting higher vapor concentrations for the vertical column rectifier inlet reduce the required water condensation rate in the rectifier, leading to lower reflux flow rates and rectifier duties while maintaining the same vapor outlet concentration. However, using the branched tray design, it is possible to implement a more effective rectifier geometry. This is due to more flexibility in the manufacturing process, since the full-scale branched tray solution plates are machined, while the full-scale vertical column solution passages are made with a chemical etching process. The constraints associated with the full-scale components were applied to the test sections as well, to provide the most realistic results. The flexibility in the design of the branched tray rectifier allows for rectifier passages with a smaller hydraulic diameter, resulting in higher vapor heat transfer coefficients (approximately 180 W m^{-2} K^{-1}, versus 140 W m^{-2} K^{-1}in the vertical column). This increase leads to higher condensation rates, per unit area, and allows the two designs to produce similarly high refrigerant concentrations and flow rates in approximately the same envelope size.

3.1.2 **Test Section Design**

The heat and mass transfer modeling methods described above are utilized in the design of integrated VGU components for an ammonia-water absorption cooling system. Designs based on both the branched tray and vertical column geometries are developed and the resulting major dimensions and predicted capacities are reported here. The design conditions for the modeled components are specified from a cycle-level simulation of a representative absorption cooling system and the test sections were sized to support an absorption chiller with a nominal cooling capacity of 300 W per VGU consisting of one assembly of the configurations described above, with a heat input of approximately 590 W. For larger cooling duties, in an actual application, these VGUs would be duplicated as necessary. Key design conditions and geometric specifications are given in Table 3.1.

The microchannel geometry used in these designs is similar to that used by Nagavarapu and Garimella (2011), although the channel pitch and length have been modified for the present application. Compared to the larger capacity (13 kW) tube-bank falling-film desorber studied by Determan and Garimella (2011), the present concepts can be produced more readily at high volumes and can be more effectively packaged in a

Table 3.1: Test section design inputs and outputs

	Input Conditions	
$\dot{m}_{l,in}$ **(g s^{-1})**	0.946	
$x_{l,in}$	0.477	
$q_{l,in}$	0.0	
P **(kPa)**	2094	
$T_{des,CF,in}$ **(^{o}C)**	180.0	
$\dot{m}_{cf,des}$ **(g s^{-1})**	7.716	
$T_{rect,CF,in}$ **(^{o}C)**	39.95	
$\dot{m}_{cf,rect}$ **(g s^{-1})**	1.241	
	Geometric Specifications	
	Branched Tray	**Vertical Column**
$L_{T,des}$ **(m)**	0.152	0.146
No. desorber microchannels	101	88
$L_{T,rect}$ **(m)**	0.114	0.133
No. rectifier microchannels	101	88
	Output Conditions	
$\dot{m}_{v,out}$ **(g s^{-1})**	0.282	0.290
$x_{v,out}$	0.996	0.994
$\dot{Q}_{des}$ **(W)**	585	590
$\dot{Q}_{rect}$ **(W)**	87.4	60.0

compact monolithic or semi-monolithic system. Additionally, the present designs are expected to offer a reduction in volume (per unit component capacity) of approximately 20% compared to the falling-film design described by Determan and Garimella (2011). This number should be expected to favor the present designs to a larger degree as capacities are increased.

Unlike the full-scale branched tray and vertical column components, which were described previously, the test sections feature visual access to the working-fluid passages and are more highly instrumented. To accommodate the additional instrumentation and visual access, each test section features only a single solution plate with working-fluid passages, and a single microchannel shim. The assemblies for the branched tray and vertical column test sections, including the major components, are shown in Figures 3.4 and 3.5, respectively.

Multiple thermocouple ports are available to allow for detailed measurements of both the coupling- and working-fluid streams at multiple locations during experiments. The locations of these thermocouple ports are noted for the branched tray test section in Figure 3.6. Thermocouple port locations for the vertical column are noted in Figure 3.7. Temperature measurements taken at these locations are used in subsequent data analysis.

3.1.3 Test Section Fabrication

To produce the test sections, several different fabrication techniques were used for the individual components. Once complete, the components were assembled and bonded to form the enclosed microchannel passages. The solution plates for both test sections were designed to replicate the geometries of the full-capacity components and were machined from precision-ground 304L stainless steel plate using conventional milling. In

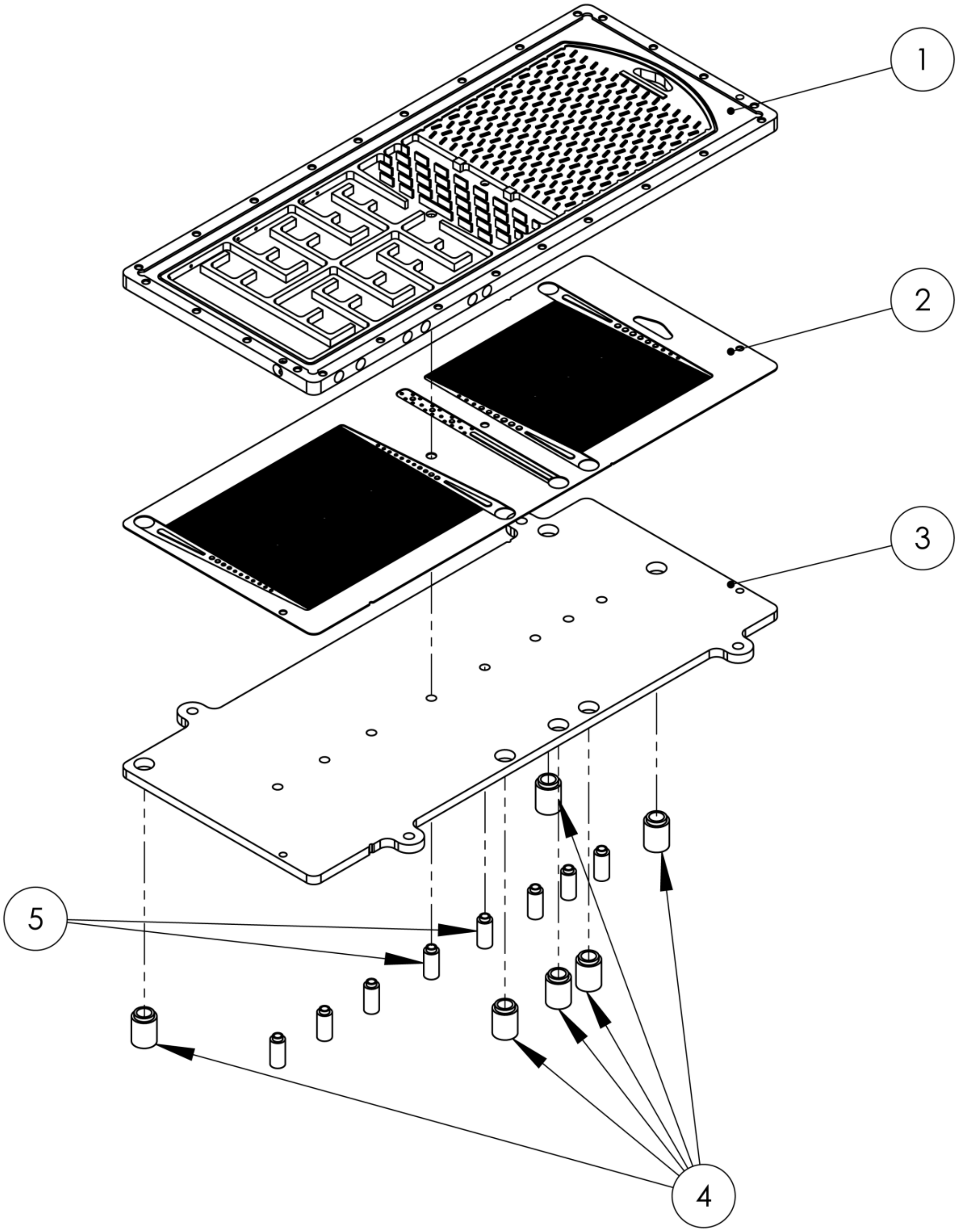

Figure 3.4: Branched tray test section bonded assembly: solution plate (1), microchannel shim (2), back plate (3), and tube bosses (4, 5)

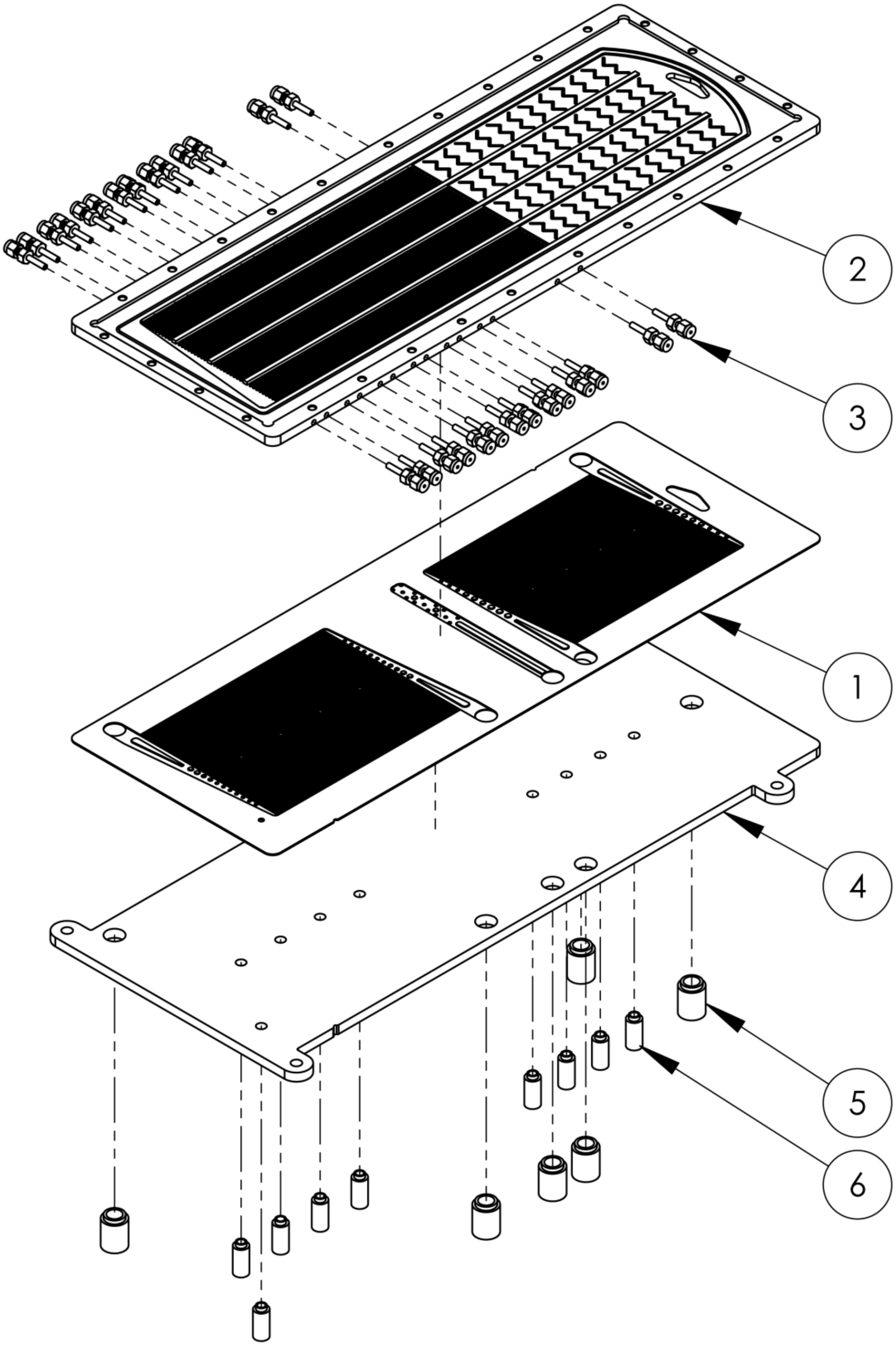

Figure 3.5: Vertical column test section bonded assembly: microchannel shim (1), solution plate (2), thermocouple fittings (3), back plate (4), and tube bosses (5, 6)

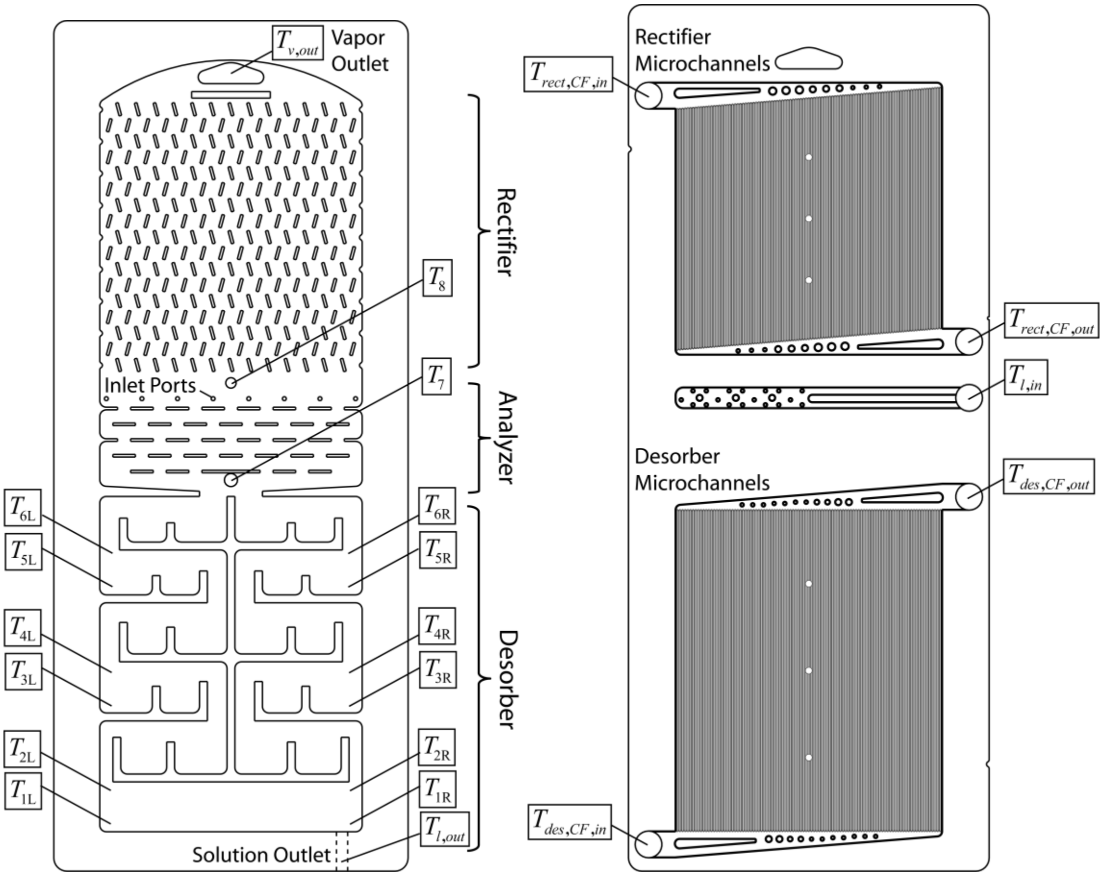

Figure 3.6: Branched tray thermocouple locations

the full-capacity vertical column prototype, described in Section 2.1.2, etched surface treatments were used to enhance heat transfer on the falling-film surfaces (indicated in Figure 2.1). During fabrication, these features were replicated using micro-milling in the vertical column test section.

Figure 3.8 shows the surface treatments used in the rectifier and desorber-analyzer sections. The rectifier uses a herringbone-like pattern, designed to coalesce droplets and promote rivulet formation at the downward-facing points of the features, thus reducing the mean condensate film thickness. The desorber and analyzer sections feature a cross-hatch pattern that is used to promote liquid wetting and reduce rivulet formation. The surface features were machined with a 0.8 mm ball-nosed endmill at a depth of

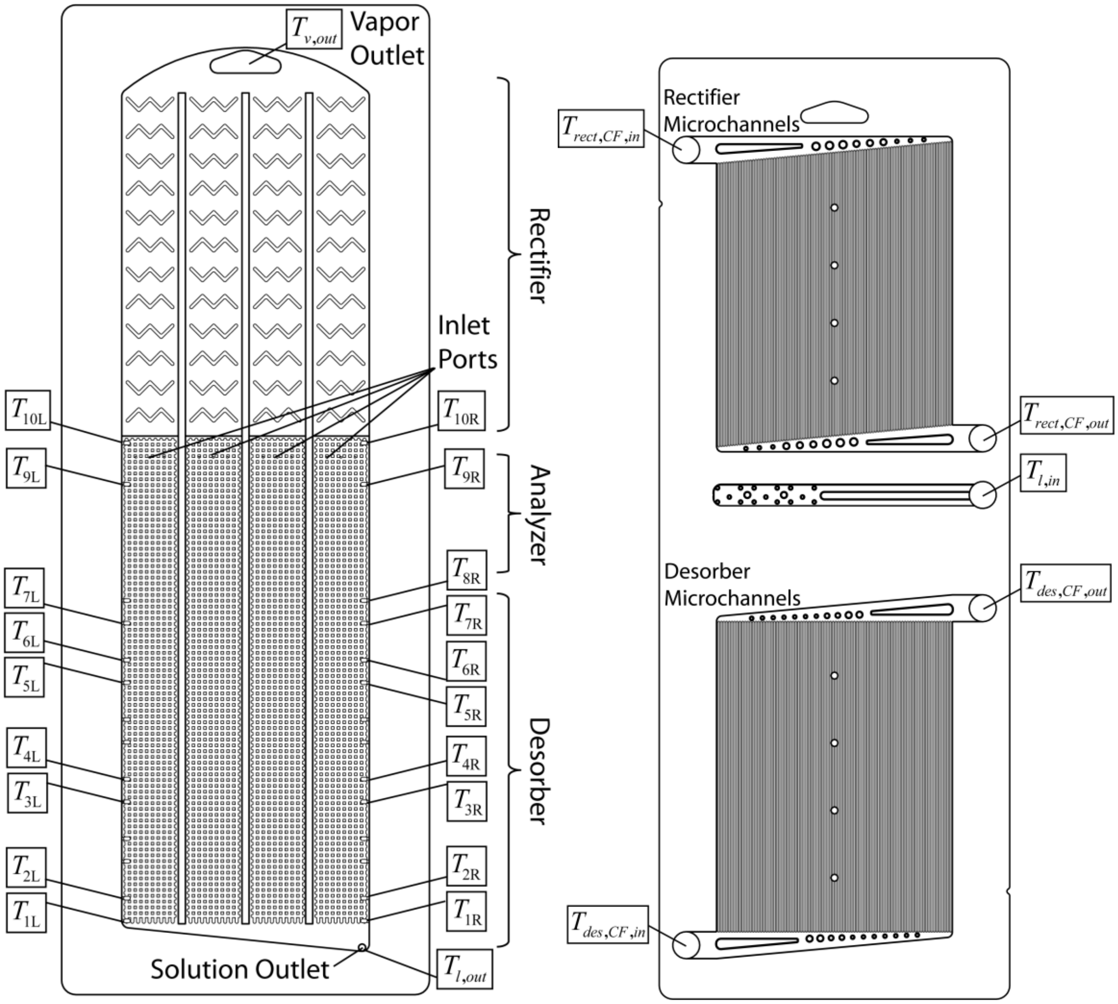

Figure 3.7: Vertical column thermocouple locations

approximately 0.3 mm. The desorber trays of the branched tray test section, as well as the analyzer and rectifier fins were machined using conventional methods. A detailed image of the solution plate is shown in Figure 3.9. The back plates for both test sections, which serve as structural components and allow for ease of plumbing and attachment of thermocouple probe fittings, were also machined from 304L stainless steel plate using conventional machining methods.

The microchannel shims were fabricated from 304 stainless steel shim-stock using photochemical etching. This process allows chemical material removal of specific areas

Figure 3.8 : Vertical column surface treatment in rectifier (top) and desorber-analyzer (bottom); solution distributors also shown

of the shim to form the microchannels, headers, and other flow features that compose the coupling-fluid channel arrays. The photochemical etching process has been described in detail in previous studies (Determan, 2008; Nagavarapu, 2012). The etched microchannel shims for both test sections are shown in Figure 3.10. Details of the etched headers are shown in Figure 3.11.

The resulting channels, once bonded, are approximately semi-circular in cross-section and have a nominal hydraulic diameter of 442 μm. A representative cross-section of the microchannel array, with specified dimensions, is shown in Figure 3.12. Bonding of the test section assemblies is achieved through controlled atmosphere brazing. A thin layer of nickel braze alloy is applied to the components by electro-plating, or as a foil layer. The components are assembled in a fixture and placed in a furnace. The furnace is evacuated or charged with inert gas and brought to elevated temperatures, allowing the braze alloy to melt. The temperature is then reduced, solidifying the braze alloy and

Figure 3.9 : Branched tray solution plate features in rectifier (top), analyzer (middle), and desorber (bottom)

Figure 3.10: Vertical column (left) and branched tray (right) microchannel shims

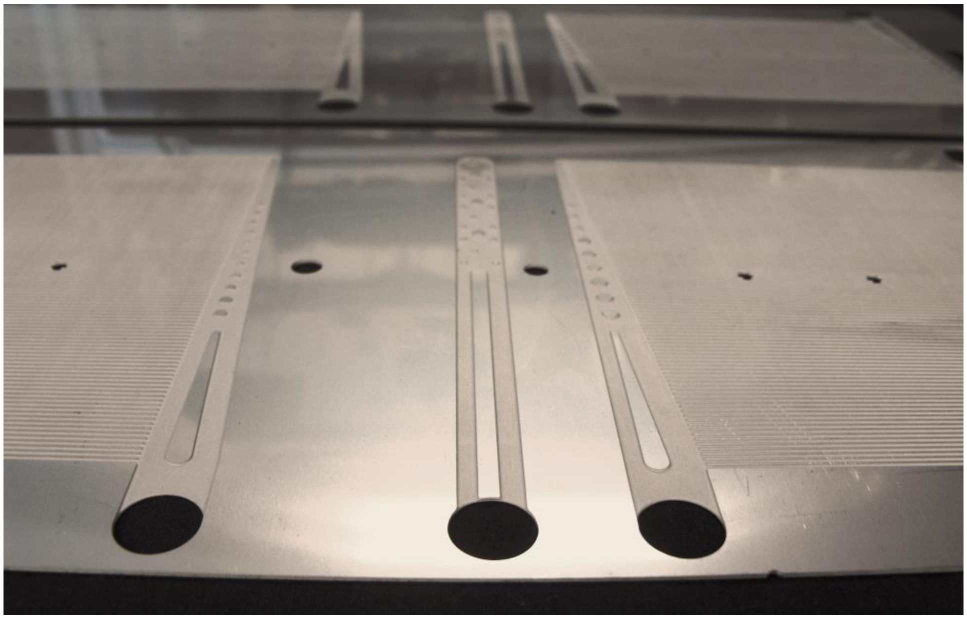

Figure 3.11: Etched fluid ports, headers, and microchannel arrays

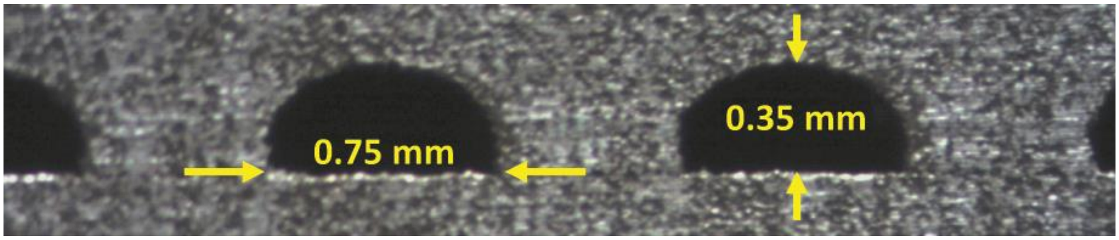

Figure 3.12 : Microscopy image of microchannel array

bonding the components. This process creates a hermetic seal for the desorber and rectifier microchannel arrays.

3.1.4 Visual Access

To achieve visual access, the solution plate features a machined pocket and O-ring groove for positioning and sealing a glass viewing window over the front of the test section. Borosilicate glass plate, with a thickness of 15.9 mm, was used for the viewing window due to its optical clarity, compatibility with ammonia-water, and stability at high temperatures and pressures. The glass is retained with a machined stainless steel retaining plate. Neoprene O-ring stock, 1.6 mm in diameter, was used to provide a seal between the glass and solution plate working-fluid passages. The completed test section assemblies are shown in Figure 3.13. The branched tray and vertical column test sections are 41 and 44 cm in height, respectively, not including the mounts.

3.2 Experimental Facility

The experimental facility used to evaluate the VGU test sections is designed to provide and maintain the working- and coupling-fluid conditions at desired values, and allows for measurement of relevant temperatures, pressures, and flow rates. The test facility and insulated pressure chamber are shown in Figure 3.14. It consists of four fluid loops: the working-fluid (ammonia-water) loop, and separate coupling-fluid loops for the

Figure 3.13 : Assembled vertical column (left) and branched tray (right) test sections, shown with glass viewing windows and retaining plates installed

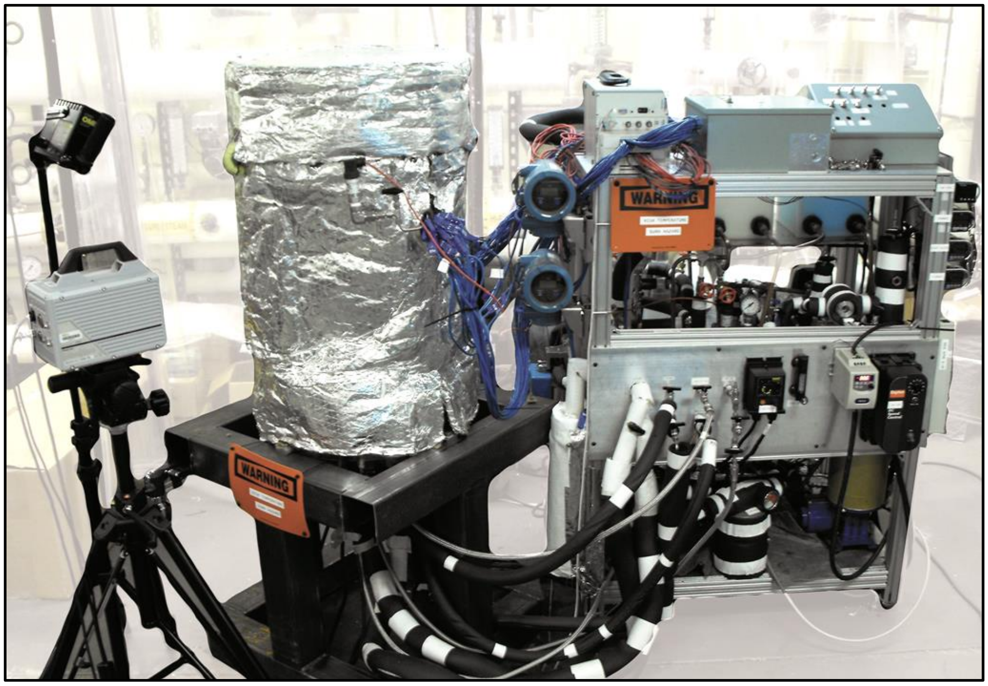

Figure 3.14: Desorption heat and mass transfer facility

desorber heating fluid, rectifier coolant, and absorber coolant. The operating conditions, facility layout, and details of the hardware are discussed in this section.

3.2.1 Operating Conditions

To determine the sensitivity of the novel VGU designs to operating conditions, and to gain insight into the changes in performance with varying system-level parameters, the test sections must be evaluated across a range of realistic operating conditions. The impact of three independent variables, including the source temperature, concentrated solution concentration, and concentrated solution flow rate, on VGU performance is investigated. These parameters were chosen as they commonly vary during system operation, or may be varied based on the specific application of a system. For example, source temperature may fluctuate in many applications where waste heat or solar thermal sources are used, or may be varied to optimize system capacity or COP. Solution flow rate is often controlled to manage operation at part-load, or to limit component flooding or dry-out. The solution concentration is frequently adjusted to balance the performance of the absorber and desorber, or to optimize system performance for different ambient or conditioned-space temperatures.

Concentrated solution flow rate, heating fluid inlet temperature, and concentrated solution ammonia concentration are varied independently about the design conditions of 0.9 g s^{-1}, 180°C, and 0.475 respectively. The ranges of source temperature, solution concentrations, and solution flow rates considered in the present study are provided in Table 3.2. During experiments, a specific source temperature may be established through control of the desorber coupling-fluid heater and pump speed, while maintaining a set coupling-fluid flow rate. The solution flow rate can be set through control of the solution pump speed and expansion valves. The solution concentration is set through adjustments to the working-fluid charge, which may entail adding pure ammonia or water to the system, or discharging ammonia-water solution from the system inventory. Data from both test sections are collected at all 36 points shown in Table 3.2.

During operation, several other parameters are controlled and maintained by the

Table 3.2: Experimental test matrix
(design condition shown in black)

		Concentrated Solution Nominal Concentration (Mass Fraction)											
		40.0%				47.5%				55.0%			
		Concentrated Solution Mass Flow Rate, g s^{-1}											
		0.7	0.9	1.1	1.3	0.7	0.9	1.1	1.3	0.7	0.9	1.1	1.3
Source Temperature, °C	170	🟩	🟩	🟩	🟩	🟩	🟩	🟩	🟩	🟩	🟩	🟩	🟩
	180	🟩	🟩	🟩	🟩	🟩	⬛	🟩	🟩	🟩	🟩	🟩	🟩
	190	🟩	🟩	🟩	🟩	🟩	🟩	🟩	🟩	🟩	🟩	🟩	🟩

operator. For example, the rectifier coupling-fluid flow rate is controlled to maintain the desired vapor outlet concentration. These additional parameters are discussed in further detail in Section 3.4.

3.2.2 Working-Fluid Loop

The experimental facility must allow for operator control over a wide range of conditions. The primary components of the working-fluid loop are the VGU test section, absorber, solution heat exchanger, solution pump, expansion valves, and solution tank. These components are shown in the schematic of the experimental facility, which is presented in Figure 3.15.

The working-fluid loop nominally operates at a single pressure. Ammonia-water solution is conditioned to the appropriate temperature, pressure, concentration, and flow

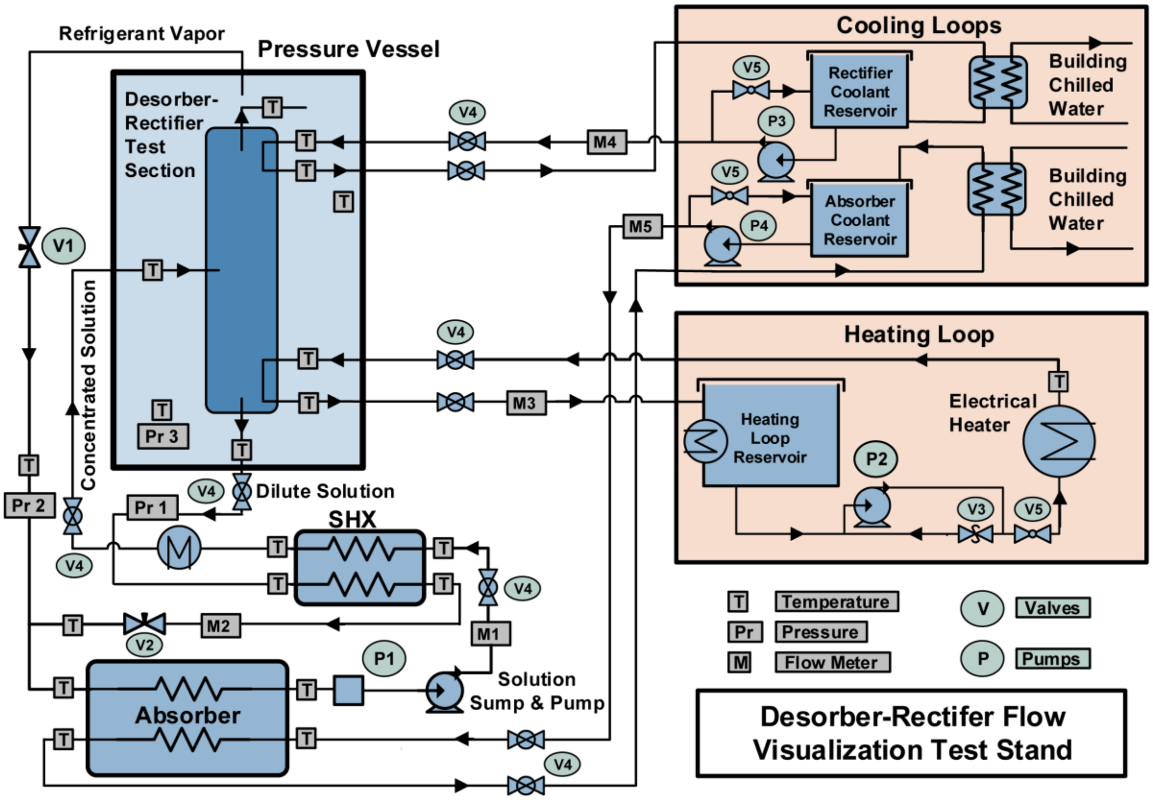

Figure 3.15: Facility schematic

rate and circulated through the loop to the test section. Starting at the absorber outlet, ammonia-water solution with a high ammonia concentration (0.40 - 0.55) is fed into a solution tank, which is used as a sump and reduces any occurrence of vapor at the pump inlet. The solution tank is a custom stainless steel tank with integrated sight glass and discharge port. Fluid is pumped from the solution tank to the high-side pressure.

For the branched tray experiments, an ammonia-water compatible gear pump was used (Tuthill, model DGS.38). A diaphragm pump (Hydra-cell P100 metering pump, model P100NSJSS005C) was used for the vertical column testing, due to failure of the original gear-type pump. Fluid leaving the solution pump flows through the solution heat exchanger. The solution heat exchanger is a stainless steel brazed-plate recuperative heat exchanger (Bell and Gossett, Model BPN400-10 LCA), which is used to reduce the required heat duty of the absorber and desorber, and to precondition the solution before it enters the VGU test section. Exiting the solution heat exchanger, the concentrated solution flows through an auxiliary solution heater. This heater is composed of a length of stainless steel tubing wrapped with a 125 W high-temperature heat cable. This resistance-type heater is manually controlled by the operator to achieve saturated conditions at the desorber inlet in the event that recuperative exchange in the solution heat exchanger is insufficient. After flowing through the heater, the concentrated solution enters the VGU test section through the injection ports. Dilute solution is removed from the bottom of the test section, passes through the hot side of the solution heat exchanger, and is expanded back to the low-side pressure using an expansion valve (Swagelok, model SS-4MG-NEMH). As noted previously, the system operates near a single pressure and the expansion valve is used primarily to aid in control of the solution flow rate. During testing, the pressure drop across the expansion valve varied to maintain the pressure chamber and test section near the design conditions. In most cases, the pressure drop was less than 100 kPa. The expansion valve pressure drop and low-side pressure were not of primary concern in the present study, and the facility expansion valves were used primarily for flow control and control of the test section pressure. The solution returns to the absorber, where refrigerant vapor is absorbed into the dilute liquid solution. Concentrated solution exits the absorber and is returned to the solution tank. The absorber, like the solution heat exchanger, is a brazed-plate unit (Bell and Gossett, Model BPN400-10 LCA).

Refrigerant vapor generated in the test section exits through the top of the rectifier. The vapor flows through the interior of the pressure chamber, which allows the pressure in the chamber to equal that within the test section, eliminating any appreciable pressure difference across the test section viewing window and seals. The refrigerant vapor exits the chamber through a pass-through port and is then expanded back to the low-side pressure using an expansion valve (Swagelok, model SS-4MG-NEMH). Again, this expansion valve is used primarily in flow control. The expanded vapor passes directly into the absorber, where it is absorbed by the dilute solution returning from the test section.

3.2.3 Coupling-Fluid Loops

Coupling-fluid loops are used to supply (desorber) and reject (rectifier and absorber) heat from the working-fluid loop. Figure 3.15 shows the coupling-fluid loops as part of the facility schematic.

The heat input to the desorber is supplied by the heating-fluid loop. The desorption process is driven by heat input from this loop utilizing a mineral-oil coupling fluid (Paratherm NF). Heat is supplied by a 1,750 W electrical cartridge heater installed upstream of the desorber test section. Heater power is manually controlled with an AC voltage regulator (Dart Controls, model 55AC series) to maintain the desired inlet temperature at the test section. The fluid pump is a gear-type unit designed for hydraulic oil (Concentric, model 4F649). An adjustable fluid bypass valve and pump speed variation allows for control of the flow rate of the heating fluid to the test section. Fluid returning from the test section is accumulated in a reservoir near the top of the test stand. The reservoir is vented to the atmosphere to avoid excessive pressures within the loop that would otherwise occur due to the thermal expansion of the oil. The reservoir also includes an auxiliary coupling-fluid heater. This 325 W resistance-type cartridge heater is used to maintain the temperature of the fluid within the reservoir and decrease start-up times.

Heat is rejected from both the rectifier and absorber to separate cooling loops. The heat of absorption is removed by an intermediate chilled water loop with a dedicated centrifugal coolant pump (Laing Thermotech, model SM-1212-NT-26). Flow is controlled manually via a rotameter (Key Instruments, 40 GPH) to maintain slightly subcooled conditions at the absorber outlet. Rather than controlling pump speed, a bypass loop is used to return excess coolant flow to the reservoir. The absorber coolant loop is coupled to the building chilled water supply through a brazed-plate heat exchanger (FlatPlate, model FPN 3x8-12). Fluid returning from the absorber is collected in a coolant reservoir, which is also vented to the ambient to avoid excessive pressures that would be caused by thermal expansion of the fluid. The reservoir serves as a sump for the absorber coolant pump.

Rectifier cooling is achieved through a similar coupling-fluid loop employing chilled water and utilizing the building chilled water supply as a heat sink. The coolant pump is a gear-type unit (Greylor, model PQ-24) and the coolant loop is coupled to the building chilled water supply with a brazed-plate heat exchanger (FlatPlate, model FPN3x8-4). Flow is controlled manually with a globe valve and bypass loop to maintain the desired rectifier vapor outlet concentration. Fluid returning from the test section or bypass loop is collected in a reservoir, which is open to ambient pressure. The reservoir serves as a sump for the rectifier coolant pump.

3.2.4 Pressure Chamber

To allow for visual access and safe operation of the test sections at the elevated temperatures and pressures needed for realistic desorber experiments, a large pressure chamber is used (Figure 3.16). The chamber houses the test section, and is maintained at the same pressure as the working-fluid passages of the test section, minimizing the pressure difference across the test section glass window and seals.

The pressure chamber is a custom unit, constructed of 304/304L stainless steel and features a number of fluid ports, thermocouple pass-through fittings, and viewing windows to accommodate experiments. The chamber was constructed by PresSure Products Co. and is rated for operation at 230°C and 4135 kPa. The interior volume of the chamber is approximately 0.254 m in diameter and 0.686 m in height. The main body of the chamber is constructed of schedule 80S stainless pipe, with a minimum wall thickness of 12.7 mm and nominal outside diameter of 0.273 m. The main viewing

Figure 3.16: Pressure chamber, heaters and insulation not shown

window is a tempered Pyrex sight glass measuring 0.051 m wide by 0.305 m in height. All gaskets used for the chamber and integrated sight glasses are constructed of steel-reinforced PTFE or steel-reinforced carbon.

A total of 10 flexible silicone-rubber heater sheets are applied to the exterior of the pressure chamber using high-temperature metal-foil tape. These electrical resistance-type heaters are used to maintain the temperature of the pressure chamber near the saturation temperature of the working fluid to reduce heat loss. The heaters also aided in reducing start-up times by bringing the chamber to steady-state temperature in a shorter period. The heaters have a combined maximum power of 4330 W and are controlled by four programmable PID temperature controllers to reduce operator input and avoid excessive temperatures. During testing, the pressure chamber and heaters are insulated with high-temperature fiberglass wrap. Insulation 5.1 cm thick, with a thermal conductivity of 0.0389 W m^{-1} K^{-1}, foil coating, and maximum temperature rating of 232°C is used.

3.3 Data Acquisition and Instrumentation

A PC-based data acquisition system is used to read and record values from sensors during testing. A National Instruments SCXI-1000 chassis is used as an interface between the PC and instrumentation. Three SCXI-1303 cards, installed in the chassis, accept inputs from the various instruments. An SCXI-1600 card provides a USB interface with the PC. Real-time values are conditioned, displayed and recorded using a LabView visual interface.

Instrumentation on the experimental facility includes a number of temperature sensors (thermocouples), pressure transducers, and flow meters, which output signals to the acquisition system. All thermocouples are ungrounded-tip, T-type probes. Thermocouples are calibrated before final installation using a temperature-controlled silicone oil bath (HART Scientific, model 7340) and a calibrated platinum RTD (HART Scientific, model 5612), which has an accuracy of ±0.012°C. The thermocouples have a calibrated accuracy of ±0.25°C. The locations of the facility thermocouple probes are provided in the facility schematic (Figure 3.15). Locations of the thermocouple probes within the test section passages are given in Figures 3.6 and 3.7. The locations of the pressure transducers and flow meters are noted in the facility schematic (Figure 3.15). Details of these instruments are provided in Table 3.3.

In addition to the instrumentation noted above, a high-speed digital camera is used to record video and photographs of the test section during operation. The camera used in the present study is a FastCam SA4 model manufactured by Photron. A Nikon

Table 3.3: Experimental facility instrumentation

Instrument	Location	Manufacturer	Model	Uncertainty	Span
Concentrated Solution Mass Flow Meter	Solution Pump Outlet	Micromotion	CMFS010 M319N5 BMECZZ	±0.1% of reading	0.034-1.36 kg min^{-1}
Dilute Solution Mass Flow Meter	Solution Heat Exchanger Outlet	Micromotion	CMFS010 M319N5 BMECZZ	±0.1% of reading	0.034-1.36 kg min^{-1}
Rectifier Coolant Mass Flow Meter	Test Section Feed Line	Rheonik	RHM 015	±0.5% of reading	0.0036-0.6 kg min^{-1}
Heating Fluid Volumetric Flow Meter	Test Section Return Line	AW-Lake	JVS-20KG	±0.5% of reading	2.27-454.2 L hr^{-1}
Pressure Transducer	Pressure Chamber	WIKA	S-10	±0.5% of span	0-3447 kPa
Pressure Transducer	Refrigerant Expansion Valve Outlet	WIKA	S-10	±0.5% of span	0-3447 kPa

Micro-Nikkor 105 mm lens is used to maintain focus. Images, including video frames, are recorded at a resolution of 1024 by 1024 pixels. Video is recorded at a frame rate of 1000 frames per second. A pair of Lowel Omni-Light incandescent lamps, rated at 500 W each, is used to provide lighting. Photographs and video are transferred to PC-based storage via Ethernet connection. A schematic of the camera setup is provided in Figure 3.17.

3.4 Experimental Procedure

The procedures used in assembling, charging, and operating the experimental facility are presented here, along with safety procedures and considerations.

3.4.1 Assembly and Charging

Prior to testing, the test section and pressure chamber must be assembled. After completing leak-checks on the microchannel passages, the test section is cleaned with

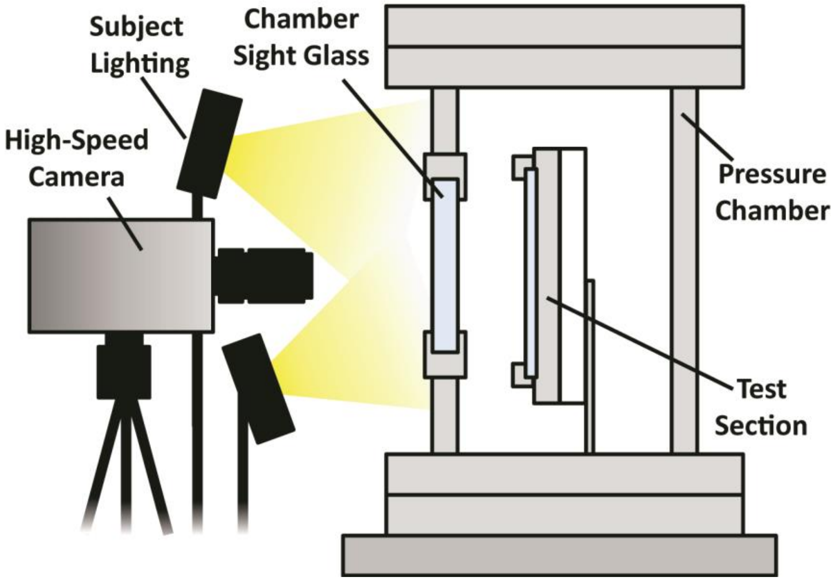

Figure 3.17: Photography schematic

acetone and rinsed thoroughly with distilled water. The neoprene O-rings are installed in the solution plate and retaining plate and the glass window and retaining plate are installed. When assembling the vertical column test section, small distributors (shown in Figure 3.8) are placed over the solution injection ports and are held into place by the glass window, once assembled. These distributors are made of 0.2 mm thick stainless steel sheet and are used to help distribute solution across the solution plate, promoting film formation and reducing liquid impingement on the glass window. (The distributors were necessitated by the use of the diaphragm-type solution pump, which generated pulses of fluid flow, rather than a continuous flow, resulting in increased jet formation at the solution injection ports. Distributors were not found to be necessary when using the gear-type pump in the branched tray experiments.) The test section is fastened to the stainless steel test section stand (Figure 3.18) and two sheets of 6.35 mm thick PTFE insulation are placed between the stand and test section to reduce auxiliary heat transfer. The test section is placed on pressure chamber stand, as shown in Figure 3.18. The fluid

Figure 3.18: Test section on pressure chamber stand

connections to the test section are made using flexible PTFE hoses with stainless steel braided reinforcement. The hoses connect to pass-through fittings that are routed through the bottom flange of the pressure chamber (Figure 3.18). The main body of the pressure chamber is lowered over the test section. This is accomplished through the use of a 2-ton hydraulic hoist. As the chamber body is lowered into place, thermocouple probes are inserted into the test section and sealed with compression fittings. Additional leak-checks are conducted on the coupling-fluid lines to ensure hermetic seals. The top is lowered onto the chamber and the main flanges are bolted together to seal the chamber.

A final leak-check is conducted on the chamber. The flexible silicone-rubber chamber heaters are then connected and tested, and the chamber is insulated (Figure 3.14).

Once assembled, system charging may be conducted. The chamber, experimental facility, and test section are evacuated using a model DV-142N Platinum-series vacuum pump manufactured by JB Industries. The vacuum pump outlet line is submerged in a water tank and evacuation continues until no vapor bubbles are observed to exit the pump outlet over a period of at least 15 minutes. Additionally, facility temperatures are monitored to ensure that no residual liquid remains in the system. Presence of any liquid within the plumbing of the facility is indicated by temperature readings below ambient, indicating the evaporation of residual water or ammonia-water solution. If this is observed, evacuation is continued until the readings return to ambient temperature. Vacuum pressure is confirmed through use of the facility pressure transducers, the details of which are provided in Table 3.3. However, the accuracy of these transducers is limited for vacuum conditions, requiring the procedure described above.

Following evacuation, the system is charged with distilled water and pure ammonia. To measure the mass of charge added to the system, a Wey-TEK refrigerant charging scale manufactured by Inficon Instruments is used. A mass of approximately 0.5 kg of water is charged into the system from a stainless steel tank. Initial and final mass of the tank are recorded, with the use of the charging scale, to determine the mass of water charged. A cylinder of compressed, pure ammonia is then connected to the facility, and a mass of approximately 1.0 kg of ammonia is charged into the system. Again, initial and final masses of the ammonia cylinder are recorded to determine the charge added. The recorded charge values are used to make subsequent charge adjustments to achieve the desired concentrated solution concentration, but are not used in any of the data analysis calculations.

3.4.2 **Test Procedure**

Prior to collecting data, the experimental facility and test section conditions must be brought to steady state. The pressure chamber heaters are turned on, and the building chiller is set to a sufficiently low temperature (approximately 20°C). The solution pump is started, and ammonia-water solution is allowed to circulate through the analyzer and desorber of the test section. Typically, the refrigerant expansion valve is closed completely, which facilitates flow of the solution through the solution expansion valve and aids in reducing pump dry-out during startup. Once sufficient wetting has been observed in the desorber, the desorber coupling-fluid pump is started and the coupling-fluid heater is turned on. The auxiliary solution heater and auxiliary coupling-fluid heater may also be used at this stage to reduce start-up times, which ranged from approximately 30 minutes to two hours, depending on the desired desorber coupling-fluid inlet temperature.

As the system components, working fluid, and coupling fluids increase in temperature, the system pressure rises. The solution pump speed is adjusted to maintain wetting in the test section, without causing flooding. Once sufficient desorber coupling-fluid temperature is achieved, vapor desorption begins to increase rapidly. The refrigerant expansion valve is then opened, and adjustments are made to the solution pump speed and solution expansion valve. As the pressure, temperatures, and desorption rate continue to increase, the absorber outlet temperature and rectifier temperatures begin to approach normal operating ranges. At this point, the absorber and rectifier coolant pumps are started and flow rates are adjusted to maintain the appropriate temperatures. Adjustments to the coolant flow rates are made through manual control of the coolant-loop bypass valves.

During initial startup of the facility, and periodically during testing, small amounts of the working fluid are discharged from several discharge ports, located at high-elevation points within the system. This is done to reduce the inventory of any non-condensable gases that may not have been completely evacuated prior to the charging procedure. Fluid is discharged into a large water vessel, and diluted to appropriately low concentration prior to disposal.

As the system approaches steady state, the outputs of the auxiliary heaters and chamber heaters are typically reduced, and the test section conditions are brought to the desired specifications. The heating-fluid temperature is brought to the desired value by manually adjusting the voltage of the primary heater. The heating-fluid flow rate is also set to the desired value of approximately 7.72 g s^{-1}. The concentrated solution flow rate is set by control of the solution pump speed. Test section flooding and dry-out is avoided by adjusting the expansion valves. Measurements are taken of the solution and vapor conditions (temperature and pressure) at the test section inlets and outlets to determine the solution inlet concentration and vapor outlet concentration (the exact method is described in Section 4.1.2). The vapor outlet concentration may be adjusted to the specified value of approximately 0.991 by controlling the rectifier coolant flow rate.

Once the desired conditions are achieved and the system is observed to be stable and steady, a data file is recorded. File size is specified at 1.85 KB, corresponding to a duration of approximately five minutes, or approximately 260 discrete readings for each sensor, which are averaged during the data analysis process. Values were recorded at a rate of 500 Hz. If operation was stable during the length of the data file, conditions are adjusted to the next point on the experimental matrix, and the process is repeated.

To adjust the solution concentration, additional ammonia or water may be charged into the system (typically before start-up), or ammonia-water solution may be discharged from the system (typically done during steady-state operation). This process may also be used to make larger adjustments to fluid levels within the system to avoid flooding or dry-out.

Shutdown of the facility is accomplished through a specific procedure to avoid elevated temperatures or pressures. After concluding experiments, all heaters are turned off. Rectifier and absorber coolant flow rates are increased to provide additional heat removal, and the solution flow rate and heating-fluid flow rate are maintained at near-baseline conditions. As the temperature of the test section and chamber drop, the system pressure decreases. Once the heating-fluid temperature and system pressure decrease sufficiently, the solution pump and heating-fluid pump are turned off. Working-fluid isolation valves are closed, and the coolant pumps are turned off. The building chiller lines are then isolated from the test facility. Finally, the facility instrumentation and data acquisition system are turned off.

3.4.3 Safety Considerations

When operating the experimental facility, a number of safety precautions are taken. This is necessary due to the elevated temperatures and pressures of the working fluid, as well as the toxicity of ammonia.

Personal safety equipment including safety glasses, closed-toe shoes, and long pants are worn by operators at all times. Additionally, full-face respirators (North brand, P/N: 80802; equipped with North brand filters, P/N: 7584P100) are maintained at the facility for use by operators in the event of any ammonia leaks.

When the system is charged with ammonia, and during charging and discharging procedures, the facility is enclosed by sealed vinyl curtains under a ventilation hood. Building blowers provide negative pressure to the hood, removing any ammonia vapor that may be released in the event of a leak. Additionally, ammonia sensors and alarms (Honeywell MDA Scientific Midas series, P/N: Midas-E-NH3) are installed on the hood to alert operators of any significant leaks. Isolation valves are also integrated into the system at several key locations to allow leaking plumbing or other components to be isolated from the rest of the system, reducing the volume of ammonia that may be released in the event of a leak.

During the discharge process, all ammonia-water solution must be removed from the system. To accomplish this in a safe manner, the ammonia-water solution is discharged into a large vessel, containing approximately 175 kg of water. The vessel is located under the ventilation hood, and after the charge is sufficiently diluted, the contents of the vessel can be safely disposed of.

In addition to the safety procedures associated with ammonia, several precautions are taken to accommodate the high temperatures and pressures of the working and coupling fluids. Alarms are established in the LabView VI to alert operators if the system pressure increases beyond normal operating ranges. High temperature alarms are also implemented for the electrical heaters and heating fluid.

All surface heaters are controlled by PID temperature controllers, which have integrated over-temperature alarms and shut-off limits. Additionally, these controllers feature open-circuit shut-off protocols, which engage automatically in the event that the thermocouple probe used to control the heater is accidentally disconnected, or fails. All heater electrical circuits include fuses matched to the maximum amperage rating of the heaters, in addition to the building breakers for the circuit.

Finally, for the case of the heating-fluid pump, which is capable of achieving very high pressures, well beyond the limits of several of the facility components, a pressure relief valve is integrated into a bypass loop. This allows for safe operation in the event of any blockage in components downstream of the pump. This is considered a critical feature due to the high temperature of the heating fluid, which could cause serious injury in the event of ruptured plumbing or components.

CHAPTER 4

DATA ANALYSIS

The desorber-rectifier test sections described above were evaluated experimentally, using zeotropic mixtures of ammonia and water as the working fluid. Experiments were conducted using the facility and approach described in the previous chapter. The range of solution flow rates, ammonia concentrations, and source temperatures was shown previously (Table 3.2). Analysis of the data includes calculation of ammonia-water properties and evaluation of component and sub-component heat duties, heat and mass transfer coefficients, and component-level performance parameters. All data analysis was conducted using the *Engineering Equation Solver* (Klein, 2011) platform.

The following quantities are evaluated using the data, assumptions, and analysis methods discussed in this chapter:

1. Working-fluid state points
2. Overall desorber-rectifier heat duties
3. Discrete desorber and rectifier heat duties
4. Overall heat transfer coefficients
5. Solution-side heat and mass transfer coefficients
6. Component performance parameters

The following sections describe the analysis methods and assumptions in detail. Sample calculations using a representative data point are also presented. The conditions and direct measurements recorded for the sample point, taken with the branched tray test section at the baseline or design conditions (Table 3.2), are shown in Table 4.1. Note that each of the intermediate ammonia-water temperatures (T_1-T_6 in Table 4.1) is an average of the left and right bank measurements shown in Figure 3.6.

4.1 Ammonia-Water Mixture Properties

Due to the zeotropic nature of ammonia-water mixtures, both species are present in both the liquid and vapor phases within the desorber-rectifier test section. Thermodynamic properties of the mixture are determined using the correlations of Ibrahim and Klein (1993), which are valid over the range of temperatures and pressures

Table 4.1: Sample point data

Nominal Conditions	
$\dot{m}_{l,in}$ (g s^{-1})	0.90
$x_{l,in}$	0.475
$T_{des,CF,in}$ (^{o}C)	180.0
Measured Value	
$\dot{m}_{l,in}$ (g s^{-1})	0.890
$\dot{m}_{l,out}$ (g s^{-1})	0.595
P (kPa)	1626
$T_{l,in}$ (^{o}C)	82.8
$T_{l,out}$ (^{o}C)	143.8
$T_{v,out}$ (^{o}C)	81.7
T_1 (^{o}C)	145.6
T_2 (^{o}C)	146.9
T_3 (^{o}C)	129.7
T_4 (^{o}C)	129.4
T_5 (^{o}C)	107.0
T_6 (^{o}C)	111.8
T_7 (^{o}C)	97.11
T_8 (^{o}C)	88.34
$\dot{V}_{des,CF}$ (cm^{3} s^{-1})	9.45
$T_{des.CF,in}$ (^{o}C)	179.5
$T_{des,CF,out}$ (^{o}C)	141.6
$\dot{m}_{rect,CF}$ (g s^{-1})	0.790
$T_{rect,CF,in}$ (^{o}C)	56.9
$T_{rect,CF,out}$ (^{o}C)	87.9

observed in the present study. Mixture transport properties for both the vapor and liquid phase are determined using the correlations of Meacham (2002).

4.1.1 Sample Point Temperature Profiles

Temperature profiles for the sample points (taken at the design condition, as provided in Table 3.2) are shown in Figures 4.1 and 4.2 for the branched tray and vertical column test sections, respectively. The counter-current flow patterns for the various fluid streams were described previously. Noted in the figures are the major working-fluid temperatures required for subsequent calculations. These figures and the indicated temperatures are referred to during the discussion of the data analysis techniques. Several of the temperatures shown are direct measurements, such as the liquid solution inlet and outlet, vapor outlet, and branched tray reflux outlet. All others are based on

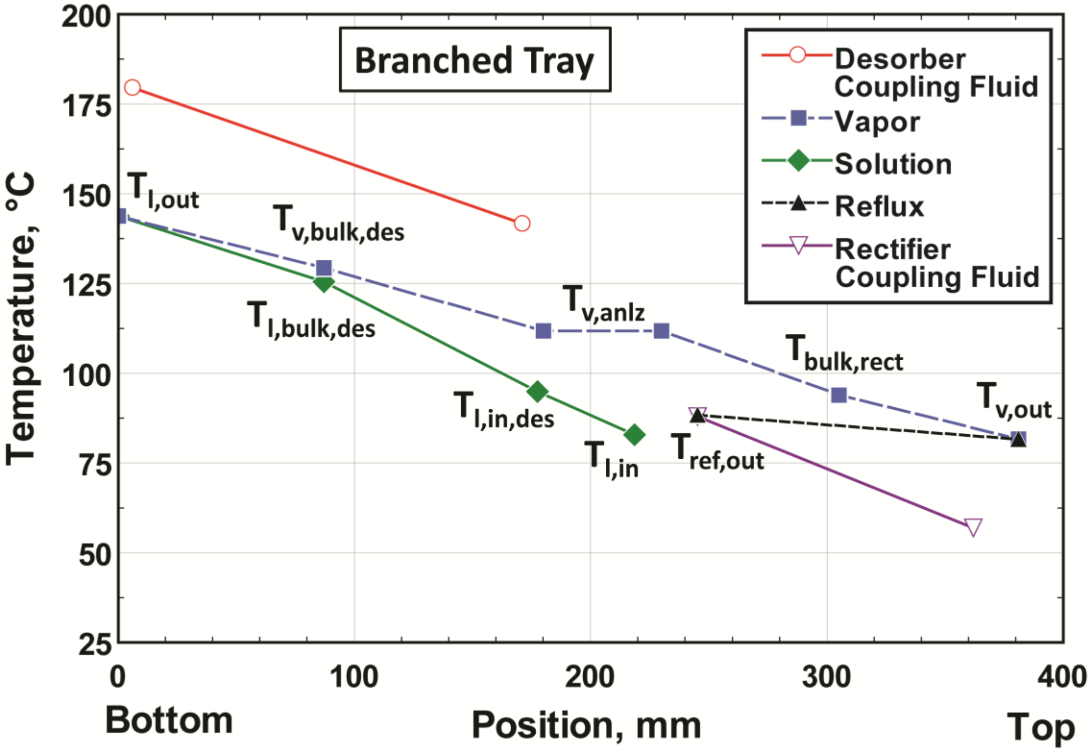

Figure 4.1: Branched tray temperature profiles

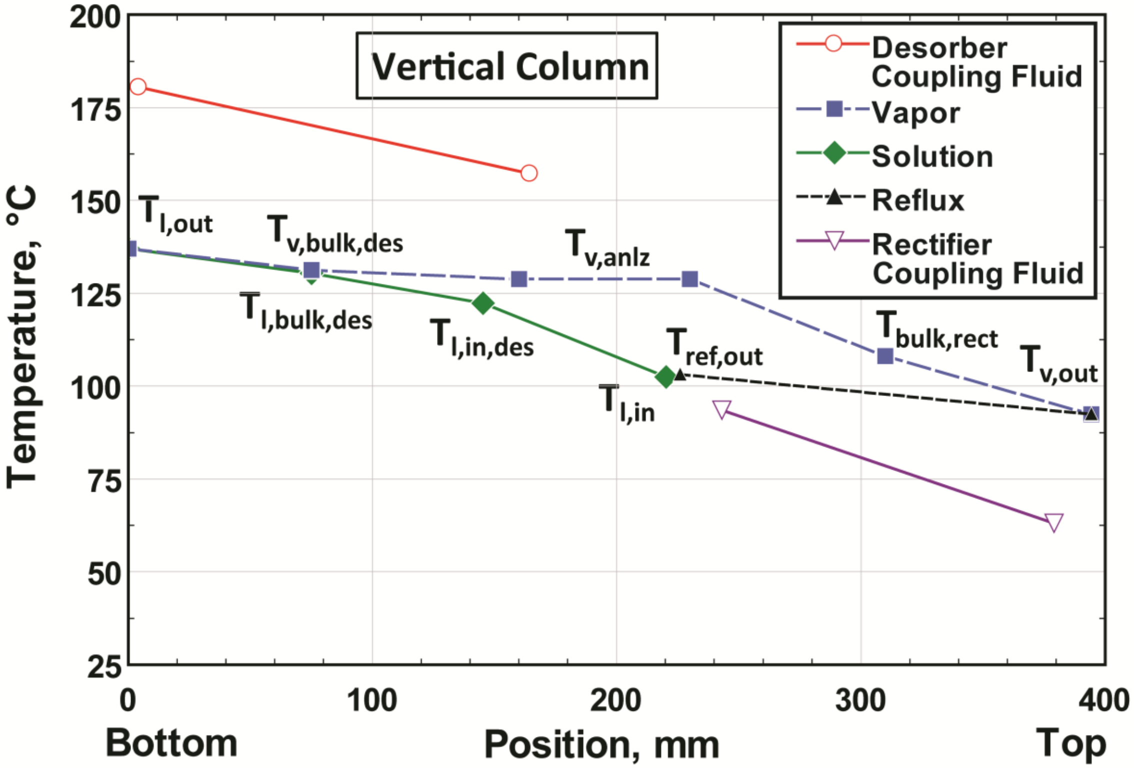

Figure 4.2: Vertical column temperature profiles

averages of nearby temperature measurements, as discussed in detail in following sections. In comparing Figures 4.1 and 4.2, it should be noted that the chamber pressure is somewhat different, leading to differences in saturation temperatures.

4.1.2 Component Inlet and Outlet State Points

As described in the previous chapter, ammonia-water flow rate measurements were made for the solution inlet stream as well as the solution outlet stream, with data collected upon confirmation of steady state operation. The vapor outlet flow rate is then determined through a mass balance.

$$\begin{gathered}\dot{m}_{v,out} = \dot{m}_{l,in} - \dot{m}_{l,out} \\ 2.96\cdot10^{-4}\ \text{kg s}^{-1} = 8.90\cdot10^{-4}\ \text{kg s}^{-1} - 5.95\cdot10^{-4}\ \text{kg s}^{-1}\end{gathered} \tag{4.1}$$

The concentration of the solution outlet ($x_{l,out}$), located at the bottom of the desorber section, may be determined by assuming that the mixture is a saturated liquid, and by applying the measured temperature for the solution outlet and test section pressure, which is assumed to be constant and uniform at all points.

$$x_{l,out} = f\left(T_{l,out}, P, q_{l,out}\right) = f\left(143.8°\text{C}, 1626\text{ kPa}, 0\right) = 0.226 \tag{4.2}$$

Concentration of the vapor outlet ($x_{v,out}$), located at the top of the rectification section, may be determined by assuming a saturated vapor condition and using the measured vapor outlet temperature.

$$x_{v,out} = f\left(T_{v,out}, P, q_{v,out}\right) = f\left(81.7°\text{C}, 1626\text{ kPa}, 1\right) = 0.987 \tag{4.3}$$

Applying a species balance to the component, the solution inlet concentration ($x_{l,in}$) may be found.

$$\begin{gathered} \dot{m}_{l,in} \cdot x_{l,in} - \dot{m}_{l,out} \cdot x_{l,out} = \dot{m}_{v,out} \cdot x_{v,out} \\ 8.90 \cdot 10^{-4}\text{ kg s}^{-1} \cdot x_{l,in} - 5.95 \cdot 10^{-4}\text{ kg s}^{-1} \cdot 0.226 = \\ 2.96 \cdot 10^{-4}\text{ kg s}^{-1} \cdot 0.987 \\ x_{l,in} = 0.479 \end{gathered} \tag{4.4}$$

With concentration defined for the component inlet and outlets, and pressure and temperature measurements available for these locations, the state points are fully defined.

4.2 Heat Duties

4.2.1 Component Heat Duties

For the component control volumes (Figure 4.3) an overall ammonia-water heat duty ($\dot{Q}_{comp,WF}$) and an overall coupling-fluid heat duty ($\dot{Q}_{comp,CF}$) may be calculated. Having defined the state points for the ammonia-water solution and vapor inlet and outlets, the enthalpies can be determined.

$$h_{l,out} = f\left(T_{l,out}, P, q_{l,out}\right) = f\left(143.8°\text{C}, 1626\text{ kPa}, 0\right) = 477.5\text{ kJ kg}^{-1} \tag{4.5}$$

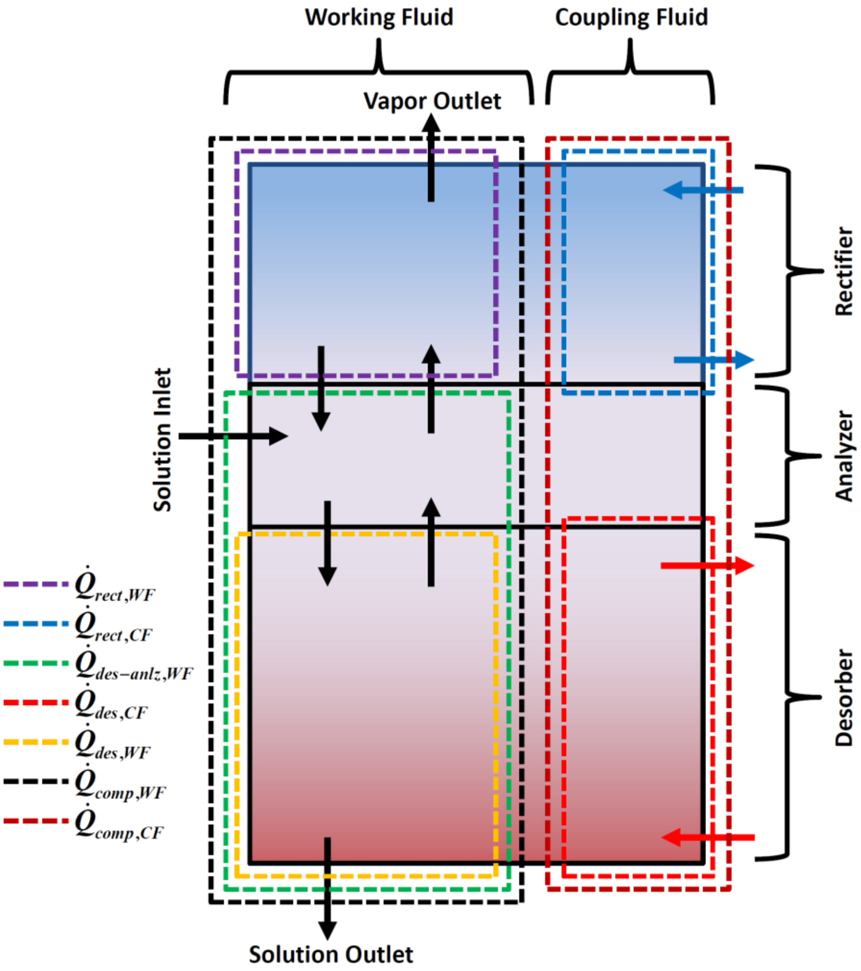

Figure 4.3: Test section control volumes

$$h_{v,out} = f\left(T_{v,out}, P, q_{v,out}\right) = f\left(81.7°\text{C}, 1626\text{ kPa}, 1\right) = 1429\text{ kJ kg}^{-1} \tag{4.6}$$

$$h_{l,in} = f\left(T_{l,in}, P, x_{l,in}\right) = f\left(82.8°\text{C}, 1626\text{ kPa}, 0.479\right) = 135.5\text{ kJ kg}^{-1} \tag{4.7}$$

Applying an energy balance to the ammonia-water solution and vapor streams of the component, the overall ammonia-water heat duty is found.

$$\begin{gathered}\dot{Q}_{comp,WF} = \dot{m}_{v,out}h_{v,out} + \dot{m}_{l,out}h_{l,out} - \dot{m}_{l,in}h_{l,in} \\ 586\text{ W}\frac{1\text{ kW}}{1000\text{ W}} = 2.96\cdot10^{-4}\text{ kg s}^{-1}\cdot1429\text{ kJ kg}^{-1} + \\ 5.95\cdot10^{-4}\text{ kg s}^{-1}\cdot477.5\text{ kJ kg}^{-1} - 8.90\cdot10^{-4}\text{ kg s}^{-1}\cdot135.5\text{ kJ kg}^{-1}\end{gathered} \tag{4.8}$$

The heat duty sign convention is relative to the ammonia-water streams, a positive value indicates heat addition to the ammonia-water working-fluid. Note that the component heat duty above represents the net heat addition to the working fluid, and includes heat addition in the desorber section and heat removal in the rectifier section.

An energy balance may also be applied at the component level based on the coupling-fluid heat duties for each of the sub-components (desorber and rectifier sections).

$$\dot{Q}_{comp,CF} = \dot{Q}_{des,CF} + \dot{Q}_{rect,CF} \tag{4.9}$$

To determine the desorber section coupling-fluid heat duty $(\dot{Q}_{des,CF})$, the specific heat of the fluid ($c_{p,des,CF}$) must be found. An average fluid temperature is used in the property calculation, and constant specific heat is assumed.

$$T_{des,CF,avg} = \frac{\left(T_{des,CF,in} + T_{des,CF,out}\right)}{2} = \frac{\left(179.5°\text{C} + 141.6°\text{C}\right)}{2} = 160.6°\text{C} \tag{4.10}$$

$$c_{p,des,CF} = f\left(T_{des,CF,avg}\right) = f\left(160.6°\text{C}\right) = 2.57\ \text{kJ kg}^{-1}\text{K}^{-1} \tag{4.11}$$

The mass flow rate of the desorber coupling-fluid must be calculated from the measured volumetric ($\dot{V}_{des,CF}$) flow rate. The fluid density ($\rho_{des,CF}$) is determined using a return temperature measured immediately upstream of the flow meter.

$$\rho_{des,CF} = f\left(T_{des,CF,rtn}\right) = f\left(132.2°\text{C}\right) = 809.6\ \text{kg m}^{-3} \tag{4.12}$$

$$\begin{aligned} \dot{m}_{des,CF} = \dot{V}_{des,CF} \cdot \rho_{des,CF} &= 9.45 \cdot 10^{-6}\ \text{m}^3\ \text{s}^{-1} \cdot 809.6\ \text{kg m}^{-3} \\ &= 7.65 \cdot 10^{-3}\,\text{kg s}^{-1} \end{aligned} \tag{4.13}$$

Fluid properties for Paratherm NF mineral oil (Paratherm Corporation), which was used for the desorber coupling-fluid, were obtained from the manufacturer's supplied property information.

The desorber coupling-fluid heat duty can then be determined from the coupling-fluid inlet and outlet temperatures.

$$\begin{gathered}\dot{Q}_{des,CF} = \dot{m}_{des,CF} \cdot c_{p,des,CF}\left(T_{des,CF,in} - T_{des,CF,out}\right) \\ 745\text{ W}\frac{1\text{ kW}}{1000\text{ W}} = 7.65\cdot 10^{-3}\text{kg s}^{-1}\cdot 2.57\text{ kJ kg}^{-1}\text{K}^{-1}\left(179.5°\text{C} - 141.6°\text{C}\right)\end{gathered} \tag{4.14}$$

To determine the rectifier coupling-fluid heat duty $(\dot{Q}_{rect,CF})$, the specific heat of the fluid must be calculated. Pure distilled water was used as the rectifier coupling-fluid and all properties were obtained from the *1995 Formulation for the Thermodynamic Properties of Ordinary Water Substance for General and Scientific Use* (Wagner and Pruß, 2002). The specific heat is assumed to be constant, and an average fluid temperature is used. The fluid pressure, having minimal effect on the specific heat, is determined from a manual recording taken from a gauge on the test stand, and is not recorded in the data file.

$$T_{rect,CF,avg} = \frac{\left(T_{rect,CF,out} + T_{rect,CF,in}\right)}{2} = \frac{\left(87.9°\text{C}+56.9°\text{C}\right)}{2} = 72.4°\text{C} \tag{4.15}$$

$$c_{p,rect,CF} = f\left(T_{rect,CF,avg}, P_{rect,CF}\right) = f\left(72.4°\text{C},170\text{ kPa}\right) = 4.19\text{ kJ kg}^{-1}\text{K}^{-1} \tag{4.16}$$

The desorber coupling-fluid heat duty can then be determined from the coupling-fluid inlet and outlet temperatures and measured mass flow rate. A negative value indicates heat removal from the ammonia-water streams in the rectifier.

$$\begin{gathered}\dot{Q}_{rect,CF} = \dot{m}_{rect,CF} \cdot c_{p,rect,CF}\left(T_{rect,CF,in} - T_{rect,CF,out}\right) \\ -103\text{ W}\frac{1\text{ kW}}{1000\text{ W}} = 7.90\cdot 10^{-4}\text{kg s}^{-1}\cdot 4.19\text{ kJ kg}^{-1}\text{K}^{-1}\left(56.9°\text{C} - 87.9°\text{C}\right)\end{gathered} \tag{4.17}$$

An overall or net coupling-fluid heat duty for the component can then be calculated.

$$\begin{gathered}\dot{Q}_{comp,CF} = \dot{Q}_{des,CF} + \dot{Q}_{rect,CF} \\ 642\text{ W} = 745\text{ W} - 103\text{ W}\end{gathered} \tag{4.18}$$

4.2.2 Sub-Component Heat Duties

In addition to the coupling-fluid heat duties, described above for the desorber and rectifier sub-components, it is useful to estimate the ammonia-water heat duty for these sections of the component. Due to the difficulty in making intermediate measurements of the solution and vapor mass flow rates within the component, additional assumptions must be employed in determining the sub-component duties. However, the same general approach of applying a mass, species, and energy balance, is employed here.

To determine the ammonia-water heat duty for the desorber section $(\dot{Q}_{des,WF})$, the inlet and outlet state points must be defined. The solution outlet state point, which was defined in the component-level analysis, is the same for the desorber section analysis; therefore, the solution outlet flow rate and properties are known.

$$h_{l,out,des-anlz} = h_{l,out} = 477.5 \text{ kJ kg}^{-1} \tag{4.19}$$

$$x_{l,out,des-anlz} = x_{l,out} = 0.226 \tag{4.20}$$

$$\dot{m}_{l,out,des-anlz} = \dot{m}_{l,out} = 5.95 \cdot 10^{-4} \text{ kg s}^{-1} \tag{4.21}$$

However, the solution inlet and vapor outlet state points for the desorber section differ from the component-level analysis. To simplify the analysis, and due to constraints on the position of local temperature measurements within the test sections, the solution inlet and vapor outlet for the desorber section are taken to be the analyzer solution inlet and analyzer vapor outlet, expanding the control volume to include the analyzer $(\dot{Q}_{des-anlz,WF})$. This simplification is well-justified as the analyzer is a recuperative section, and externally adiabatic. Therefore, the analyzer section may be included as part of the desorber, for the purposes of the heat duty calculation, without affecting the results (Figure 4.3).

$$\begin{aligned}\dot{Q}_{des-anlz,WF} &= \dot{Q}_{des,WF} + \dot{Q}_{anlz,WF} \\ \dot{Q}_{anlz,WF} &\approx 0 \\ \therefore \dot{Q}_{des-anlz,WF} &= \dot{Q}_{des,WF}\end{aligned} \tag{4.22}$$

Without intermediate measurements of the ammonia-water vapor or reflux mass flow rates, an assumption must be made to proceed with the mass, species and energy balances. The magnitude of the reflux mass flow rate is expected to be much less than the solution inlet flow rate. Moreover, the reflux properties are expected to be similar to the solution inlet conditions. As such, the analyzer solution inlet conditions may be approximated by the component-level solution inlet properties, neglecting any effect that the addition of the reflux would have on the thermodynamic properties. For the purpose of this analysis, the assumption implies the following conditions:

$$h_{l,in,des-anlz} = h_{l,in} = 135.5\ \text{kJ}\,\text{kg}^{-1} \tag{4.23}$$

$$x_{l,in,des-anlz} = x_{l,in} = 0.479 \tag{4.24}$$

In evaluating the desorber-analyzer vapor outlet properties, a saturated vapor condition is assumed. For the branched tray test section, measurements from the upper-most vapor location in the desorber are used to define the desorber-analyzer vapor outlet temperature (Figure 4.4). In the vertical column test section, the measurements of the vapor flow are difficult to make with certainty due to the shallow channel depth, which leads to wetting of thermocouple probes. In this case, the averages of the vapor temperature measurements from the two upper-most locations in the desorber are used (Figure 4.4). While temperature readings are made at locations higher in the component, readings from these locations were found to be representative of liquid, rather than vapor temperatures.

The analyzer vapor outlet enthalpy and concentration are determined as follows.

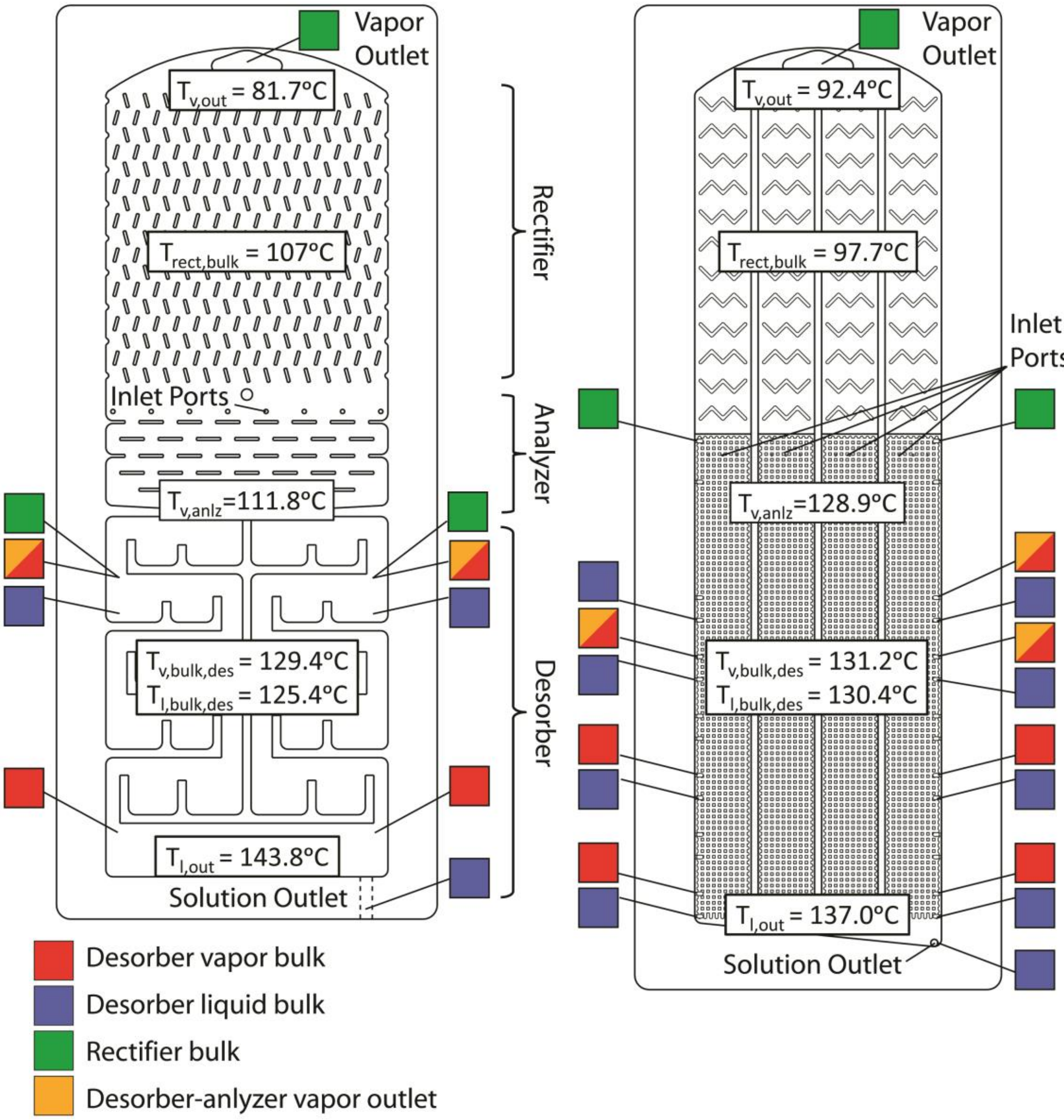

Figure 4.4: Temperature probe locations, shown for branched tray (left) and vertical column (right)

$$\begin{aligned} h_{v,out,des-anlz} &= f\left(T_{v,out,des-anlz}, P, q_{v,out,des-anlz}\right) \\ &= f\left(111.8^{\circ}\mathrm{C}, 1626\ \mathrm{kPa}, 1\right) = 1560\ \mathrm{kJ\ kg^{-1}} \end{aligned} \tag{4.25}$$

$$\begin{aligned} x_{v,out,des-anlz} &= f\left(T_{v,out,des-anlz}, P, q_{v,out,des-anlz}\right) \\ &= f\left(111.8^{\circ}\mathrm{C}, 1626\ \mathrm{kPa}, 1\right) = 0.938 \end{aligned} \tag{4.26}$$

The mass, species and energy balance equations are then applied for the desorber-analyzer control-volume. These three independent equations contain three unknown parameters: the desorber-analyzer heat duty, the analyzer solution inlet mass flow rate, and the vapor outlet mass flow rate.

$$\begin{gathered}\dot{m}_{l,in,des-anlz} \cdot x_{l,in,des-anlz} - \dot{m}_{l,out,des-anlz} \cdot x_{l,out,des-anlz} \approx \dot{m}_{v,out,des-anlz} \cdot x_{v,out,des-anlz} \\ \dot{m}_{l,in,des-anlz} \cdot 0.479 - \dot{m}_{l,out,des-anlz} \cdot 0.225 \approx 2.96 \cdot 10^{-4} \text{ kg s}^{-1} \cdot 0.938\end{gathered} \tag{4.27}$$

$$\begin{aligned}\dot{Q}_{des,WF} &= \dot{m}_{v,out,des\text{-}anlz} h_{v,out,des\text{-}anlz} + \dot{m}_{l,out,des\text{-}anlz} h_{l,out,des\text{-}anlz} - \dot{m}_{l,in,des\text{-}anlz} h_{l,in,des\text{-}anlz} \\ &= \dot{m}_{v,out,des\text{-}anlz} \cdot 1560 \text{ kJ kg}^{-1} + 5.95 \cdot 10^{-4} \text{ kg s}^{-1} \cdot 477.5 \text{ kJ kg}^{-1} - \dot{m}_{l,in,des\text{-}anlz} \cdot 135.5 \text{ kJ kg}^{-1}\end{aligned} \tag{4.28}$$

$$\begin{aligned}\dot{m}_{v,out,des-anlz} &= \dot{m}_{l,in,des-anlz} - \dot{m}_{l,out,des-anlz} \\ \dot{m}_{v,out,des-anlz} &= \dot{m}_{l,in,des-anlz} - 5.95 \cdot 10^{-4} \text{ kg s}^{-1}\end{aligned} \tag{4.29}$$

Solving Eq. (4.27) through (4.29) iteratively yields the following results:

$$\dot{m}_{v,out,des-anlz} = 3.28 \cdot 10^{-4} \text{ kg s}^{-1} \tag{4.30}$$

$$\dot{m}_{l,in,des-anlz} = 9.22 \cdot 10^{-4} \text{ kg s}^{-1} \tag{4.31}$$

$$\dot{Q}_{des,WF} = \dot{Q}_{des-anlz,WF} = 671 \text{ W} \tag{4.32}$$

The overall ammonia-water heat duty for the component was reported above in Eq. (4.8). The rectifier ammonia-water heat duty may be obtained with the desorber heat duty from Eq. (4.32).

$$\begin{gathered}\dot{Q}_{comp,WF} = \dot{Q}_{des,WF} + \dot{Q}_{rect,WF} \\ 586 \text{ W} = 671 \text{ W} + \left(-85 \text{ W}\right)\end{gathered} \tag{4.33}$$

4.2.3 Sensible Heat Duties

In subsequent discussion, the experimental heat transfer results are compared with values predicted by correlations and methods available in the literature. Several of the methods, such as the equilibrium mass transfer correction method of Silver, Bell and Ghaly (Silver, 1947; Bell and Ghaly, 1972), make use of the vapor sensible heat duty.

$$\dot{Q}_{v,s} = \dot{m}_v c_{p,v} \left(T_{v,o} - T_{v,i}\right) \tag{4.34}$$

The specific heat values are calculated for the bulk vapor properties. The bulk vapor temperatures, $T_{v,bulk,des}$ and $T_{bulk,rect}$, are determined by averaging several pertinent vapor temperatures, as shown in Figure 4.4. The bulk temperatures are shown relative to other major temperatures in Figures 4.1 and 4.2. The vapor inlet temperature, $T_{v,o}$, for the desorbers is taken to be the analyzer vapor temperature, $\mathrm{T}_{v,anlz}$. The vapor inlet temperature, $T_{v,i}$, or lower vapor temperature (no actual vapor inlet exists in the desorber), is represented by the bottom-most vapor measurement for the branched tray. In the vertical column, the solution outlet temperature is used, because no local vapor temperature is available. For the desorber, an assumption of uniform vapor generation rate gives the following estimate of the vapor flow rate.

$$\dot{m}_{v,des,bulk} = \frac{\dot{m}_{v,out}}{2} \tag{4.35}$$

Sensible heat duty values for the sample point are determined as follows.

$$\begin{gathered} \dot{Q}_{v,s,des} = \frac{\dot{m}_{v,des}}{2} c_{p,v,bulk,des} \left(T_{v,anlz} - T_{l,out} \right) \\ 13.7\text{ W} \frac{1\text{ kW}}{1000\text{ W}} = \frac{0.296\,\text{g s}^{-1}}{2} 2.63\text{ kJ kg}^{-1}\text{ K}^{-1} \left(143.8°\text{C} - 111.8°\text{C} \right) \end{gathered} \tag{4.36}$$

For the rectifier, the vapor outlet temperature is measured directly and the vapor inlet temperature is taken to be the analyzer vapor temperature, $T_{v,anlz}$. The mass flow rate is assumed to be constant.

$$\begin{gathered} \dot{Q}_{v,s,rect} = \dot{m}_{v,out} c_{p,v,bulk,rect} \left(T_{v,out} - T_{v,anlz} \right) \\ \text{-25.6 W} \frac{1\text{ kW}}{1000\text{ W}} = 0.296\,\text{g s}^{-1} 2.87\text{ kJ kg}^{-1}\text{ K}^{-1} \left(81.7°\text{C} - 111.8°\text{C} \right) \end{gathered} \tag{4.37}$$

4.2.4 **Test Section Heat Loss**

As discussed in the previous sections, heat duties can be calculated for both the coupling-fluid and working-fluid sides of the desorber and rectifier sections and for the overall component. Due to the large temperature differences between the coupling fluids and the ambient ammonia-water vapor, which surrounds the test section, a significant amount of heat can be lost from the desorber coupling-fluid and gained by the rectifier coupling-fluid during testing. This is indicated by the differences in the coupling-fluid and working-fluid heat duties, shown in Table 4.2 for the sample data point. Sample data point values for the branched tray are provided in Table 4.1. The sample point is taken at the design conditions, provided in Table 3.2. Note that the desorber coupling-fluid has a higher heat duty than the desorber solution, indicating heat loss. The higher coupling-fluid heat duty, compared to solution heat duty, in the rectifier indicates that the coupling-fluid is gaining heat (due to the elevated temperature of the surroundings). To minimize heat transfer to the surrounding vapor, a 12.7 mm thick layer of PTFE was attached to the back of the test section as insulation. Additionally, the surrounding vapor and pressure chamber walls were heated with high-power electric heaters (described in the Experimental Approach) to minimize the temperature difference with the test section. Ten silicone surface heaters were applied to the chamber and had a combined heating power of approximately 4.3 kW. Heater power was adjusted to maintain the surrounding vapor at approximately the average of the desorber and rectifier coupling fluid temperatures. For the sample point, the average rectifier coupling-fluid temperature was

Table 4.2: Test section heat duty and heat loss/gain

	Heat Duty (W)		
	Desorber	**Rectifier**	**Overall**
Coupling-Fluid	745	-103	642
Working-Fluid	671	-85	586
Difference	74	-18	56
Percent Difference	9.9%	17.2%	8.8%

72.4°C, the average surrounding vapor temperature was 112.5°C, while the average desorber coupling-fluid temperature was 160.6°C (Figure 4.5). On average, over the range of conditions tested, the branched tray test section had a difference between desorber coupling-fluid and working-fluid heat duties of 13.8% (13.4% for the vertical column). The branched tray rectifier, with a much smaller heat duty, but similar areas and temperature differences, had a difference in heat duties of 42.8% on average, over the range of conditions tested (40.0% for the vertical column).

To estimate these auxiliary heat losses and gains expected due to natural convection and radiation between the respective transfer surfaces, a one-dimensional model was developed. The model utilizes data for the coupling-fluid, working-fluid, and surrounding vapor temperatures to estimate heat loss from the desorber coupling-fluid, and heat addition to the rectifier coupling-fluid. Details of the model, and representative values for the sample data point under consideration here, are provided in Appendix A.

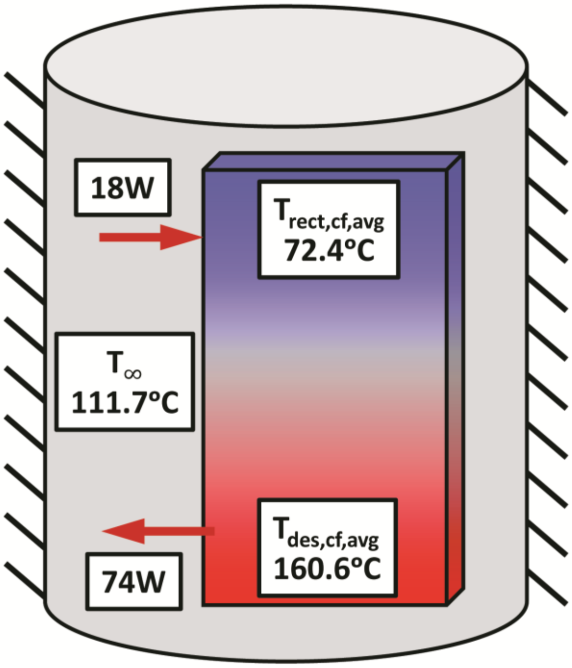

Figure 4.5: Test section auxiliary heat transfer; values shown for branched sample data point

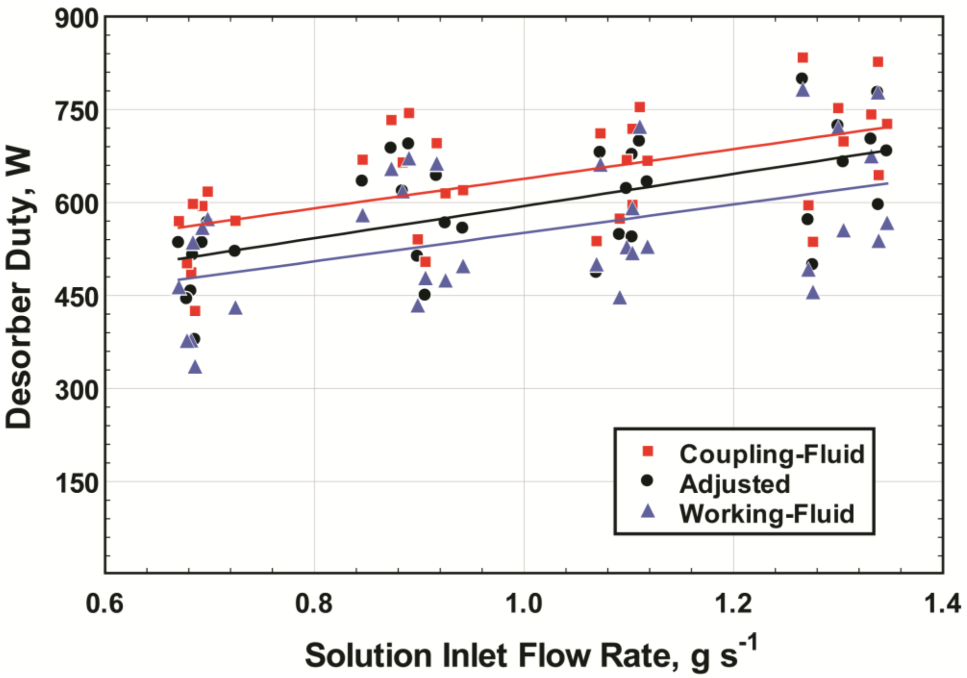

Figure 4.6: Experimental and adjusted desorber heat duties

The coupling-fluid and working-fluid heat duties as well as the adjusted heat duty, which corrects the coupling-fluid duty to account for heat transfer to the surroundings, are provided in Figures 4.6 and 4.7 for the branched tray desorber and rectifier, respectively. First-order polynomial curve fits for the heat duties are also shown. Results for the vertical column are similar, and are provided in Appendix A.

While adjusting for natural convection and radiation heat transfer can improve agreement between the coupling- and working-fluid heat duties, some difference remains. This difference is likely due to two factors: external condensation and evaporation of the surrounding vapor on the outside faces of the test section, and small departures in the actual conditions of the rectifier vapor inlet from the assumptions used in the analysis of the sub-component heat duties (Section 4.2.2).

The effect of external condensation of the surrounding vapor on the back and sides of the rectifier section, and evaporation of any condensate or liquid droplets from

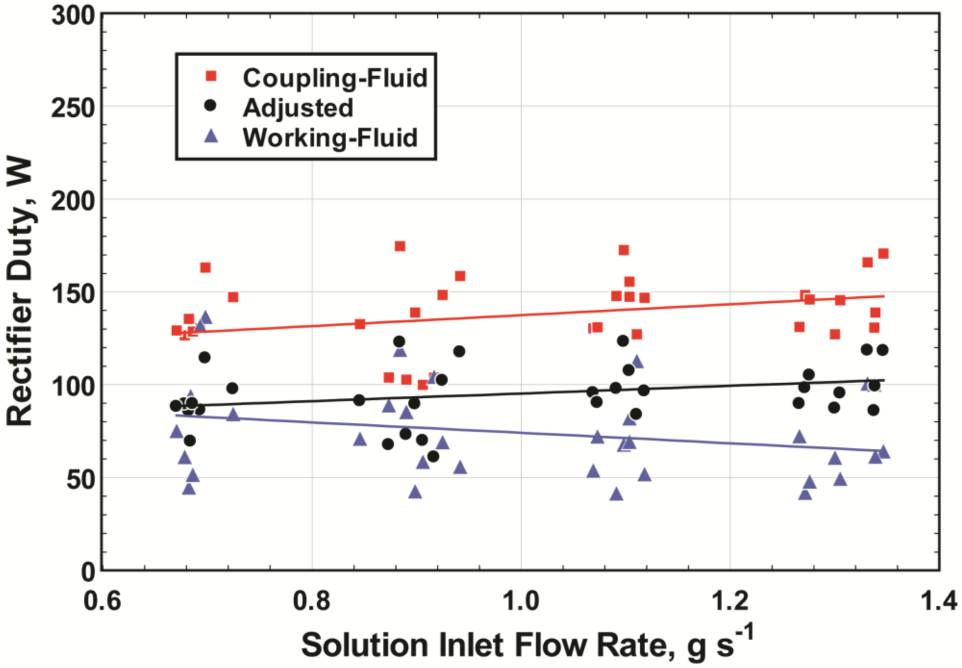

Figure 4.7: Experimental and adjusted rectifier heat duties

the back of the desorber section could easily account for the difference in observed heat duties. Using properties estimated from the data for the vapor, an evaporation rate of, on average, 0.028 g s^{-1} (11.8% of the average desorption rate inside the desorber) on the exterior of the desorber section would account for the remaining difference in heat duties. Similarly, a condensation rate of, on average, 0.010 g s^{-1} (38.3% of the average condensation rate inside the rectifier section) on the exterior of the rectifier section would account for the difference in rectifier heat duties. Additional detail on the heat loss analysis is provided in Appendix A.

An additional factor that can contribute to differences in the coupling- and working-fluid duties is the possibility of differences in the actual rectifier vapor inlet properties, and those determined in the analysis. Calculation of the working-fluid heat duty for the desorber and rectifier sections requires knowledge of the fluid conditions and flow rate for the vapor stream exiting the desorber-analyzer (entering the rectifier). If the fluid enthalpy or mass flow rate for this vapor stream is calculated to be lower than actual values, the resulting working-fluid heat duty for both the desorber and rectifier will be lower than the actual value, shown in Eq. (4.28). It is likely that this effect also plays a role in the difference in heat duties, particularly given the limited vapor temperature measurements, and use of assumptions to determine the intermediate vapor flow rate. This factor provides some explanation for the trend seen in Figure 4.7 for the rectifier working-fluid heat duty. While external heat transfer and condensation would not account for the increasing difference between the heat duties at higher solution flow rates, the conditions within the test sections are likely affected and may result in reduced applicability of the assumptions used to determine the vapor flow rate and properties at the rectifier inlet.

Considering these factors, an average of the coupling- and working-fluid heat duties is used in subsequent sections for calculation of heat and mass transfer coefficients.

4.3 Heat Transfer Coefficients

With the heat duties defined, overall and ammonia-water heat transfer coefficients can be are determined. The analysis methods used in the calculation of the heat transfer coefficients are described in the following sections.

4.3.1 Overall Heat Transfer Coefficients

The overall heat transfer coefficient (U) may be determined with knowledge of the heat transfer area (A), temperature difference between coupling-fluid and ammonia-water streams, and heat duty. A counter-flow log mean temperature difference ($LMTD$) is used:

$$\dot{Q} = UA \cdot LMTD \tag{4.38}$$

$$LMTD = \frac{\left(T_{h,i} - T_{c,o}\right) - \left(T_{h,o} - T_{c,i}\right)}{\ln\left(\dfrac{T_{h,i} - T_{c,o}}{T_{h,o} - T_{c,i}}\right)} \tag{4.39}$$

For the desorber section, the log mean temperature difference can be defined as follows:

$$\begin{gathered} LMTD_{des} = \frac{\left(T_{des,cf,in} - T_{l,out}\right) - \left(T_{des,cf,out} - T_{l,in,des}\right)}{\ln\left(\dfrac{T_{des,cf,in} - T_{l,out}}{T_{des,cf,out} - T_{l,in,des}}\right)} \\ 40.9°\text{C} = \frac{\left(179.5°\text{C} - 143.8°\text{C}\right) - \left(141.6°\text{C} - 94.9°\text{C}\right)}{\ln\left(\dfrac{179.5°\text{C} - 143.8°\text{C}}{141.6°\text{C} - 94.9°\text{C}}\right)} \end{gathered} \tag{4.40}$$

For the branched tray test section, the desorber solution inlet temperature, $T_{l,in,des}$, is taken to be the average of the two closest available measurements: the top-most measured liquid pool temperature (T_5 in Figure 3.6), and the solution inlet temperature ($T_{l,in}$). For the vertical column test section, the desorber solution inlet temperature is measured at the upper-most desorber liquid location. Solution outlet temperatures are taken from the solution outlet port for both test sections. These values are shown in Figures 4.1 and 4.2.

The heat transfer area for the desorber was defined during the physical design of the test sections. For both test sections, the heat transfer area used here is the ammonia-water solution-side area ($A_{des,WF}$). In the vertical column test section, this is the area of the vertical wall in the desorber section that is wetted by ammonia-water solution. In the branched tray test section, the area used is the pool-boiling heated wall area, which is discussed in detail in the following section on the ammonia-water heat transfer coefficients (Eqs. (4.50) and (4.51)). With a value for the heat transfer area, the overall heat transfer coefficient can be determined for the desorber.

$$\begin{gathered}\dot{Q}_{des,avg} = \frac{\dot{Q}_{des,WF} + \dot{Q}_{des,CF}}{2} = U_{des} A_{des,WF} \cdot LMTD_{des} \\ 708\text{ W} = \frac{671\text{ W} + 745\text{ W}}{2} = 1505\text{ W m}^{-2}\text{ K}^{-1}\left(0.0115\text{ m}^2\right)40.9°\text{C}\end{gathered} \tag{4.41}$$

Note that the heat duty used in Eq. (4.41) is an average of the desorber working-fluid (ammonia-water) heat duty and the desorber coupling-fluid heat duty, as discussed previously.

An overall heat transfer coefficient for the rectifier section may be determined using the same approach as was described for the desorber. For the rectifier, the working-fluid outlet temperature, $T_{v,out}$, is given by the vapor outlet condition. The inlet temperature, $T_{in,rect}$, is taken to be the analyzer vapor temperature, $T_{v,anlz}$. These temperatures are shown in Figures 4.1 and 4.2.

$$\begin{gathered}LMTD_{rect} = \frac{\left(T_{in,rect} - T_{rect,CF,out}\right) - \left(T_{v,out} - T_{rect,CF,in}\right)}{\ln\left(\dfrac{T_{in,rect} - T_{rect,CF,out}}{T_{v,out} - T_{rect,CF,in}}\right)} \\ 24.3°\text{C} = \frac{\left(111.8°\text{C} - 87.9°\text{C}\right) - \left(81.7°\text{C} - 56.9°\text{C}\right)}{\ln\left(\dfrac{111.8°\text{C} - 87.9°\text{C}}{81.7°\text{C} - 56.9°\text{C}}\right)}\end{gathered} \tag{4.42}$$

It should be noted that the vapor inlet temperature is used in the rectifier LMTD, rather than the reflux outlet temperature. This method is used because the condensation correlations that will be employed in subsequent discussion are typically based on a wall temperature difference that uses the fluid saturation temperature, T_{sat} - T_{wall}. In the present study, the liquid reflux outlet condition is expected to be significantly sub-cooled. Therefore, any experimental heat transfer coefficients that were determined using the reflux temperature would not be comparable to those calculated using a saturated fluid temperature. Hence, the analyzer vapor temperature, $T_{v,anlz}$, which is expected to be at saturated conditions, is used for the rectifier LMTD hot inlet temperature. This method of LMTD calculation accounts for the thermal resistances in the vapor as well as liquid phases.

The heat transfer area is obtained from the physical design of the rectifier for each test section. As in the desorber section, the ammonia-water-side area ($A_{rect,WF}$) is used for the calculation of the overall heat transfer coefficient. The vertical wall area of the rectifier is used for the vertical column test section. For the branched tray design, the wall includes fins and a modified wall area that includes the fin area and fin efficiency is used. Details of the calculations for this area are given in the following section (Eqs. (4.50) and (4.52)). After obtaining the heat transfer area, the overall heat transfer coefficient may be calculated from Eq. (4.41). The average of the coupling-fluid and ammonia-water heat duties is used, as with the desorber.

$$\begin{gathered}\dot{Q}_{rect,avg} = \frac{\dot{Q}_{rect,WF} + \dot{Q}_{rect,CF}}{2} = U_{rect} A_{rect,WF} \cdot LMTD_{rect} \\ 94\text{ W} = \frac{85\text{ W} + 103\text{ W}}{2} = 207\text{ W m}^{-2}\text{ K}^{-1}\left(0.0186\text{ m}^2\right)24.3°\text{C}\end{gathered} \tag{4.43}$$

4.3.2 Coupling-Fluid Heat Transfer Coefficients

To quantify the heat transfer performance of the test sections in a manner that is readily compared to alternate configurations and can also provide guidance for future designs using similar geometries, the ammonia-water heat transfer coefficients must be evaluated. To do so, a thermal resistance network approach is used (Figure 4.8). It is assumed that the liquid sensible heat load is removed at the phase interface. Evaluation

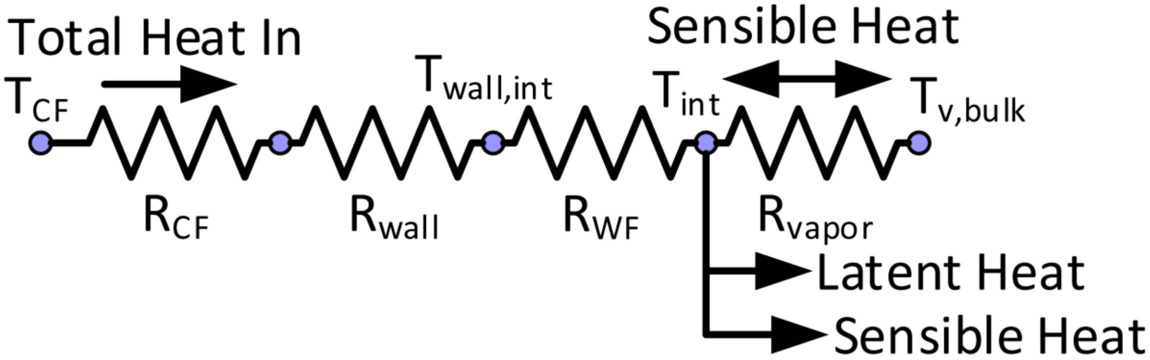

Figure 4.8: Desorption thermal resistance network

of the coupling-fluid thermal resistances and thus coupling-fluid heat transfer coefficients is required before the ammonia-water heat transfer coefficients can be calculated.

All properties for the desorber coupling-fluid, Paratherm NF mineral oil, were evaluated at an average coupling-fluid temperature, as described previously. The coupling-fluid Reynolds number can then be evaluated.

$$\begin{aligned} \mathrm{Re}_{des,CF} &= \frac{\dot{m}_{des,CF} D_{h,CF}}{A_{flow,CF,ch} N_{des,CF,ch} \mu_{des,CF}} \\ 121 &= \frac{7.65\cdot 10^{-3}\ \mathrm{kg\ s^{-1}}\left(4.42\cdot 10^{-4}\ \mathrm{m}\right)}{2.10\cdot 10^{-7}\ \mathrm{m^{2}}\left(103\right)1.29\cdot 10^{-3}\ \mathrm{kg\ m^{-1}s^{-1}}} \end{aligned} \tag{4.44}$$

The coupling-fluid heat transfer coefficient is evaluated using the correlation of Sparrow and Haji-Sheikh (1965) for laminar flow in circular-section ducts.

$$\begin{aligned} \alpha_{des,CF} &= f\left(\mathrm{Re}_{des,CF}, D_{h,CF}, k_{des,CF}, \phi\right) \\ \alpha_{des,CF} &= f\left(121,\ 4.42\cdot 10^{-4}\ \mathrm{m},\ 9.77\cdot 10^{-2}\ \mathrm{W\ m^{-1}\ K^{-1}}, \frac{\pi}{2}\right) = 903\ \mathrm{W\ m^{-2}\ K^{-1}} \end{aligned} \tag{4.45}$$

Here, $k_{des,CF}$ is the fluid conductivity and ϕ is a geometric parameter representing the half-angle of the duct.

The rectifier coupling-fluid heat transfer coefficient is evaluated using the same method.

$$\mathrm{Re}_{rect,CF} = \frac{\dot{m}_{rect,CF} D_{h,CF}}{A_{flow,CF,ch} N_{rect,CF,ch} \mu_{rect,CF}}$$
$$41 = \frac{7.90 \cdot 10^{-4}\ \mathrm{kg\ s^{-1}} \left(4.42 \cdot 10^{-4}\ \mathrm{m}\right)}{2.10 \cdot 10^{-7}\ \mathrm{m^2} \left(103\right) 3.91 \cdot 10^{-4}\ \mathrm{kg\ m^{-1} s^{-1}}} \tag{4.46}$$

$$\alpha_{rect,CF} = f\left(\mathrm{Re}_{rect,CF}, D_{h,CF}, k_{rect,CF}, \phi\right)$$
$$\alpha_{rect,CF} = f\left(41,\ 4.42 \cdot 10^{-4}\ \mathrm{m},\ 0.665\ \mathrm{W\ m^{-1}\ K^{-1}}, \frac{\pi}{2}\right) = 6140\ \mathrm{W\ m^{-2}\ K^{-1}} \tag{4.47}$$

4.3.3 Ammonia-Water Heat Transfer Coefficients

Once the coupling-fluid heat transfer coefficients are calculated, the ammonia-water heat transfer coefficients may be evaluated. As stated previously, a resistance network approach is used (Figure 4.8).

$$\frac{1}{UA} = R_T = R_{wall} + R_{CF} + R_{WF}$$
$$\frac{1}{\alpha_{WF}} = \frac{1}{U} - R_{wall} A_{WF} - \frac{1}{\alpha_{CF} A_{CF}} A_{WF} \tag{4.48}$$

As shown in Eq. (4.48), the ammonia-water heat transfer coefficient (α_{WF}) deduced from the measured UA depends on the calculation of the coupling-fluid heat transfer coefficient (α_{CF}), and its uncertainty. As the coupling-fluid heat transfer coefficient is determined from correlations available in the literature, the most significant source of uncertainty in the calculated values of α_{WF} originate from the assigned uncertainty of α_{CF}. This is discussed further in following chapter.

In Eq. (4.48), R_{wall} can be determined from the following, where x_{wall} is the wall thickness, A_{wall} is the wall area in the plane normal to the driving temperature difference, and k_{wall} is the thermal conductivity of the stainless steel wall (evaluated at an iteratively determined wall temperature as shown in Eq. (4.52)).

$$R_{wall} = \frac{x_{wall}}{k_{wall} A_{wall}} \tag{4.49}$$

For the desorber section:

$$\begin{gathered} R_{wall,des} = \frac{x_{wall,des}}{k_{wall,des} A_{wall,des}} \\ 6.89 \cdot 10^{-3} \text{ K W}^{-1} = \frac{2.22 \cdot 10^{-3} \text{ m}}{16.7 \text{ W m}^{-1} \text{ K}^{-1} \left(1.94 \cdot 10^{-2} \text{ m}^2\right)} \end{gathered} \tag{4.50}$$

For the rectifier section:

$$\begin{gathered} R_{wall,rect} = \frac{x_{wall,rect}}{k_{wall,rect} A_{wall,rect}} \\ 3.09 \cdot 10^{-2} \text{ K W}^{-1} = \frac{7.05 \cdot 10^{-3} \text{ m}}{15.7 \text{ W m}^{-1} \text{ K}^{-1} \left(1.45 \cdot 10^{-2} \text{ m}^2\right)} \end{gathered} \tag{4.51}$$

The required desorber wall temperature is given by:

$$\begin{gathered} \dot{Q}_{des,avg} = \left(R_{CF,des} + \frac{R_{wall,des}}{2} \right)^{-1} \cdot \left(T_{des,CF,avg} - T_{wall,des} \right) \\ 708 \text{ W} = \left(3.75 \cdot 10^{-2} \text{ K W}^{-1} + \frac{6.89 \cdot 10^{-3} \text{ K W}^{-1}}{2} \right)^{-1} \cdot \left(160.6°\text{C} - 131.6°\text{C} \right) \end{gathered} \tag{4.52}$$

For the rectifier:

$$\begin{gathered} \dot{Q}_{rect,avg} = \left(R_{CF,rect} + \frac{R_{wall,rect}}{2} \right)^{-1} \cdot \left(T_{rect,CF,avg} - T_{wall,rect} \right) \\ \text{-94 W} = \left(7.74 \cdot 10^{-3} \text{ K W}^{-1} + \frac{3.09 \cdot 10^{-2} \text{ K W}^{-1}}{2} \right)^{-1} \cdot \left(72.4°\text{C} - 74.6°\text{C} \right) \end{gathered} \tag{4.53}$$

Evaluation of the heat transfer areas for the coupling-fluid (A_{CF}) and ammonia-water (A_{WF}) thermal resistances both require additional consideration. The coupling-fluid microchannels are considered extended surfaces, as shown in Figure 4.9, and a fin

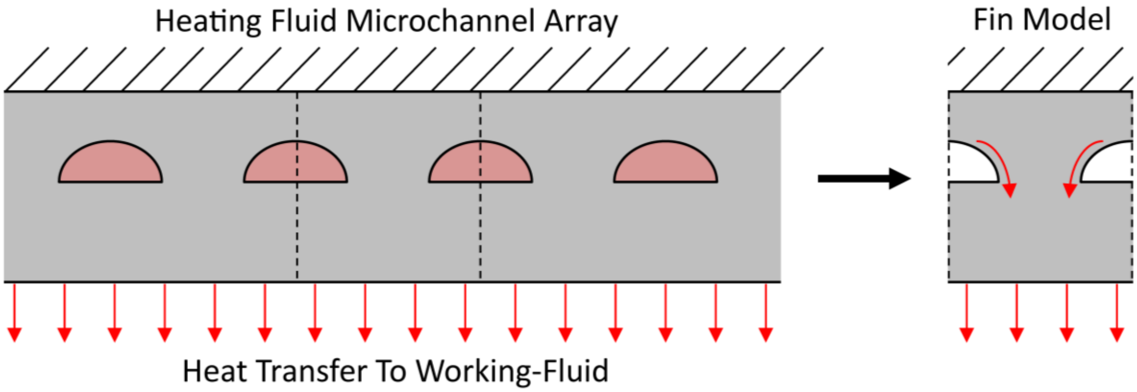

Figure 4.9: Desorber microchannel cross-section and fin idealization

efficiency term (η_{fin}) is applied to the heat transfer area to account for the addition conduction resistance. $A_{CF,ch}$ is the surface area of one microchannel, N_{ch} is the number of channels and t_{fin} and L_{fin} are the fin thickness and length, respectively.

The fin efficiency for an adiabatic tip condition is estimated using the following equation. Values for the various fin efficiencies are given in Table 4.3.

$$\eta_{fin} = \frac{\tanh\left(\left(\frac{2\cdot\alpha}{k_{wall}t_{fin}}\right)^{0.5} L_{fin}\right)}{\left(\frac{2\cdot\alpha}{k_{wall}t_{fin}}\right)^{0.5} L_{fin}} \tag{4.54}$$

For the desorber section:

$$\begin{gathered} A_{CF,des} = A_{CF,ch} N_{ch,des} \eta_{fin,ch,des} \\ 2.96\cdot 10^{-2}\ \mathrm{m}^2 = 2.90\cdot 10^{-4}\ \mathrm{m}^2 (103) 0.991 \end{gathered} \tag{4.55}$$

For the rectifier section:

$$\begin{gathered} A_{CF,rect} = A_{CF,ch} N_{ch,rect} \eta_{fin,ch,rect} \\ 2.10\cdot 10^{-2}\ \mathrm{m}^2 = 2.90\cdot 10^{-4}\ \mathrm{m}^2 (103) 0.941 \end{gathered} \tag{4.56}$$

For the vertical column test section, the ammonia-water-side heat transfer area is simply the vertical wall surface area, for both the desorber (Figure 4.10) and the rectifier. For the branched tray desorber, the ammonia-water-side heat transfer area in the desorber

Table 4.3: Fin efficiency summary

	Desorber CF	**Rectifier CF**	**Desorber Ribs**	**Rectifier Fins**
α (W m^{-2} K^{-1})	903	6144	6456	244
k_{wall} (W m^{-1} K^{-1})	16.7	15.7	16.7	15.7
t_{fin} (m)	$5.0\cdot10^{-4}$	$5.0\cdot10^{-4}$	$3.8\cdot10^{-3}$	$1.23\cdot10^{-3}$
L_{fin} (m)	$3.5\cdot10^{-4}$	$3.5\cdot10^{-4}$	$5.7\cdot10^{-3}$	$8.9\cdot10^{-4}$
η_{fin} (-)	0.991	0.941	0.384	0.993

is the pool-boiling area (Figure 4.10). This includes prime area (the vertical back faces of the pools), as well as the sides or walls of the pools, which are formed by the ribs separating adjacent pool and vapor passages. These ribs are also modeled as extended surfaces and have an associated fin efficiency term.

$$A_{WF} = A_{WF,prime} + A_{WF,fin}\eta_{WF,fin} \tag{4.57}$$

Finally, the ammonia-water heat transfer area for the rectifier section must be considered. The vertical column rectifier heat transfer area again uses a simple vertical wall surface area. The branched tray rectifier features small fins or vanes, which are treated as extended surfaces and the heat transfer area is modeled as in Eq. (4.57).

For the desorber:

$$\begin{gathered} A_{WF,des} = A_{WF,prime,des} + A_{WF,fin,des}\eta_{WF,fin,des} \\ 1.15\cdot10^{-2}\ \text{m}^2 = 9.05\cdot10^{-3}\ \text{m}^2 + 6.36\cdot10^{-3}\ \text{m}^2\left(0.384\right) \end{gathered} \tag{4.58}$$

For the rectifier:

$$\begin{gathered} A_{WF,rect} = A_{WF,prime,rect} + A_{WF,fin,rect}\eta_{WF,fin,rect} \\ 1.86\cdot10^{-2}\ \text{m}^2 = 1.55\cdot10^{-2}\ \text{m}^2 + 3.12\cdot10^{-3}\ \text{m}^2\left(0.993\right) \end{gathered} \tag{4.59}$$

Note that the solutions to Eq. (4.58) and Eq. (4.59) require values of the ammonia-water heat transfer coefficients. In practice, these equations must be solved simultaneously with Eq. (4.48).

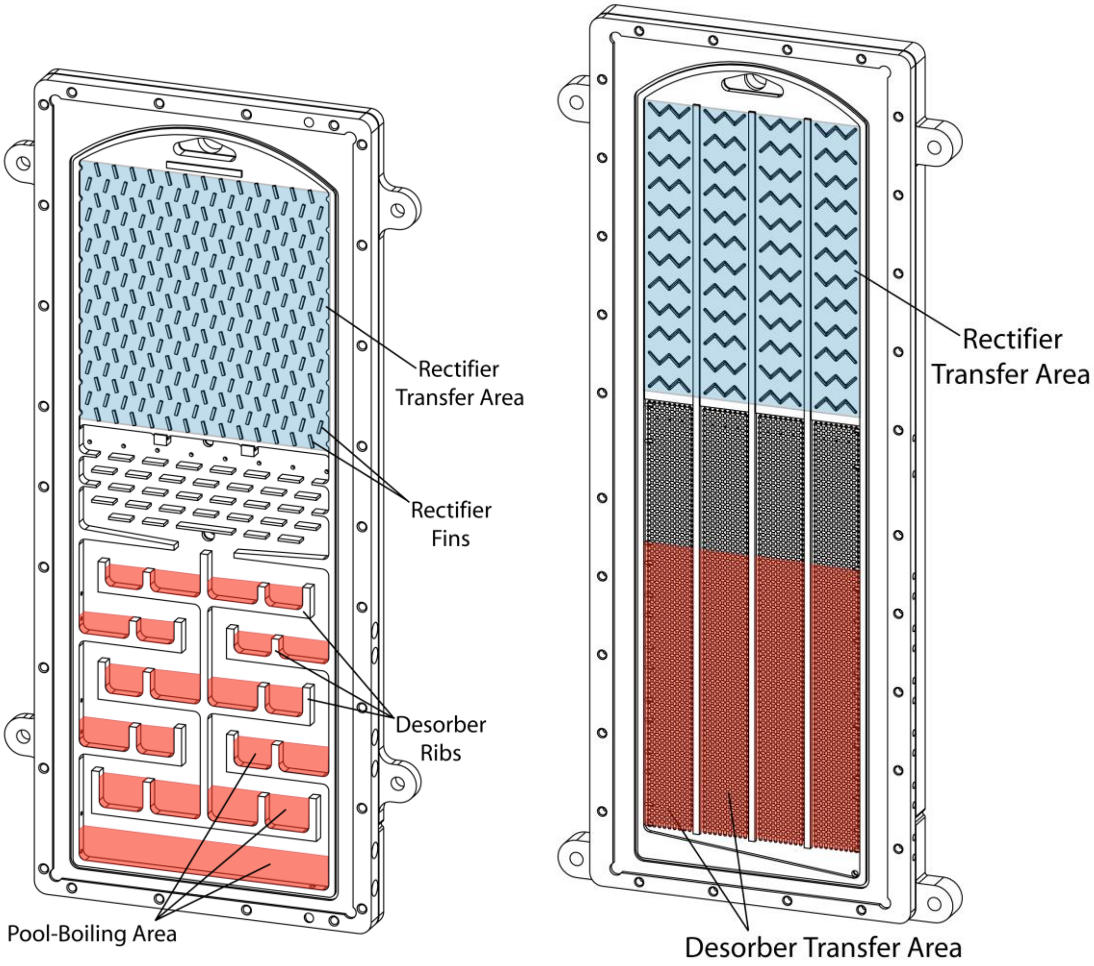

Figure 4.10: Test section heat transfer features (not to scale)

With Eq. (4.50) through Eq. (4.59), Eq. (4.48) can now be solved. For the desorber:

$$\begin{gathered}\frac{1}{\alpha_{WF,des}}=\frac{1}{U_{des}}-R_{wall,des}A_{WF,des}-\frac{1}{\alpha_{des,CF}A_{CF,des}}A_{WF,des}\\ \frac{1}{6456\text{ W m}^{-2}\text{ K}^{-1}}=\\ \frac{1}{1505\text{ W m}^{-2}\text{ K}^{-1}}-\left(6.89\cdot10^{-3}\text{ K W}^{-1}\left(1.15\cdot10^{-2}\text{ m}^{2}\right)\right)-\\ \left(\frac{1}{903\text{ W m}^{-2}\text{ K}^{-1}\left(2.96\cdot10^{-2}\text{ m}^{2}\right)}1.15\cdot10^{-2}\text{ m}^{2}\right)\end{gathered}\tag{4.60}$$

For the rectifier:

$$\begin{gathered}\frac{1}{\alpha_{WF,rect}}=\frac{1}{U_{rect}}-R_{wall,rect}A_{WF,rect}-\frac{1}{\alpha_{rect,CF}A_{CF,rect}}A_{WF,rect}\\ \frac{1}{244\text{ W m}^{-2}\text{ K}^{-1}}=\\ \frac{1}{207\text{ W m}^{-2}\text{ K}^{-1}}-\left(3.09\cdot10^{-2}\text{ K W}^{-1}\left(1.86\cdot10^{-2}\text{ m}^{2}\right)\right)-\\ \left(\frac{1}{6140\text{ W m}^{-2}\text{ K}^{-1}\left(2.10\cdot10^{-2}\text{ m}^{2}\right)}1.86\cdot10^{-2}\text{ m}^{2}\right)\end{gathered}\tag{4.61}$$

4.4 Mass Transfer Coefficients

Due to the nature of the desorption process as a coupled heat and mass transfer phenomenon, it is important to determine the mass transfer coefficients to compare the data with other studies and correlations in the literature, and to be able to provide a more accurate tool for use in the design of future compact counter-flow desorbers.

Three mass transfer problems can be identified in the branched tray desorber design. During the nucleate boiling process, vaporization at the bubble interfaces leads to a deficiency of the more volatile component (ammonia) in the surrounding liquid. This creates a concentration difference between the liquid interface and the liquid bulk, causing diffusion of ammonia towards the liquid/bubble interface from the bulk, and water away from the interface and into the bulk. Additionally, a concentration gradient would be expected to develop in the vapor region of growing bubbles as ammonia diffuses from the interface into the vapor bulk of the bubble. Finally, once the rising bubbles reach the stratified liquid/vapor interface at the top of the liquid pools, the vapor contained within the bubble is released and must diffuse into the vapor stream, which flows past the top of the liquid pools (Figure 4.11). Due to the difficulty in obtaining accurate measurements of the vapor conditions, the mass transfer process inside the vapor

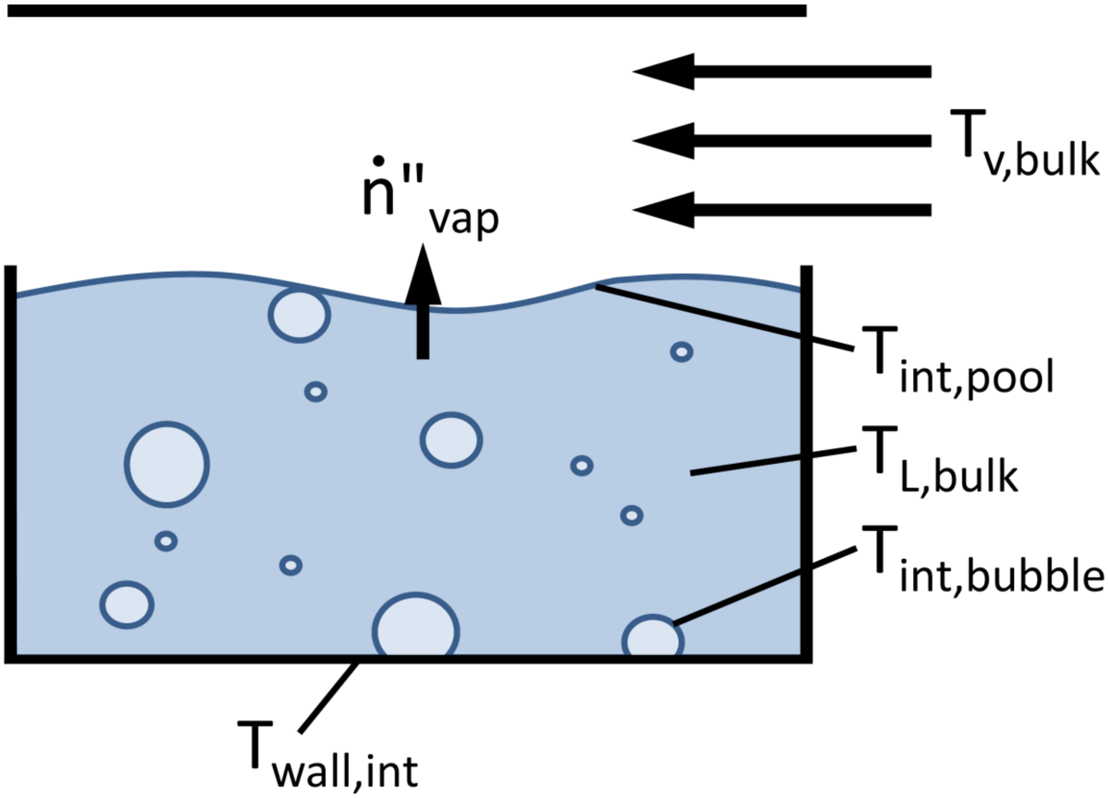

Figure 4.11: Branched tray temperatures

bubbles is not easily characterized. However, the liquid mass transfer process, and the vapor mass transfer process at the stratified interface can be analyzed based on the data, with appropriate assumptions. Schematics of representative temperature, concentration, and velocity profiles for the pool-boiling process are shown in Figure 4.12.

In contrast to the branched tray test section, the vertical column test section has only two mass transfer processes: the diffusion of ammonia through the falling liquid film, towards the interface, and the diffusion of ammonia from the vapor interface into the vapor bulk (and the corresponding counter-diffusion of water). Both of these processes may also be characterized from the data and appropriate assumptions. Schematics of representative temperature, concentration, and velocity profiles for the falling-film process are shown in Figure 4.13. Note that the vapor bulk temperature is

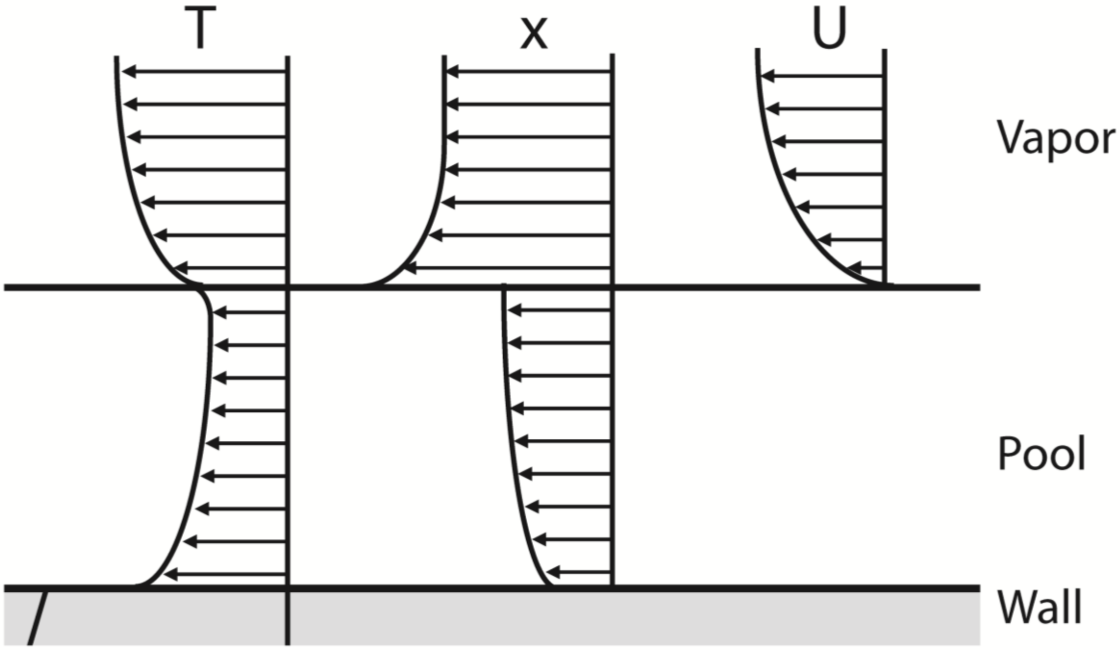

Figure 4.12: Pool-boiling transport profiles

shown to be above the film interface temperature. This is a result of advection of vapor from the lower sections of the desorber where the solution has a lower ammonia concentration and generates vapor that is relatively hotter than the interface at positions higher in the desorber.

To determine the mass transfer coefficients for vapor and liquid in both test sections, a number of parameters, including fluid concentrations, are necessary. The analysis process for both phases is described below.

4.4.1 Liquid-Phase Mass Transfer Coefficient

Assuming liquid mass transfer is dominated by convective processes and diffusion is negligible, the liquid mass transfer coefficient can be calculated from the following equation, containing the molar flux of ammonia $(\dot{n}''_{NH_3})$, convective mass

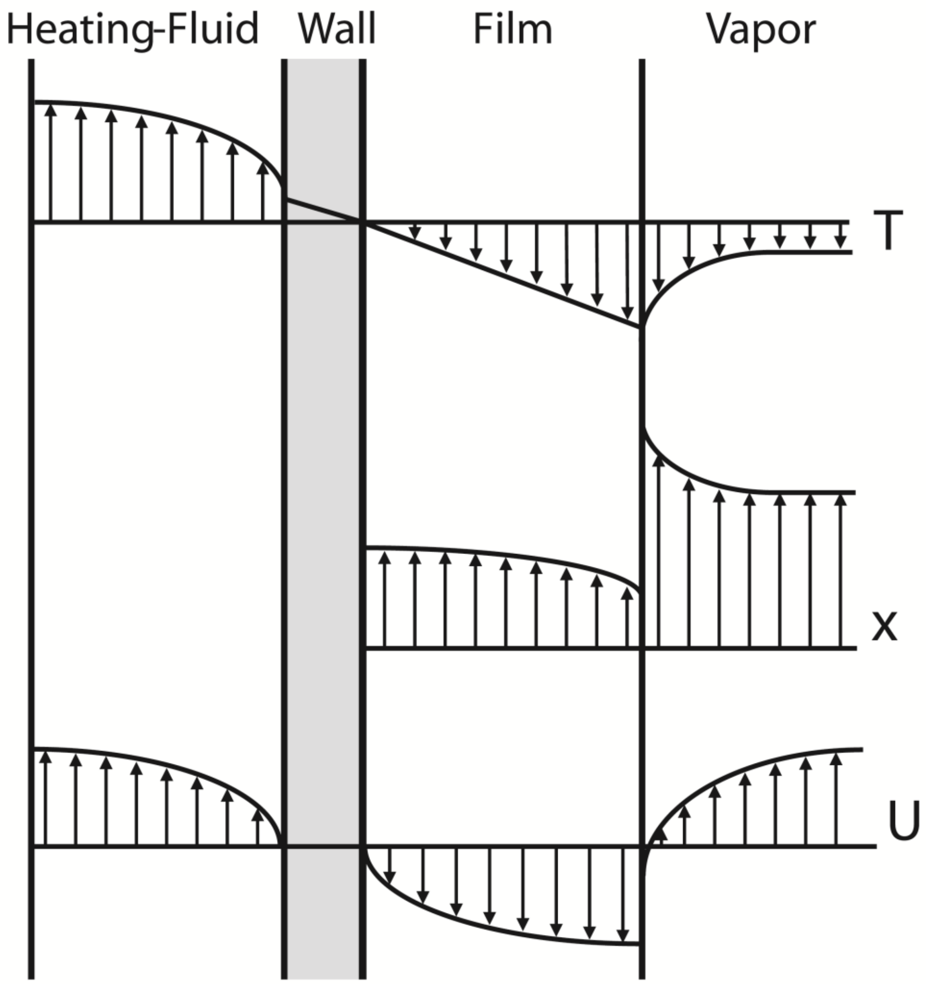

Figure 4.13: Falling-film transport profiles

transfer coefficient for the liquid phase (β_l), and the molar concentration difference between the bubble interface and the liquid bulk (ΔC_{NH_3}).

$$\dot{n}''_{NH_3} = \beta_l \Delta C_{NH_3} \tag{4.62}$$

Arranging on a mass basis:

$$\frac{\dot{m}_{NH_3}}{A_{WF,des}} = \beta_l \Delta \rho_{NH_3} \tag{4.63}$$

The ammonia density terms can then be given as the product of concentration (mass fraction) and total mass density:

$$\frac{\dot{m}_{v,T}x_{v,out}}{A_{WF,des}} = \beta_l \left(x_{l,bulk} \cdot \rho_{l,bulk} - x_{l,int,bubble} \cdot \rho_{l,int} \right) \tag{4.64}$$

Here, the expression on the left represents the mass flux of ammonia into the vapor phase from the liquid bulk. This is defined on a mean basis for the desorber section. As such, the mass flow rate of ammonia to the bubble interface can be taken to be the product of the vapor flow rate ($\dot{m}_{v,T}$) and vapor concentration ($x_{v,out}$), which are known at the rectifier outlet. This assumes the condensation of ammonia in the rectifier is negligible relative to the total vapor flow rate, which is expected to be a reasonable estimate. The transfer area ($A_{WF,des}$) is taken to be the pool-boiling area defined previously (Figure 4.6). While an area representative of the actual interface between the liquid bulk and vapor bubbles would be the most appropriate from a fundamental perspective, it is challenging to quantify and leads to difficulties when comparing mass transfer coefficients in cases with different nucleation sites, bubble sizes, etc. This is analogous to the use of the pool-boiling area in the calculation of nucleate-boiling heat transfer coefficients.

To calculate the liquid mass transfer coefficient, the concentration and density at both the liquid bulk and bubble interface must be determined. The bulk liquid temperatures for both test sections are determined by averaging measurements from a number of the liquid pool (branched tray) and film (vertical column) probe locations. The locations used are shown in Figure 4.4. The measured pressure, and an average liquid concentration, determined from the liquid inlet and outlet conditions described previously, are also used.

$$x_{l,bulk} = \frac{x_{l,out} + x_{l,in}}{2} = \frac{0.226 + 0.479}{2} = 0.352 \tag{4.65}$$

Table 4.4 lists the independent parameters used to define the liquid bulk state, as well as the other states used in the mass transfer analysis. In all cases, the liquid bulk is determined to be at a superheated liquid condition. As such, the density is assumed to be equal to that of a saturated liquid at the defined bulk liquid temperature and concentration, which would be a reasonable approximation for an incompressible fluid.

$$\rho_{l,bulk} = f(T_{l,bulk}, x_{l,bulk}, q_{sat}) = f(125.4°\text{C}, 0.352, 0) = 772.4 \text{ kg m}^{-3} \tag{4.66}$$

To define the interface condition between the liquid phase and vapor bubbles, a saturation assumption is used, which is typical of other approaches in the literature. Additionally, the interface is taken to be at the same temperature and pressure as the liquid bulk, fully defining the state.

The concentration and density at the liquid interface conditions can be determined.

$$x_{l,int,bubble} = f(T_{l,bulk}, P, q_{l,int}) = f(125.4°\text{C}, 1626 \text{ kPa}, 0) = 0.300 \tag{4.67}$$

$$\rho_{l,int,bubble} = f(T_{l,bulk}, P, q_{l,int}) = f(125.4°\text{C}, 1626 \text{ kPa}, 0) = 794.8 \text{ kg m}^{-3} \tag{4.68}$$

For all cases, the liquid interface concentration is lower than the bulk liquid

Table 4.4: Branched tray state points

State	Independent Parameters
Liquid bulk	$T_{l,bulk}, P, x_{l,bulk}$
Liquid bubble interface	$T_{l,bulk}, P, q = 0$
Vapor bubble interface	$T_{l,bulk}, P, q = 1$
Vapor pool interface	$T_{l,bulk}, P, q = 1$
Vapor bulk	$T_{v,bulk}, P, q = 1$

concentration, as expected due to the depletion of ammonia in the liquid near the interface.

The liquid mass transfer coefficient may then be determined, recalling Eq. (4.64).

$$\begin{gathered}\dot{m}_{v,NH_3} = \dot{m}_{v,T} x_{v,out} = \beta_l A_{WF,des}\left(x_{l,bulk}\cdot\rho_{l,bulk} - x_{l,int,bubble}\cdot\rho_{l,int,bubble}\right)\\ 2.87\cdot 10^{-4}\text{ kg s}^{-1} = 0.296\text{ kg s}^{-1}\left(0.987\right) = \\ \left(7.65\cdot 10^{-4}\text{ m s}^{-1}\right)1.15\cdot 10^{-2}\text{ m}^2\left(0.352\cdot 772.4\text{ kg m}^{-3} - 0.300\cdot 794.8\text{ kg m}^{-3}\right)\end{gathered}\tag{4.69}$$

The vertical column test section properties are determined using the same method as described above for the branched tray test section, although no nucleation is considered and the interface of interest is between the liquid film and vapor. As stated, the temperature probe locations used to define the bulk liquid temperature are shown in Figure 4.4. The liquid mass transfer coefficient for the vertical column test section is then determined as above.

4.4.2 Vapor-Phase Mass Transfer Coefficient

As discussed previously, a mass transfer coefficient for the vapor bubbles is not determined from the data. However, a vapor mass transfer coefficient for diffusion from the pool surfaces into the rising vapor bulk can be calculated. The following equation applies:

$$\dot{n}''_T = \beta_v \cdot C_T \ln\left(\frac{\tilde{z} - \tilde{x}_{v,int,pool}}{\tilde{z} - \tilde{x}_{v,bulk}}\right)\tag{4.70}$$

Here, the total molar flux $\left(\dot{n}''_T\right)$ is related to the vapor mass transfer coefficient (β_v), the total molar concentration (C_T) given in kmol kg^{-1}, and a driving concentration difference. The concentration terms (defined here on a molar basis) include the concentration of the vaporizing flux $\left(\tilde{z}\right)$, the concentration of the bulk vapor phase

$\left(\tilde{x}_{v,bulk}\right)$, and the interface concentration of the vapor phase $\left(\tilde{x}_{v,\mathrm{int}}\right)$. Molar- and mass-basis concentrations can be readily converted through the relation of the molar masses of the two species.

$$\tilde{x} = \frac{\dfrac{x}{M_{NH_3}}}{\dfrac{x}{M_{NH_3}} + \left(\dfrac{(1-x)}{M_{H_2O}}\right)} \tag{4.71}$$

The total molar flux is then calculated, again assuming the desorber vapor generation rate can be approximated by the rectifier vapor outlet flow rate. The area used is the interface area between the bulk vapor flow and the liquid pools.

$$\dot{n}''_T = \frac{\dot{m}_{v,out}}{A_{\mathrm{int},des} \cdot \left(\tilde{z} M_{NH3} + (1-\tilde{z}) M_{H_2O}\right)} \tag{4.72}$$

As shown in Eq. (4.70), the molar concentration of the vaporizing flux is needed to determine the molar flux. This can be determined from the difference in the liquid and vapor enthalpies at the interface. Using the states defined in the liquid analysis above:

$$h_{l,int,bubble} = f(T_{l,bulk}, P, q_{l,int}) = f(125.4°\mathrm{C}, 1626\ \mathrm{kPa}, 0) = 363.0\ \mathrm{kJ\ kg^{-1}} \tag{4.73}$$

$$h_{v,int,bubble} = f(T_{l,bulk}, P, q_{v,int}) = f(125.4°\mathrm{C}, 1626\ \mathrm{kPa}, 1) = 1648\ \mathrm{kJ\ kg^{-1}} \tag{4.74}$$

With the enthalpy of the vapor and liquid phases at the interface, the mass concentration of the vaporizing flux can be estimated using the enthalpy of desorption.

$$h_{des,latent} = h_{v,\mathrm{int},bubble} - h_{l,\mathrm{int},bubble} = 1648\ \mathrm{kJ\ kg^{-1}} - 363.0\ \mathrm{kJ\ kg^{-1}} = 1285\ \mathrm{kJ\ kg^{-1}} \tag{4.75}$$

$$\begin{gathered} h_{des,latent} = z \cdot h_{fg,NH_3} + (1-z) \cdot h_{fg,H_2O} \\ 1285\ \mathrm{kJ\ kg^{-1}} = 0.770 \cdot 1092\ \mathrm{kJ\ kg^{-1}} + (1-0.770) \cdot 1931\ \mathrm{kJ\ kg^{-1}} \end{gathered} \tag{4.76}$$

Here, the enthalpy of vaporization for pure ammonia (h_{fg,NH_3}) and water (h_{fg,H_2O}) are evaluated at the measure pressure.

The molar concentration of the vaporizing flux may then be calculated from the mass concentration using the relation given by Eq. (4.71). The molar flux at the pool interface may then be determined.

$$\begin{gathered}\dot{n}''_T = \frac{\dot{m}_{v,out}}{A_{\text{int},des}\cdot\left(\tilde{z}\,M_{NH3}+\left(1-\tilde{z}\right)M_{H_2O}\right)}\\ 3.62\cdot10^{-3}\ \text{kmol m}^{-2}\ \text{s}^{-1} = \\ \frac{0.2957\ \text{kg s}^{-1}}{4.74\cdot10^{-3}\ \text{m}^2\left(\left(0.780\right)17.0\ \text{kmol kg}^{-1}+\left(1-0.780\right)18.0\ \text{kmol kg}^{-1}\right)}\end{gathered} \tag{4.77}$$

Revisiting Eq. (4.70), the total molar concentration (C_T) is needed and is calculated using the ideal gas law.

$$\begin{gathered}C_T = \frac{P}{R\cdot\left(T_{v,bulk}+273.2°\text{C}\right)}\\ 0.486\ \text{kmol m}^{-3} = \frac{1626\ \text{kPa}}{8.314\ \text{kJ kmol}^{-1}\ \text{K}^{-1}\cdot\left(129.4°\text{C}+273.2°\text{C}\right)}\end{gathered} \tag{4.78}$$

Finally, the vapor interface and bulk molar concentrations are required. A vapor interface mass concentration is calculated at the pool surface using the measured pressure, saturated vapor assumption, and the bulk liquid temperature, an idealization used in other studies.

$$x_{v,int,pool} = f\left(T_{l,bulk}, P, q_{v,int,pool}\right) = f(125.4°\text{C},1626\ \text{kPa},1) = 0.891 \tag{4.75}$$

The vapor bulk mass concentration is determined using the bulk vapor temperature, measured pressure, and an assumption of saturated vapor. The bulk vapor temperature, as was explained for the bulk liquid temperature, is determined by averaging a number of vapor temperature measurements taken in the desorber section. The locations used are shown in Figure 4.4 for both test sections.

$$x_{v,bulk} = f\left(T_{v,bulk}, P, q_{v,bulk}\right) = f(129.4°\text{C},1626\ \text{kPa},1) = 0.873 \tag{4.79}$$

The mass fraction vapor interface and bulk concentration and the concentration of the vaporizing flux can be converted to molar-basis concentrations using Eq. (4.71).

Finally, the vapor mass transfer coefficient may be calculated.

$$\begin{gathered}\dot{n}''_T = \beta_v \cdot C_T \ln\left(\frac{\tilde{z}-\tilde{x}_{v,int,pool}}{\tilde{z}-\tilde{x}_{v,bulk}}\right) \\ 3.62\cdot 10^{-3}\ \text{kmol m}^{-2}\ \text{s}^{-1} = \\ 4.69\cdot 10^{-2}\ \text{m s}^{-1}\left(0.486\ \text{kmol m}^{-3}\right)\ln\left(\frac{0.780-0.896}{0.780-0.879}\right)\end{gathered} \tag{4.80}$$

Table 4.5 gives the mass- and molar-basis concentration for the various parameters used in the analysis. The equations and assumptions used to determine these concentrations are given in Table 4.6.

The vapor mass transfer coefficient for the vertical column test section is also determined using this method. However, for the vertical column geometry, the interface area is taken to be the same as the area used for the liquid mass transfer and heat transfer calculations.

4.5 Performance Metrics

To better understand the implications of desorber-rectifier performance on system-level operation, it is useful to define several performance metrics. As the

Table 4.5: Fluid concentrations, shown for sample data point

Fluid Concentration	
Mass-Basis	**Molar-Basis**
$z = 0.770$	$\tilde{z} = 0.780$
$x_{l,int,bubble} = 0.300$	$\tilde{x}_{l,int,bubble} = 0.312$
$x_{l,bulk} = 0.352$	$\tilde{x}_{l,bulk} = 0.365$
$x_{v,int,pool} = 0.891$	$\tilde{x}_{v,int,pool} = 0.896$
$x_{v,bulk} = 0.873$	$\tilde{x}_{v,bulk} = 0.879$

Table 4.6: Concentration equations and assumptions, shown for branched tray

Parameter	Defining Equation	Assumption/Approximation
$x_{l,bulk}$	$x_{l,bulk} = \frac{x_{l,out} + x_{l,in}}{2}$	uniform desorption rate through component
$x_{l,int,bubble}$	$x_{l,int} = f(T_{l,bulk}, P, q=0)$	$T_{int,bubble} = T_{l,bulk}$
$x_{v,int,bubble}$	$x_{v,int,bubble} = f(T_{l,bulk}, P, q=1)$	$T_{int,bubble} = T_{l,bulk}$
z	$z = \frac{h_{v,int,bubble} - h_{l,int,bubble} - h_{fg,H_2O}}{h_{fg,NH_3} - h_{fg,H_2O}}$ Eq. (4.75) and Eq. (4.76)	$h_{v,int,bubble} = f(T_{l,bulk}, P, q=1)$
$x_{v,int,pool}$	$x_{v,int,pool} = f(T_{l,bulk}, P, q=1)$	$T_{v,\text{int},pool} = T_{l,bulk}$
$x_{v,bulk}$	$x_{v,bulk} = f(T_{v,bulk}, P, q=1)$	saturated vapor bulk

desorber-rectifier test sections were operated on a single-pressure test facility, a system cooling or heating capacity cannot be determined. Instead, an ideal cooling capacity may be defined based on assumed conditions of a theoretical absorption chiller. To compute the ideal cooling capacity, all refrigerant vapor exiting the desorber is assumed to be fully condensed at the experimentally measured pressure. The refrigerant is then assumed to be expanded to a representative low-side pressure of 500 kPa before undergoing an evaporation process with a specified refrigerant outlet temperature of 12.8°C. The change in enthalpy resulting from this theoretical evaporation process is defined as the ideal cooling capacity. An ideal COP can then be defined using the experimentally determined heat input to the test section.

The vapor (refrigerant) outlet conditions from the desorber-rectifier were determined in Eq. (4.1) and Eq. (4.4) from measured parameters. A condenser outlet enthalpy may then be determined from the experimental high-side pressure, calculated test-section vapor outlet concentration, and assumed condenser outlet quality.

$$h_{cond,out} = f(P, x_{v,out}, q_{cond,out}) = f(1626 \text{ kPa}, 0.987, 0) = 191.9 \text{ kJ kg}^{-1} \tag{4.81}$$

The expansion process is assumed to be adiabatic so the evaporator inlet enthalpy may be determined with the assumed low-side pressure.

$$h_{evap,in} = h_{cond,out} = 191.9 \text{ kJ kg}^{-1} \tag{4.82}$$

Conditions for the evaporator outlet are given by the assumed temperature, previously determined concentration and assumed low side pressure.

$$h_{evap,out} = f(T_{evap,out}, P_{low}, x_{v,out}) = f(12.8°\text{C}, 500 \text{ kPa}, 0.987) = 1224 \text{ kJ kg}^{-1} \tag{4.83}$$

The ideal cooling capacity is then calculated with knowledge of the refrigerant mass flow rate, determined in Eq. (4.1).

$$\begin{gathered} \dot{Q}_{cooling,ideal} = \dot{m}_{v,out} \cdot \left(h_{evap,out} - h_{evap,in}\right) \\ 305 \text{ W} = 2.96 \cdot 10^{-4} \text{ kg s}^{-1} \cdot \left(1224 \text{ kJ kg}^{-1} - 191.9 \text{ kJ kg}^{-1}\right) \end{gathered} \tag{4.84}$$

To determine the ideal cooling COP, the source heat duty must be known. In this case the desorber coupling-fluid side heat duty, from Eq. (4.14), is used.

$$\text{COP}_{ideal} = \frac{\dot{Q}_{cooling,ideal}}{\dot{Q}_{des,CF}} = \frac{305 \text{ W}}{745 \text{ W}} = 0.410 \tag{4.85}$$

CHAPTER 5

RESULTS AND DISCUSSION

The experimental results for ammonia-water desorption and rectification are presented in this chapter. Results are presented for both the branched tray and vertical column test section and compared with the predictions from correlations available in the literature. Additionally, flow visualization images for the desorber, analyzer, and rectifier sections are presented and discussed.

The test matrix presented in Table 3.2 lists the range of solution flow rates, heating fluid inlet temperatures, and solution concentrations over which experiments were conducted. All 36 data points in the matrix were completed for both test sections. Heat duties, overall and solution-side heat transfer coefficients, and vapor and liquid mass transfer coefficients were calculated for all data points based on the analysis methods presented in Chapter 4.

5.1 Flow Visualization

During desorption experiments, flow visualization images and high-speed video of the test sections were recorded to provide insight to the internal heat and mass transfer, and fluid flow mechanisms. The images shown here were captured at nominal baseline conditions, defined in Table 3.2, as ammonia-water desorption was occurring, and are largely representative of the conditions observed across the range of points shown in the test matrix. Qualitative observations from these images and accompanying high-speed video are used to identify modes of heat transfer and flow regimes, determine transfer areas, and to substantiate assumptions used in the quantitative analysis of the data.

5.1.1 Branched Tray Images

Figure 5.1 shows a representative image of the branched tray desorber section during operation. Liquid pools of ammonia-water solution are contained within the stainless steel desorber trays and are subject to nucleate boiling, caused by heating of the back wall of the test section by the coupling-fluid microchannel array. Vapor bubbles generated at the bottom and sides of the solution pools rise to the pool surface where the vapor contained in the bubble is released and combines with the bulk vapor flow, which is advected upwards in a serpentine path past additional pools. Vapor bubbles are generally seen to increase significantly in diameter as they rise through the pools, indicating the presence of a superheated liquid solution. A net flow of ammonia-water

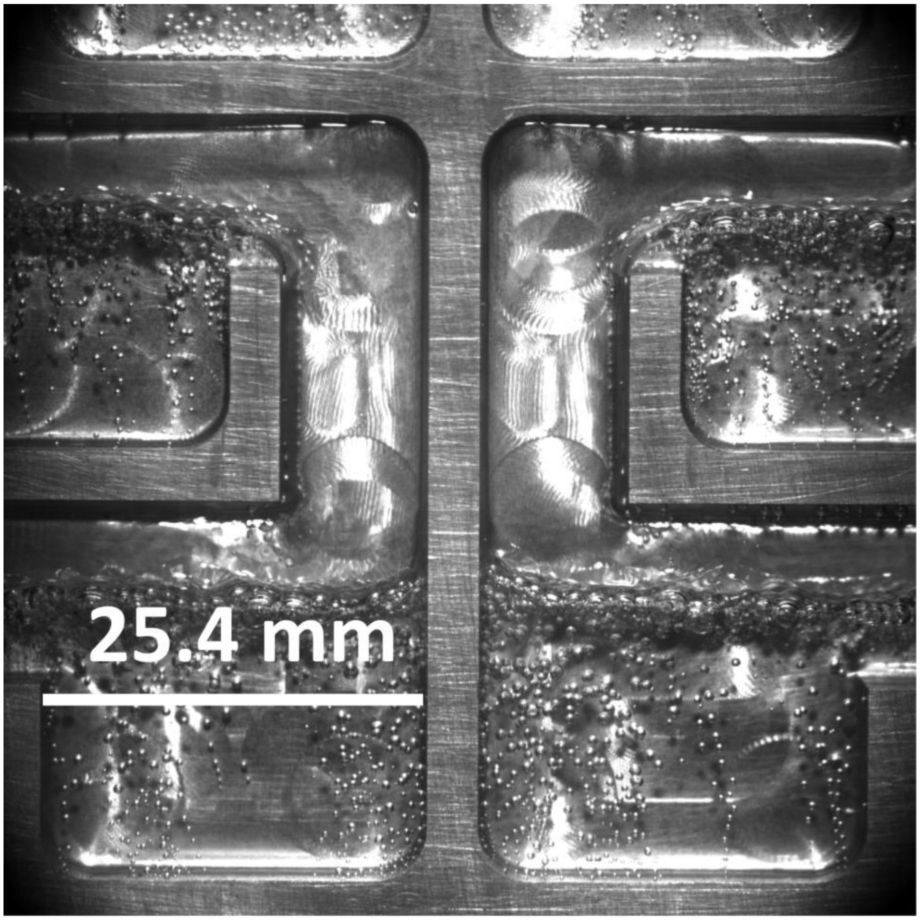

Figure 5.1: Branched tray desorber

solution spills over the sides of the pools, and flows downward through successive trays. Dilute solution is ultimately removed from the bottom of the desorber section through a drain port. It should be noted that the bulk generated vapor does not appear in the images, as it is colorless and transparent at these conditions. However, shear phenomena are apparent at vapor-liquid interfaces, particularly at conditions with high vapor flow rates. The vapor-liquid shear phenomena are discussed in additional detail in Section 5.4 and shown in detail in Figure 5.51.

Figure 5.2 shows the branched tray analyzer section. As described previously, this is a recuperative section with horizontal fins that facilitate formation of liquid films providing high interfacial area for heat and mass exchange between the vapor and

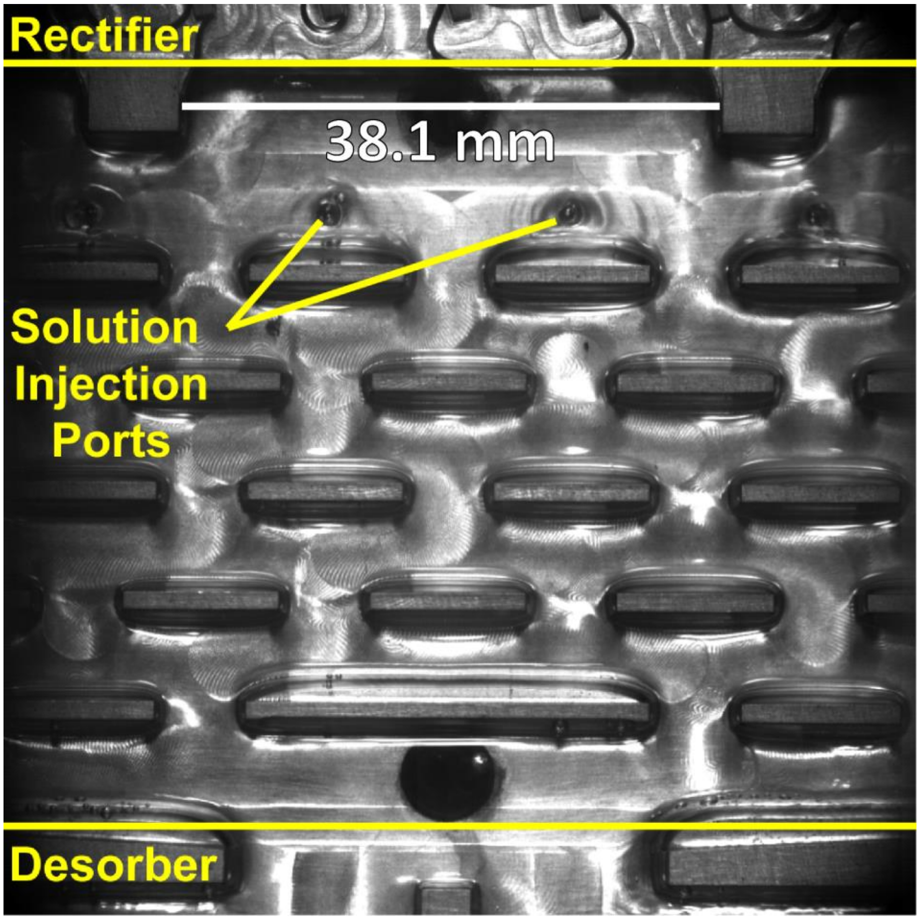

Figure 5.2: Branched tray analyzer

solution streams. The entrances to the rectifier and desorber sections are visible at the top and bottom of the image, respectively. The horizontal row of solution injection ports can be seen above the top-most row of fins and two thermocouple ports are also visible. Thin liquid films can clearly be seen on the top and bottom surfaces of the horizontal fins. A film also exists along the entire back wall, and as indicated by the ripple formation around the injection holes.

Figure 5.3 shows the rectifier section for the branched tray test section. The back wall is cooled via the adjacent coupling-fluid microchannel array, as described previously. The vapor generated lower in the desorber-rectifier flows upwards along this surface and around the diagonal fins, which are designed to provide additional interface

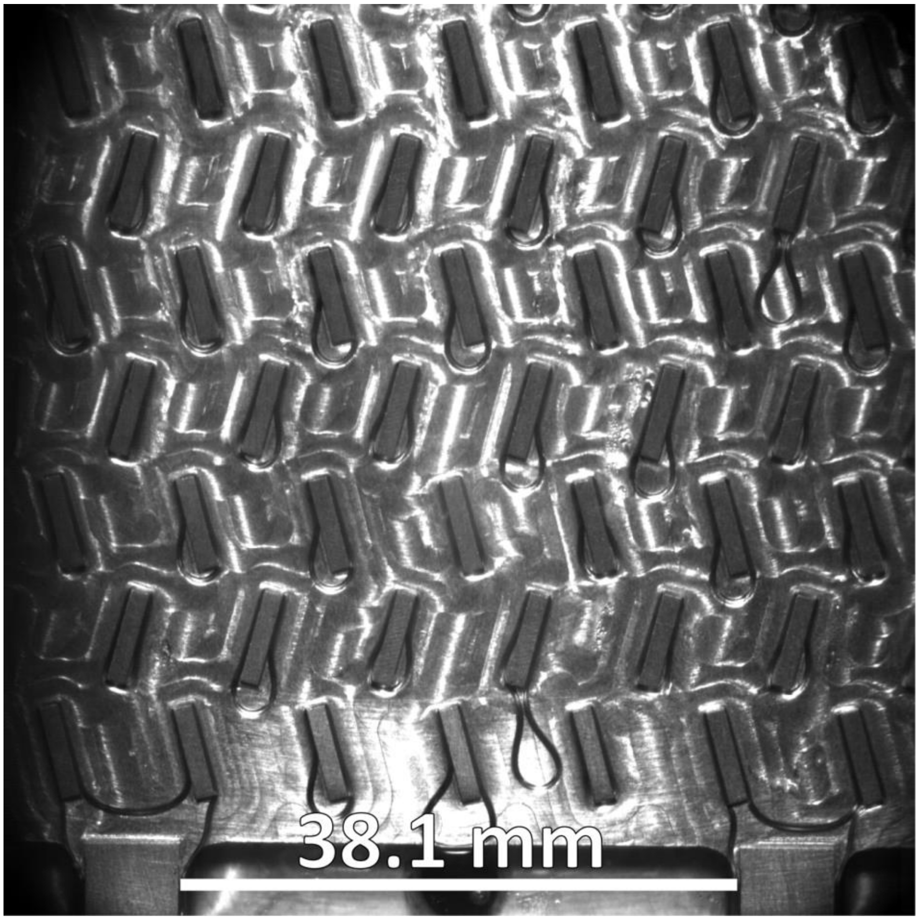

Figure 5.3: Branched tray rectifier

area and mixing. Ammonia-water condensate, or reflux, can be seen on the back wall and is observed to form pendant droplets around the bottom edges of the fins. In some areas, a thin film of condensate coats the back wall, particularly at lower locations where the condensate flow rate would be the greatest. In other locations, typically higher in the rectifier, condensation is observed to be drop-wise, and irregular liquid droplets are seen on the back wall. This condition persists over long periods of operation and the areas of dropwise condensation are not seen to evolve into film condensation over the entire area of the rectifier.

5.1.2 Vertical Column Images

Figure 5.4 shows the two center-most columns for the desorber section of the

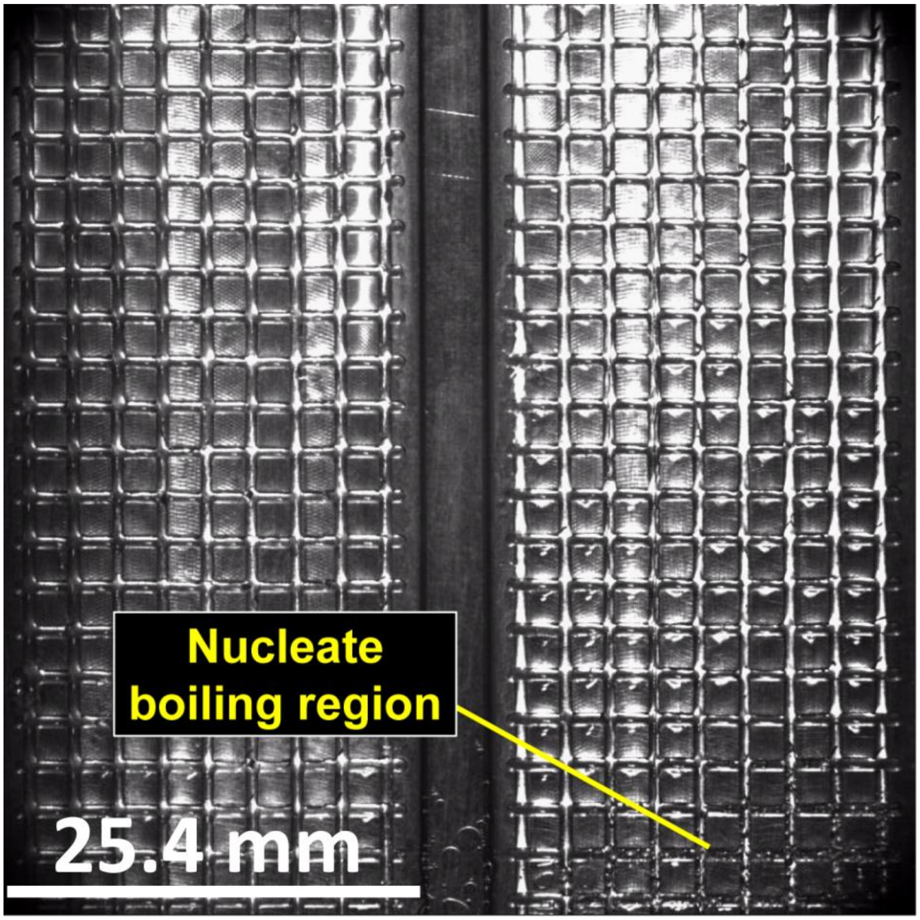

Figure 5.4: Vertical column desorber

vertical column geometry. As in the branched tray design, the back wall is heated via the adjacent coupling-fluid microchannel array. The back wall of the column features a cross-hatch pattern of machined grooves on the solution side (visible in the image), designed to reduce isolated rivulet formation and promote formation of a more uniform film. A thin falling film of ammonia-water solution coats the surface of the back wall. Generated vapor, evaporating from the liquid film-vapor interface, flows upwards through the column. Areas of reduced film thickness are observed towards the bottom of the column, in some cases. This is indicated by increased refraction around the cross-hatch grooves, and is typically accompanied by regions of nucleate boiling within the grooves (seen in the lower right of Figure 5.4). The area of the nucleate boiling region varied with test conditions, but was not observed to cover more than half of the desorber wall, and was typically much less, only occurring at the hotter, lower sections of the component. The region of nucleate boiling shown in Figure 5.4 is shown to occur predominantly in the right side of the image. It was not uncommon to observe some asymmetry in flow phenomena, boiling mechanisms, et cetera, during a test. However, the results of the present study and comparison with model predictions (Chapter 6) indicate that any asymmetry and resulting local changes in heat transfer coefficient do not have a significant impact on the ability to predict the desorber mean heat transfer coefficient.

Figure 5.5 shows the vertical column analyzer, which features the same geometry as the desorber section, but is a non-heated recuperative section, as discussed above. The solution injection ports are covered by the thin stainless steel distributor, which was described previously and is designed to eliminate jet formation at the solution injection

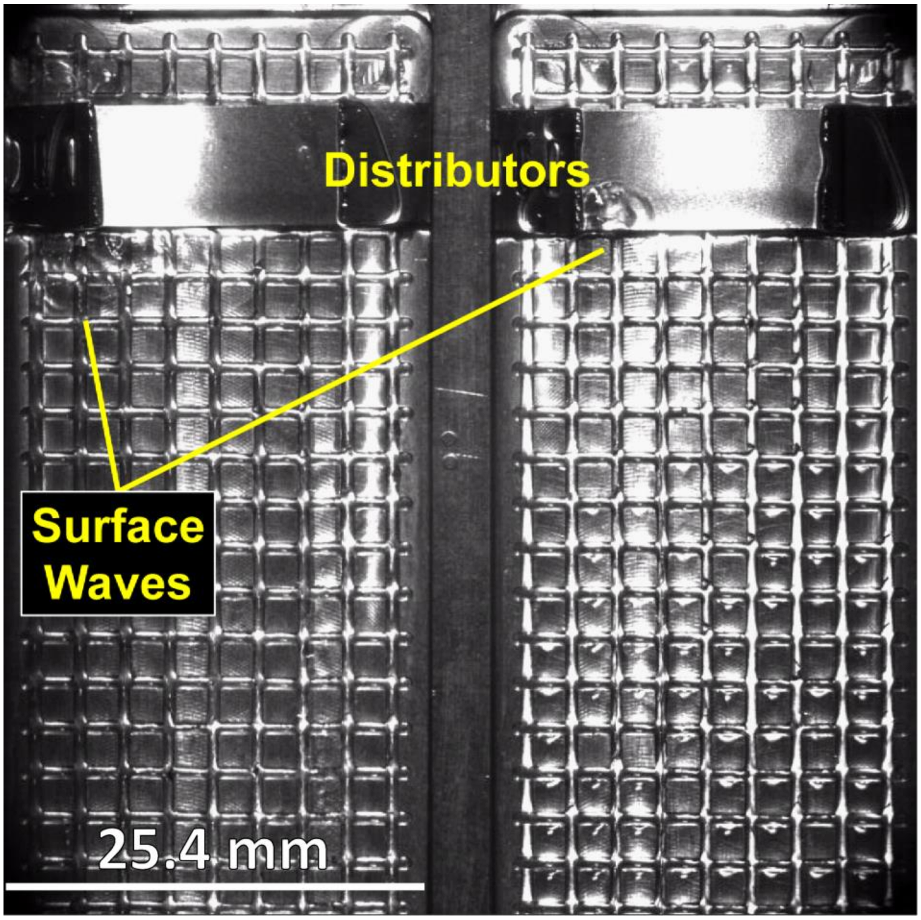

Figure 5.5: Vertical column analyzer

ports and help form an evenly-distributed liquid film on the heated back wall. As in the desorber section, a thin falling-film of ammonia-water solution forms on the back wall and flows downward past the rising vapor. The high-speed video shows significant surface waves or ripples that are formed and travel outward from the distributor, coinciding with the pulses of the solution pump, which is a diaphragm-type positive-displacement unit. These waves are visible, to some degree, in Figure 5.5, immediately below the distributor. No areas of dry-out or film breakup were observed in the analyzer section.

Figure 5.6 shows the vertical column rectifier section. The column geometry shown consists of a plain vertical wall with shallow diagonal grooves machined into the

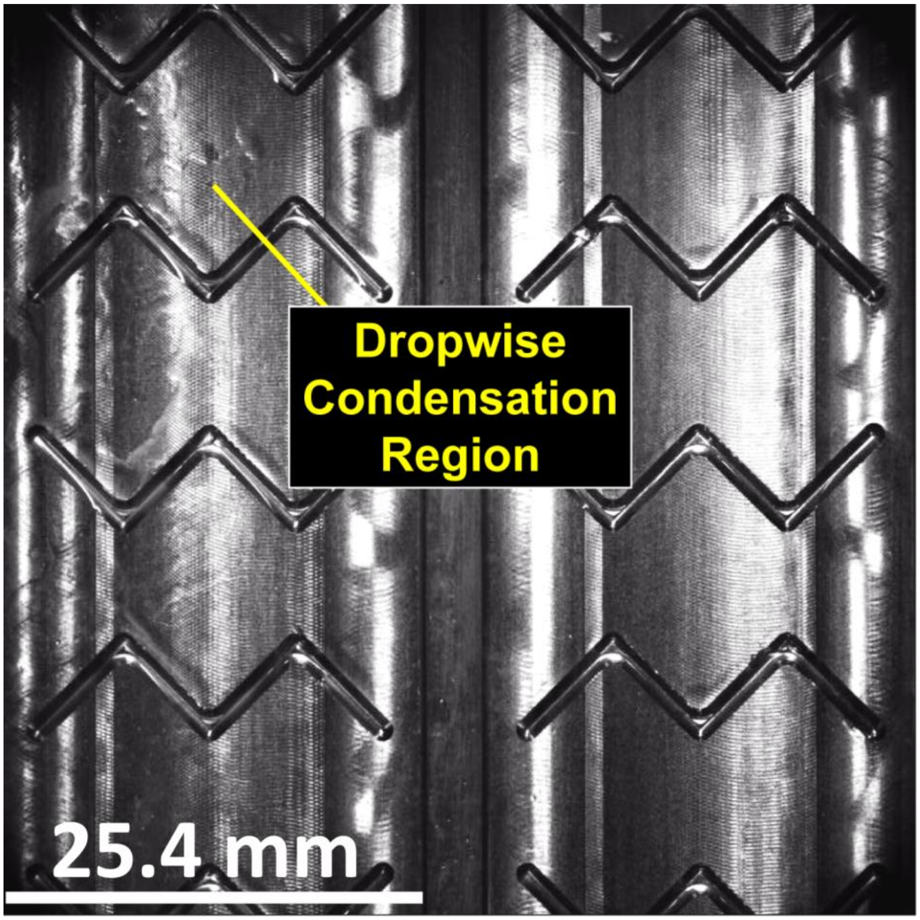

Figure 5.6: Vertical column rectifier

surface. These grooves are designed to promote rivulet formation and aid in removal of condensate from the rectifier. The back wall is cooled with the adjacent coupling-fluid microchannel array, which provides the heat removal required for condensation. A falling film of condensate forms on the back wall and the vapor bulk flows upwards, past the condensate. As in the branched tray rectifier, regions of film condensation are seen, particularly in the lower locations. Near the top of the rectifier section, regions of drop-wise condensation are observed. This can be seen in the upper left of Figure 5.6. Typically, a region of rivulet formation is noted between the drop-wise and film regions. Visible in the high-speed video, regions of increased films thickness are noted around the downward converging points of the machined grooves, leading to quasi-rivulets lower in the component and more well-defined rivulets in areas of drop-wise or transitional condensation.

5.2 Uncertainty Calculations

An uncertainty propagation study was conducted in conjunction with the data analysis. Uncertainties in the various instruments were noted previously, and used with the uncertainty propagation tools in *Engineering Equation Solver* (Klein, 2011) to determine uncertainty values for many of the calculated parameters, including:

- Calculated flow rates, and concentrations
- Temperature differences
- Heat duties
- Thermal resistances
- Overall, coupling-fluid side and solution-side heat transfer coefficients
- Mass transfer coefficients

Detailed desorber and rectifier heat transfer calculations, vapor and liquid phase mass transfer calculations, as well as uncertainty calculations, for the vertical column sample point are provided in Appendix B.

Uncertainty values are shown for these parameters on all plots, provided the resulting error bars are large enough to be legible (typically when uncertainty is greater than 1%). In general, the heat and mass transfer coefficients are the only parameters discussed in detail that have significant uncertainty. This is primarily a result of the calculation method required to determine the working-fluid-side heat transfer coefficient. Recalling Eq. (4.48):

$$\frac{1}{UA} = R_T = R_{wall} + R_{CF} + R_{WF}$$
$$\frac{1}{\alpha_{WF}} = \frac{1}{U} - R_{wall} A_{WF} - \frac{1}{\alpha_{CF} A_{CF}} A_{WF} \tag{5.1}$$

Here, it can be seen that the working-fluid heat transfer coefficient, α_{WF}, is dependent on the coupling-fluid heat transfer coefficient, α_{CF}, which much be calculated from an applicable correlation. Because this is a calculated parameter, an uncertainty must be assigned to the resulting value. In this case, an uncertainty of ±10% has been assigned to the coupling-fluid heat transfer coefficients calculated in both the desorber and rectifier analyses. This is expected to be a reasonable value, as this is a well-understood and studied geometry and coupling-fluid flow remains at very low Reynolds numbers (less than approximately 200).

This assigned uncertainty, which is significantly higher than any instrumentation uncertainty, is propagated to all subsequently calculated parameters. Typically, this would be limited to the working-fluid heat transfer coefficient. However, in this case, the fin efficiencies, which are used to determine a portion of the transfer area, are also dependent on the heat transfer coefficients. Recalling Eq. (4.54):

$$\eta_{fin} = \frac{\tanh\left(\left(\frac{2\cdot\alpha}{k_{wall} t_{fin}}\right)^{0.5} L_{fin}\right)}{\left(\frac{2\cdot\alpha}{k_{wall} t_{fin}}\right)^{0.5} L_{fin}} \tag{5.2}$$

As a result, several other parameters that rely on the transfer area, such as the overall heat transfer coefficients, heat and mass fluxes, and mass transfer coefficients have somewhat larger uncertainty than would be expected due to uncertainty in instrumentation alone.

In cases where the coupling-fluid resistance becomes the dominant thermal resistance (Eq. 5.2), uncertainty in some of the calculated parameters can become quite large. In the present study, this is limited to cases where the working-fluid heat transfer coefficient becomes very large, causing the dominant thermal resistance to shift to the coupling-fluid side. To illustrate this, a thermal resistance ratio may be defined.

$$Ratio_R = \frac{R_{WF}}{R_{CF} + R_{wall}} \tag{5.3}$$

Considering the branched tray desorber as an example, Figure 5.7 shows the uncertainty in the working-fluid side heat transfer coefficient and the resistance ratio versus the overall heat transfer coefficient. The desorber working-fluid heat transfer coefficient is the parameter most affected by the uncertainty associated with the

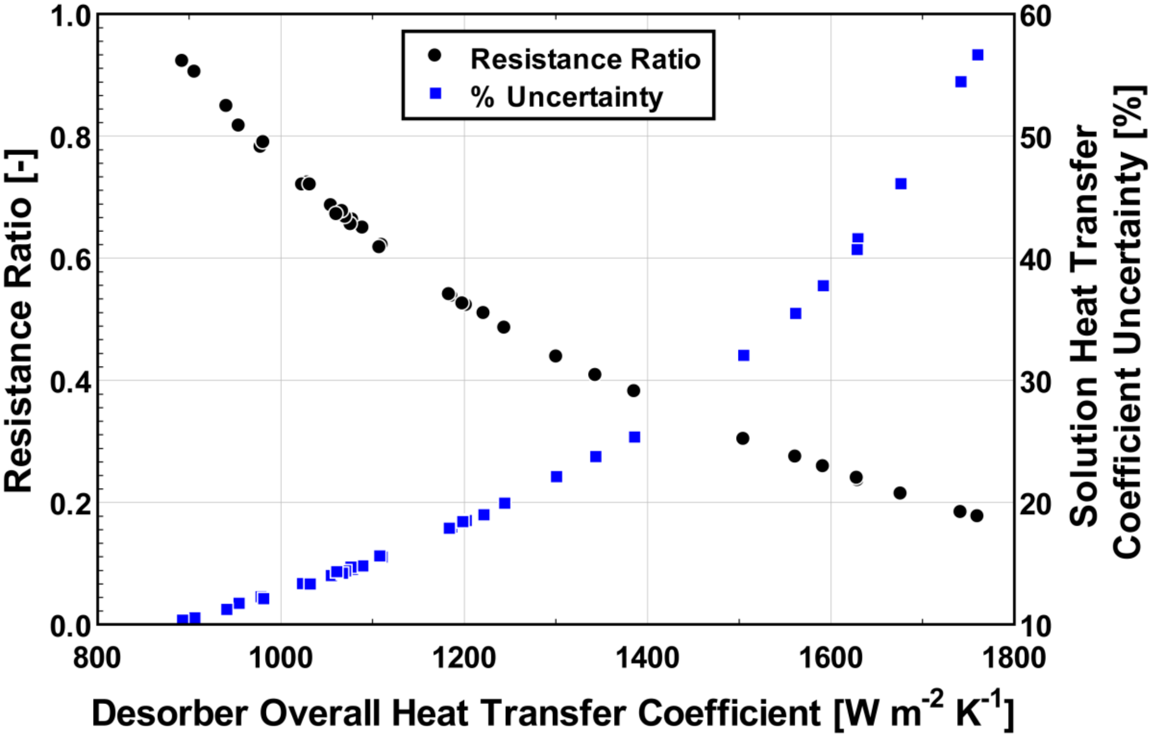

Figure 5.7: Effect of heat transfer coefficient on resistance ratio and uncertainty; shown for branched tray desorber

resistance ratio. It can be clearly seen that the resistance ratio and uncertainty are inversely proportional and for high overall heat transfer coefficients, the resistance ratio decreases, resulting in larger uncertainties. For the branched tray test section, the average resistance ratio was 0.56. The average uncertainty in the working-fluid heat transfer coefficient was 21.7% and ranged between 10.3 and 56.7% for the data set. Uncertainties are generally lower in the vertical column test section, where the solution-side resistance remained larger across the conditions tested.

5.3 Heat Transfer Results

Heat duties and heat transfer coefficients of the test sections are presented here for the desorber and rectifier regions. As discussed previsouly, all results are reported based on average heat duties.

5.3.1 **Desorber Heat Transfer**

Figure 5.8 shows the desorber heat duty as a function of solution inlet mass flow rate for the branched tray and vertical column tests sections. Mass flow rate is used here rather than a Reynolds number or mass flux as a length scale is not easily defined that would be equivalent in both geometries and representative of the flow conditions through the entire desorber section, particularly when considering the branched tray pools. In both cases, the heat duty generally increases with all three independent parameters specified in the test matrix: inlet solution flow rate, inlet solution concentration, and source temperature. In the development of the branched tray and vertical column test sections, both desorbers were designed to operate at approximately the same heat duty at baseline conditions. However, it can be seen that the heat duty of the branched tray desorber is significantly higher than that of the vertical column unit in most cases. The

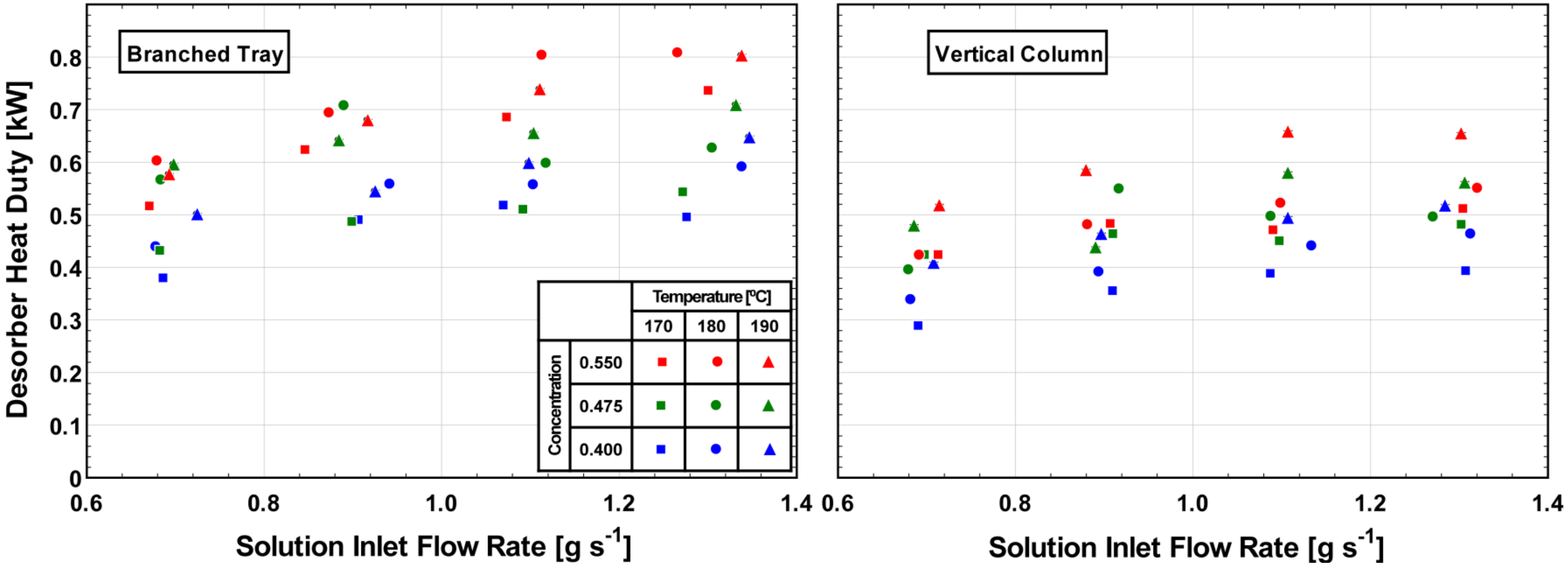

Figure 5.8: Influence of solution flow, concentration, and source temperature on desorber heat duty

average desorber heat duties for the branched tray and vertical column were 0.602 and 0.473 kW, respectively.

Revisiting the equation for component heat duty:

$$\dot{Q} = UA \cdot LMTD \tag{5.4}$$

Here it can be seen that the desorber heat duty is related to the overall heat transfer coefficient, transfer area, and driving temperature difference between the coupling- and working-fluid. To be able to directly compare the heat transfer performance of the two test sections, the impact of the transfer area and temperature difference should be removed, and the corresponding heat transfer coefficients examined.

5.1.1 Desorber Heat Transfer Coefficients

In this section, the overall and solution-side heat transfer coefficients for the branched tray and vertical column test sections are presented and compared. Trends for each test section are then discussed. Finally, results are compared with predictions of correlations and modeling methods from the literature.

The overall heat transfer coefficients for both test sections are shown in Figure 5.9. Values range from 893 to 1760 W m^{-2} K^{-1} for the branched tray and 614 to 915 W m^{-2} K^{-1} for the vertical column unit. These values, particularly for the vertical column geometry, are similar to those reported by Determan and Garimella (2011) for a compact falling-film tube-bank desorber, where overall heat transfer coefficients ranging from 388 to 617 W m^{-2} K^{-1} were observed. The highest values shown in Figure 5.9 for the branched tray test section have noticeable uncertainty. At these conditions, the coupling-fluid resistance becomes a significant portion of the overall thermal resistance and the coupling-fluid-side heat transfer coefficient affects the overall heat coefficient through the fin efficiency (and hence heat transfer area) calculations. This does not influence the vertical column results significantly, as the fin efficiency calculations for that geometry have only a more minor influence on the effective area calculations.

The solution-side heat transfer coefficients are shown in Figure 5.10. For the majority of the data points, trends are very similar to those of the overall heat transfer coefficients, shown in Figure 5.9. This indicates that the solution-side is the dominant thermal resistance in the heat transfer process. However, at solution heat transfer coefficients above approximately 4000 W m^{-2} K^{-1}, the solution-side thermal resistance drops to the point where the coupling-fluid side resistance is significant. For these cases, the uncertainty in the solution-side heat transfer coefficients becomes very large, as discussed in Section 5.2. For the branched tray test section, the solution-side heat transfer coefficient ranged from 1860 to 11686 W m^{-2} K^{-1} with an average value for all points of 4241 W m^{-2} K^{-1}. Uncertainty ranged from 10.3 to 56.7% with an average uncertainty of 21.7% for all points. All eight data points (out of 36 total) with heat transfer coefficients above approximately 5000 W m^{-2} K^{-1} have resulting uncertainties greater than 30%.

This issue is not as prominent in the vertical column desorber, where solution-side heat transfer coefficients greater than 5000 W m^{-2} K^{-1} were not observed. For this geometry, the solution-side heat transfer coefficient ranged from 1292 to 4313 W m^{-2} K^{-1}, with an average value for all points of 2177 W m^{-2} K^{-1}. Uncertainty ranged from 9.5 to 32.8% with an average uncertainty of 16.1% for all points. The results for the vertical column are, again, similar to those reported by Determan and Garimella (2011), who observed solution-side heat transfer coefficients of 659 to 2560 W m^{-2} K^{-1}.

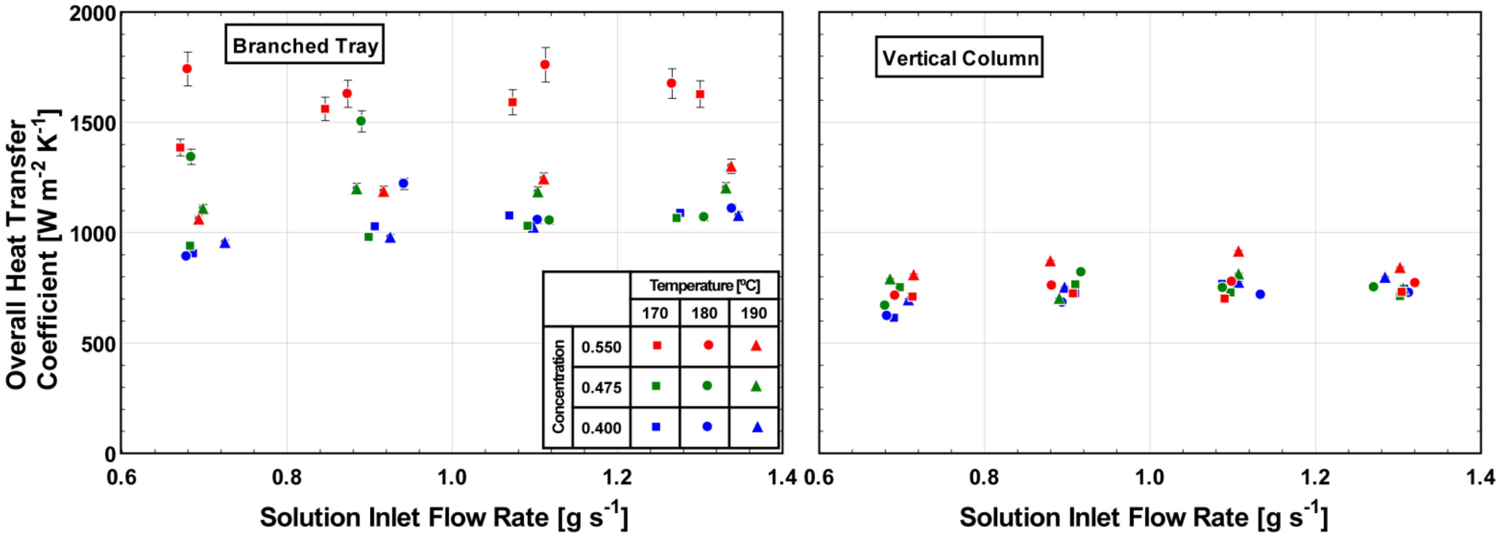

Figure 5.9: Influence of solution flow, concentration, and source temperature on desorber overall heat transfer coefficient

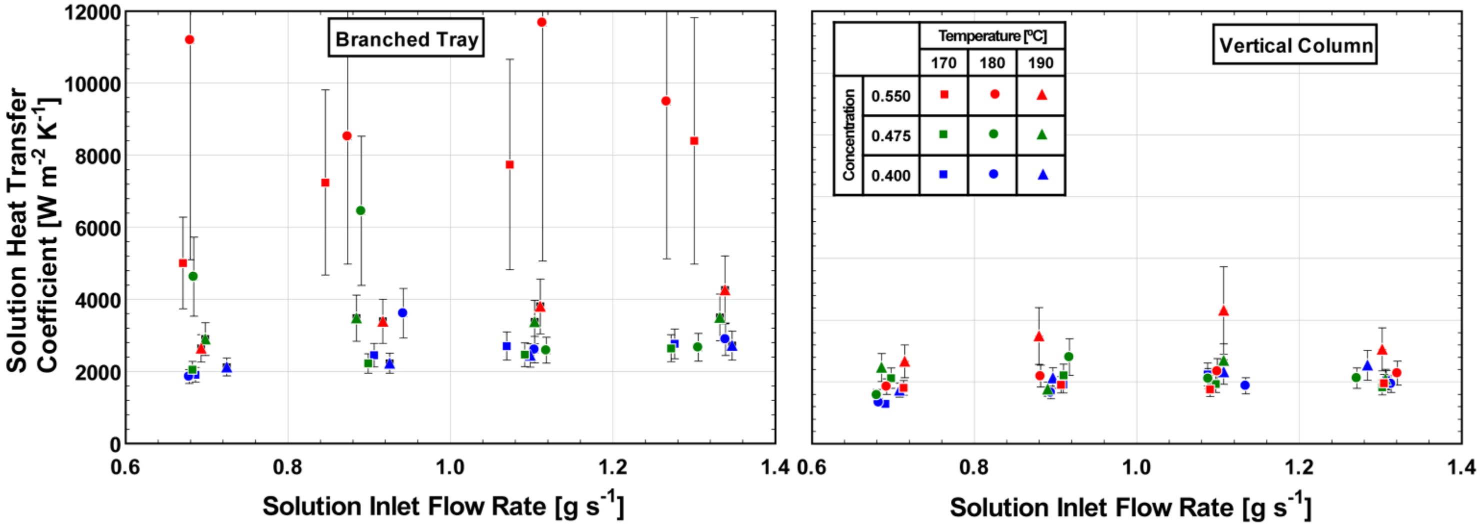

Figure 5.10: Influence of solution flow, concentration, and source temperature on solution-side heat transfer coefficient

5.1.2 Branched Tray Solution Heat Transfer Coefficient

Solution heat transfer coefficient results for the branched tray test section are discussed in detail here, and compared with the predictions of correlations and models from the literature.

Figure 5.11 shows the solution heat transfer coefficient as a function of heat flux for the three solution inlet concentrations tested. As expected for nucleate boiling, the heat transfer coefficient is a strong function of heat flux. At heat fluxes greater than 60 kW m^{-2}, the heat transfer coefficient increases significantly. Additionally, the heat transfer coefficient also appears to increase somewhat with solution concentration. Heat transfer coefficients > 7000 W m^{-2} K^{-1} are only observed for the highest value of solution concentration, 0.550.

The trend of increasing heat transfer coefficient versus solution concentration is

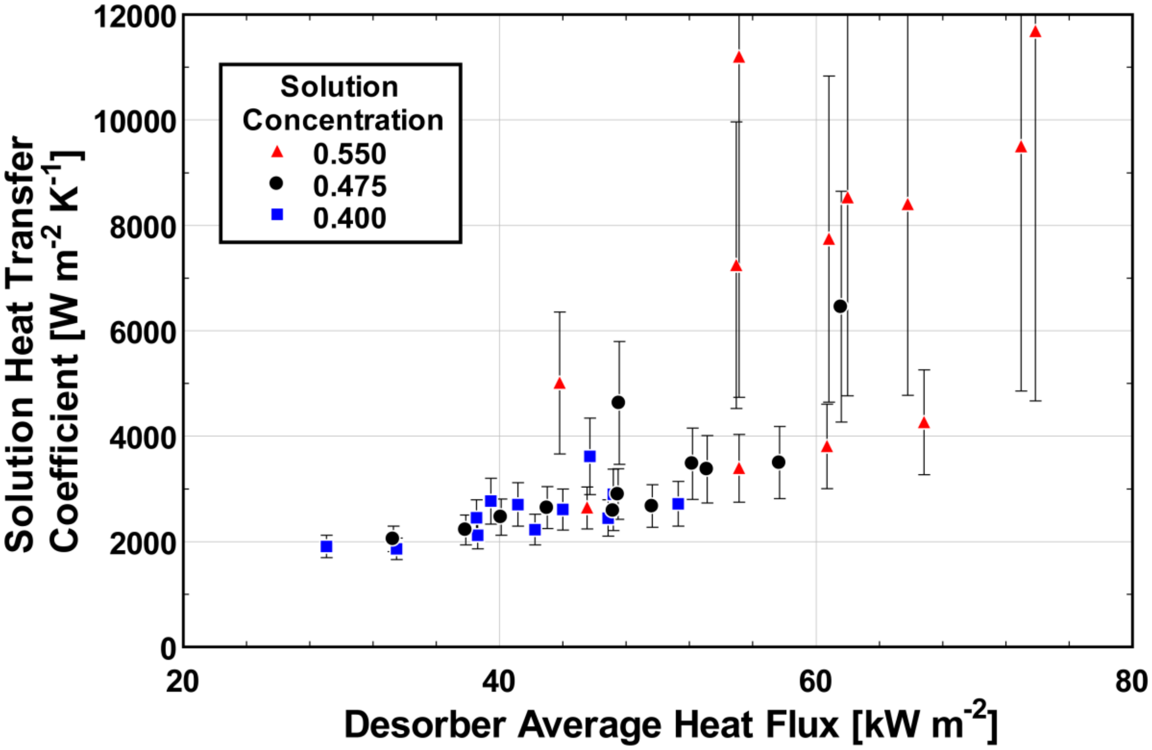

Figure 5.11: Influence of heat flux and on solution-side heat transfer coefficient

seen more clearly in Figure 5.12. A slight increase in heat transfer coefficient is seen, on average, as the solution concentration is increased from 0.400 to 0.475. However, a significant increase is observed as the concentration is increased to 0.550. This corresponds well with the results of Arima *et al.* (2003) and Inoue *et al.* (2002a) for nucleate boiling of ammonia water mixtures. In both studies, a local minimum in heat transfer coefficient versus solution concentration was reported around concentration values of 0.50, with heat transfer rates increasing significantly between concentrations of 0.50 and 0.60. In many binary-mixture boiling studies and correlations in the literature, the mass transfer resistance, which suppresses boiling heat transfer coefficients for mixtures, is found to be a function of temperature glide (difference in bubble- and dew-point temperatures), ΔT_{glide}, or the molar concentration difference between the liquid and

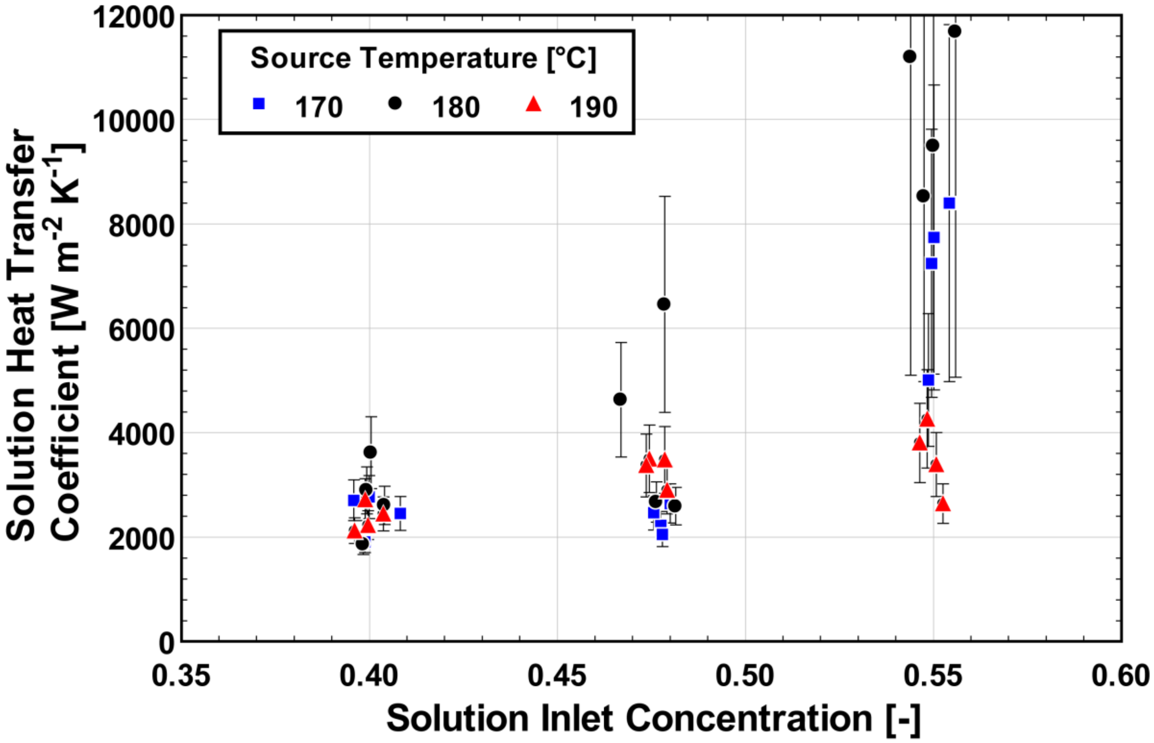

Figure 5.12: Influence of solution concentration and coupling fluid inlet temperature on solution-side heat transfer coefficient

vapor phases, ($\tilde{x}_v - \tilde{x}_l$), or both. During the boiling process of a zeotropic mixture, heat must be transferred through the liquid bulk to the liquid-vapor interface, where fluid is vaporized. At the interface, a deficiency of the more volatile component is established in the liquid as that component is preferentially vaporized. This creates a locally lower concentration of the volatile component in the liquid at the interface. For zeotropic fluids, the saturation temperature is a function of fluid concentration; therefore, the local liquid saturation temperature is higher at the interface than in the liquid bulk. This reduces the driving temperature difference between the wall and the interface, suppressing the heat transfer process. This reduction in the wall superheat is shown in Figure 5.13. For many binary zeotropic mixtures, this suppression of the heat transfer process can be correlated to the temperature glide or the molar concentration difference between the liquid and vapor phases.

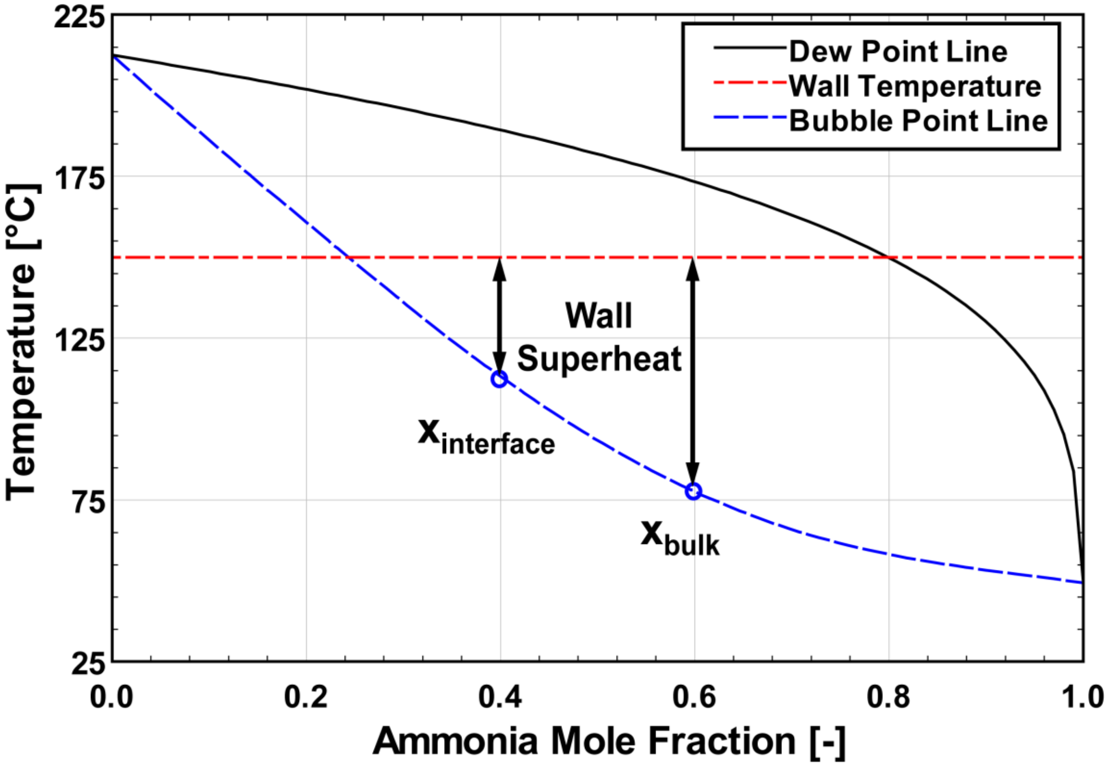

Figure 5.13: Driving temperature difference at interface and bulk concentration

Figure 5.14 shows these parameters across the range of ammonia molar concentrations, assuming a pressure of 2000 kPa. From this, it can be seen why a local minimum in heat transfer coefficient would exist for mid-range values (values near 0.500) of ammonia concentration. In practice, experimental studies of ammonia-water boiling (Inoue *et al.*, 2002a; Arima *et al.*, 2003) have shown that neither the temperature glide, nor the vapor-liquid molar concentration difference, predict the magnitude and trends of the mass transfer resistance with high accuracy over a wide range of conditions.

Figure 5.12 also indicates that the source temperature plays an increasingly significant role in heat transfer at higher concentrations. Little impact of source temperature is observed at lower concentrations. However, at concentration values of 0.550, heat transfer coefficient values are highest for points with 180°C source temperature, somewhat lower for 170°C, and significantly lower for 190°C. At the

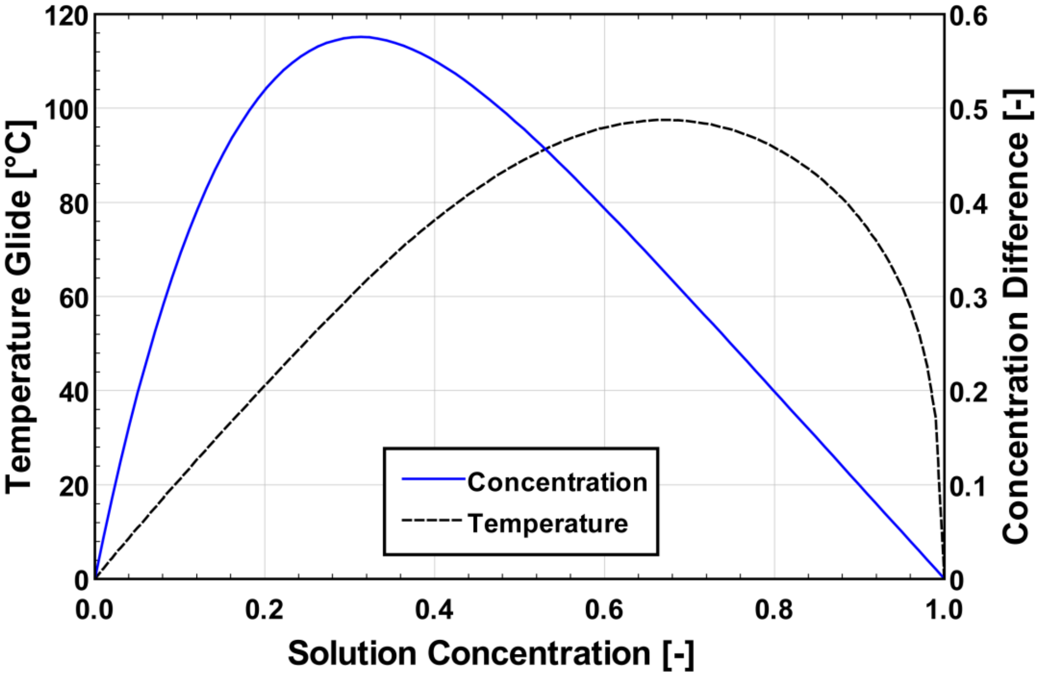

Figure 5.14: Temperature glide and saturated vapor-liquid concentration (mole fraction) difference

highest solution concentrations (0.550), the saturation temperature of the mixture is at the lowest value for the conditions tested, and the increase in temperature from 170°C to 180°C could lead to activation of additional nucleation sites and more effective heat transfer (higher heat transfer coefficients). Increasing from 180°C to 190°C likely resulted in some degree of local dry-out caused by flow restriction or flow instabilities as the counter-current flow limitation was approached, suppressing the heat transfer coefficient. This phenomenon is predicted to occur at the highest capacities, which correspond to the highest solution concentrations and temperatures. The onset of flooding is discussed in detail in Section 5.6.

A comparison of the experimental results from the present study and those available for similar conditions in the literature, is shown in Figure 5.15. Solution heat transfer coefficient data are shown across a range of heat fluxes. The complete data set

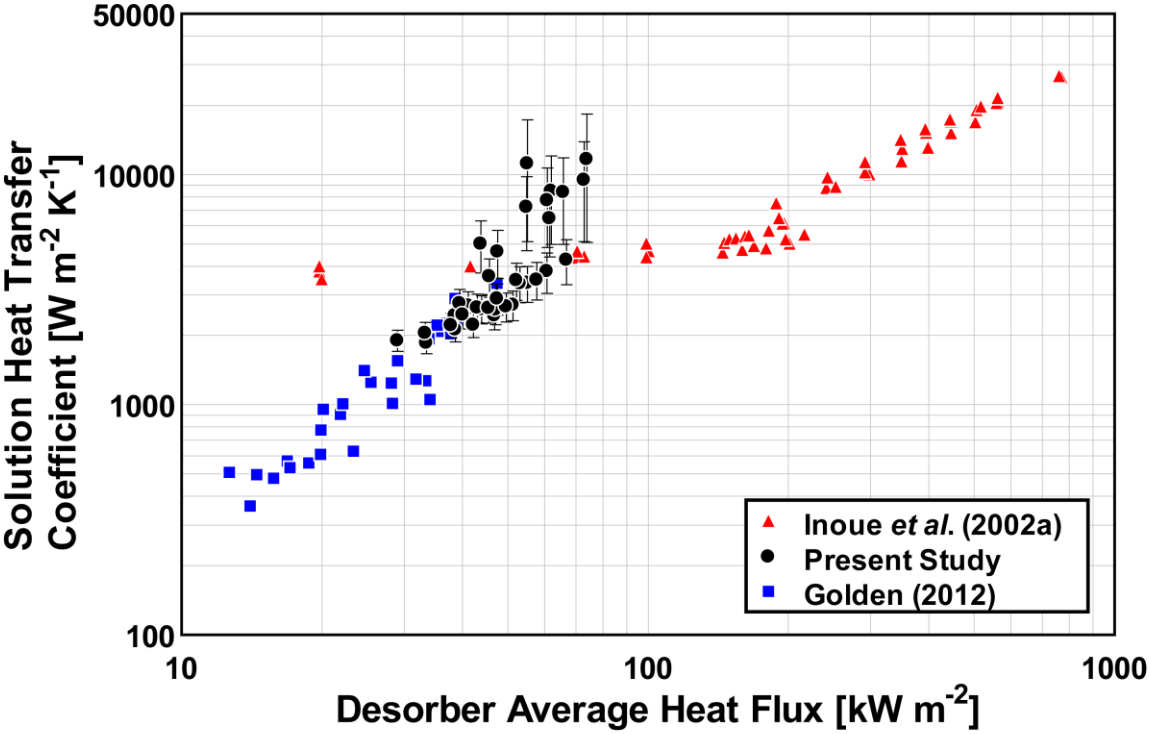

Figure 5.15: Present solution heat transfer coefficients and results from the literature

from the study by Golden (2012), as well as data for similar heat fluxes and ammonia concentration of 0.500 from Inoue *et al.* (2002a) are shown. Results from the present study show trends nearly identical to those reported for the flooded-column geometry studied by Golden (2012). This indicates that the branched tray desorber is functioning primarily in the pool boiling regime. At heat fluxes > 100 kW m^{-2}, the results of Inoue *et al.* (2002a) show a similar trend in heat transfer coefficient versus heat flux. However, Inoue *et al.* (2002a) observed a region of nearly constant heat transfer coefficient versus heat flux at low fluxes. They referred to this as a natural convection region. The difference in heat transfer coefficients in this region is likely due to the difference in geometries and heat input, as the study performed by Inoue *et al.* (2002a) used an electrically-heated platinum wire, suspended in a pool of ammonia-water solution held at the calculated saturation temperature (Inoue and Monde, 1994), while the study of Golden (2012) and the present investigation use a heating fluid to provide the heat input, and feature a net flow of ammonia-water solution through the test section. In the latter case, the bulk ammonia-water solution is not necessarily at the saturation temperature and in the present study, is often found to be a superheated liquid. It is also of note that the range of heat fluxes investigated in the present study represents the lower limit of those studied by Inoue *et al.* (2002a) who investigated heat fluxes up to 2000 kW m^{-2}.

In addition to a comparison with experimental results from the literature on ammonia-water nucleate boiling, predicted values of heat transfer coefficient from a number of correlations for binary mixture boiling were examined. To determine the binary mixture heat transfer coefficient, an ideal binary heat transfer coefficient is first calculated from pure-component water and ammonia boiling correlations.

$$\alpha_{id} = f\left(\alpha_{H_2O}, \alpha_{NH_3}\right) \tag{5.5}$$

In all correlations compared in this study, the pure-component coefficients are combined using a molar average to define the ideal mixture coefficient, as follows:

$$\frac{1}{\alpha_{id}} = \frac{\tilde{x}_{H_2O}}{\alpha_{H_2O}} + \frac{\tilde{x}_{NH_3}}{\alpha_{NH_3}} \tag{5.6}$$

Several pure-component correlations were used. For water, the correlations of Gorenflo (1993) and Stephan and Abdelsalam (1980) were applied. Both were found to perform well when compared with experimental results from several studies for ranges of heat flux similar to those in the present study (Táboas *et al.*, 2007). They were found to work particularly well compared to data from studies with heat fluxes that were in the relevant range for the present work, such as those of Kang (2000) and Borishanskii *et al.* (1964), where investigated heat fluxes were 1.4-155 and 20 kW m^{-2}, respectively. The correlation of Gorenflo (1993) requires that the reduced pressure of the fluid be specified. In the present study, the reduced pressure of the mixture was used, as is suggested when applying this correlation (Gorenflo, 1993; Garimella *et al.*, 2011). The critical pressure required to calculate the reduced pressure was determined from the Tillner-Roth and Friend (1998) equation of state developed for ammonia-water mixtures. The pure-fluid saturation temperature and fluid properties required for use of the correlation of Stephan and Abdelsalam (1980) were determined using the experimental test section pressure as the saturation pressure. For pure fluids at saturated liquid conditions, as is the case for a boiling fluid, only a single additional independent property must be known to define the state. Therefore, the measured pressure is sufficient to determine the required properties.

The correlations of Gorenflo (1993) and Stephan and Abdelsalam (1980) were also used to predict pure ammonia heat transfer coefficients (Eqs. (5.5) and (5.6)). These studies were also reported to agree well with some of the limited experimental results for ammonia-water boiling in the relevant range of heat fluxes (Táboas *et al.*, 2007). The correlation of Nishikawa and Fujita (1977) was also considered for pure ammonia. This correlation was found to result in predicted heat transfer coefficients that were mid-way between those of Gorenflo (1993) and Stephan and Abdelsalam (1980) for the range of conditions considered. The formulations of these correlations are given in Table 5.1 for water and ammonia. The bubble departure diameter, D_{Bd}, required for the correlation of Stephan and Abdelsalam (1980) is determined using the constant contact angles listed, and is calculated using the correlation of Fritz (1935), as suggested by them. The saturation pressure required by the correlation of Nishikawa and Fujita (1977) is taken to be the experimental test section pressure.

As stated, an ideal mixture heat transfer coefficient was defined by combining those of the pure components using Eq. 5.6. To correct for the mass transfer resistance, an additional binary mixture boiling correlation must be applied to the ideal mixture coefficient. Many binary fluid mixture boiling correction correlations are available in the literature, and several prior studies (Inoue *et al.*, 2002a; Arima *et al.*, 2003; Táboas *et al.*, 2007; Golden, 2012) have investigated applicability of these correlations to the nucleate boiling of ammonia-water mixtures. However, the ability of existing correlations to accurately predict ammonia-water boiling heat transfer over a wide range of conditions has been limited. This has been attributed to the fact that most correction correlations in the literature are based on the temperature glide or the molar concentration difference

Table 5.1: Pure component boiling correlations

Pure Component Correlation	Formulation	Comments
(Gorenflo, 1993)	$\frac{\alpha}{\alpha_0} = F_{PR}\left(q''_w / q''_0\right)^n \left(R_P / R_{P0}\right)^{0.133}$ For water: $F_{PR} = 1.73P_r^{0.27} + \left(6.1 + \frac{0.68}{1-\mathrm{P}_r}\right)P_r^2$; $n = 0.9 - 0.3P_r^{0.15}$ For ammonia: $F_{PR} = 1.2P_r^{0.27} + \left(2.5 + \frac{1}{1-\mathrm{P}_r}\right)P_r$; $n = 0.9 - 0.3P_r^{0.3}$	$q''_0 = 20,000 \text{ W m}^{-2}$ $\alpha_{0,H2O} = 2,800 \text{ W m}^{-2} \text{ K}^{-1}$ $\alpha_{0,NH3} = 4,000 \text{ W m}^{-2} \text{ K}^{-1}$ $R_{P0} = 0.4\ \mu\text{m}$
(Stephan and Abdelsalam, 1980)	$\alpha = Nu \cdot k_l$ For water: $Nu = \left(0.245\times10^7\right)\left(\frac{q''D_{Bd}}{k_l T_{sat}}\right)^{0.673} \times$ $\left(\frac{h_{fg}D_{Bd}^2}{a_l^2}\right)^{-1.58}\left(c_{p,l}T_{sat}D_{Bd}^2 / a_l^2\right)^{1.26}\left(\frac{\Delta\rho}{\rho_l}\right)^{5.22}$ For ammonia: $Nu = 207\left(\frac{q''D_{Bd}}{k_l T_{sat}}\right)^{0.745}\left(\frac{\rho_v}{\rho_l}\right)^{0.851} P_r^{0.533}$	For water: $10^{-4} \le P_r \le 0.886$ $\theta = 45°$ For ammonia: $3\times10^{-3} \le P_r \le 0.78$ $\theta = 35°$
(Nishikawa and Fujita, 1977)	$\alpha = C_1\left[\left(\frac{P}{P_{atm}}\right)^{C_2}\left(f_\varsigma q''\right)^{C_3}\right] / L_c^{C_4}$	For ammonia, $C_1 = 0.23$ $C_2 = 0.8$ $C_3 = 0.2$ $C_4 = 0.3073$ $f_\varsigma = 1.0$

between the liquid and vapor phase, neither of which capture the trends in ammonia-water mixtures accurately over a wide range of conditions (Inoue *et al.*, 2002a). Additionally, it has been noted that the temperature glide and molar concentration difference observed for ammonia-water mixtures are commonly much larger than for other fluid pairs for which the available correlations were developed (Inoue *et al.*, 2002a).

In the present study, seven different binary fluid mixture boiling correlations were used to predict the corrected mixture heat transfer coefficient. Several of those that agreed most closely with the experimental data were also evaluated using different pure component correlations. The resulting average and average absolute deviations for the predictions of these correlations from the data from the present study are shown in Table 5.2.

All correlations investigated in the present study make use of either the temperature glide, or the molar vapor-liquid concentration difference in correcting the ideal mixture heat transfer coefficient to account for mass transfer resistance. In general, the form of all correlations considered is as follows.

$$\alpha_{soln} = \frac{\alpha_{id}}{\left(1+K\right)^{A}} \tag{5.7}$$

In Eq. 5.7, the binary solution heat transfer coefficient is determined by modifying the ideal mixture coefficient with a correction factor, $K > 0$. Thome (1981) suggests $A = 7/5$. For all other correlations, A is unity. Values of K for the correlations considered are provided in Table 5.3. The correlations of Thome (1981), Stephan and Körner (1969), and Schlunder (1982) employ the molar concentration difference, $\left(\tilde{x}_v - \tilde{x}_l\right)$, in the correction factor. Alternately, the correlations of Thome and Shakir (1987), Inoue *et al.* (1998), and Fujita and Tsutsui (1997) use the temperature glide, ΔT_{glide}, in the correction factor. The correlation of Táboas *et al.* (2007) combines the correction parameters of Schlunder (1982) and Thome and Shakir (1987), and therefore

Table 5.2: Binary fluid mixture boiling correlations (orange highlight indicates molar concentration-based correction factor)

Binary Fluid Mixture Boiling Correlation	**Pure Component Correlation**		**Average Deviation**	**Average Absolute Deviation**
	H_2O	**NH_3**	**[%]**	**[%]**
Thome (1981)	Stephan and Abdelsalam (1980)	Nishikawa and Fujita (1977)	-18.3	22.4
Stephan and Körner (1969)	Gorenflo (1993)	Gorenflo (1993)	-4.5	24.1
Thome (1981)	Stephan and Abdelsalam (1980)	Stephan and Abdelsalam (1980)	-23.2	25.8
Schlunder (1982)	Gorenflo (1993)	Gorenflo (1993)	-24.4	28.7
Thome and Shakir (1987)	Stephan and Abdelsalam (1980)	Stephan and Abdelsalam (1980)	31.0	31.0
Schlunder (1982)	Stephan and Abdelsalam (1980)	Stephan and Abdelsalam (1980)	-32.4	33.4
Stephan and Körner (1969)	Stephan and Abdelsalam (1980)	Nishikawa and Fujita (1977)	-34.6	34.6
Fujita and Tsutsui (1997)	Gorenflo (1993)	Gorenflo (1993)	37.6	37.6
Stephan and Körner (1969)	Stephan and Abdelsalam (1980)	Stephan and Abdelsalam (1980)	-38.5	38.5
Thome and Shakir (1987)	Gorenflo (1993)	Gorenflo (1993)	39.7	39.7
Thome (1981)	Gorenflo (1993); (Inoue *et al.*, 2002a; Arima *et al.*, 2003)	Gorenflo (1993)	19.5	40.5
Táboas *et al.* (2007)	Stephan and Abdelsalam (1980)	Stephan and Abdelsalam (1980)	20.3	44.9
Stephan and Körner (1969)*	Gorenflo (1993)	Gorenflo (1993)	-45.4	45.4
Inoue *et al.* (1998)	Gorenflo (1993)	Gorenflo (1993)	-62.8	62.8
Táboas *et al.* (2007)	Gorenflo (1993)	Gorenflo (1993)	47.8	65.7
Present Study: Modified (Schlunder, 1982)	Gorenflo (1993)	Gorenflo (1993)	-5.2	16.1
*Uses value of A_0=3.10; recommended by Inoue *et al.* (2002b)				

Table 5.3: Correction factors for Eq. (5.7)
(orange highlight indicates molar concentration-based correction factor)

Binary Fluid Mixture Boiling Correlation	**Correction Factor, *K***	**Comments**
Thome (1981)	$-\left(\frac{a_l}{D_{l,a-w}}\right)^{1/2}\left(\frac{c_{p,l}}{h_{fg}}\right)\left(\frac{dT_{bp}}{d\tilde{x}_l}\right)\left(\tilde{x}_v-\tilde{x}_l\right)$	
Stephan and Körner (1969)	$A_0\left(0.88+0.12P\left[\text{bar}\right]\right)\left(\tilde{x}_v-\tilde{x}_l\right)$	$A_0=1.53$, unless noted (mixture dependent)
Schlunder (1982)	$\frac{\alpha_{id}}{q''}\left(T_{sat,2}-T_{sat,1}\right)\left(1-\exp\left(-\frac{B_0 q''}{\rho_l h_{fg}\beta_l}\right)\right)\left(\tilde{x}_v-\tilde{x}_l\right)$	$B_0=1$ $\beta_l=2\times10^{-4}\left[\text{m s}^{-1}\right]$
Táboas *et al.* (2007)	$A_0 x_l\frac{\alpha_{id}}{q''}\left(T_{sat,2}-T_{sat,1}\right)\left(1-\exp\left(-\frac{B_0 q''}{\rho_l h_{fg}\beta_{l,1}}\right)\right)\left(\tilde{x}_v-\tilde{x}_l\right)+$ $A_0\left(1-x_l\right)\frac{\alpha_{id}}{q''}\left(1-\exp\left(-\frac{B_{0,2} q''}{\rho_l h_{fg}\beta_{l,2}}\right)\right)\Delta T_{glide}$	$A_0=0.5$ $B_0=1$ $\beta_{l,1}=2\times10^{-4}\left[\text{m s}^{-1}\right]$ $\beta_{l,2}=3\times10^{-4}\left[\text{m s}^{-1}\right]$
Thome and Shakir (1987)	$\frac{\alpha_{id}}{q''}\left(1-\exp\left(-\frac{B_0 q''}{\rho_l h_{fg}\beta_l}\right)\right)\Delta T_{glide}$	$B_0=1$ $\beta_l=3\times10^{-4}\left[\text{m s}^{-1}\right]$
Inoue *et al.* (1998)	$\frac{\alpha_{id}}{q''}\left(1-\exp\left(-0.75\times10^{-5}q''\right)\right)\Delta T_{glide}$	
Fujita and Tsutsui (1997)	$\frac{\alpha_{id}}{q''}\left(1-\exp\left(\frac{-60\,q''}{\rho_l h_{fg}}\left(\frac{\rho_v{}^2}{\sigma g\left(\rho_l-\rho_v\right)}\right)^{1/4}\right)\right)\Delta T_{glide}$	
Present Study: Modified Schlunder (1982)	$\frac{\alpha_{id}}{q''}\left(T_{sat,2}-T_{sat,1}\right)\left(1-\exp\left(-\frac{B_0 q''}{\rho_l h_{fg}\beta_l}\right)\right)\left(\tilde{x}_v-\tilde{x}_l\right)$	$B_0=$ $C_1\exp\left(-\frac{\text{Re}_v{}^{1/2}P_r{}^{-3/2}}{C_2}\right)$ $C_1=11.3$ $C_2=220$

includes both the molar concentration difference and temperature glide terms in the correction factor.

The heat transfer coefficients predicted by these correlations are plotted against the experimental values in Figure 5.16. The best fit to the experimental data was provided by the binary correlation of Thome (1981) with pure component correlations for water and ammonia from Stephan and Abdelsalam (1980) and Nishikawa and Fujita (1977), respectively. The predictions of this correlation had an average deviation of -18.3% and average absolute deviation of 22.4% from the data, as shown in Table 5.2. It is noteworthy that the Thome (1981) correlation is the only analytical correlation considered here, and does not rely on any empirical parameters in the correction of the ideal mixture heat transfer coefficients. Additionally, this is the only correlation to account for derivative of the bubble point temperature with respect to the liquid molar concentration. The predicted values using this correlation are shown in Figure 5.16 A, including the uncertainty values from the experimental data. The uncertainties are shown only for this case, as values of the uncertainty in the experimental data are the same for all correlations. It can be seen that the Thome (1981) correlation predicts the experimental data with reasonable accuracy at experimental heat transfer coefficients up to approximately 5000 W m^{-2} K^{-1}. A similar result was also observed by Golden (2012), who showed that available correlations increasingly under predicted experimental results for values greater than approximately 1000-2000 W m^{-2} K^{-1}.

Figure 5.16 B and C show the predictions of the binary mixture correlations using the molar concentration difference and temperature glide correction factors, respectively.

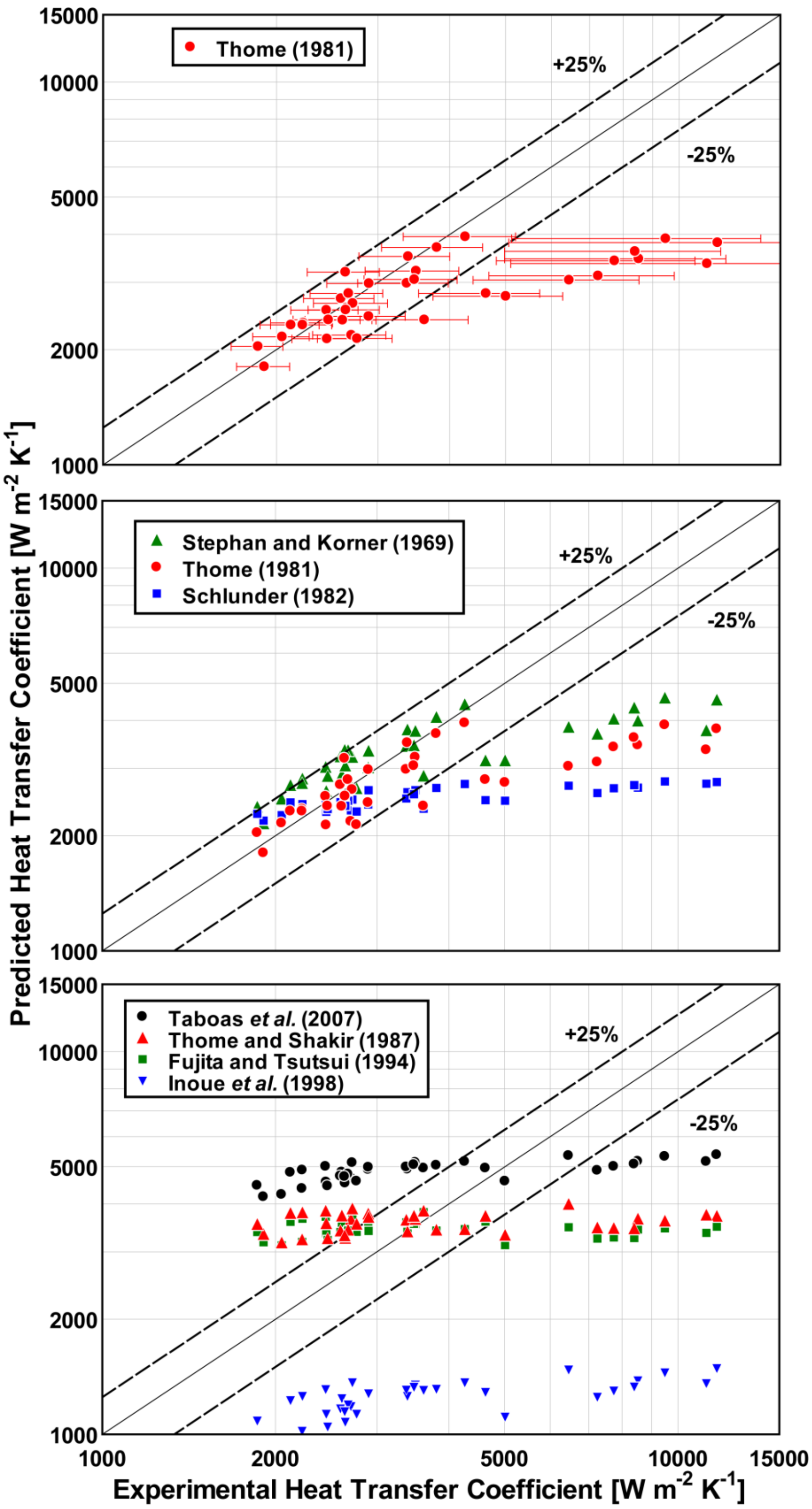

Figure 5.16: Binary fluid mixture boiling heat transfer coefficients

It can be seen from a comparison of Figure 5.16 B and C, as well as a review of Tables 5.2 and 5.3, that the correlations using the molar concentration correction factors generally have better agreement with the present experimental results. Additionally, the molar concentration correction captures the trends in the data below 5000 W m^{-2} K^{-1} more accurately. Above this value, all correlations deviate from the experimental data and under predict the observed heat transfer coefficients. This is probably due to increased vapor-liquid interaction and improved mixing of the pools as the counter-current, or flooding, limitation is approached. These increased mixing phenomena are not accounted for in the underlying pool boiling correlations, which are often based on experiments involving large volumes of near-quiescent liquid with no bulk vapor interaction at the liquid surface. Generally, the boiling correlations examined here are developed to predict boiling heat transfer coefficients over very large ranges of heat flux and temperature glide or molar concentration difference and these parameters are closely correlated to the predicted heat transfer coefficient, as shown in Tables 5.1 and 5.3. In the present study, these parameters vary only over a narrow range. Therefore, there is often very little change in heat transfer coefficient predicted by the correlations across the range of experimental conditions considered, while the experimental values, which are heavily influenced by bulk vapor and liquid motion and mixing, vary significantly. In the following section, the underlying causes of the divergence between the experimental results and the correlations from the literature are discussed, and a new correlation is proposed that accounts for these effects.

5.1.3 Branched Tray Modified Binary Fluid Mixture Boiling Correlation

Figure 5.17 shows that the vapor Reynolds number within the desorber passages (calculated for a mean vapor passage diameter, mean desorber vapor flow rate, and desorber bulk vapor properties) increases at a linear rate with heat flux. Comparing this with the heat transfer coefficient results from Figure 5.18 indicates that the highest vapor Reynolds numbers will coincide with the highest heat transfer coefficients, supporting the assertion that the elevated heat transfer coefficients may be due to increased mixing caused by vapor-liquid interaction. The flooding results, which are discussed in Section 5.6, also support this hypothesis, showing that the flooding limit is approached at the highest observed desorber capacities and therefore heat fluxes. Furthermore, it can be

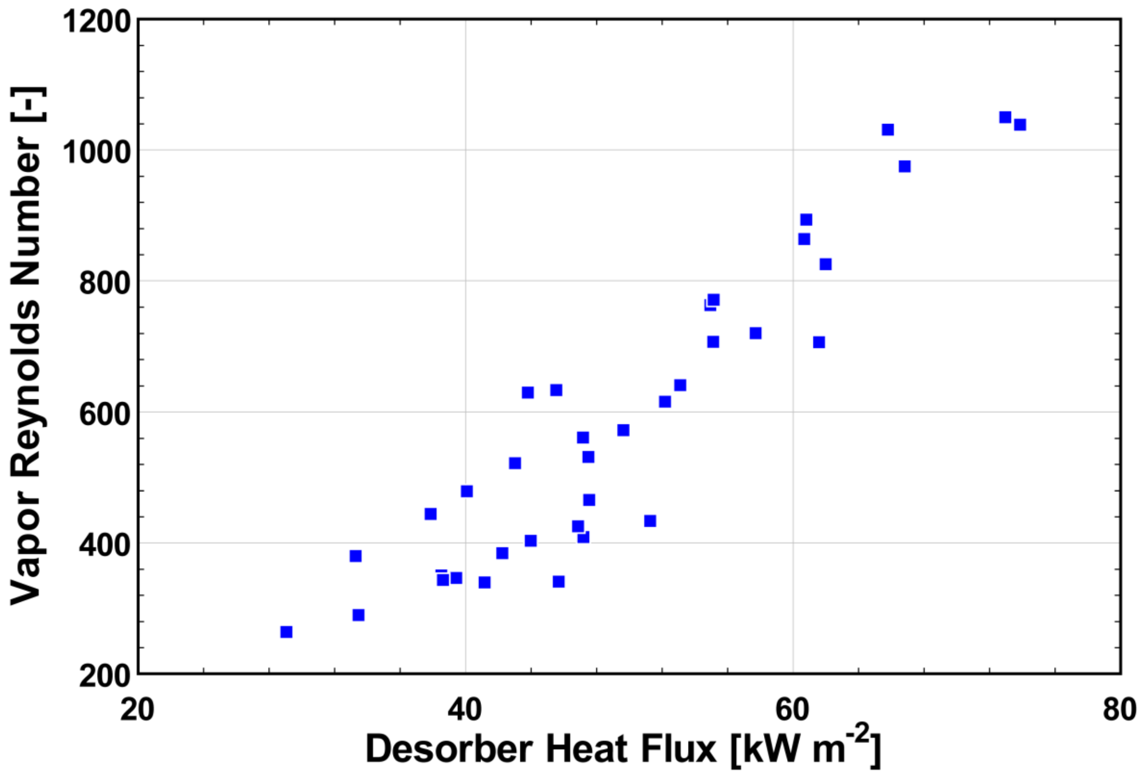

Figure 5.17: Vapor Reynolds number versus heat flux

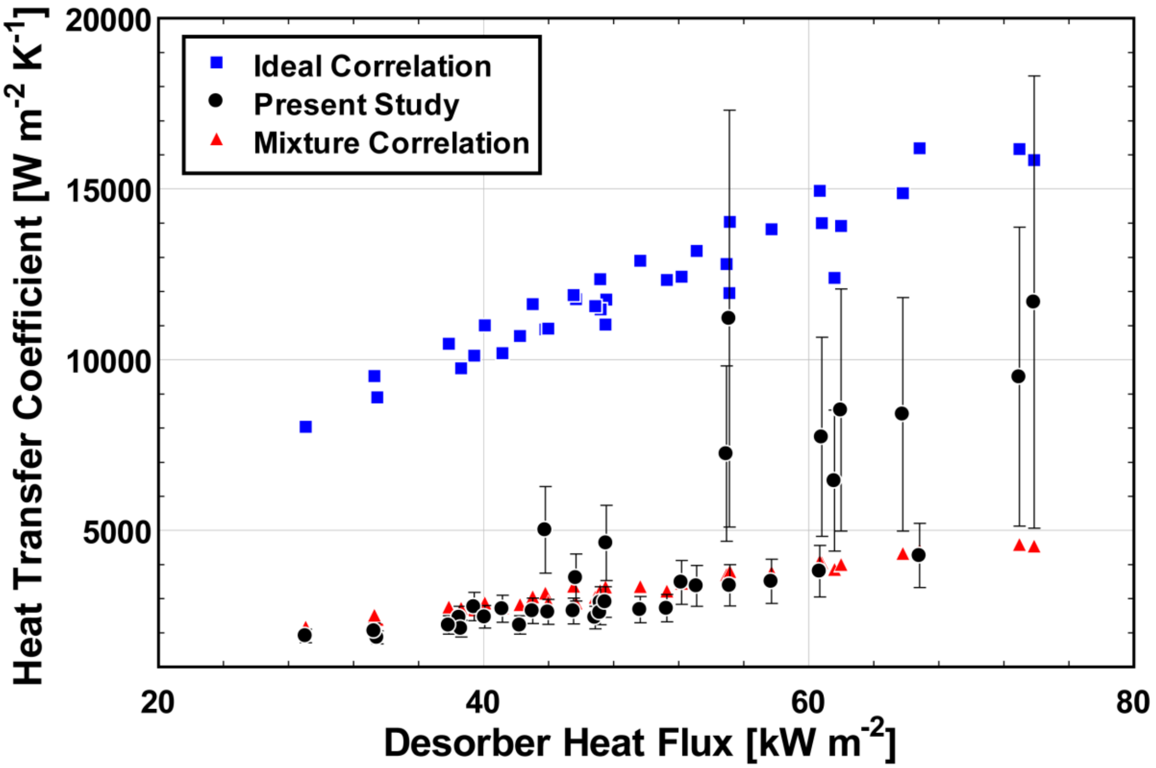

Figure 5.18: Ideal, mixture, and experimental heat transfer coefficients; ideal correlation: Gorenflo (1993), mixture correlation: Stephan and Körner (1969)

seen that the elevated heat transfer coefficients have magnitudes between those of the predicted ideal heat transfer coefficients and corrected binary mixture coefficients (shown for the correlation of Stephan and Körner (1969), Figure 5.18). This is also expected, and it has been suggested that, for cases with infinitely fast diffusion or perfect mixing, observed heat transfer coefficients would approach the ideal mixture value (Carey, 2008). As shown in Figure 5.18, in the region of high desorber heat flux (above approximately 55 kW m^{-2}), corresponding to the highest vapor Reynolds numbers, a sharp divergence is observed between the heat transfer coefficient data and binary fluid mixture correlations, as the experimental results approach ideal mixture values. This transition at higher heat flux and vapor Reynolds number is the underlying cause for the divergence in correlation and experiment al heat transfer coefficients noted in Figure 5.16 A and B.

To achieve improved agreement with the experimental results, a modified binary fluid mixture boiling correlation is developed here. The modified correlation accounts for the elevated heat transfer coefficients observed by incorporating a dependency on the vapor Reynolds number and reduced pressure of the mixture. The proposed correlation is based on a modified formulation of the binary fluid mixture correlation of Schlunder (1982). The required pure-component boiling heat transfer coefficients are determined from the correlations of Gorenflo (1993). The correlation of Schlunder (1982) was selected as a basis for the proposed correlation due to the good agreement with data at the lower range of heat transfer coefficients. Additionally, this correlation contains an exponential term and empirical constant, which can be easily modified to reduce the impact of mass transfer resistance, thereby brining the predicted values closer to the ideal case, as observed for higher vapor Reynolds numbers and heat fluxes. From Table 5.3, this term is as follows:

$$\left(1-\exp\left(-\frac{B_0 q''}{\rho_l h_{fg} \beta_l}\right)\right) \tag{5.8}$$

In the correlation proposed here, B_0, is not taken to be a constant value, but the following expression is used:

$$\begin{aligned} B_0 &= C_1 \exp\left(-\frac{\mathrm{Re}_v^{1/2} P_{r,mix}^{-3/2}}{C_2}\right) \\ C_1 &= 11.3 \\ C_2 &= 220 \end{aligned} \tag{5.9}$$

where the constants C_1 and C_2 are determined from a regression analysis of the experimental data set.

For the development of this expression, the dependence on vapor Reynolds number was discussed above, and is necessary to account for changes in the fluid dynamics. The vapor Reynolds number used here is determined using a mean vapor passage hydraulic diameter, mean vapor velocity within the desorber, and desorber bulk vapor properties. By including the influence of the vapor bulk, the proposed correlation no longer represents pure pool-boiling phenomena, and is only applicable to similar geometries and conditions with pool boiling in the presence of bulk vapor flow. The reduced pressure of the mixture, $P_{r,mix}$, was also found to have a significant influence on the binary correction factor. This can be explained by examining the pure-component correlations given in Table 5.1. In all cases, the critical pressure, or a similar parameter (P/P_{atm}, T_{sat}, etc.), is used and plays a large role in the calculation of the pure component heat transfer coefficients. By including the reduced pressure in the proposed modification, discrepancies that may result from the pure component correlations can be largely accounted for. The modified correlation, as proposed, is listed in Tables 5.2 and 5.3, for comparison with other correlations from the literature.

Figure 5.19 shows the predictions of the correlation developed here with the data. The average and average absolute deviation for the modified correlation are -5.2% and 16.1%, respectively, with 83% of the predicted values falling within ±25% of the experimental results. Also, the agreement with data > 5000 W m^{-2} K^{-1} is better, compared to what was seen with the other correlations considered here.

To further illustrate the improvement over existing correlations, the present data and proposed correlation are shown as a function of vapor Reynolds number in Figure 5.20. The correlation of Schlunder (1982), without modification, is also shown for

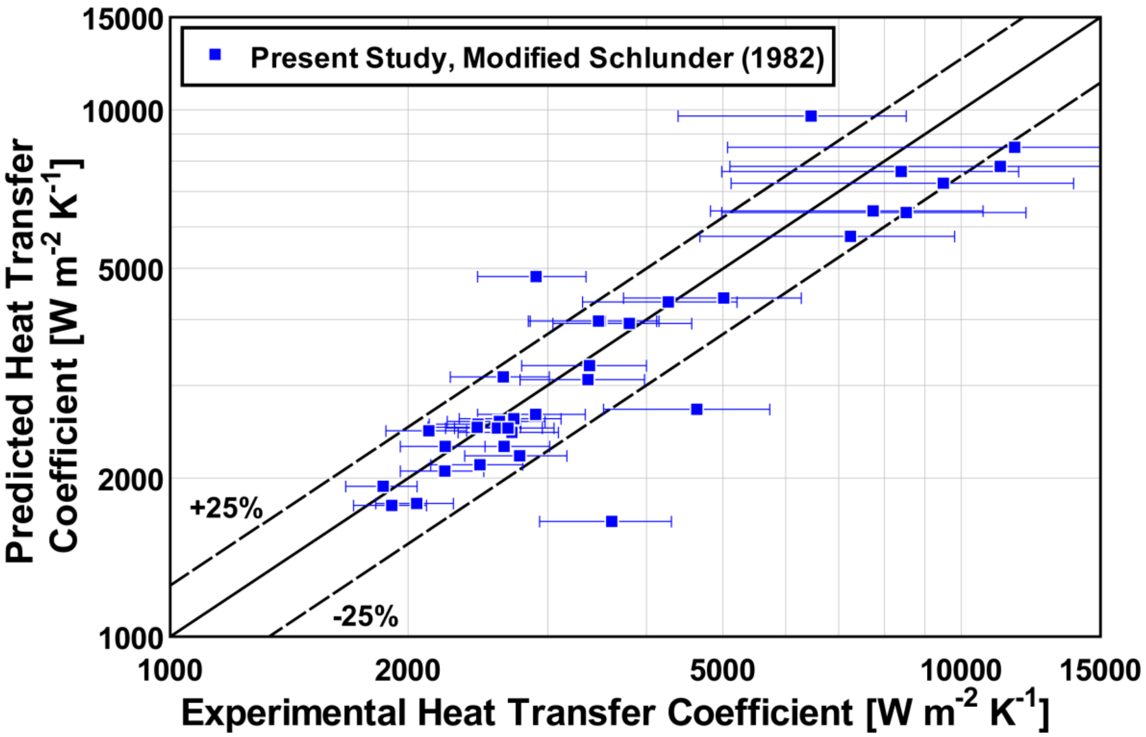

Figure 5.19: Proposed correlation versus present data

comparison. Additionally, the correlation of Thome (1981), which provided the best agreement among the correlations in the literature, is shown. Here, the correlations of Thome (1981) and Schlunder (1982) do not capture the increase in heat transfer coefficient with vapor Reynolds number. This is expected as these correlations were developed for conventional boiling applications that are typically limited to quiescent liquid pools. The proposed correlation achieves significantly better agreement with the experimental results, providing a more accurate prediction of the heat transfer coefficient across the range of conditions investigated, as was shown in Figure 5.19.

5.1.4 Vertical Column Solution Heat Transfer Coefficient

Desorption in the vertical column test section occurs in a falling-film mode. Regions of both pure film evaporation and regions of falling-film and nucleate boiling

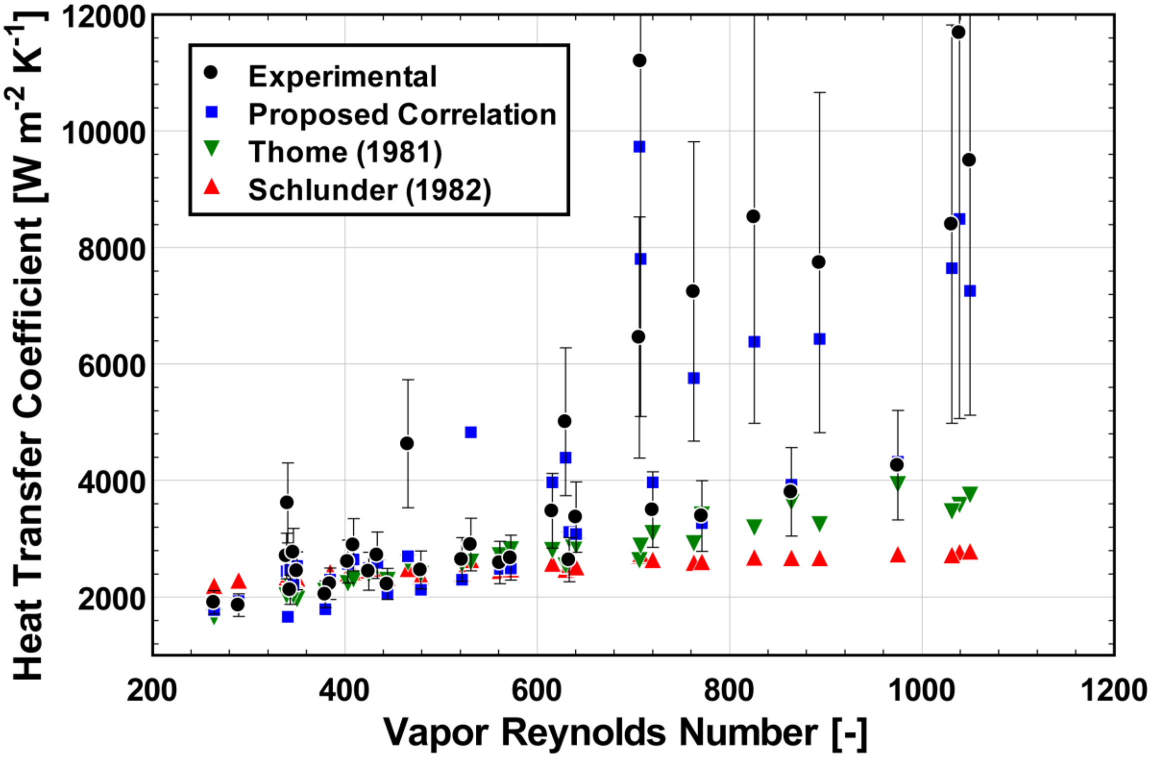

Figure 5.20: Influence of vapor Reynolds number on heat transfer coefficient

were observed during testing. Figures 5.9 and 5.10, presented above, show the experimental values of overall and solution-side heat transfer coefficients.

To predict the desorber heat transfer coefficient for this geometry, the approximate design method proposed by Silver (1947), and further extended by Bell and Ghaly (1972), is used. The Silver-Bell-Ghaly (SBG) method has been widely used to model phase-change processes that involve binary zeotropic mixtures, including ammonia-water processes (Fronk and Garimella, 2013). To simplify the coupled heat and mass transfer process that occurs during zeotropic phase-change processes, this method assumes that the vapor-phase temperature follows the equilibrium temperature curve, neglecting any vapor-phase mass transfer resistance. Additionally, it is assumed that that all heat, latent and sensible (for both phases), is passed through the vapor-liquid interface. By applying these assumptions, the apparent heat transfer coefficient, α', can be approximated.

$$\frac{1}{\alpha'} = \frac{1}{\alpha_{id}} + \frac{Z_{SBG}}{\alpha_v} \tag{5.10}$$

Here, α_{id} and α_v are the ideal phase-change heat transfer coefficient and the vapor-to-interface heat transfer coefficients, respectively. Z_{SBG} is given by the ratio of vapor sensible heat duty to total heat duty (heat duty removed by the coolant).

$$Z_{SBG} = \frac{\dot{Q}_{S,V}}{\dot{Q}_T} \tag{5.11}$$

Analysis of the vapor sensible heat duties is provided in Section 4.2.3.

As mentioned previously, the desorption process was observed to have at least two regions of operation: film evaporation and film boiling. Therefore, three film evaporation/boiling correlations are used here to predict the ideal film heat transfer coefficient. Each correlation was developed for slightly different flow conditions or heat transfer regimes. In all cases, the bulk mixture properties of the ammonia-water solution are used.

The correlation of Chun and Seban (1971) for laminar saturated films is as follows.

$$\frac{\alpha_f}{k_l}\left(\frac{\nu^2}{g}\right)^{1/3} = 0.821\left(\mathrm{Re}_f\right)^{-0.22} \tag{5.12}$$

Here, and in subsequent discussions of film heat transfer, the film Reynolds number, Re_f, is defined as follows.

$$\mathrm{Re}_f = \frac{4\Gamma}{\mu_l} \tag{5.13}$$

where Γ is defined as the liquid mass flow rate per unit width of the wetted wall. For the vertical column desorber, values of the film Reynolds number varied from 89.0 to 215, with an average value of 144.

The correlation given by Eq. 5.12 was recommended for the lowest range of film Reynolds numbers investigated by Chun and Seban (1971). That study reported results for conditions down to approximately $\mathrm{Re}_f = 300$.

The correlation of Wilke (1962) is recommended (Rohsenow *et al.*, 1985) primarily for use with subcooled films. The general form of the correlation is given for a range of film Reynolds numbers.

$$\frac{\alpha_f}{k_l}\delta = C_0\left(\mathrm{Re}_f\right)^m\left(\frac{\mu_l c_{p,l}}{k_l}\right)^{0.344} \tag{5.14}$$

The average film thickness, δ, is determined from the following equations, which equate the gravitation and frictional forces for a no-slip boundary condition and no vapor shear (Rohsenow *et al.*, 1985).

$$\frac{\delta\left(g\delta\right)^{0.5}}{\nu_l} = 0.866\,\mathrm{Re}_f^{\;0.5} \tag{5.15}$$

For $\mathrm{Re}_f < 1600$, the recommended values or C_0 and m are 0.029 and 0.533, respectively.

Little prior work is found in the literature on the topic of nucleate boiling heat transfer correlations for zeotropic falling films. However, the correlation of Damman (1973), for saturated films of aqueous solution, was presented by Rohsenow *et al.* (1985). The applicable film Reynolds numbers ($80 < \mathrm{Re}_f < 1600$) and heat fluxes (40 – 140 kW m^{-2}) are remarkably similar to those in the present study.

$$\frac{\alpha_f}{k_l}\delta = 3.83\left(\mathrm{Re}_f\right)^{0.23}\left(\frac{q''\delta}{k_l T_{sat}}\right)^{0.76} \tag{5.16}$$

Here the average film thickness is defined as in Eq. 5.15 for this range of Reynolds numbers.

The vapor-to-interface heat transfer coefficient in the vertical column desorber is determined using a constant Nusselt number determined analytically by Schmidt and Newell (1967) for developed flow through rectangular channels with one adiabatic face and, otherwise constant heat flux, presented by Shah and Bhatti (1987). A simultaneous developing flow correlation for rectangular channels, developed and presented by Nellis and Klein (2009), was also used and included in the comparison, as the vapor flow through the rectifier is expected to be in the developing region. Figure 5.21 shows a

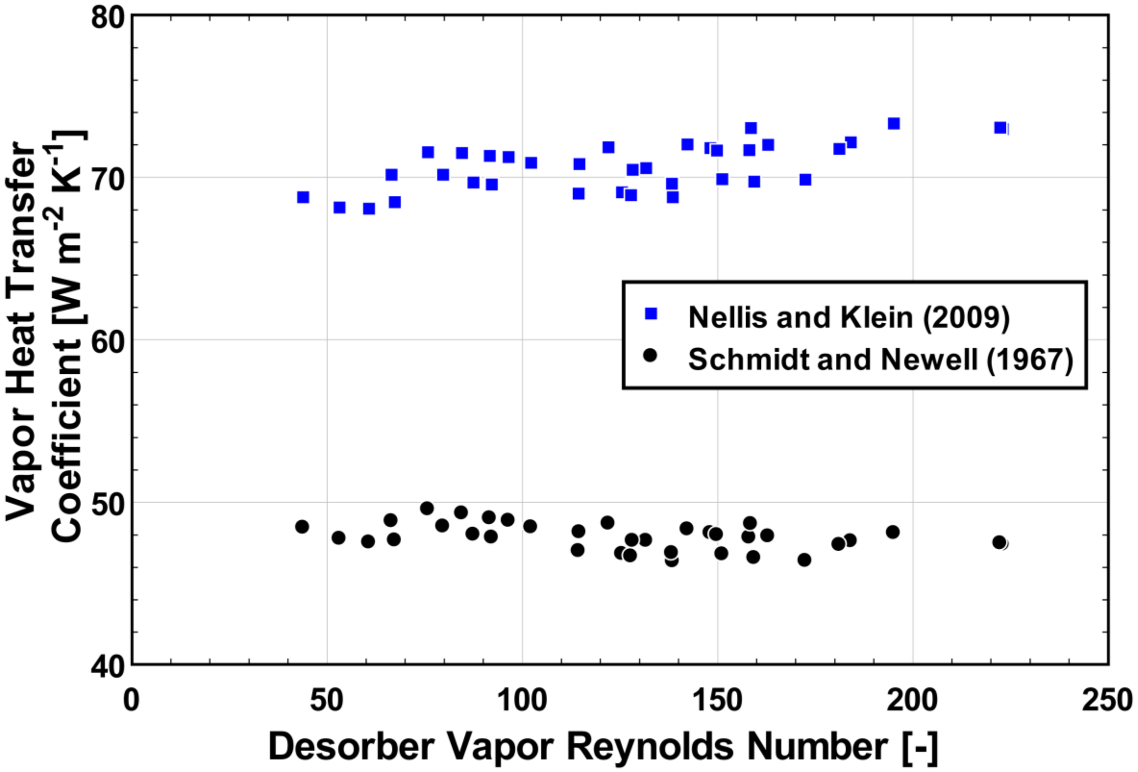

Figure 5.21: Vapor-to-interface heat transfer coefficients

comparison of the two correlations across the range of vapor Reynolds numbers observed during testing. The developing flow correlation of Nellis and Klein (2009) predicts significantly higher average heat transfer coefficients, although trends for the two approaches are similar. When applying the SBG method, results that utilized the correlation of Nellis and Klein (2009) were found to more closely match experimental values. Therefore, subsequent discussion and figures are given for predictions made using this correlation.

Figure 5.22 shows the predicted film heat transfer coefficients described previously, as well as the corrected heat transfer coefficients for these correlations as determined from the SBG method and vapor heat transfer coefficients of Nellis and Klein (2009). The correlation of Chun and Seban (1971) is seen to over predict the experimental data, particularly at low heat fluxes. The correlation of (Wilke, 1962) generally matches the magnitude of the experimental results, but does not capture the trend of increasing heat transfer coefficient with heat flux. Predicted values from Damman (1973) match the experiments well and capture the trends in the data for all but the highest heat fluxes. For heat fluxes over approximately 35 kW m^{-2}, the experimental results and those predicted by Damman (1973) begin to diverge. This may be due to the increase in vapor Reynolds number that occurs in this region, as shown in Figure 5.23, which could lead to increased film waviness and higher heat transfer coefficients. However, none of the available film evaporation or boiling correlations predicts an increase in film heat transfer coefficient with vapor Reynolds number. This is shown in Figure 5.24.

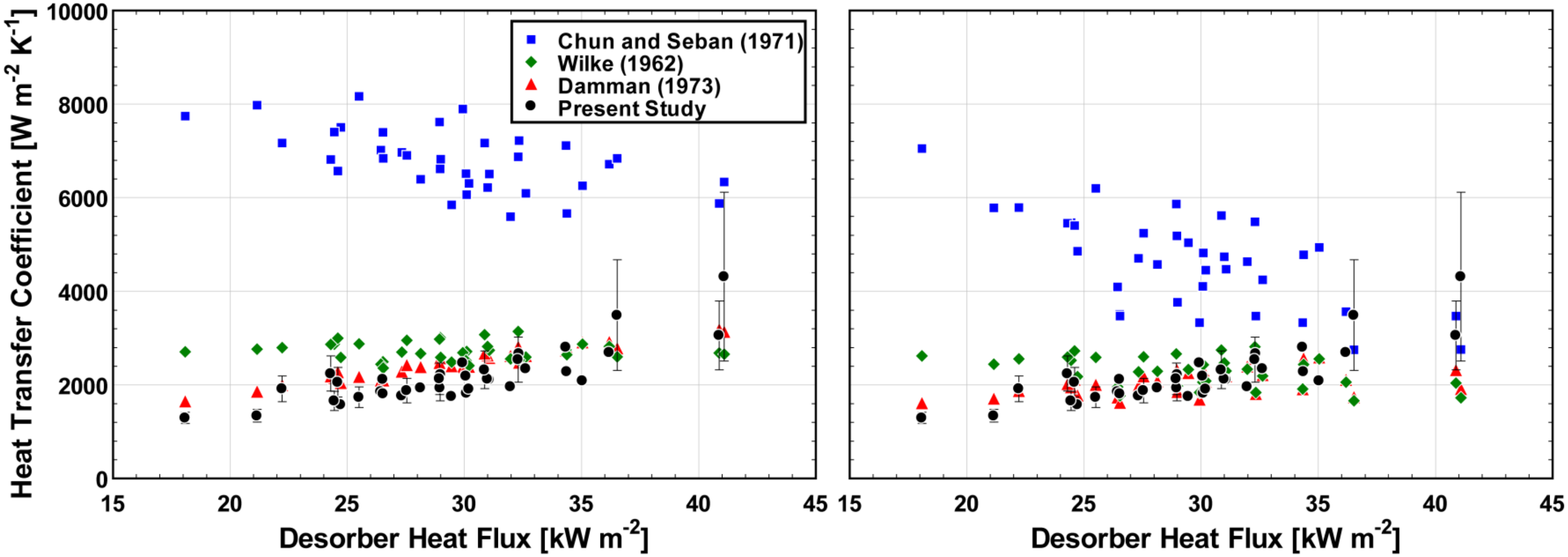

Figure 5.22: Ideal (left) and corrected (right) film heat transfer coefficients

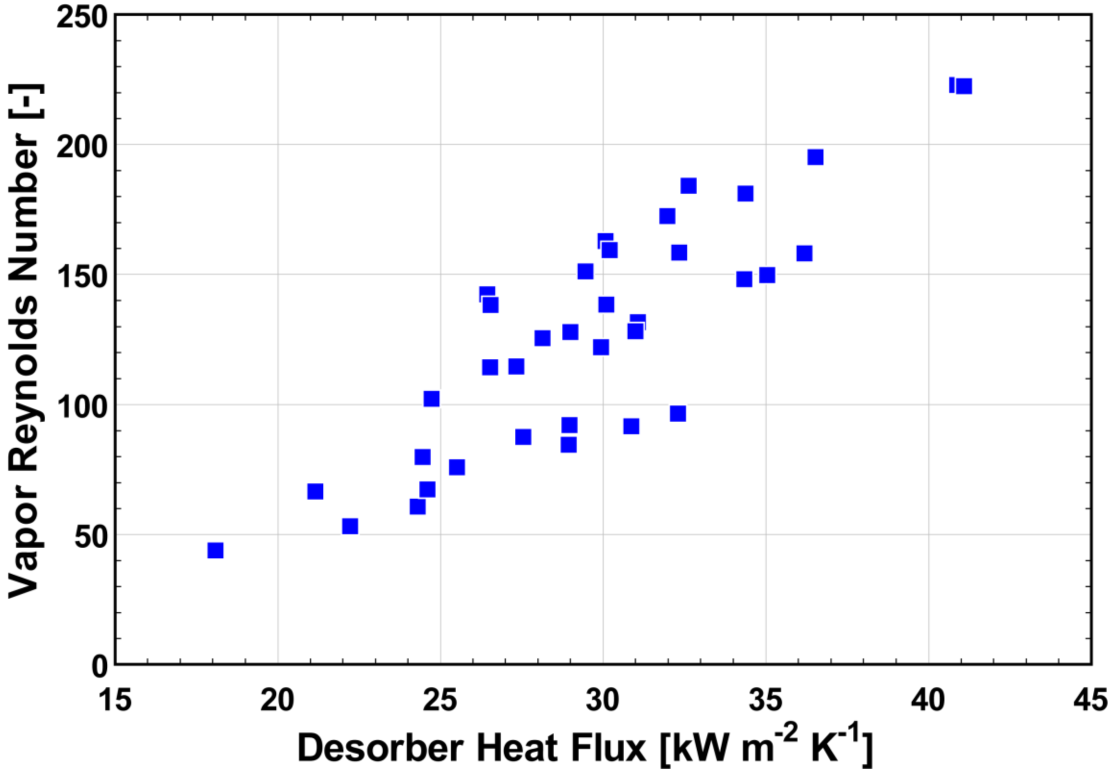

Figure 5.23: Vapor Reynolds number versus heat flux

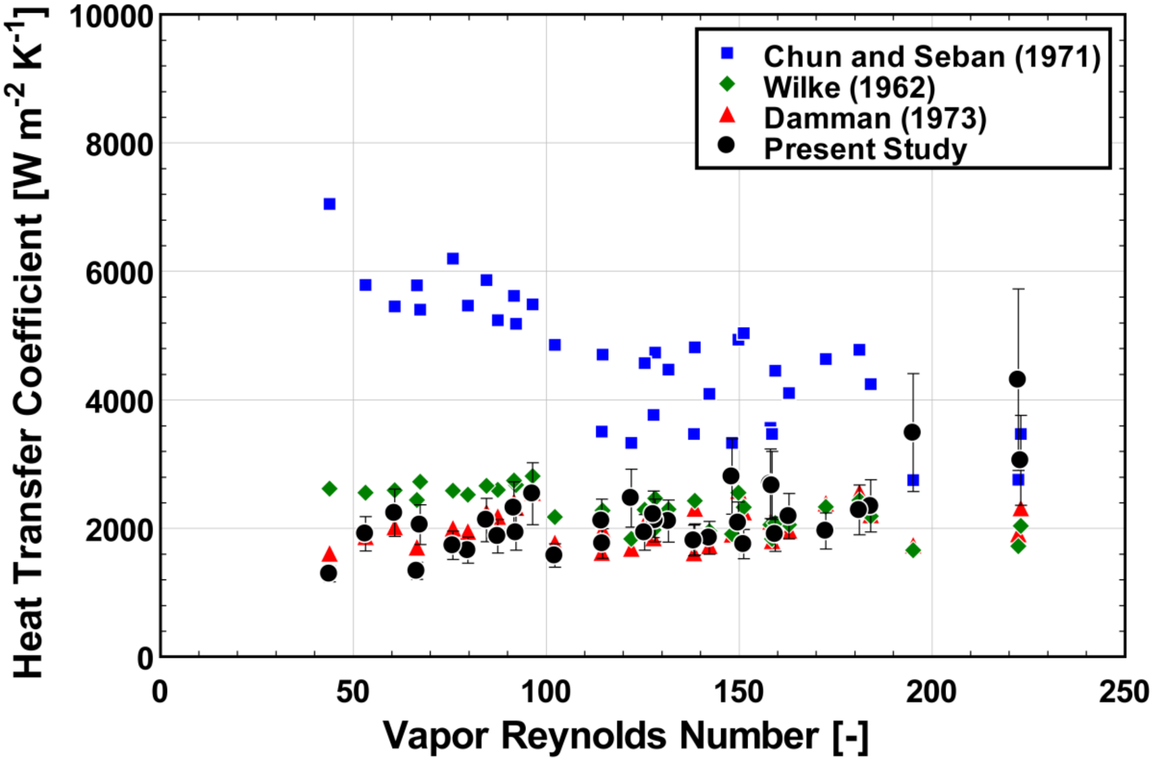

Figure 5.24: Film heat transfer coefficient versus vapor Reynolds number

While this trend is not predicted well at the higher heat fluxes, the SBG method applied to the correlations of Damman (1973) and Nellis and Klein (2009) does adequately predict the experimental results (Figure 5.25). The average deviation and average absolute deviation for this method across all data points are found to be -1.3% and 17.5%, respectively, with 86.1% of the data predicted to within 25% of the experimental values. It is expected that the correlation of Damman (1973) yields the best agreement with the experimental results because the range of heat fluxes and film Reynolds numbers for which that correlation was developed most closely match those of the present study.

5.2 Rectifier Heat Transfer

Figure 5.26 shows a comparison of the rectifier heat duty and vapor outlet

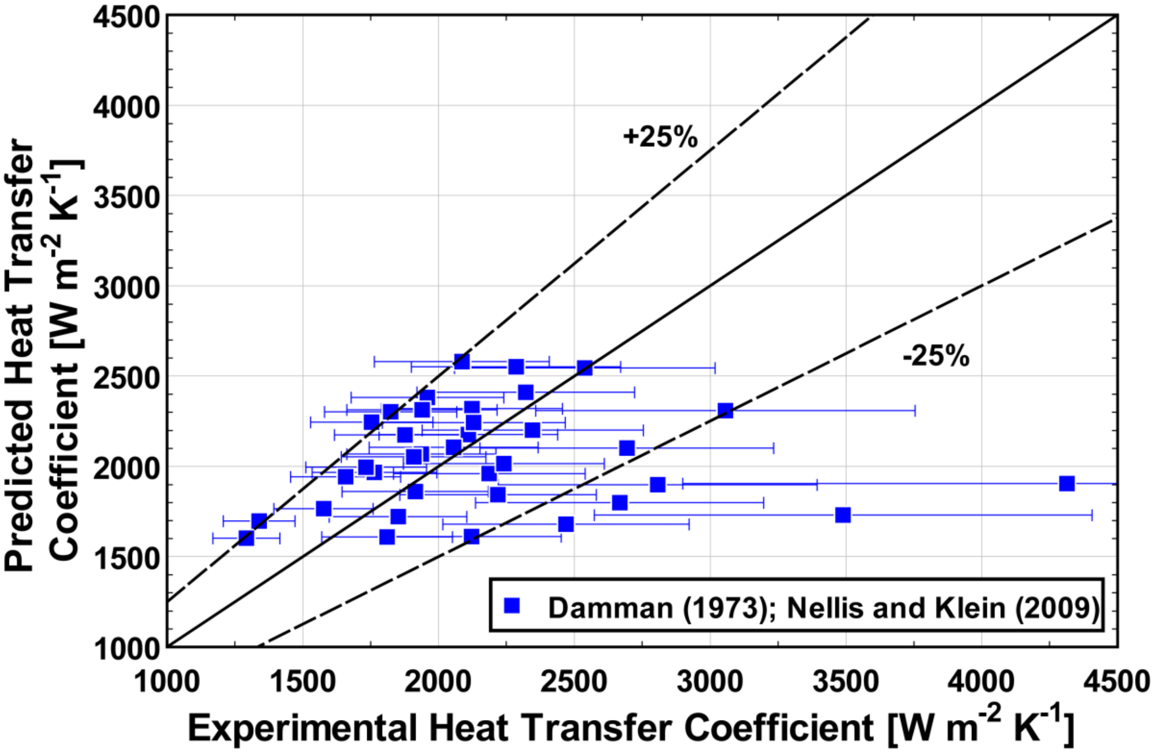

Figure 5.25: Heat transfer correlation versus the present data

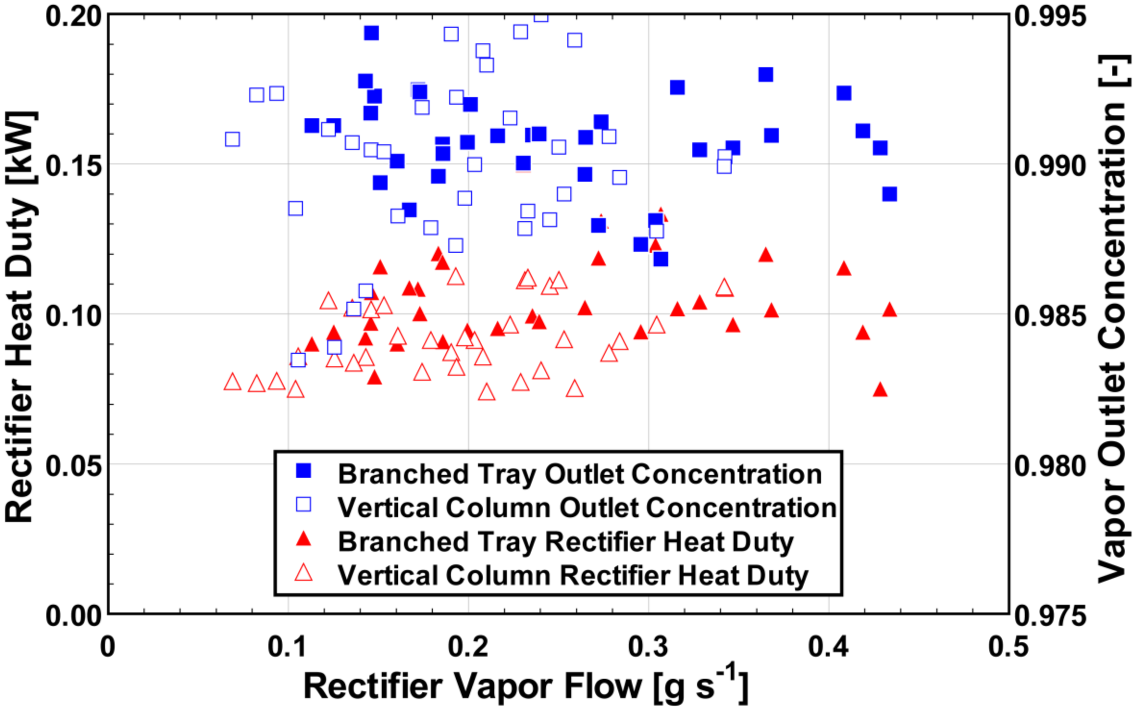

Figure 5.26: Rectifier heat duties and vapor outlet concentrations

concentration (given on a mass basis), across the range of vapor flow rates observed. Both geometries are capable of providing high vapor outlet concentration. The branched tray vapor outlet concentration was, on average 0.991, while the outlet concentration for the vertical column was 0.990. The heat duty did not show a clear dependence on the vapor flow rate for either test section, but the vertical column duty was found to be somewhat lower. The rectifier duty was, on average 92 W for the vertical column, and 105 W for the branched tray.

While the rectifier heat duty does not show a strong relation to vapor flow rate, it does correlate well with the reflux generation rate. Figure 5.27 shows the reflux flow rate as a function of rectifier heat duty for both geometries. An increasing reflux flow rate with heat duty is evident. This is expected, and indicates that a significant portion of the heat removal by the coolant is the latent heat of condensation, as intended. The branched

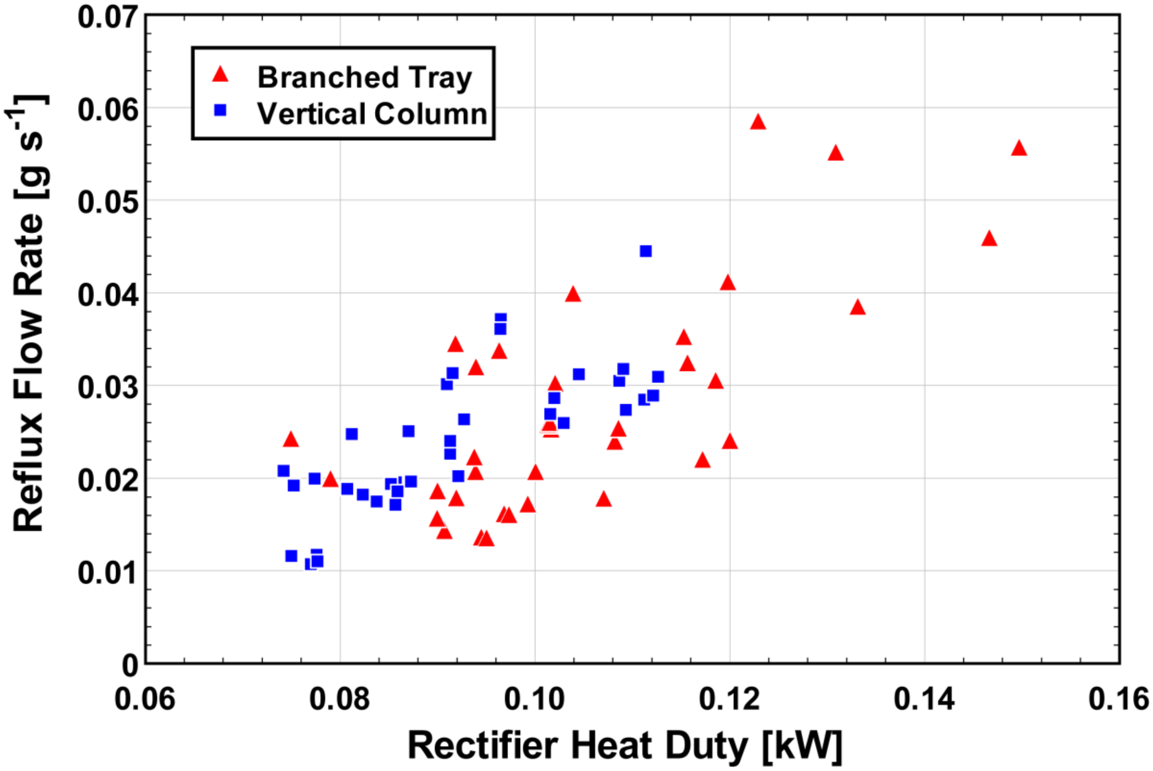

Figure 5.27: Influence of rectifier heat duty on reflux rates

tray rectifier is shown to achieve higher reflux generation rates and heat fluxes. This is due to the fact that larger amounts of vapor were generated in the branched tray desorber.

Discussion of the rectifier heat transfer coefficients is given below for both tests sections.

5.2.1 Branched Tray Rectifier

To predict the rectifier solution heat transfer coefficient, the SBG method is applied, as described above (Eq. 5.10 and 5.11). The ideal condensation heat transfer coefficient was calculated using the film condensation method of Rohsenow *et al.* (1956), which is a Nusselt-type analysis for film condensation that accounts for the influence of vapor-liquid shear on the film condensation process. Details of this method are available in Carey (2008).

For comparison, the empirical correlation for the dropwise condensation of steam, developed by Rose *et al.* (1999), was also used.

$$\alpha = T_v^{0.8}\left[5 + 0.63\left(T_{sat} - T_{wall}\right)\right] \tag{5.17}$$

In Eq. 5.17 the vapor temperature, T_v, must be in °C. This correlation has been reported (Carey, 2008) to be in good agreement with experimental results available in the literature.

The vapor-to-interface heat transfer coefficient was estimated using a constant Nusselt number determined analytically by Schmidt and Newell (1967) for developed flow through rectangular channels with one adiabatic face and, otherwise constant heat flux, presented by Shah and Bhatti (1987). A simultaneously developing flow correlation for rectangular channels, developed and presented by Nellis and Klein (2009), was also used for comparison, as the vapor flow through the rectifier is expected to be in the developing region. The latter correlation is expected to over predict actual performance, but is used to provide a comparison.

With the ideal condensation and vapor-to-interface heat transfer coefficients determined, and knowledge of the sensible and total heat duties for the rectifier, an apparent heat transfer coefficient may be calculated using the SBG method. The ideal condensation and vapor-to-interface heat transfer coefficients are shown in Figure 5.28. The vapor heat transfer coefficients calculated using the two methods are of the same order of magnitude, with the developing flow values being higher. The condensation correlations predict an order of magnitude difference, as is typical when comparing dropwise to film condensation. There is also little change in the predicted values, which is expected for the narrow range of vapor flow rates under consideration.

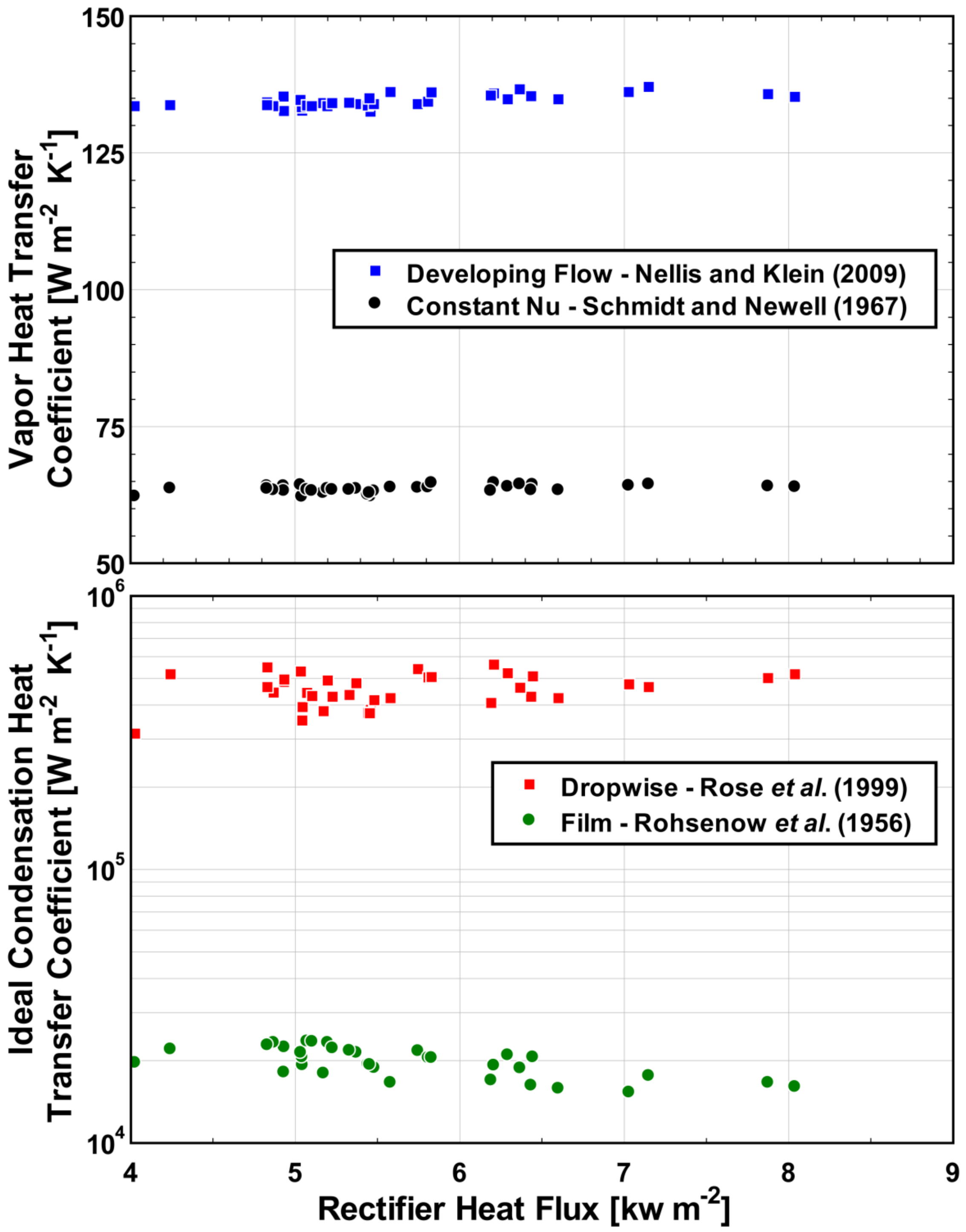

Figure 5.28: Vapor-to-interface and ideal condensation heat transfer coefficeints

The apparent heat transfer coefficients, determined using the SBG method and the heat transfer coefficients discussed above, are shown with the experimental results in Figure 5.29. It is interesting that predictions using the same vapor-side correlation give similar results. This can be attributed to the fact that the vapor sensible heat load is very high for ammonia-water condensation, where very large temperature glides exist. For the experimental data set, values of Z_{SBG} varied from 0.173 to 0.370. Considered along with the fact that the ideal condensation coefficients are several orders of magnitude higher than the vapor coefficients, it can be seen from Eq. 5.10 that the apparent heat transfer coefficient becomes almost entirely dependent on the vapor-to-interface heat transfer coefficient. This explains why there is little difference in the predictions of the solution-side heat transfer coefficient when using the dropwise versus film condensation ideal

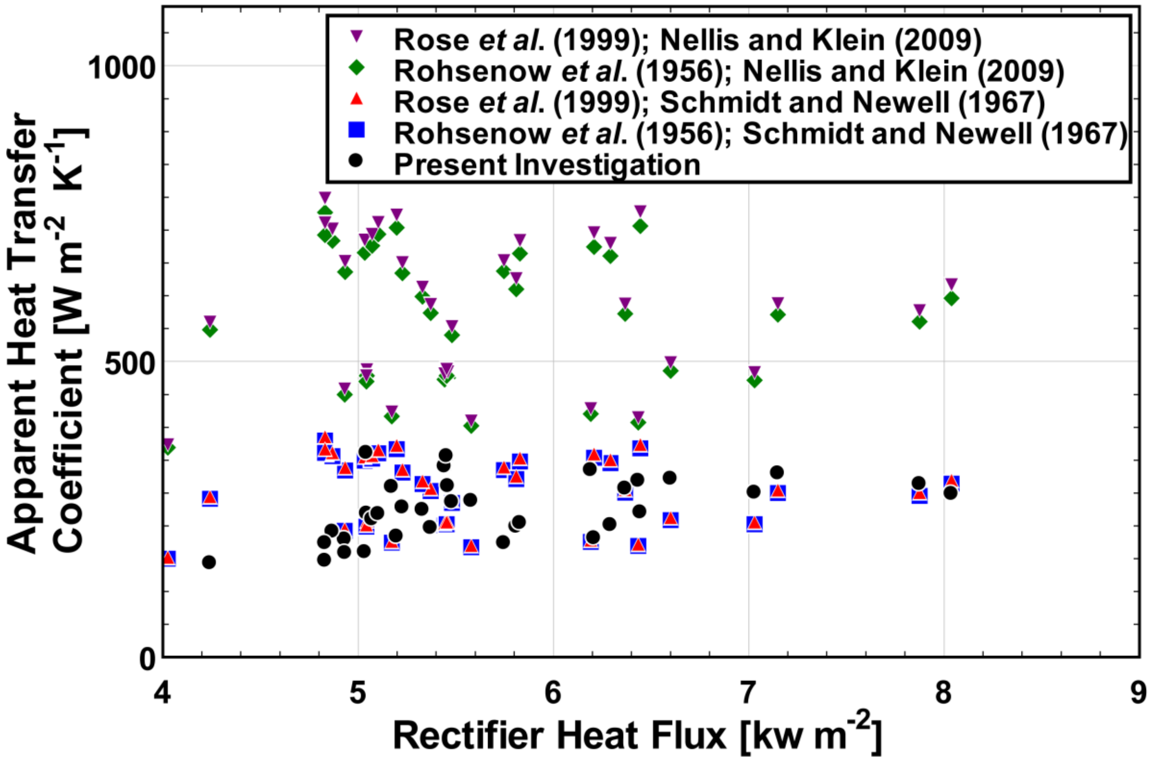

Figure 5.29: Heat transfer coefficeints versus heat flux

correlations. It is clear from Figure 5.29 that the predictions using the vapor-side correlation of Nellis and Klein (2009) over predict the experimental results. This is to be expected, as the correlation of Schmidt and Newell (1967) is more applicable to the geometry of the rectifier, accounting for the adiabatic wall formed by the glass plate.

Also shown in Figure 5.29, is a large difference between the experimental and predicted heat transfer coefficients, even when only considering the predictions that utilize the correlation of Schmidt and Newell (1967). This can be explained by considering the results versus the rectifier vapor Reynolds number, as shown in Figure 5.30. The experimental results increase with vapor Reynolds number. This is not represented well by the predicted values, despite the fact that the analysis of Rohsenow *et al.* (1956) does account for the influence of vapor shear. Rather than having a direct impact on the local film heat transfer coefficient, it is plausible that at higher vapor

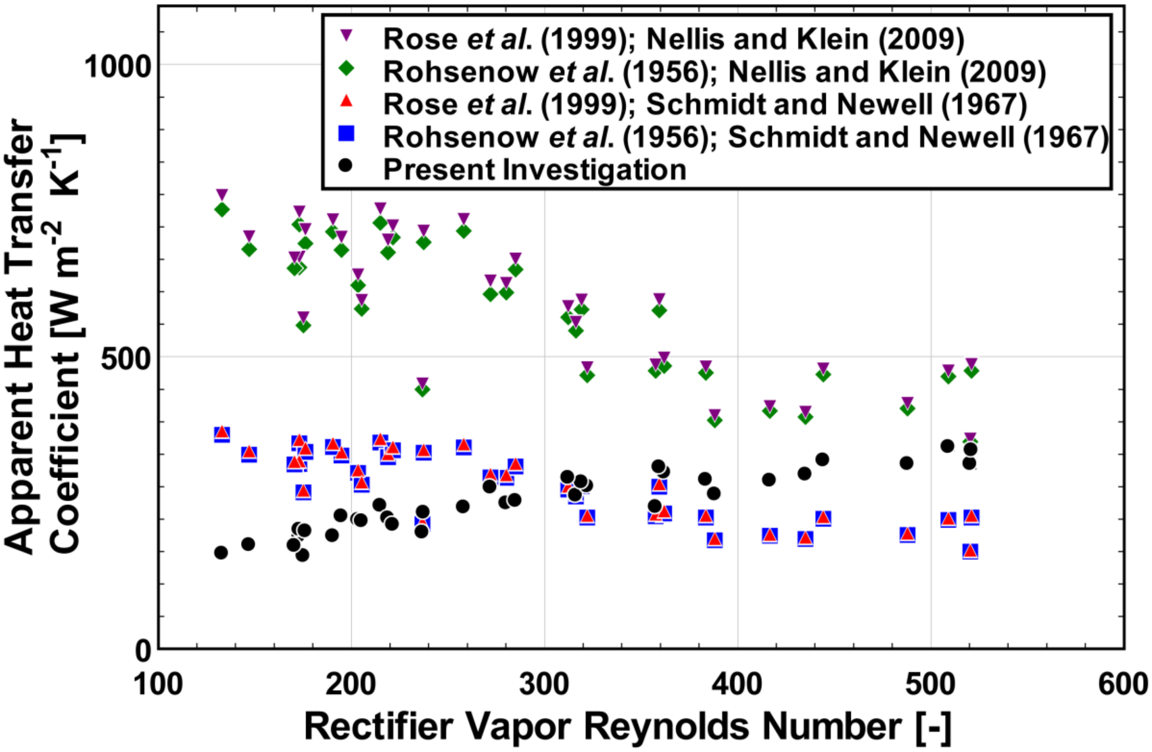

Figure 5.30: Heat transfer coefficients versus vapor Reynolds number

Reynolds numbers, the distribution of vapor through the rectifier section is improved. At Reynolds numbers below 350, where agreement with the predicted values is poor, it may be that the vapor is flowing in a more direct path between the rectifier inlet and outlet, and not distributing well across the entire rectifier cross-section. Additionally, given the small dimensions of the rectifier passages, condensate may build up in areas with low vapor flow, blocking flow completely. As the Reynolds number increases, the flow would be expected to distribute more evenly due to higher pressure drop, and may assist in breaking up any liquid blockages. Above Reynolds numbers of approximately 350, the experimental results agree well with predicted values, indicating that in these cases the full heat transfer area is being utilized. At lower Reynolds numbers, the local heat transfer coefficients may be near the predicted values, but the actual heat transfer area is less that what is assumed in the analysis of the experimental heat transfer coefficients.

This issue is made more pronounced by the fact that the measured desorber vapor generation rates were, on average, lower than the design values. The design condition vapor generation rate was 0.28 g s^{-1}, while the average experimental vapor generation rate was 0.24 g $s^{-1,}$ with a minimum of 0.11 g s^{-1}. At these lower vapor generation rates, the rectifier is significantly oversized, which leads to the lower experimental heat transfer coefficients as the heat transfer area in the component is underutilized due to flow mal-distribution and build-up of condensate. However, in future designs, it may be possible to avoid this by modifying the geometry to improve flow distribution. Additionally, increasing vapor velocities by reducing flow area may also be effective in improving flow distribution, although this method would be subject to flooding limitations. This is discussed in additional detail in connection with the counter-current flow limits (Section 5.6).

While it is likely that flow distribution is the primary factor leading to lower-than-predicted experimental heat transfer coefficients, examination of the rectifier wall subcooling, $T_{sat} - T_{wall}$, does indicate that another factor could play a role. The rectifier apparent heat transfer coefficients are shown as a function of wall subcooling in Figure 5.31. It is apparent that the highest experimental heat transfer coefficients occur for low driving temperature difference, and decrease at higher temperature differences. This could be due to a transition from predominantly dropwise condensation to film condensation. This result has been presented in several other sources for condensation of binary fluids, organic compounds, and condensation in the presence of non-condensable vapor (Rose *et al.*, 1999; Carey, 2008). The transition from dropwise to film

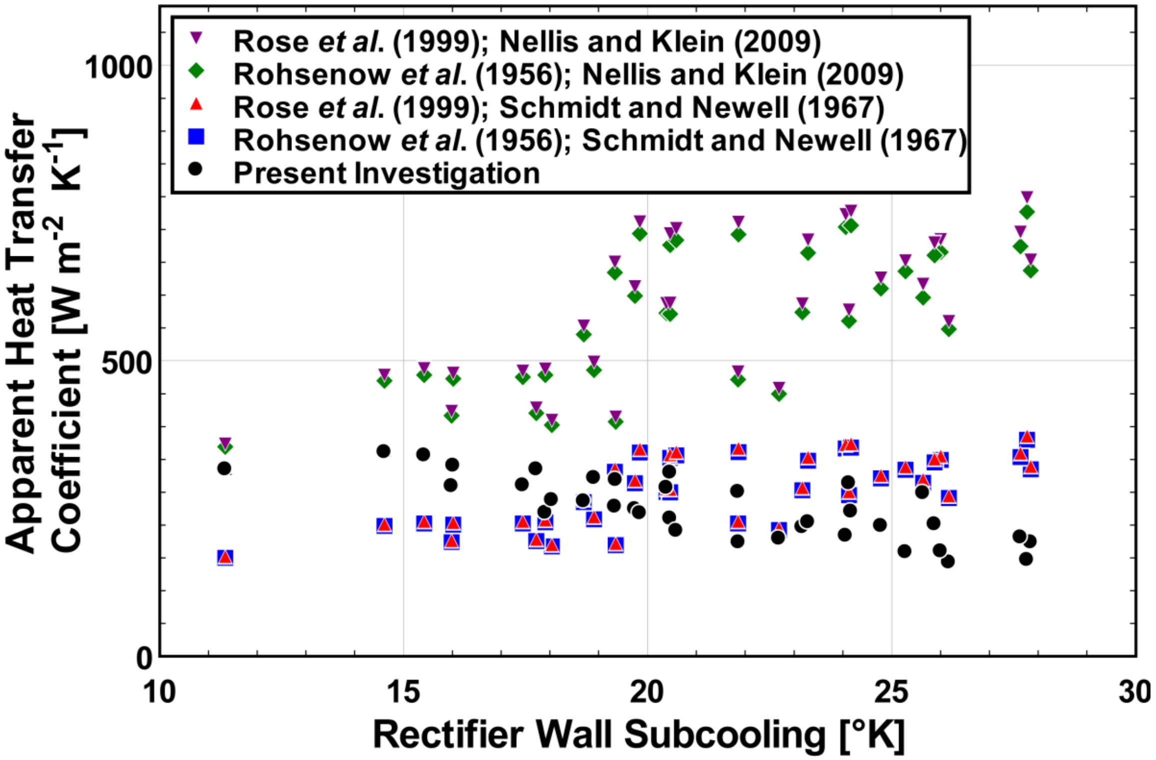

Figure 5.31: Heat transfer coefficients versus wall subcooling

condensation typically occurs within the temperature difference range that was observed in this study. Due to the high values of Z_{SBG} and the large difference in the vapor and film heat transfer coefficients, as discussed previously, the impact of the change in the ideal condensation coefficient (from dropwise to film-wise) is not captured well by the SBG method at these conditions. It is also important to note that in the dropwise condensation region, some of the most significant assumptions of the SBG method may not remain valid. For instance, the assumption that all heat is removed from the vapor-liquid interface would not necessarily be appropriate, particularly when sensible cooling of the vapor can be a relatively large portion of the total rectifier duty. The study of Fronk (2014), which considered forced convective condensation of ammonia-water mixtures for some similar concentrations, also found the SBG method to under predict ammonia-water condensation heat transfer coefficients and attributed this to the large sensible heat load and temperature glide. Very little additional information is available on the dropwise-to-film transition phenomenon in the literature and no correlations were found for determining the transition point or proper transitional model for the region between dropwise and film condensation for zeotropic mixtures. While this effect is likely secondary to the impact of any flow mal-distribution, this possible transition from dropwise to film condensation, may account for some of the difference between the predicted and experimental results.

Despite these issues, the SBG method does offer reasonable predictions in the film condensation region for vapor Reynolds > 300 and could be used to provide a good estimate of heat transfer coefficients for similar rectifiers operating at in this range. The best agreement was found by applying the SBG method with the film condensation coefficient from Rohsenow *et al.* (1956), and the vapor coefficient determined from Schmidt and Newell (1967). Figure 5.32 shows a comparison of the predicted values, determined using these correlations and the SBG method, and the present data. This provided an average deviation of 18.2% and an average absolute deviation of 39.3. For points with vapor Reynolds > 300, the average absolute deviation drops to 22.8%. Significant scatter is seen and only 36% of points are predicted to within 25% error. However, 75% of points are predicted within 50% error. It should be noted that the validity of this method may not continue at Reynolds numbers above 550, and that under these conditions the SBG method may begin to under predict experimental results. Additional investigation would be required to draw more general conclusions.

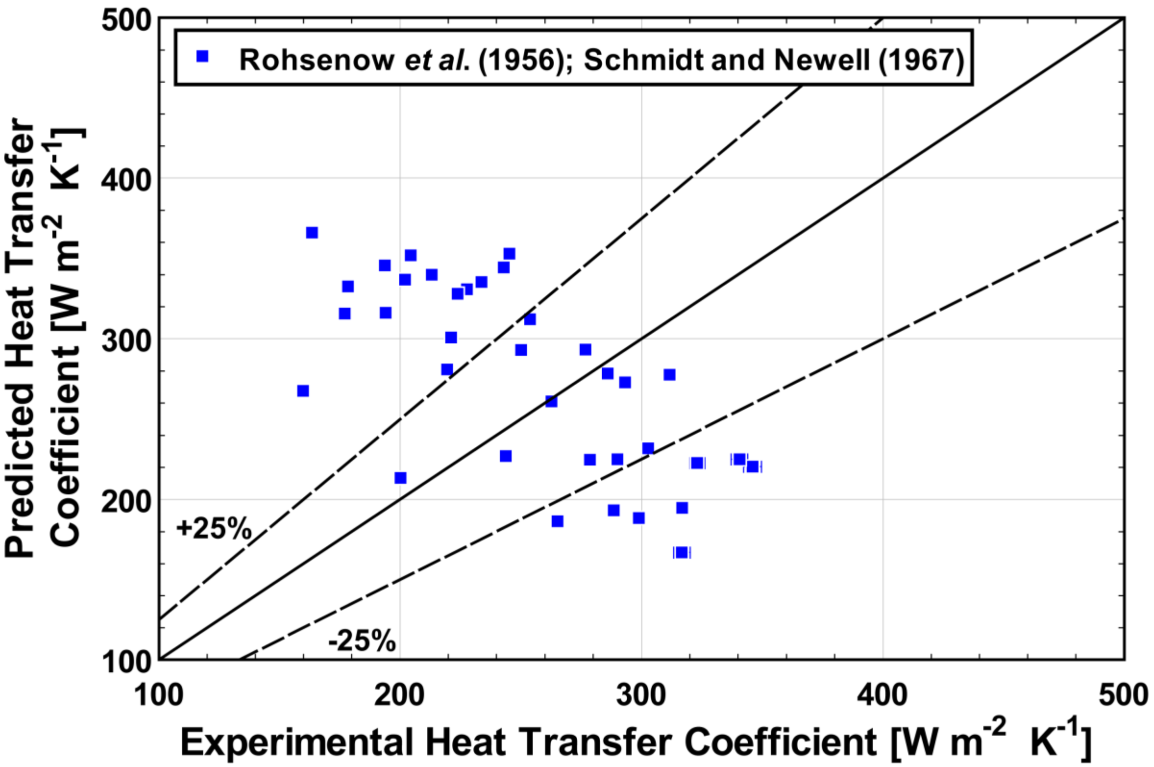

Figure 5.32: Heat transfer coefficients versus present data

5.2.2 Vertical Column Rectifier

Heat transfer results for the vertical column rectifier are quite similar to those for the branched tray. This is expected as the heat transfer mechanisms and conditions are similar for the two geometries.

The correlations employed in the branched tray comparison are also used in the SBG method for the vertical column. Results for the predicted and experimental values of the rectifier heat transfer coefficient are shown in Figure 5.33. Again there is substantial disagreement between the predicted values and experimental results, while predicted values using the same vapor-side correlation are very similar for any given point. This is due to the high values of Z_{SBG} and large difference in the condensation and vapor heat transfer coefficients, which cause the various correlations to converge to

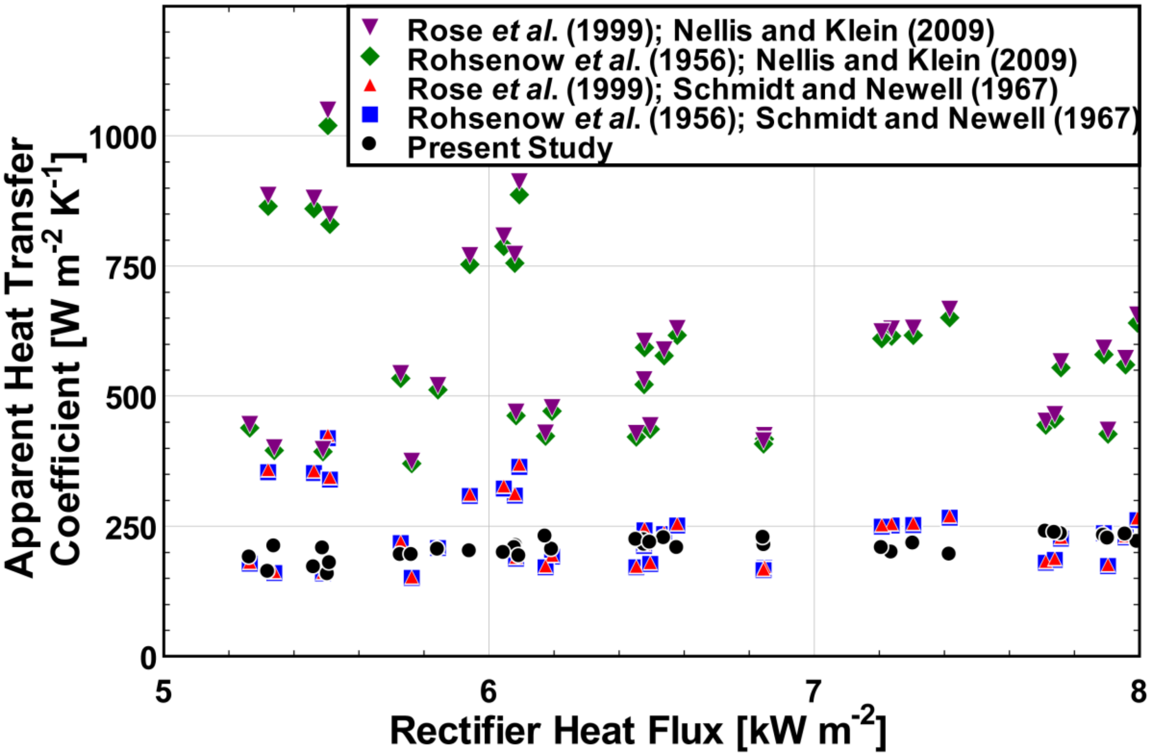

Figure 5.33: Heat transfer coefficeints versus heat flux

similar values when corrected using the SBG method.

Figure 5.34 shows the measured heat transfer coefficients increasing with vapor Reynolds number. As the vapor Reynolds number increases, flow mal-distribution between the channels is expected to decrease, leading to higher experimental heat transfer coefficients. Additionally, it is apparent that at the higher vapor Reynolds numbers, the predicted values converge to lower values. This is caused by higher vapor sensible heat duties that correspond to the increase in vapor Reynolds number and result in higher values of Z_{SBG}. The higher values of Z_{SBG} suppress the predicted heat transfer coefficients leading to better agreement in this range.

The SBG method again offers reasonable predictions in the film condensation region for vapor Reynolds number > 150. For points in this region, the best agreement between experimental and predicted heat transfer coefficients was found by applying the

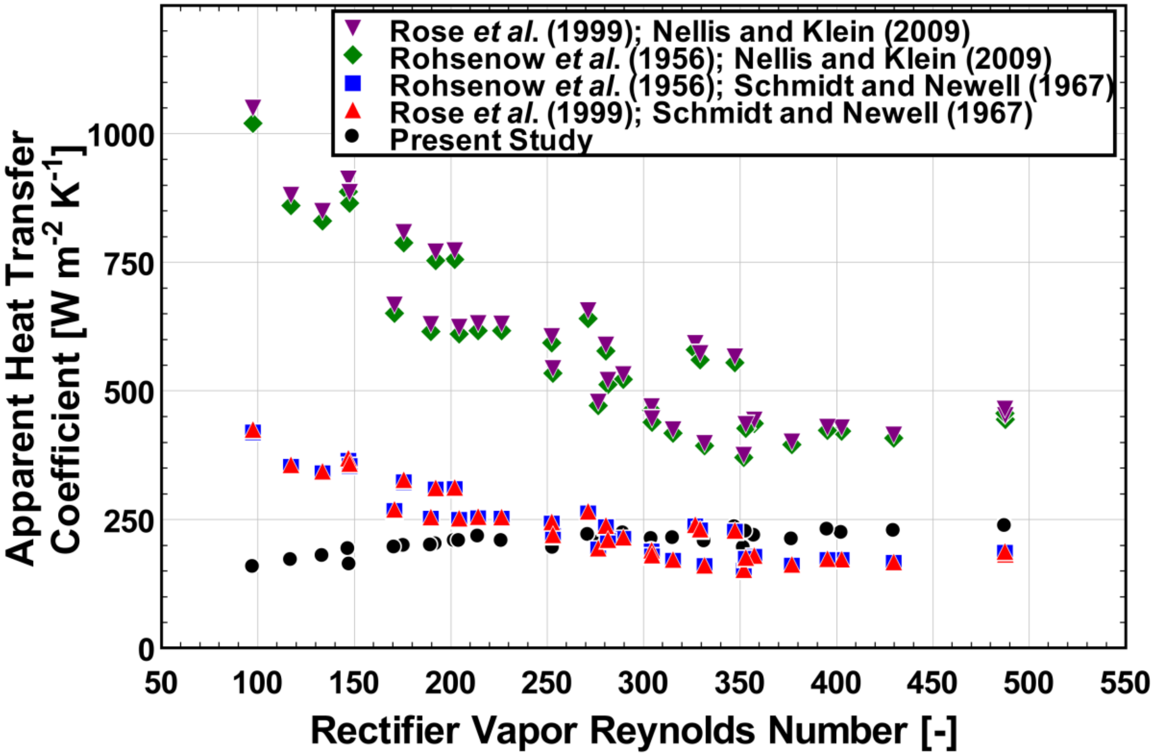

Figure 5.34: Heat transfer coefficients versus vapor Reynolds number

SBG method with the film condensation coefficient from Rohsenow *et al.* (1956), and the vapor coefficient determined from Schmidt and Newell (1967). A comparison of predicted values determined using these correlations and the SBG method, with the present data is shown in Figure 5.35. Using these correlations, the average and absolute average deviation were found to be 16.6 and 32.9%, respectively. Of the predicted values, 72% are within 25% of the data. Above vapor Reynolds numbers of 150, the average and average absolute deviation decrease to 10.2 and 20.1%, respectively.

5.3 Mass Transfer Results

The mass transfer performance of both desorbers was quantified by calculating the liquid- and vapor- phase mass transfer coefficients.

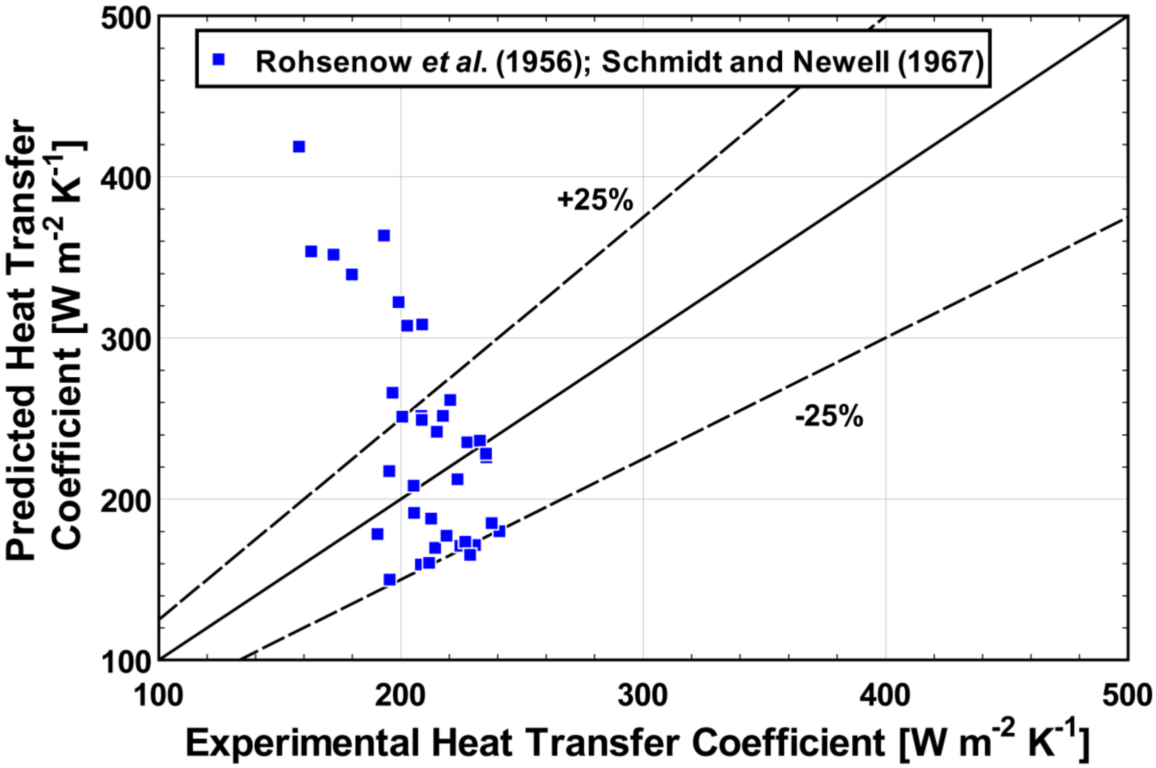

Figure 5.35: Heat transfer coefficients versus present data

5.3.1 Comparison of Desorber Mass Transfer Coefficients

Table 5.4 provides a summary of the experimental results for the vapor- and liquid-phase mass transfer coefficients for both test sections. Additionally, the best-fitting correlations, of those compared, are noted. A detailed discussion of these results for each test section follows.

5.3.2 Branched Tray Mass Transfer Coefficients

While experimental studies are limited for similar geometries, mass transfer coefficients for the conditions under consideration were calculated using the correlations of Calderbank and Moo-Young (1961) and Akita and Yoshida (1974). Both correlations were developed for chemical processes. The correlation of Akita and Yoshida (1974) pertains to bubble columns, while the correlations of Calderbank and Moo-Young (1961) pertain to agitators and mass exchangers of several designs. In the study of Calderbank and Moo-Young (1961), several correlations were presented for various conditions and bubble sizes. The results shown here are for the correlation specified for the smaller range of bubble diameters, which move primarily under buoyancy forces and are approximately spherical in shape. In this section, the data from the present study are also

Table 5.4: Mass transfer coefficient results

	Branched Tray		**Vertical Column**	
	Liquid	**Vapor**	**Liquid**	**Vapor**
Experimental Average, m s^{-1}	0.00154	0.0594	0.00079	0.0868
Best-Fitting Correlation	Analogy of the Present Study	Onda *et al.* (1968)	Calderbank and Moo-Young (1961)	Onda *et al.* (1968)
Correlation AD, %	-4.7	-0.3	8.7	-10.5
Correlation AAD, %	48.2	45.7	36.5	62.5

compared with mass transfer coefficients, calculated using the heat transfer analogy and the previously proposed correlation for binary fluid mixture boiling heat transfer, presented above (Section 5.3.4).

The applicable correlation of Calderbank and Moo-Young (1961) is as follows.

$$\beta_l \, Sc_l^{2/3} = 0.31 \left(\frac{\Delta\rho \times \mu_l g}{\rho_l^{\,2}} \right)^{1/3} \tag{5.18}$$

The correlation of Akita and Yoshida (1974) is as follows.

$$\beta_l = 0.5 g^{5/8} \cdot D_{aw,l}^{\;1/2} \cdot \rho_l^{3/8} \cdot \sigma_l^{-3/8} \cdot d_{vs}^{\;1/2} \tag{5.19}$$

The average bubble size, d_{vs}, is also correlated by the Akita and Yoshida (1974) correlation.

$$d_{vs} / D_{bc} = 26 \cdot \left(g \cdot D_{bc}^{\;2} \cdot \rho_l / \sigma_l \right)^{-0.5} \cdot \left(g \cdot \frac{D_{bc}^{\;3}}{\left(\mu_l / \rho_l \right)^2} \right)^{-0.12} \cdot \left(\frac{J_v}{\sqrt{g \cdot D_{bc}}} \right)^{-0.12} \tag{5.20}$$

The bubble column diameter, D_{bc}, was taken to be 0.077 m, which was the smallest column diameter they investigated. The superficial velocity, J_v, was evaluated using the branched tray geometry.

For the heat transfer analogy, the modified binary fluid boiling correlation from the present study shown in Table 5.3 is used. The mass transfer coefficient is determined from the Lewis relationship.

$$\frac{\beta}{\alpha} = \frac{Le^{2/3}}{\rho c_p} \tag{5.21}$$

Figure 5.36 shows a comparison of the results. Generally, the predicted values agree with the experimental results, though a number of experimental points show significant deviation, with much higher values for the mass transfer coefficient. Additionally, one outlier point is observed at a particularly high value of 0.010 m s^{-1}.

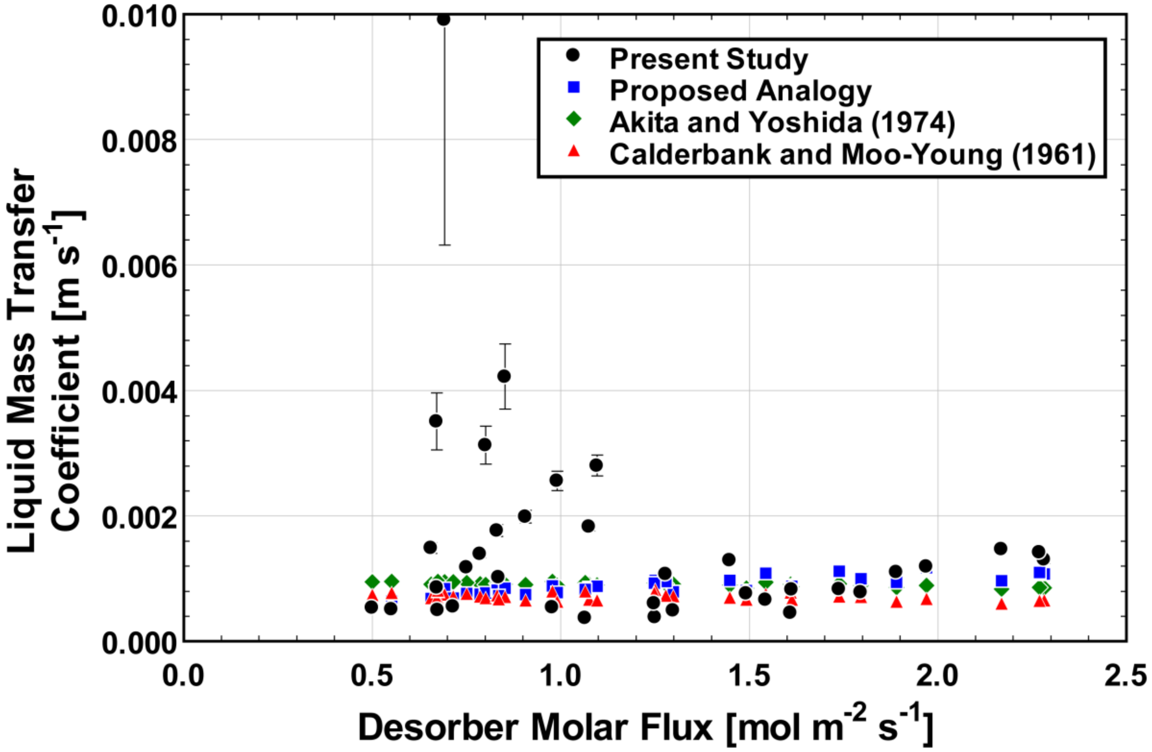

Figure 5.36: Liquid-phase mass transfer coefficients versus molar flux

The deviation from the correlations can be explained by Figure 5.37, which shows that there is a dependence on the solution flow rate (given per unit transfer area), with mass transfer coefficients generally increasing with solution flow. The solution flow per unit area is based on the solution inlet flow rate, $\dot{m}_{l,in}$, and is used in place of the liquid Reynolds number due to the significant changes in cross-sectional area through the branched tray desorber. Considering the trends shown in Figure 5.37, the increase in heat transfer coefficient with solution flow rate is likely due to increased interfacial area that is observed in the flow visualization studies, at higher flow rates. This is caused by additional wall wetting, liquid bridging of channels, and more bulk fluid motion in the liquid pools. There is also a distinct hysteresis effect observed with respect to solution flow, which explains why all high solution flow points do not indicate elevated mass transfer coefficients. This phenomenon is not captured by the mass transfer correlations,

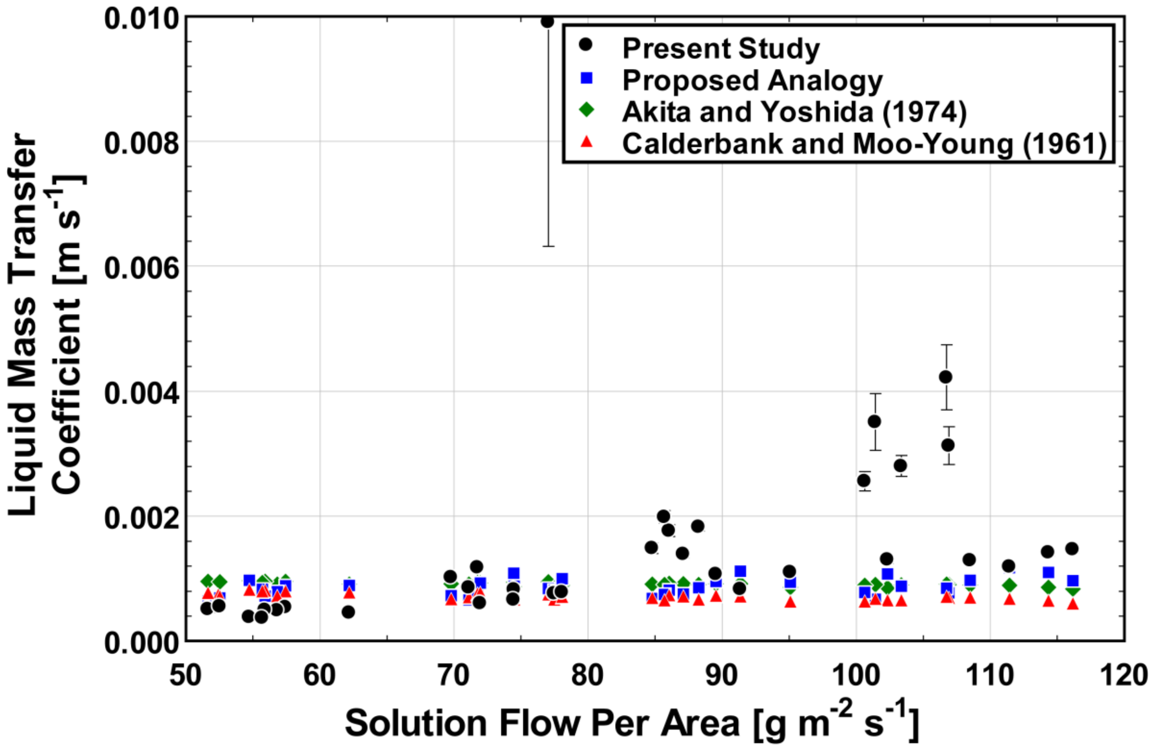

Figure 5.37: Mass transfer coefficient versus solution flow rate per area

as all three correlations employed consider large liquid pools with relatively little bulk fluid motion. The correlation by Calderbank and Moo-Young (1961) replaces the buoyancy parameters, $\Delta\rho \cdot g$, in Eq. 5.18 with a parameter that accounts for active mixing of the solution, and could provide more accurate prediction of the trend of increasing mass transfer coefficient with solution flow. However, this term is presented for applications with active agitation tanks, and relies on the quantification of the mixing power dissipated per unit volume, which is not particularly relevant in the present study. Shown in Figure 5.38, the heat and mass transfer analogy, using the correlation proposed in the present study for binary fluid mixture boiling, provides the best agreement with an average and average absolute deviation of -4.7 and 48.2%, respectively, for all data points. Due to the large span of observed mass transfer coefficients, and the inability of

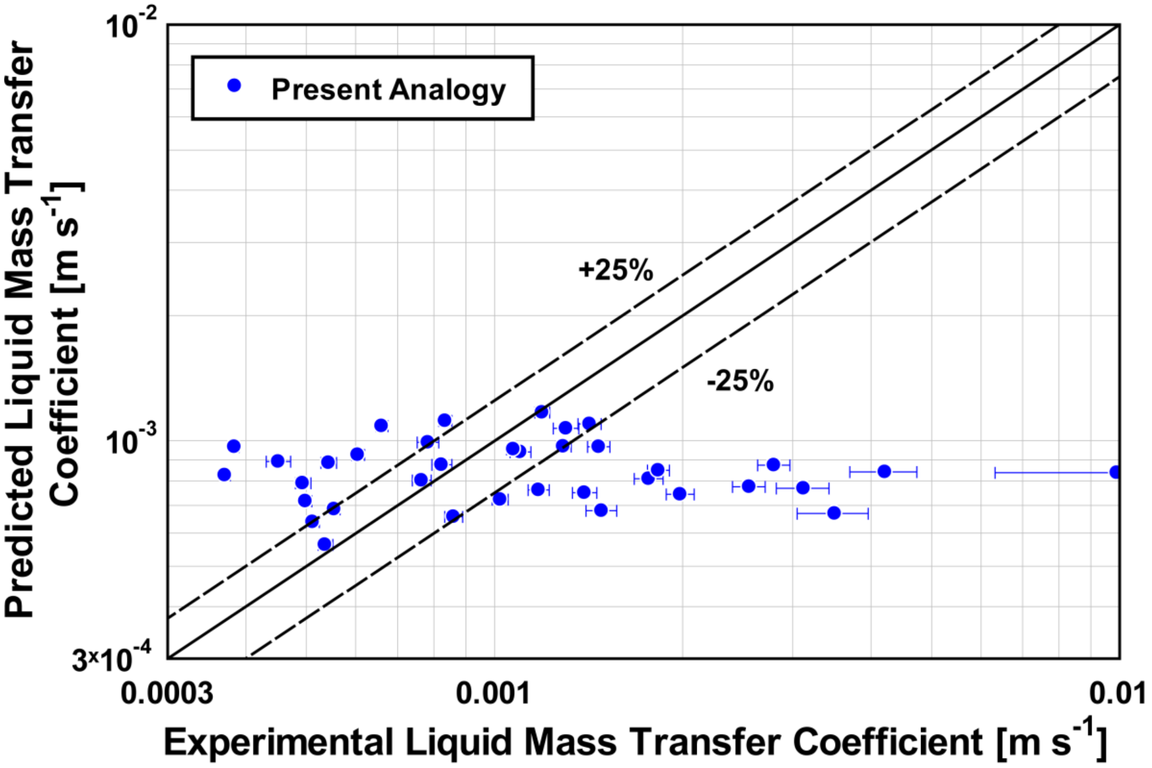

Figure 5.38: Present analogy versus data

the present analogy, or any existing correlation, to fully capture the effects of the fluid dynamics, only 33% of data are predicted to within 25% error.

Considering the vapor-phase mass transfer coefficient in the branched tray desorber, a heat transfer analogy was again applied, along with a correlation for vapor mass transfer coefficients in packed beds, given by Onda *et al.* (1968):

$$\frac{\beta_v}{D_{aw,v} \cdot a_t} = 3.615 \cdot \left(a_t \cdot D_p\right)^{-2.0} \cdot Re_v^{\ 0.7} \cdot Sc_v^{\ 1/3} \tag{5.22}$$

While a correlation for packed beds may not necessarily represent the desorber geometry under consideration here, both geometries feature counter-flow vapor and liquid streams, somewhat irregular surfaces, similar characteristic length scales, and partially wetted surfaces. Based on these similarities and a lack of available correlations for the present geometry, a comparison was conducted. Onda *et al.* (1968) suggest two limiting values for the leading numerical coefficient in Eq. 5.22. For larger packing material diameters, a value of 5.23 is suggested. For smaller packing materials, a value of 2.0 is suggested. An average of these values was used in the present study and is shown in Eq. 5.22. The surface area per volume, a_t, was taken to be the ratio of channel perimeter and cross-sectional area. The characteristic diameter of the packing, D_p, was taken to be the hydraulic diameter of the channel. Finally, a maximum vapor Reynolds number, based on the desorber outlet vapor velocity, was used.

The heat transfer coefficient used in the heat transfer analogy was determined using the correlation of Nellis and Klein (2009) for simultaneously developing flows in rectangular ducts. The Lewis relationship was used, as given in Eq. 5.21, to determine the mass transfer coefficient. The results are shown in Figure 5.39. The heat transfer

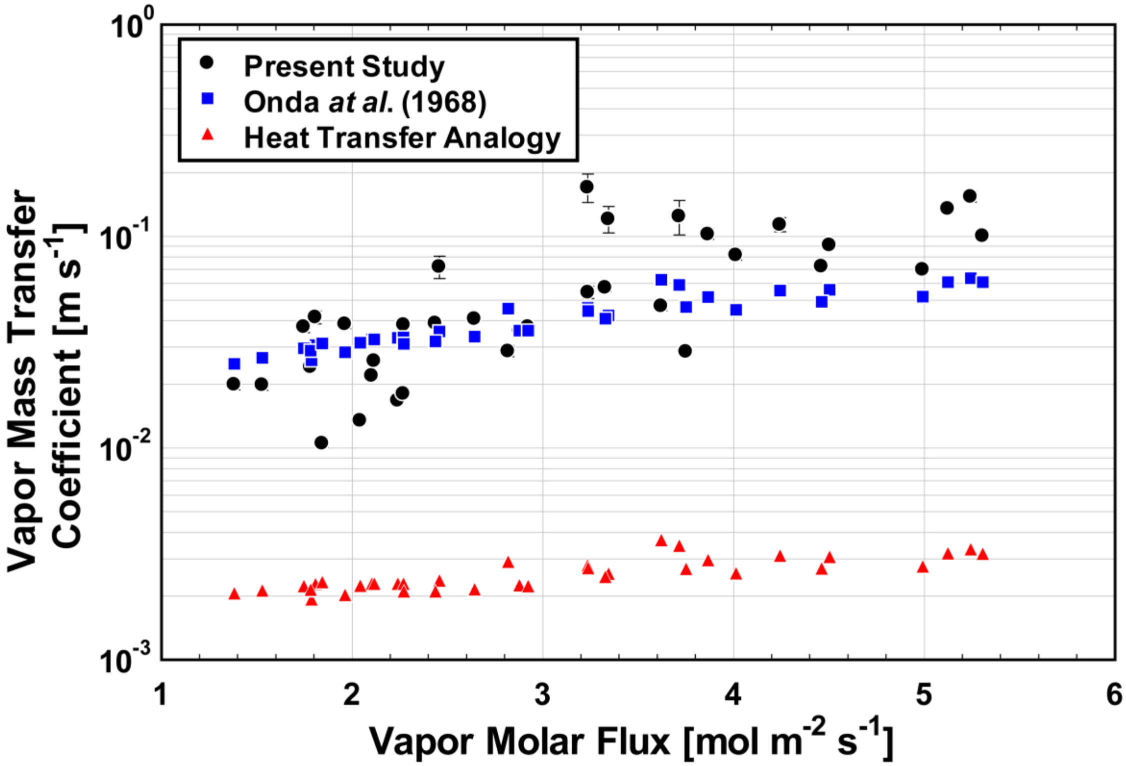

Figure 5.39: Mass transfer coefficients versus molar flux

analogy is seen to predict significantly lower values than those observed in the experiments. This is likely due to the fact that the flow is at low Reynolds number and the duct model does not capture the interaction with the dynamic vapor-liquid interface, additional mixing due to generated vapor joining the bulk vapor flow, and other hydrodynamic aspects of the flow. The correlation of Onda *et al.* (1968) predicts the magnitude and general trend of the vapor mass transfer coefficient, although it does not capture the spread in experimental data points. This difference can be seen to be primarily due to spread in the experimental results and is attributed to the difficulty in determining the vapor concentration. The calculation method used to determine the vapor bulk concentration relies on the assumption of a saturated vapor bulk in the desorber and accurate measurement of the vapor temperature. It is likely that the vapor is at least slightly superheated in some cases. Additionally, as conditions approach the counter-current limit temperature, readings may be affected by flow instabilities and impingement of liquid droplets on the thermocouple probes.

Finally, as conditions near the counter-current limit, the apparent vapor mass transfer coefficient is expected to increase significantly with the occurrence of additional interfacial area. This is observed in the experimental data; however, this trend is not captured exactly by the packed-bed predictions, which were shown by Onda *et al.* (1968) to be largely a function of the liquid Reynolds numbers for typical packed-bed geometries.

Figure 5.40 shows the predicted values of the vapor mass transfer coefficient for the correlation of Onda *et al.* (1968). The average and average absolute deviation are -0.3 and 45.7%, respectively. The higher average absolute deviation is due largely to scatter in the experimental results, as mentioned previously.

5.3.3 Vertical Column Mass Transfer Coefficients

The vertical column mass transfer results are similar to those reported for the branched tray test section. Figure 5.41 shows a comparison of experimental results and predicted values for the liquid mass transfer coefficient. Predicted values were obtained from the correlation of Calderbank and Moo-Young (1961) discussed above. Additionally, predictions were made using the heat transfer analogy applied to the film evaporation correlation of Chun and Seban (1971). Predicted values are also calculated

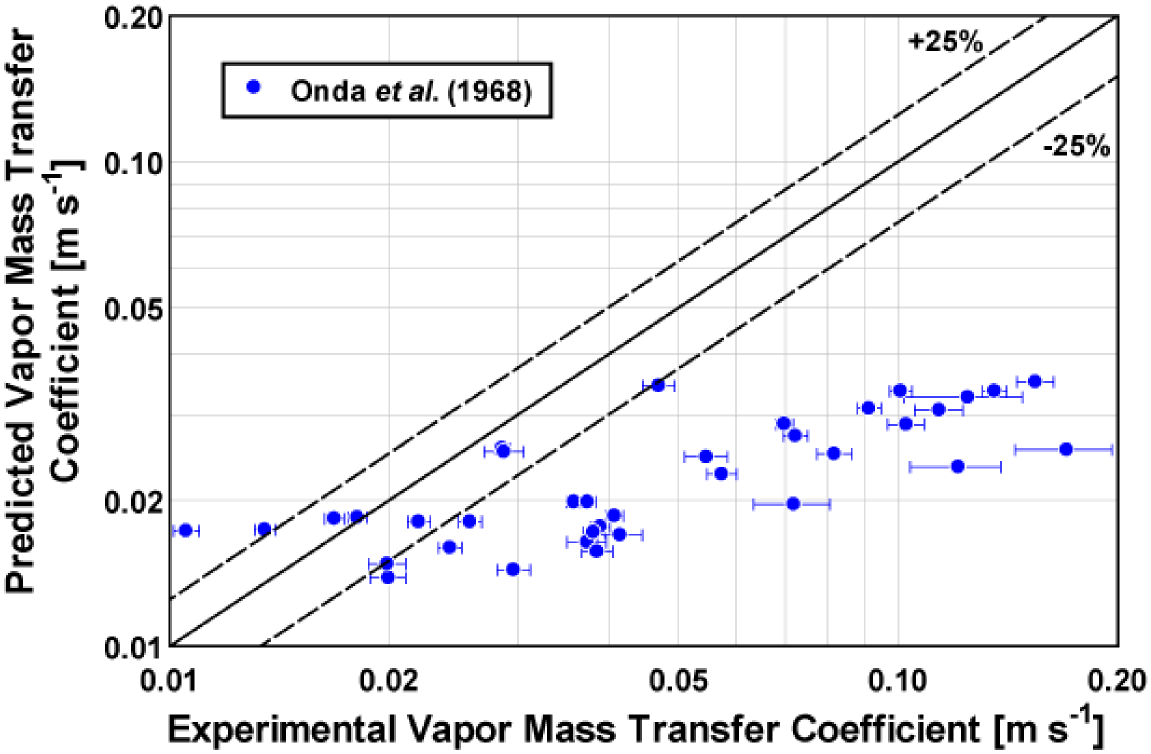

Figure 5.40: Predicted versus experimental mass transfer coefficients

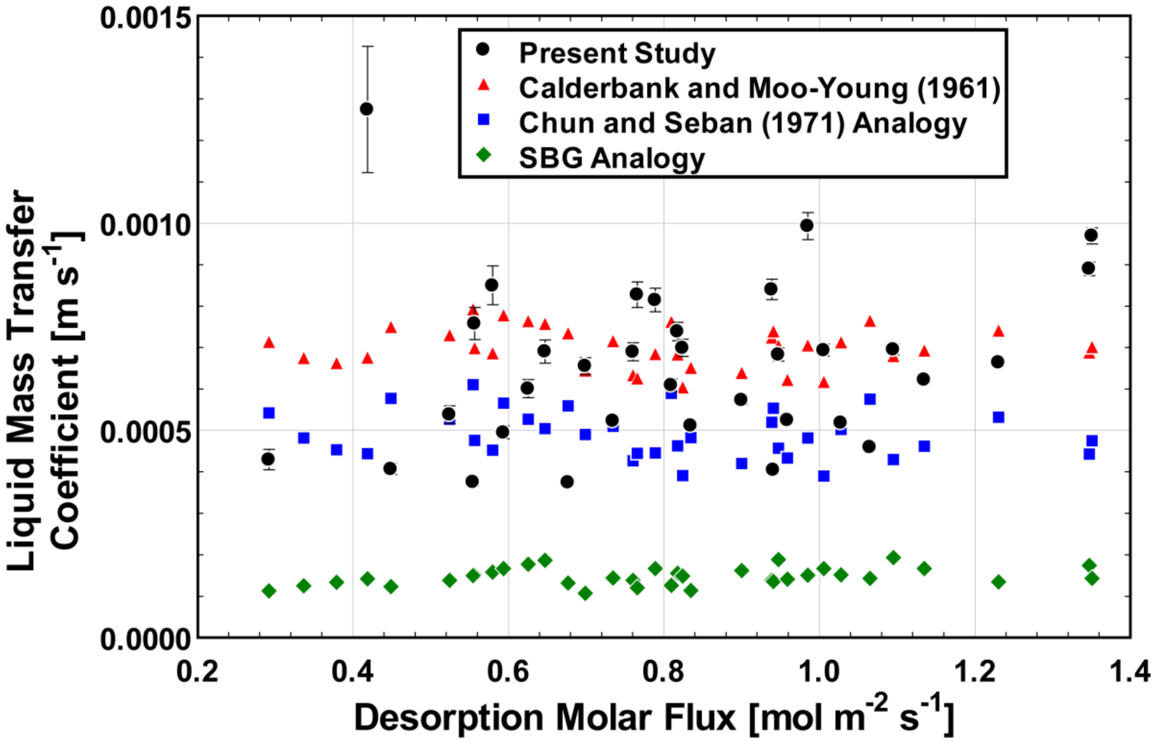

Figure 5.41: Mass transfer coefficients versus molar flux

using the heat and mass transfer analogy applied to the results of the SBG analysis with binary fluid boiling, and vapor heat transfer correlations from Damman (1973) and Nellis and Klein (2009), respectively. The results of the SBG method, applied to a heat and mass transfer analogy, are included as a possible method here to predict the mass transfer coefficients, based on the good agreement achieved in predicting the desorber heat transfer coefficients (Section 5.3.5).

While the correlation of Calderbank and Moo-Young (1961) was developed for larger agitation tanks, sieve and sintered plate columns, which have similarities to the vertical column geometry, were also considered by them.. The correlation is based entirely on fluid properties and an empirical constant, so no geometric parameters are required in the correlation. Therefore it is possible to apply it to any liquid mass exchanger. While they propose several formulations, applicable to various conditions, the formulation given in Eq. 5.18, was found to provide the best agreement with the data of the present study.

To explain the scatter seen in the experimental results, the data are shown as a function of solution mass flow rate per unit transfer area in Figure 5.42. Here the influence of the liquid flow rate is apparent in the experimental values. This is not captured well by the predicted values, leading to some disagreement across the range of conditions considered. However, the predictions obtained from Calderbank and Moo-Young (1961) and the heat transfer analogy using the film evaporation correlation of Chun and Seban (1971) give reasonable estimates of the magnitude of the mass transfer coefficient. The correlation of Calderbank and Moo-Young (1961) is shown in Figure 5.43, and provides the best fit to the data with average deviation and average absolute deviations of 8.7 and 36.5%, respectively. The results from Chun and Seban (1971)

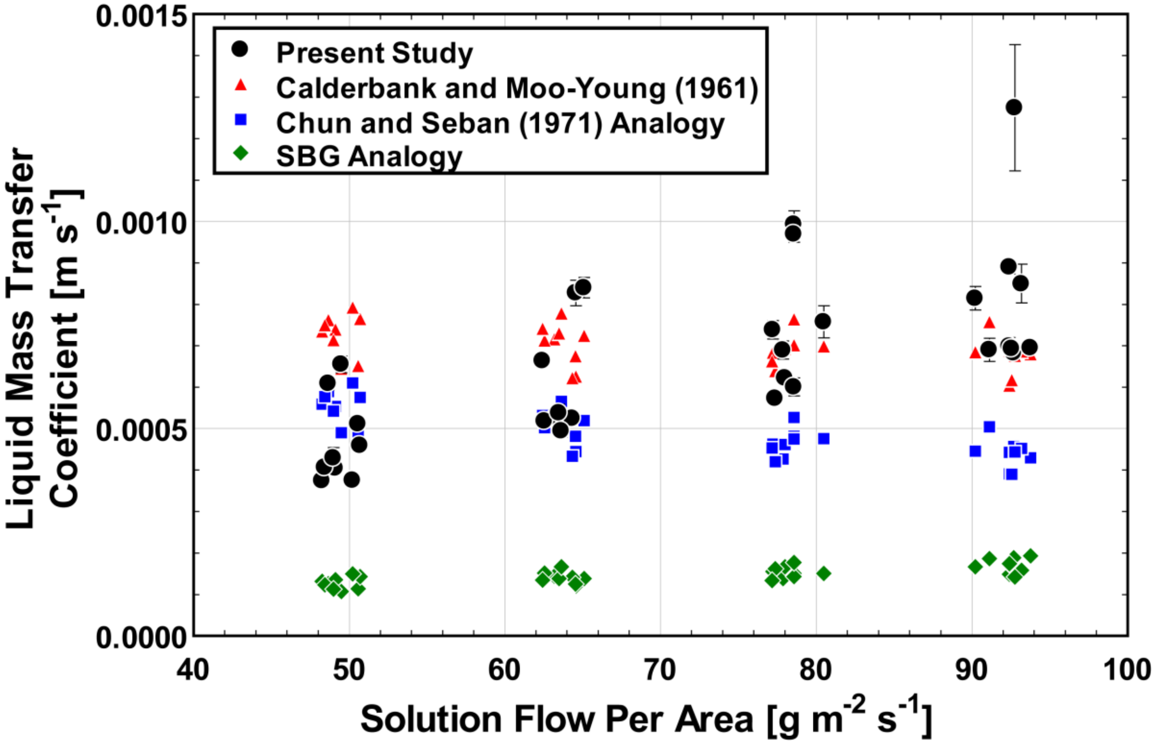

Figure 5.42: Influence of solution flow per area on mass transfer coefficients

under predict the data somewhat, with values of -22.6 and 36.8% for the average deviation and average absolute deviation, respectively.

A comparison of the vapor mass transfer coefficients, including experimental and predicted values, is shown in Figure 5.44. Heat transfer analogies using the vapor heat transfer correlations described previously do not agree well with the experimental results. As such, the packed bed correlation of Onda *et al.* (1968) was considered. The formulation was given in Eq. 5.22. For the vertical column geometry, the characteristic length scale of the packing is taken to be the channel depth. The correlation of Onda *et al.* (1968) matches the data much more closely than the heat transfer analogies; however, agreement is still poor due to scatter in the data. This was discussed above, and is due, in some part, to the difficulty of accurately assessing the vapor concentration within the desorber. By comparing the mass transfer coefficients versus the desorber flooding

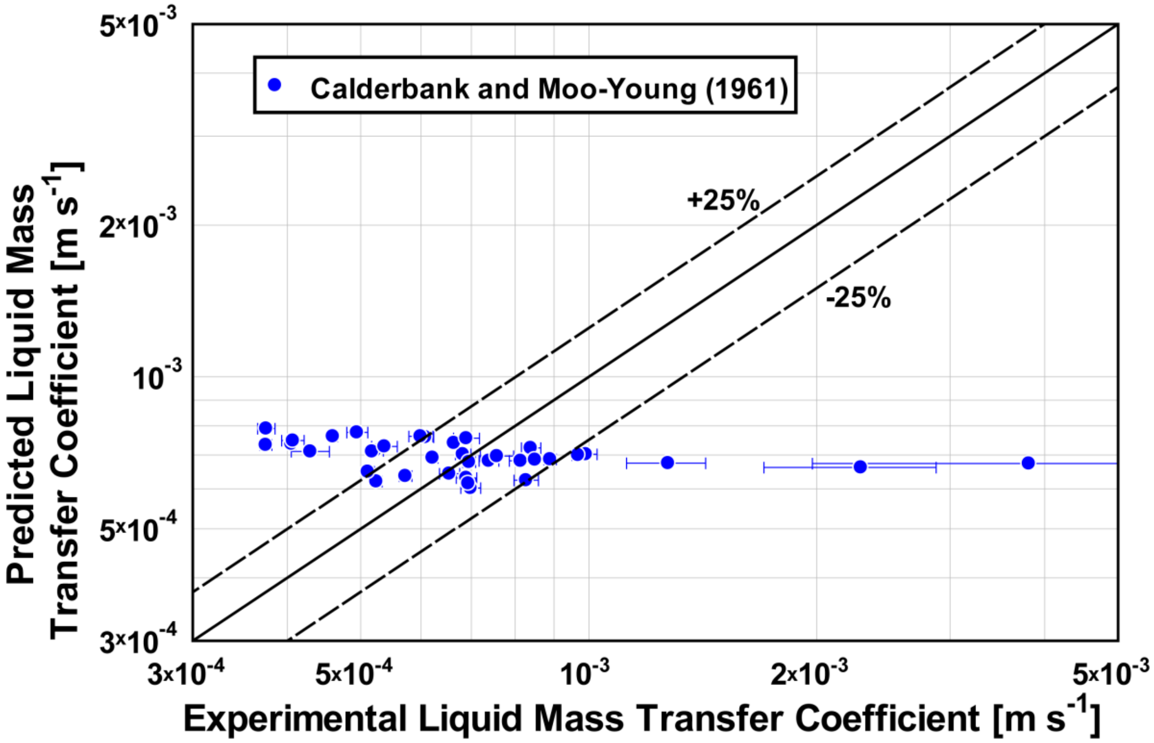

Figure 5.43: Experimental versus predicted mass transfer coefficients

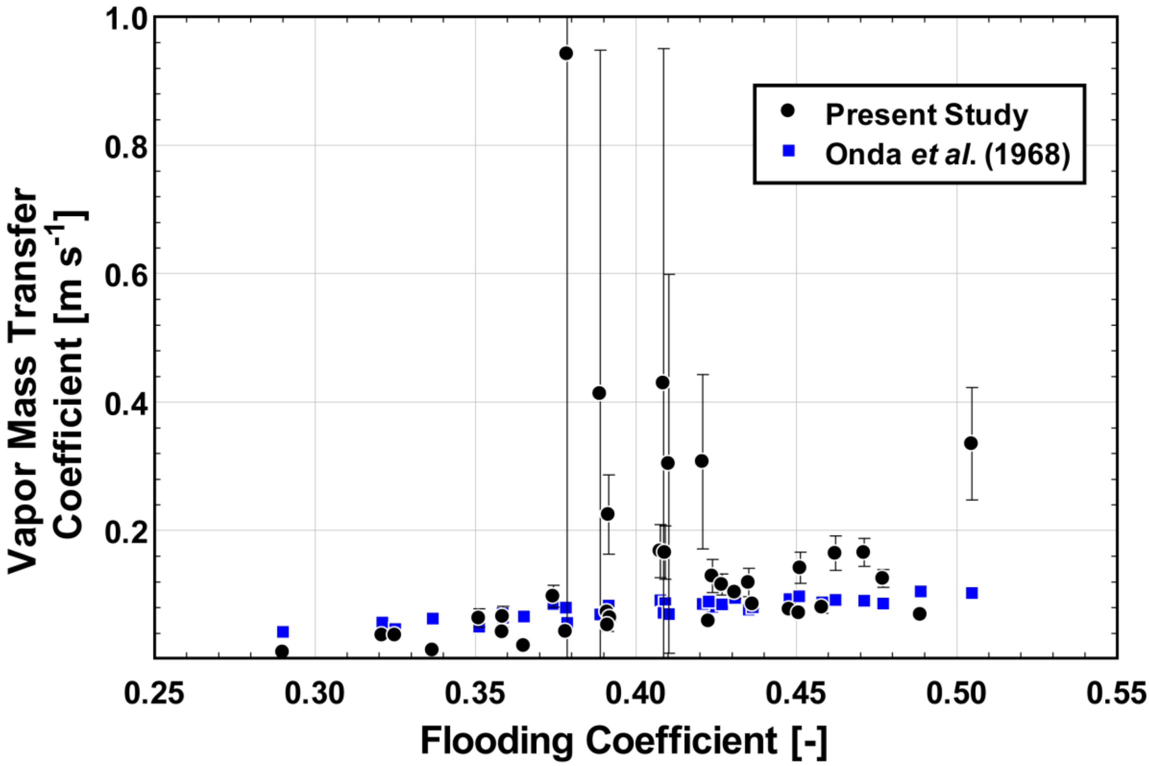

Figure 5.45: Influence of flooding coefficient on mass transfer coefficients

coefficient (Figure 5.45), it can be seen that some of the apparent scatter is associated with an increase in the flooding coefficient. The flooding coefficient is given by Wallis (1969), and is discussed in detail in the following section, but is representative of how close the flow conditions are to the counter-current flow limitation, which is expected to be reached for C = 0.725 for this geometry. As the counter-current flow limitation is approached, the experimental and predicted mass transfer coefficients increase. This is likely due to additional mixing caused by formation of waves at the vapor-liquid interface. Due to the large spread in the experimental results (Figure 5.46), the average and average absolute deviation for the correlation of Onda *et al.* (1968) are 10.5 and 62.5%.

While even the best-fitting correlations examined in the present study do not accurately predict the mass transfer coefficient data across all conditions, the suggested

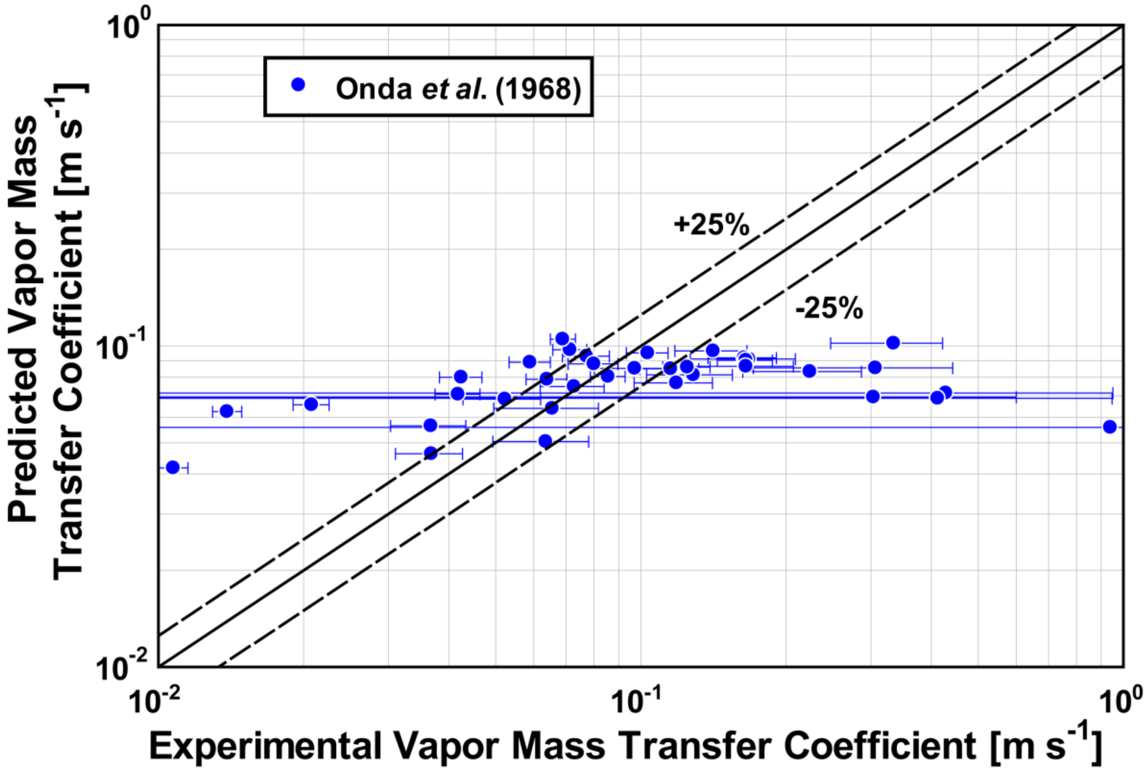

Figure 5.46: Predicted versus experimental mass transfer coefficients

correlations, which are the best-fitting correlations noted in Table 5.4, do provide much better estimates of the magnitude of the mass transfer coefficients, compared to other correlations that were examined. For example, the correlation of Onda *et al.* (1968), which does not agree well with all data points, results in average and average absolute deviation values of 10.5 and 62.5%, when compared to the vertical column vapor-phase mass transfer data, as stated above. However, the predictions of the heat and mass transfer analogy applied to the correlation of Nellis and Klein (2009) result in much higher average and average absolute deviation values of -95.2 and 95.2%. Considering that values predicted by different correlations examined here disagreed by more than an order of magnitude in several cases, the correlations suggested in Table 5.4 likely offer improved accuracy over any correlations that are not specifically tailored for use with similar geometries and conditions.

Much of the disagreement between the experimental and predicted values, particularly in the case of the vertical column vapor mass transfer coefficients, is likely due to the difficulties of measuring representative bulk fluid temperatures of the two phases in the small channels of the VGU. This is compounded by the fact that the vapor-liquid interface is not entirely steady during operation and alternating periods of wetting and dry-out occur in some regions of the test sections where measurements of both phases are desired.

In subsequent revision of the component heat and mass transfer models, the correlations given in Table 5.4 are used, replacing more basic heat and mass transfer analogies.

5.4 Counter-Current Flow Limitation

The counter-current flow or flooding limitation plays a major role in the design and operation of components that make use of gravity driven vapor-liquid counter-flow configurations, such as the test sections discussed in the present study. Generally, higher performance would be expected in these components if the fluid velocities could be increased. This is particularly true in the rectifier, where the condensation process is limited by vapor heat transfer rates. However, as the velocities in either phase increase, momentum exchange between the phases also increases. At the counter-current flow limit, momentum exchange reaches a critical point where the rising vapor phase can begin to entrain liquid, causing flow reversal and, ultimately, flooding in the component. At a system level, this would result in serious operational issues as the low concentration liquid entering the refrigerant-side of the system (condenser, expansion valve and evaporator) and degrading performance significantly.

Under these conditions, rising vapor has entrained some portion of the liquid stream and the vertical sections of the channels could become vapor locked, potentially blocking downward liquid flow. If allowed to continue, liquid inventories increase until the analyzer and rectifier flood completely. Significant hysteresis is observed when attempting to return to normal operational regimes. As such, to recover from a flooding or flow reversal condition, liquid flow rates must be reduced significantly below the normal range of operation to restore counter-flow conditions. Flow reversal and liquid bridging phenomena were typically initiated in the desorber section, but once established, would readily propagate to the analyzer and rectifier. Figure 5.47 shows liquid bridging and flow reversal immediately prior to the onset of flooding in the rectifier, analyzer and desorber sections of the branched tray test section. Images of these phenomena in the vertical column are shown in Figure 5.48.

To avoid this, the branched tray and vertical column test sections were designed with sufficient flow area to avoid flooding under normal operation. The method of Wallis (1969) was used for the design of this component, and the results are interpreted here based on this criterion. Wallis (1969) presents the following general equation to predict flooding in vertical tubes.

$$C = j_v^{*1/2} + m \cdot j_l^{*1/2} \tag{5.23}$$

Here, C is the flooding coefficient, which corresponds to the onset of flooding. The parameters j_v^* and j_l^* are dimensionless groups that relate the momentum fluxes to the hydrostatic forces for the vapor and liquid phases, respectively.

$$j_v^* = j_v \rho_v^{1/2} \left[g D_h \left(\rho_l - \rho_v \right) \right]^{-1/2} \tag{5.24}$$

$$j_l^* = j_l \rho_l^{1/2} \left[g D_h \left(\rho_l - \rho_v \right) \right]^{-1/2} \tag{5.25}$$

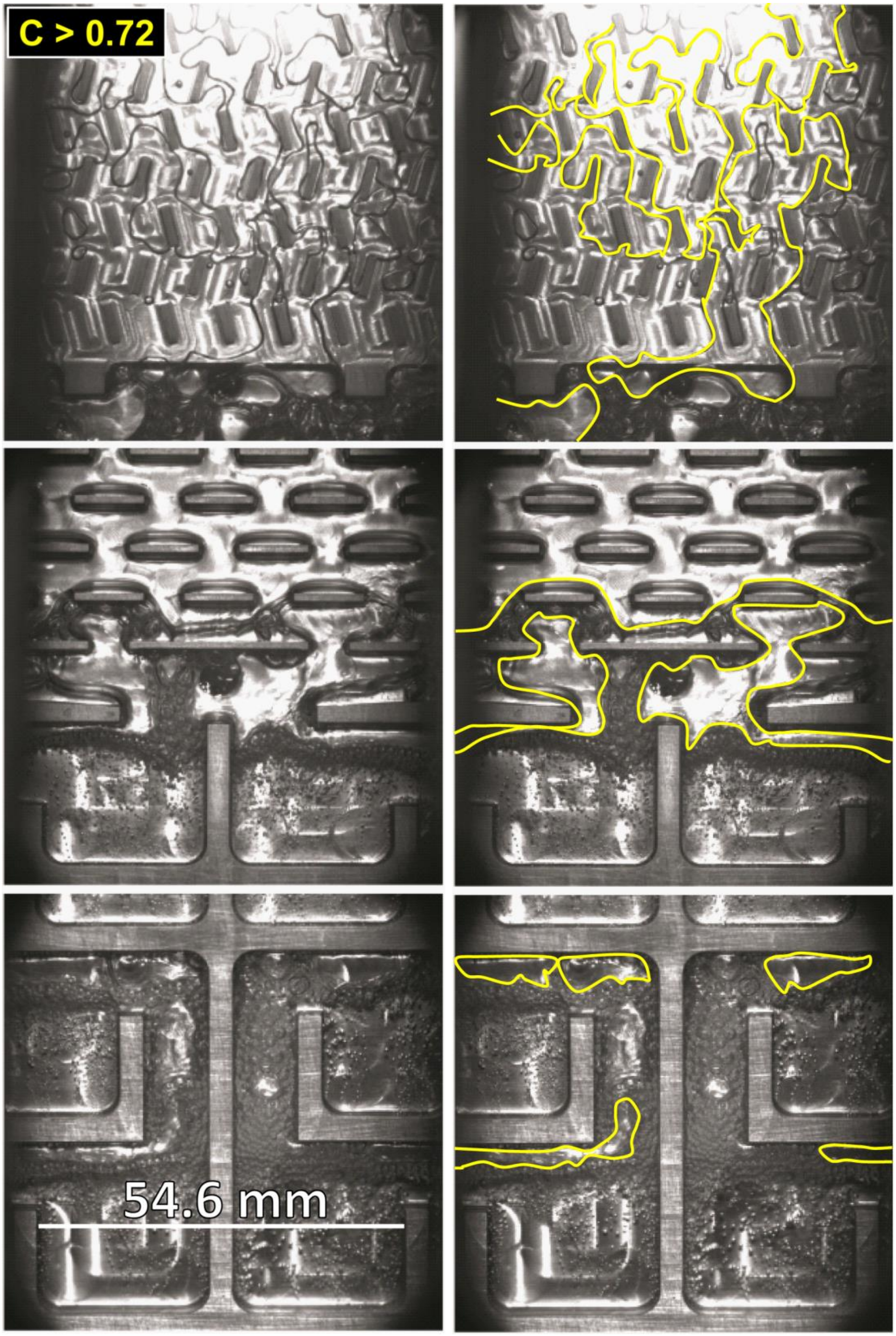

Figure 5.47: Flow reversal in rectifier (top), analyzer (middle), and desorber (bottom) of branched tray; phase boundary highlighted (right)

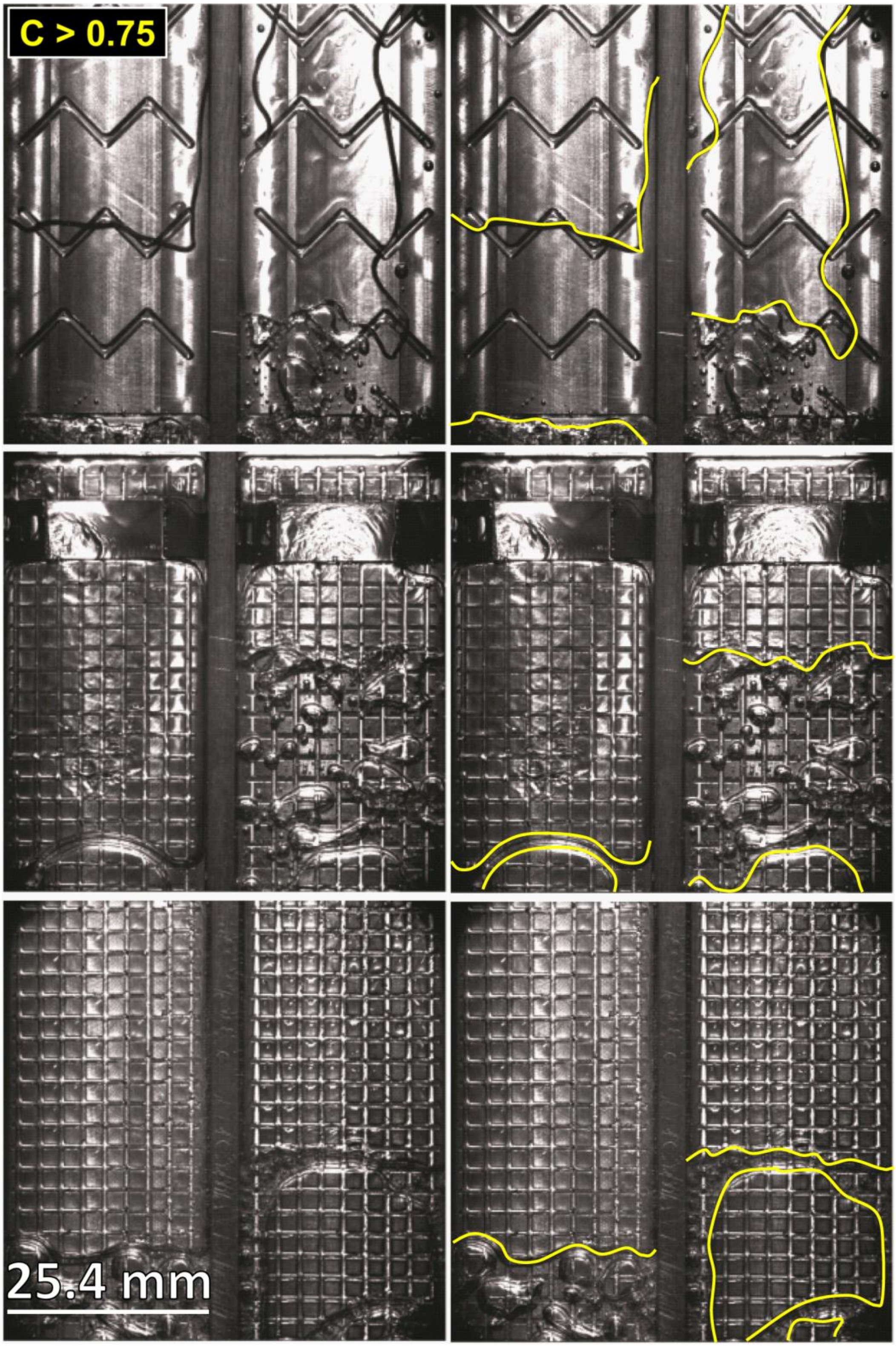

Figure 5.48: Flow reversal in rectifier (top), analyzer (middle), and desorber (bottom) of vertical column; phase boundary highlighted (right)

Here, j_v and j_l are the superficial velocities, or volume fluxes, of the vapor and liquid phases, respectively. In Eq. 5.23, the values of C and m are determined empirically. Wallis (1969) proposed that m be taken to be unity for turbulent flows. For channels with sharp edged entrances, a value of $C = 0.725$ was found to correspond to the onset of flooding. This value of C is considered to be reasonable for the branched tray and vertical column geometries. While the vapor and liquid streams considered in the present study are laminar, alternate values of m for these geometries and fluids are not readily available. Additionally, the narrow passages, surface treatments (vertical column) and changing flow directions (branched tray) are likely to increase momentum exchange between the phases. Therefore, the proposed values of $m = 1$ and $C = 0.725$ are used here. It should be noted from Eqs. 5.23 through 5.25 that, due to the large difference in the densities of the liquid and vapor phases, the flooding coefficient is almost entirely a function of the vapor-phase superficial velocity.

Liquid bridging or flow reversal is expected to occur initially at the regions of the components with the highest vapor velocities and highest flow rates. Therefore, flooding calculations were conducted at the top of the desorber section and bottom of the rectifier section. Therefore, the maximum vapor and liquid flow rates were used to calculate the superficial velocities. The hydraulic diameter used represented a mean passage diameter within the same region of the component (top of the desorber section and bottom of the rectifier section). In these locations the vapor and solution flow rates are at maximum values. Based on the flow rates, and fluid properties determined for the experimental conditions, and using the noted values of m, the flooding coefficient can be calculated for each data point.

Figure 5.49 shows the calculated flooding coefficient for the branched tray and vertical column test sections as a function of the ideal cooling capacity, which is introduced in Section 4.5. The ideal cooling capacity is used here as it gives a practical indication of the useful capacity of the desorber-rectifier. By examining the flooding coefficient as a function of ideal cooling capacity, a maximum capacity can be predicted based on the expected onset of flooding. From Figure 5.49, it can be seen that both desorbers were operating below the predicted counter-current flow limit proposed by Wallis (1969). This is as expected, because flooding was not typically observed at the conditions considered in this study. However, it is apparent that the branched tray test section is operating near the flooding limit at the highest observed capacities. Qualitatively, this matches well with observations of occasional liquid bridging, more

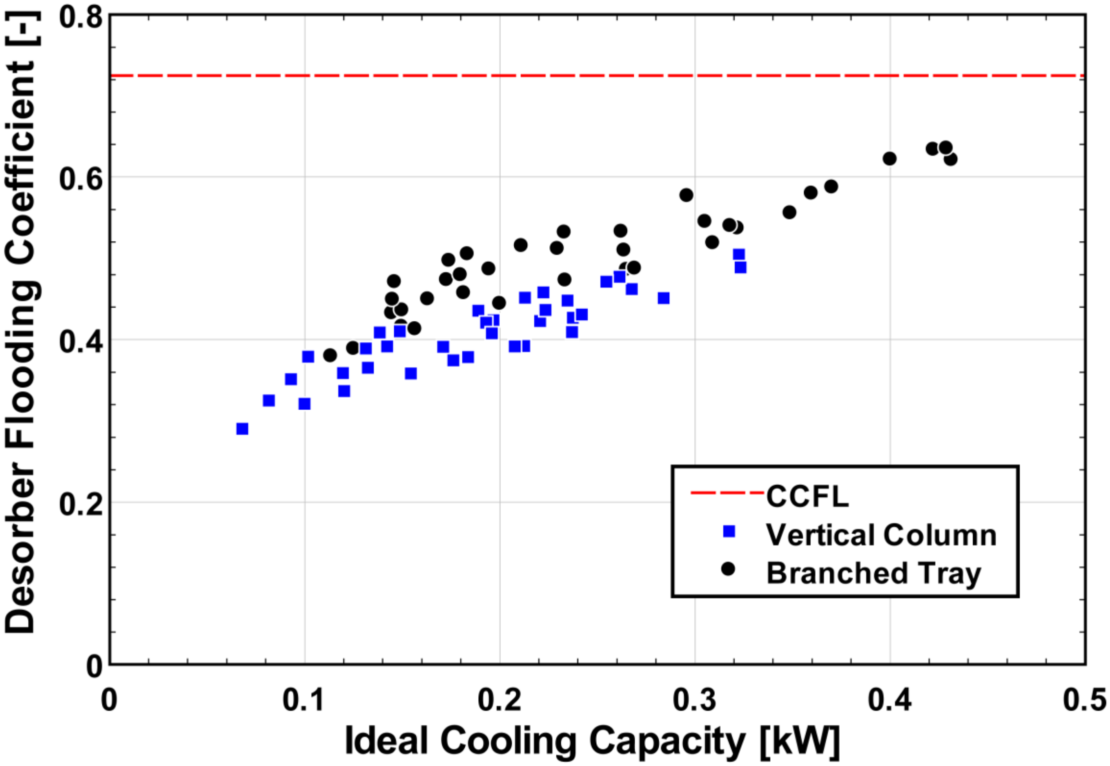

Figure 5.49: Desorber flooding coefficient versus ideal cooling capacity; counter-current flow limit (CCFL) shown

turbulent features, and entrainment of small droplets, which were noted at the conditions with the highest vapor generation rates. Additionally, flooding in the branched tray desorber could be caused by increasing the liquid flow rates slightly beyond the test matrix. In contrast, it was generally difficult to cause the onset of flooding in the vertical column geometry, which was typically found to operate at lower flooding coefficients.

While it is difficult to determine the exact conditions at which flooding occurs, due to the inherent instability of the flow at the onset of flooding, and the complete blockage of the dilute solution flow during complete flooding, values of the limiting flooding coefficient were estimated based on data collected immediately prior to flooding. For the branched tray desorber, sporadic bridging of the vapor passages by liquid slugs was often observed to occur for $C > 0.55$. Full flooding of the desorber leading to nearly complete blockage of dilute solution flow was observed at approximately $C > 0.72$, corresponding well to the predictions of Wallis (1969). If operation were maintained, the analyzer and rectifier were observed to flood rapidly.

Flooding was observed to occur much more suddenly in the case of the vertical column test section. As high as $C = 0.75$ typical operation continued with no indication of liquid bridging or onset of flooding. At approximately $C > 0.75$ the desorber was observed to completely flood, rapidly building up liquid inventory through the desorber analyzer and rectifier sections. Again, this value agrees well with the predictions of Wallis (1969). In both test sections, a hysteresis effect appeared to be present and flooding would continue unless the concentrated solution flow rate were reduced significantly below the values observed immediately prior to flooding. However, a comprehensive study of this phenomenon was not conducted and the exact values required to facilitate a return to normal operation were not quantified. The values of the flooding coefficient reported above were determined for operating conditions (other than the solution flow rates) that were near the baseline case, with desorber coupling-fluid inlet temperatures of 180°C and concentration solution concentrations of approximately 0.475.

The flooding coefficient for the rectifier sections is shown in Figure 5.50. The branched tray rectifier is seen to be operating very close to the flooding limit at the highest capacity conditions. This is beneficial from a heat transfer perspective as the highest possible vapor velocities are achieved. The vertical column test section is operating well below the flooding limit in all cases. This indicates that improvements in performance may be realized by reducing the flow area to achieve higher velocities.

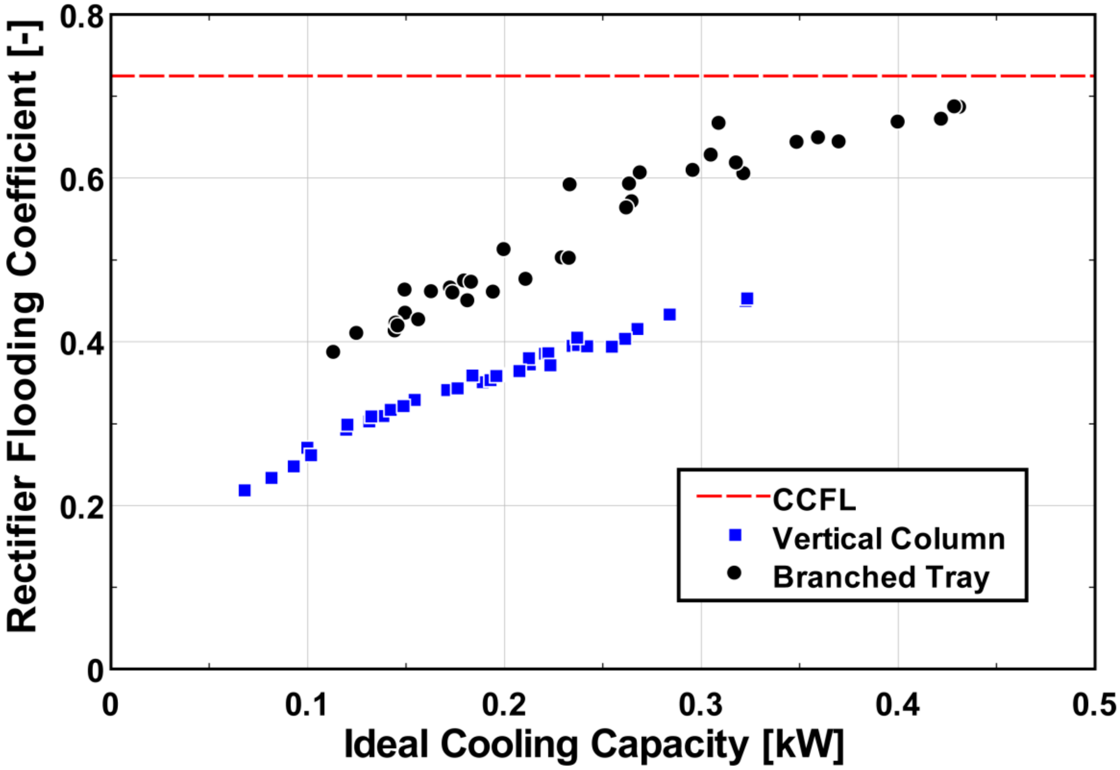

Figure 5.50: Rectifier flooding coefficient versus ideal cooling; counter-current flooding limit (CCFL) shown

Ideally, the rectifier should approach the flooding limit in conjunction with the desorber, so that vapor velocities are maximized in both sections. Examining Figure 5.50, it is notable that the vertical column rectifier is capable of supporting the same capacities as the branched tray rectifier, but at much lower flooding coefficients, giving a larger margin of safety under normal operating conditions.

In Section 5.1, it was reported that shear effects between the vapor and liquid phases could be observed during operation. Flow reversal and flooding result from fluid shear and momentum exchange; however, even at conditions below the onset of large-scale flow reversal, local shear effects are apparent. This phenomenon is shown in detail in Figure 5.51. Figure 5.51 A through E show time sequence images of the top-most pool of the branched tray desorber during operation. The region of the VGU shown in these images is indicated by Figure 5.51 F.

By tracking an individual bubble in the bulk liquid flow and one at the surface of the pool, it is shown that the bulk fluid motion is to the right, as fluid spills over the right-hand edge of the pool and into subsequent lower trays. However, by tracking an individual bubble at the surface of the pool, it is shown that the liquid near the surface has a mean velocity to the left, or in the direction of the bulk vapor flow. This phenomenon is caused by vapor-liquid shear, and was observed at vapor-liquid interfaces during operation, particularly at higher vapor flow rates, when momentum exchange would be greater.

To quantify the velocities of the bulk and interface, the difference in position of the two bubbles can be noted between frames. Figure 5.51 G shows the initial and final location of the bulk and interface bubbles that were tracked in this case. A total of 20

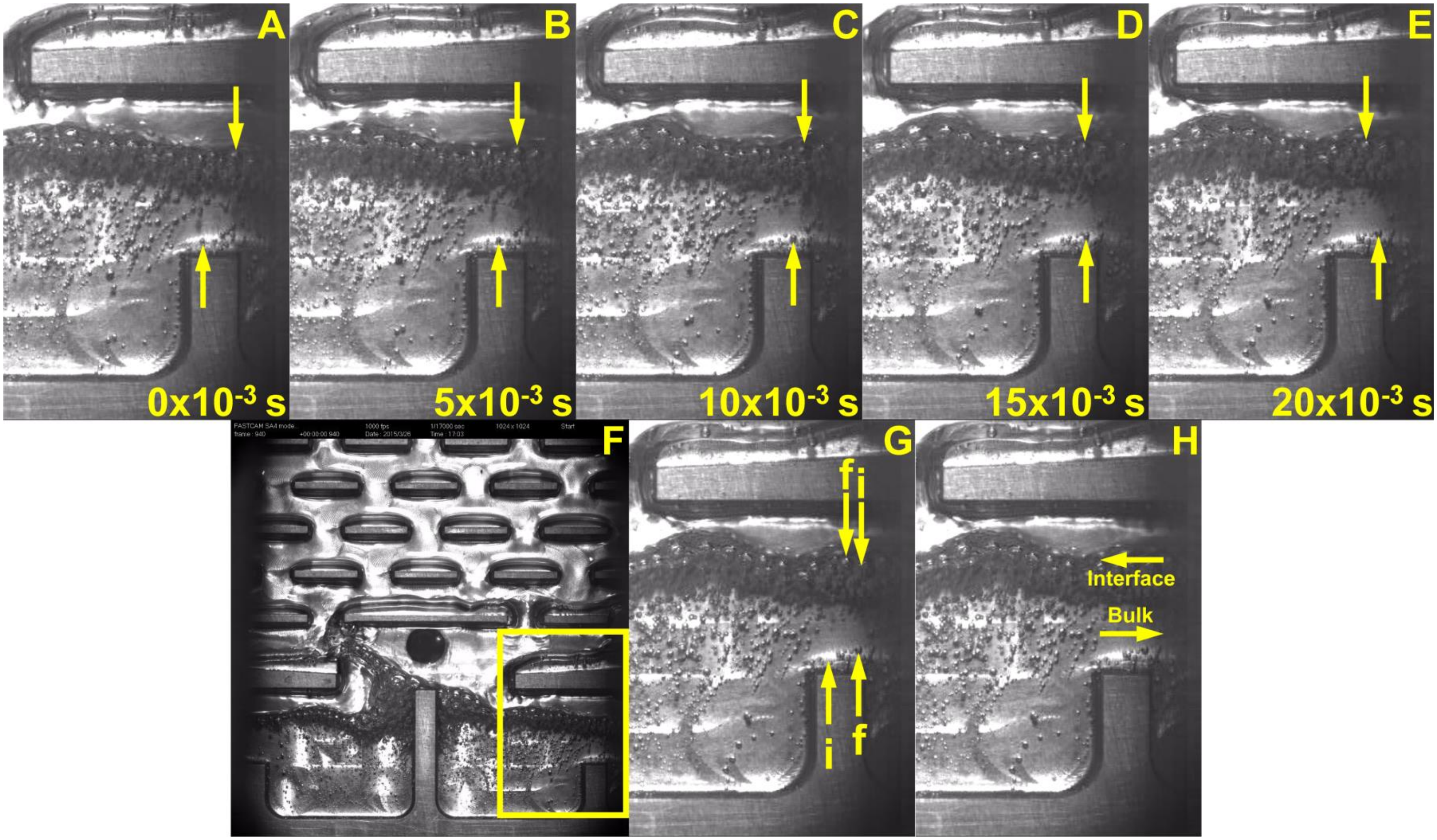

Figure 5.51: Vapor-liquid shear phenomenon

frames elapsed between the initial and final images, corresponding to 0.020 seconds (at 1000 frames collected per second). The horizontal displacement of the bubbles was determined using the known distance between machined features of the pools as a reference. Thus, the horizontal component of the velocities of the bulk and interface bubbles could be determined. For this sequence, the bubble located in the fluid bulk had a mean horizontal velocity of 0.049 m s^{-1}. The bubble on the pool surface had a mean horizontal velocity of -0.024 m s^{-1}. (Here, positive horizontal velocities indicate left to right motion.) Bulk liquid flow to the right and liquid flow at the surface to the left are indicated, as shown by the representative horizontal velocity vectors in Figure 5.51 H.

This image sequence was collected for baseline conditions (Table 3.2), with the exception of the solution flow rate, which was approximately 1.65 g s^{-1}, or approximately 25% higher than the highest condition (1.3 g s^{-1}) specified in the test matrix. The vapor generation rate at these conditions was approximately 0.35 g s^{-1}, which is near the maximum value observed during testing. This sequence is shown here as it more clearly indicates the shear effects due to the high vapor and liquid flow rates. At these conditions, the branched tray VGU is operating near the flooding limit and occasional liquid bridging is observed, as shown in the left side of Figure 5.51 G.

5.5 System-Level Performance

While the focus of this study is on characterizing component-level heat and mass transfer performance of the two novel vapor generation units, the impact of these components on system-level performance is also of interest. To evaluate this, the ideal cooling capacity and ideal COP are defined in Section 4.5. Figure 5.52 shows the ideal cooling capacity for both test sections. It is readily apparent that the branched tray test section produced significantly higher ideal cooling capacities for nearly all conditions. The average ideal cooling capacity across all data points for the branched tray was 246 W. The vertical column produced, on average, a 189 W ideal cooling capacity. This can be explained by examining the desorber heat transfer coefficients shown in Figures 5.9 and 5.10.

Additionally, Figure 5.52 shows a trend of increasing ideal cooling capacity with increasing solution concentration and solution flow rate in the branched tray test section. Increasing solution flow is thought to increase surface wetting in the desorber, leading to improved heat and mass transfer. Higher solution concentrations are expected to increase heat transfer coefficients, as discussed previously. Additionally, an interesting trend is observed with source temperature. For any specified flow rate and solution concentration, points with the highest (190°C) source temperature typically produce the greatest cooling capacity. However, for the highest cooling capacities observed (found for the branched tray with 0.55 solution concentration), performance decreases as the source temperature is raised from 180°C to 190°C. This trend is likely related to the onset of flooding, which is predicted to occur at conditions just above the highest cooling capacities observed (Figure 5.49). This phenomenon is discussed in detail in Section 5.6.

Ideal COP is shown for both test sections in Figure 5.53. While a significant difference in ideal cooling capacity was observed between the two test sections, the difference in ideal COP is much lower. The branched tray achieved an ideal COP of 0.372, on average, compared to 0.364 for the vertical column. This indicates that, while

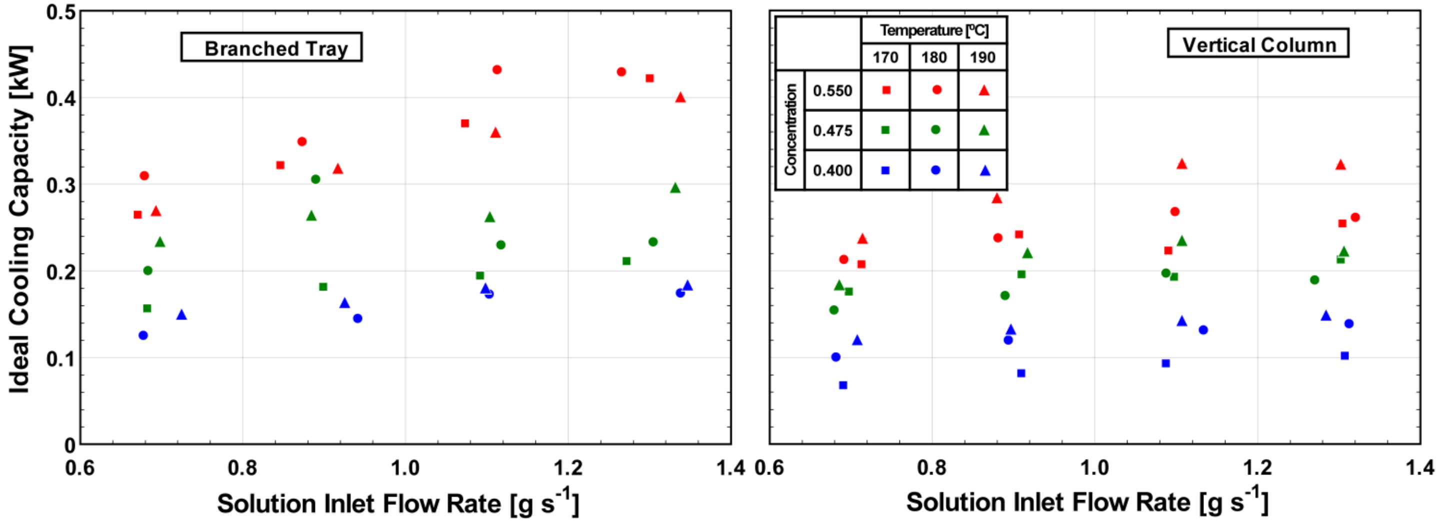

Figure 5.52: Influence of solution flow, concentration, and source temperature on ideal cooling capacity

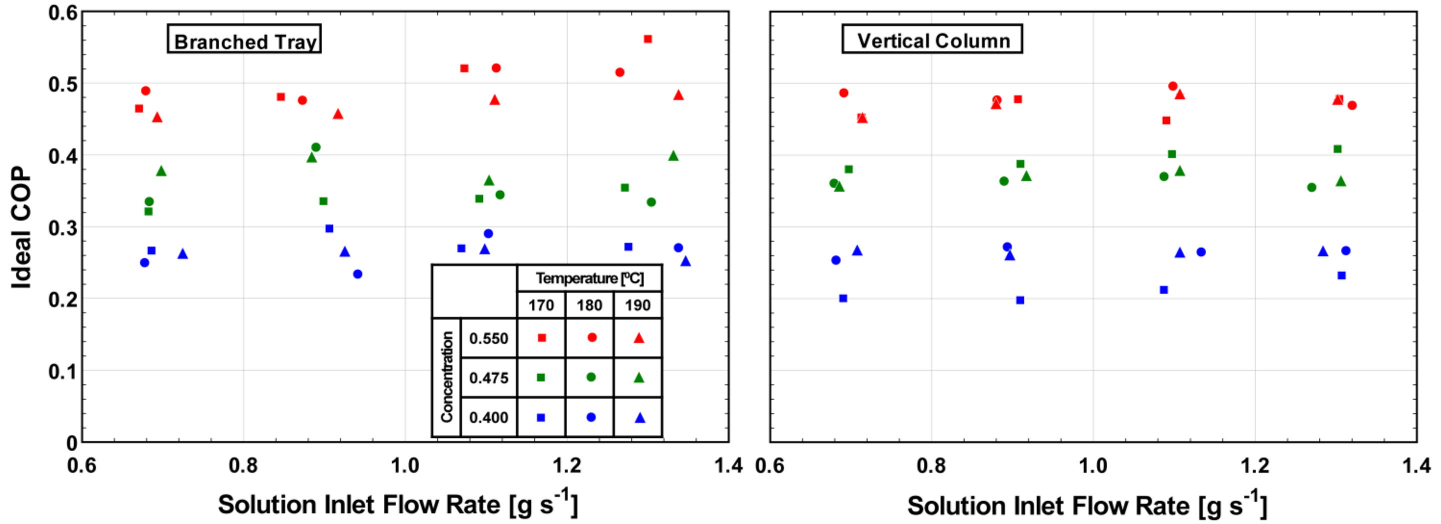

Figure 5.53: Influence of solution flow, concentration, and source temperature on ideal COP

the vertical column unit could not produce the same capacities, this is likely due to inherently lower heat transfer performance and not thermal losses, or excessive sensible heating and/or cooling of the working-fluid steams, which would adversely affect the COP. It is notable that no clear trends in COP with solution flow rate or source temperature are seen. Higher solution concentration does produce higher COPs, which is likely due to a lower sensible heating that would be associated with desorption and rectification of higher concentration fluids.

CHAPTER 6

MODELING RESULTS

Based on the comparison of experimental results and available correlations, which were discussed in detail in Chapter 5, the segmented heat and mass transfer models used to predict the performance of the branched tray and vertical column VGUs were revised. A summary of the correlations used in the models is provided in Table 6.1. The correlations of the original heat and mass transfer models, used to design the VGU test sections, are also provided for comparison. The correlations that were found to give the

Table 6.1: Summary of correlations used in models

		Original Model	**Revised Model**
Branched Tray Desorber Heat Transfer	**Pure Fluid Boiling**	Rohsenow (1952)	Gorenflo (1993)
	Binary Fluid Boiling	Stephan and Körner (1969)	Correlation of present study; modified Schlunder (1982)
	Vapor-to-Liquid	Kays *et al.* (2005)	Schmidt and Newell (1967)
Vertical Column Desorber Heat Transfer	**Film Evaporation/ Boiling**	Chun and Seban (1971)	Damman (1973)
	Vapor-to-Liquid	Kays *et al.* (2005)	Nellis and Klein (2009)
Desorber Mass Transfer	**Vapor Phase**	Heat Transfer Analogy; using Kays *et al.* (2005)	Onda *et al.* (1968)
Branched Tray and Vertical Column Rectifier Heat Transfer	**Condensation**	Chun and Seban (1971)	Rohsenow *et al.* (1956)
	Vapor-to-Interface	Kays *et al.* (2005)	Schmidt and Newell (1967)

best agreement with the experimental results were selected for use in the revised heat and mass transfer models.

In addition to using different heat and mass transfer correlations, several other revisions were made to the models based on the experimental investigation. The heat and mass transfer area definitions were updated to match observations of surface wetting made during the flow visualization study. The revised models use the same heat and mass transfer areas as were employed in the data reduction process (Section 4.3). Additionally, a de-superheating segment has been added to the rectifier heat and mass transfer model. This change was implemented to more accurately account for the required sensible cooling of the vapor stream entering the rectifier. Other than the modifications mentioned above, the structure of the heat and mass transfer models is unchanged from the description given in Section 3.1. Details of the model for a sample segment of the branched tray desorber, including equations and input and output variable values, are provided in Appendix C.

6.1 Comparison of Original and Revised Modeling Results

A comparison of the predicted temperature profiles for the branched tray VGU is given in Figure 6.1 for the original heat and mass transfer model as well as the revised model. These results are shown for the baseline conditions determined from the cycle model, and provided in Section 3.1.2. In Figure 6.1, it can be seen from the heating fluid and solution temperatures that the revised model predicts slightly lower solution heat transfer rates in the desorber. Significantly lower heat transfer rates between the vapor bulk and liquid interface are indicated, as implied by the larger difference between the vapor and liquid temperatures in the desorber and analyzer. The heat transfer rates in the

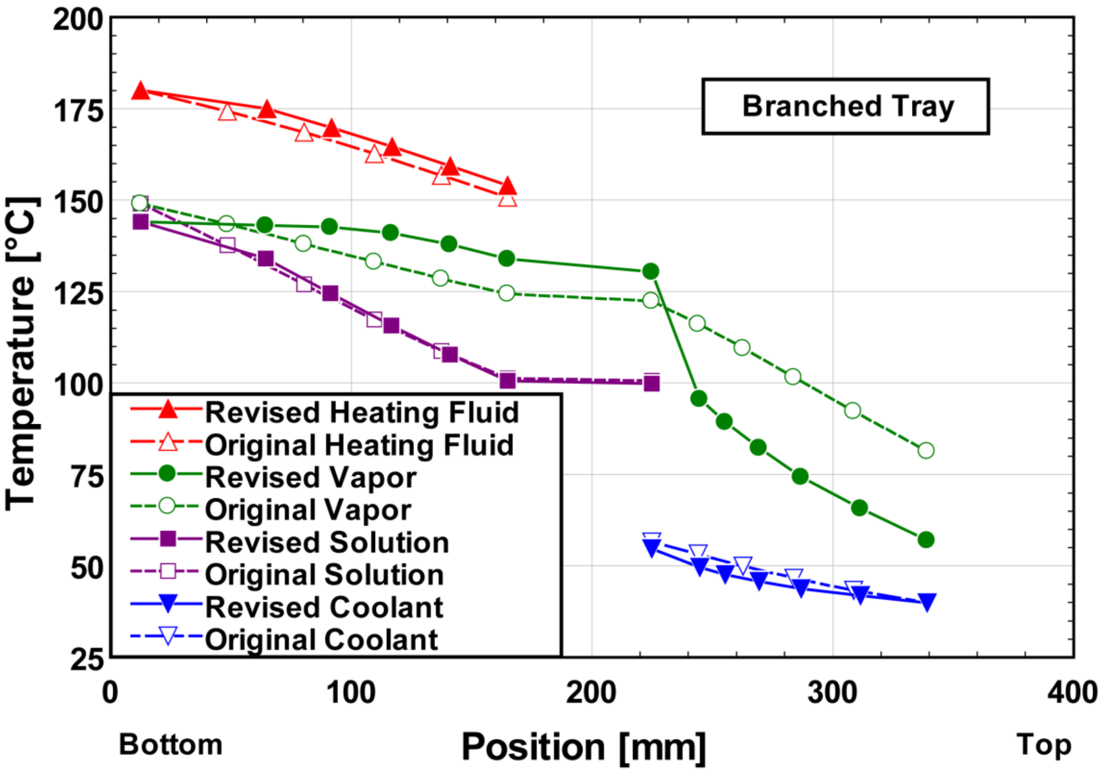

Figure 6.1: Branched tray temperature profiles

rectifier are similar for both cases, as can be seen from the coolant temperatures. However, the rectifier vapor temperature is shown to be significantly lower in the revised models, which is due to higher predicted vapor concentrations throughout the rectifier, resulting in lower saturation temperatures. The revised model predicts a vapor concentration at the rectifier inlet (analyzer outlet) of 0.9808 and a rectifier vapor outlet concentration of 0.9993. The original model predicted a significantly lower rectifier vapor inlet concentration of 0.9341 and an outlet concentration of 0.9921.

A comparison of the vertical column temperature profiles for the original and revised models is shown in Figure 6.2. As was the case for the branched tray, the revised model predicts slightly lower solution heat transfer performance in the desorber, as indicated by the coupling-fluid and desorber solution temperatures. Poorer heat transfer from the vapor bulk to the interface is again predicted, leading to a larger temperature

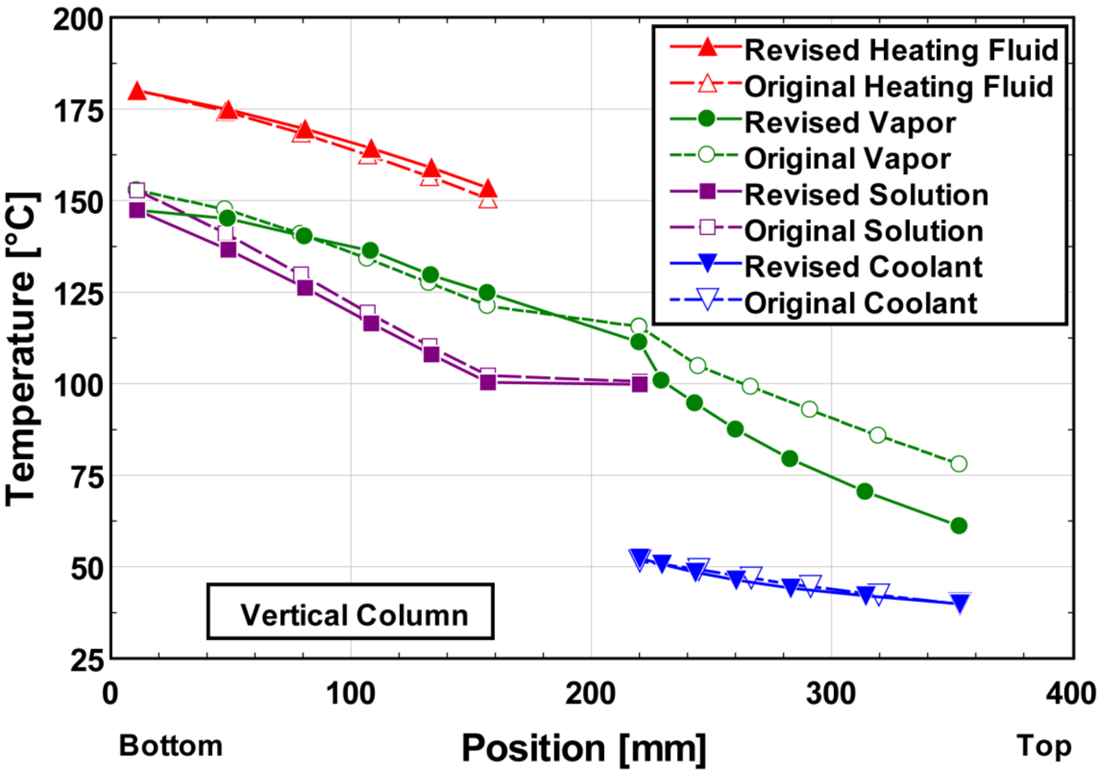

Figure 6.2: Vertical column temperature profiles

difference between the solution and vapor bulk. The rectifier also shows differences between the revised and original model that are similar to those in the branched tray models. The revised model predicts a large initial drop in temperature in the de-superheating segment, and lower temperatures through the rectifier, which is again due to higher vapor concentrations. The rectifier inlet and outlet concentrations for the revised model are 0.9745 and 0.9987, respectively. The original model predicted vapor inlet and outlet concentrations of 0.9646 and 0.9938, respectively. The higher vapor concentrations predicted in the revised model lead to the lower saturation temperatures shown in Figure 6.2.

6.2 *Comparison of Revised Model and Experimental Results*

Results from the revised models, which make use of the heat and mass transfer correlations recommended above, are compared with the experimental results to evaluate whether component-level parameters may be accurately predicted by the models, and to determine whether the correlations proposed above can be applied to accurately model the coupled heat and mass transfer processes within the VGUs. To conduct this comparison, the geometric specifications of the test sections along with fluid inlet properties and operating conditions from the experimental data points are specified as inputs to the models. The major inputs to the models, and component-level outputs from the models, are provided in Table 6.2 for the baseline data point for the branched tray and vertical column VGUs.

Two of the most critical component-level operating parameters for any desorber, or integrated vapor generation unit, are the refrigerant vapor generation rate and the generated refrigerant concentration. The refrigerant generation rate is the vapor flow rate exiting the rectifier. The refrigerant concentration is the mass fraction of the vapor

Table 6.2: Summary of major model inputs and outputs

	Branched Tray	**Vertical Column**
Inputs to Model from Experimental Data (for Baseline Experimental Data Point)		
Concentrated solution flow rate, g s^{-1}	0.890	0.890
Concentrated solution concentration, -	0.4785	0.4721
Concentrated solution temperature, °C	82.8	102.4
Desorber coupling-fluid inlet temperature, °C	179.5	180.4
Desorber coupling-fluid flow rate, g s^{-1}	7.65	7.75
Rectifier coupling-fluid inlet temperature, °C	56.9	63.1
Rectifier coupling-fluid flow rate, g s^{-1}	0.791	0.938
Test section pressure, kPa	1626	2459
Component-Level Model Outputs (at Baseline Experimental Conditions)		
Desorber heat duty, W	635	481
Rectifier heat duty, W	56	49
Vapor outlet flow rate, g s^{-1}	0.298	0.231
Vapor outlet concentration, -	0.9942	0.9957
Ideal cooling capacity, W	318	230
Ideal COP, -	0.501	0.479

stream exiting the rectifier. These two parameters are among the most important factors in determining the cooling capacity that may be achieved by any absorption system. Comparisons of the experimental and predicted refrigerant generation rate, as well as refrigerant concentration, are shown in Figures 6.3 and 6.4, respectively.

From Figure 6.3, it can be seen that the branched tray and vertical column models both capture the trends of the experimental results for the refrigerant generation rate. The branched tray model gives very good agreement with the data, predicting the results with 1.4 and 5.8% average deviation and average absolute deviation, respectively. The vertical column model gives a reasonable estimate of the experimental values, but over predicts the vapor generation rate. Average and average absolute deviation for the vertical column model are both 28.0%. It is notable that, while the experimental vapor generation rates for the branched tray are significantly higher than for the vertical column

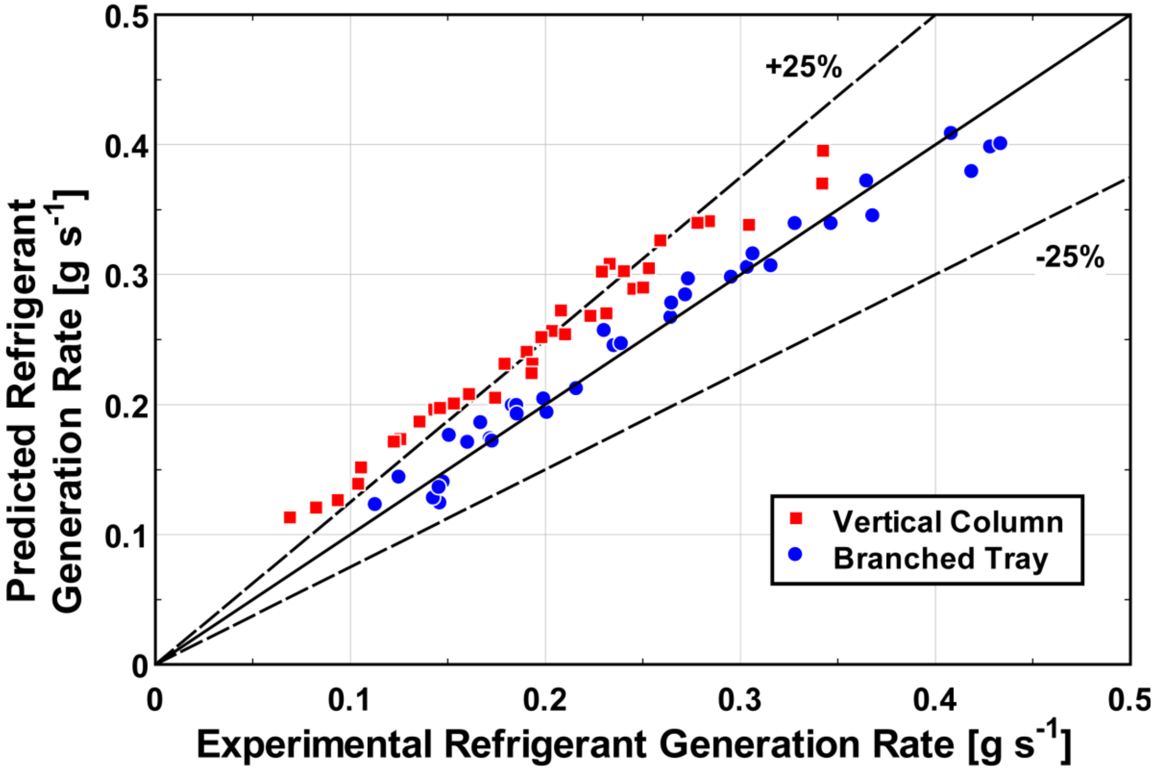

Figure 6.3: Predicted versus experimental refrigerant generation rates

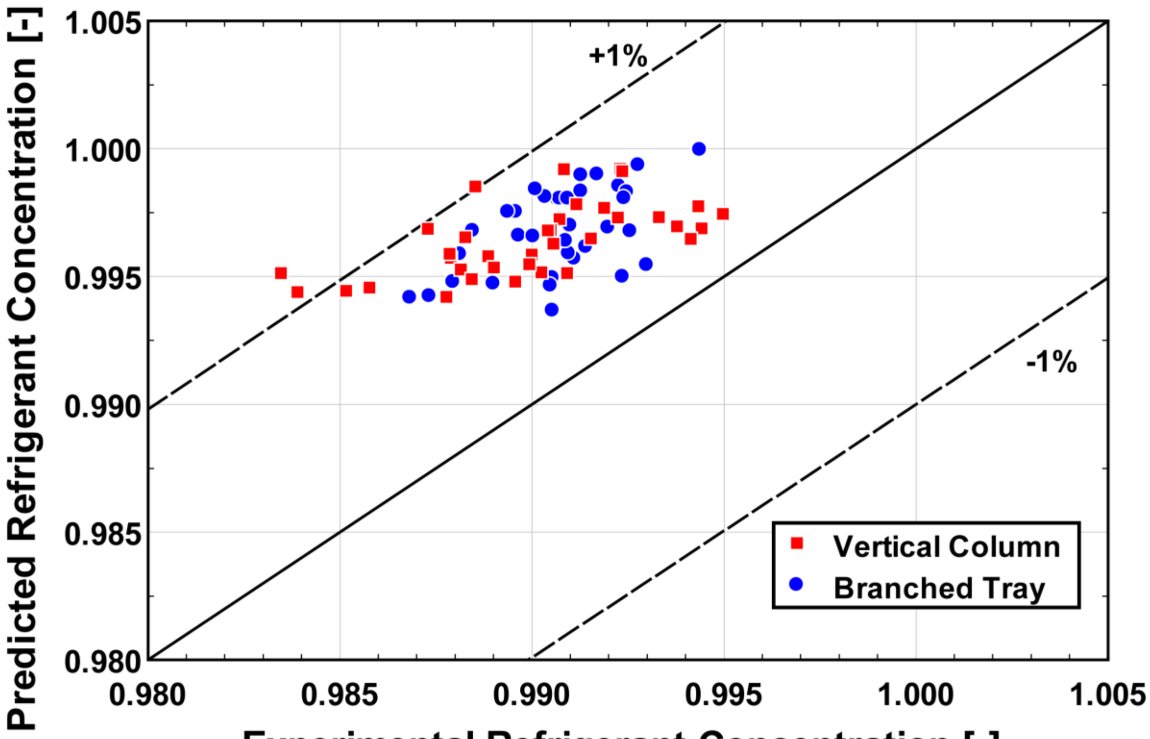

Figure 6.4: Predicted versus experimental refrigerant concentrations

(the branched tray had an average vapor generation rate of 0.248 g s^{-1} across all test points, compared with 0.196 g s^{-1} for the vertical column), the models predict very similar average vapor generation rates for both designs (0.249 and 0.244 g s^{-1} for the branched tray and vertical column, respectively). This may indicate some physical phenomenon that is present in the vertical column test section, but is not accurately captured in the vertical column model (such as possible flow mal-distribution in the desorber coupling-fluid microchannels).

Figure 6.4 shows the predicted and experimental refrigerant concentrations for both test sections. It is difficult to draw any significant conclusions from a comparison of the modeling predictions and experimental results in this case, due to the very narrow range of predicted and experimental values. However, it can be seen that nearly all data are predicted to within 1% error. The average and average absolute deviation are both

0.62% for the branched tray, and 0.65% for the vertical column. The average of the experimental values for the branched tray test section was slightly higher (0.9907) than that of the vertical column (0.9900). The average modeled values were very similar in both cases; 0.9968 for the branched tray, and 0.9964 for the vertical column.

The predicted and experimental rectifier vapor inlet concentrations are compared in Figure 6.5. The models predict the vapor inlet concentration with 4.3 and 3.9% average deviation for the branched tray and vertical column, respectively. The average absolute deviations have the same values. Here, there is significant scatter, likely due to the difficulty of measuring the vapor temperature in the small passages at the rectifier inlet. Additionally, the experimental results are analyzer assuming a saturated vapor, while the models predict that a slightly superheated vapor exists at this location. In all cases, the models over predict the vapor concentration. If the vapor were in fact slightly

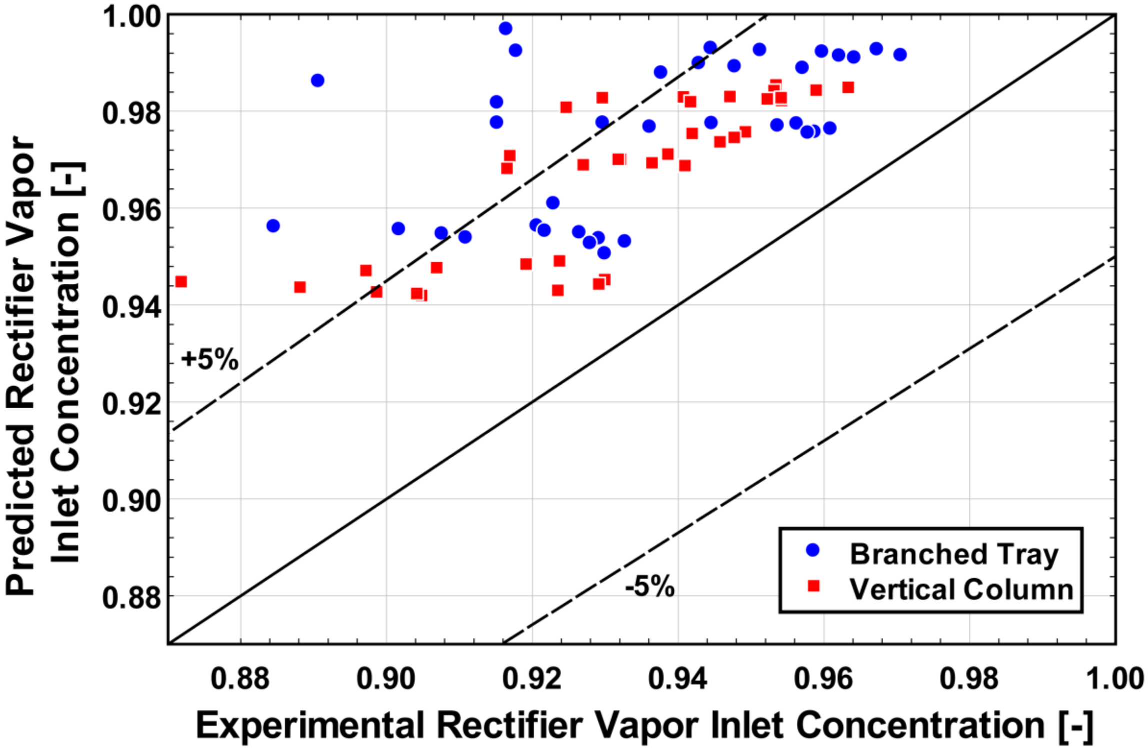

Figure 6.5: Predicted versus experimental rectifier inlet concentrations

superheated during the experiments, the concentration would be higher than predicted by a saturated vapor assumption. On average the two test sections produced similar rectifier inlet concentrations. For the branched tray and vertical column, the average experimental values were 0.935 and 0.931%, respectively. As discussed in Section 4.5, an ideal cooling capacity may be used as an indicator of the cycle-level cooling capacity that may be supported by a given set of refrigerant output conditions produced by the VGU. A comparison of the predicted and experimental ideal cooling capacities is shown in Figure 6.6. The results are very similar to those shown in Figure 6.3 for the refrigerant generation rate. This is expected, as the ideal cooling capacity is highly dependent on the refrigerant generation rate. The average experimental ideal cooling capacities are 246 and 189 W for the branched tray and vertical column, respectively. As discussed for the refrigerant generation rate, the lower performance of the vertical column was not entirely

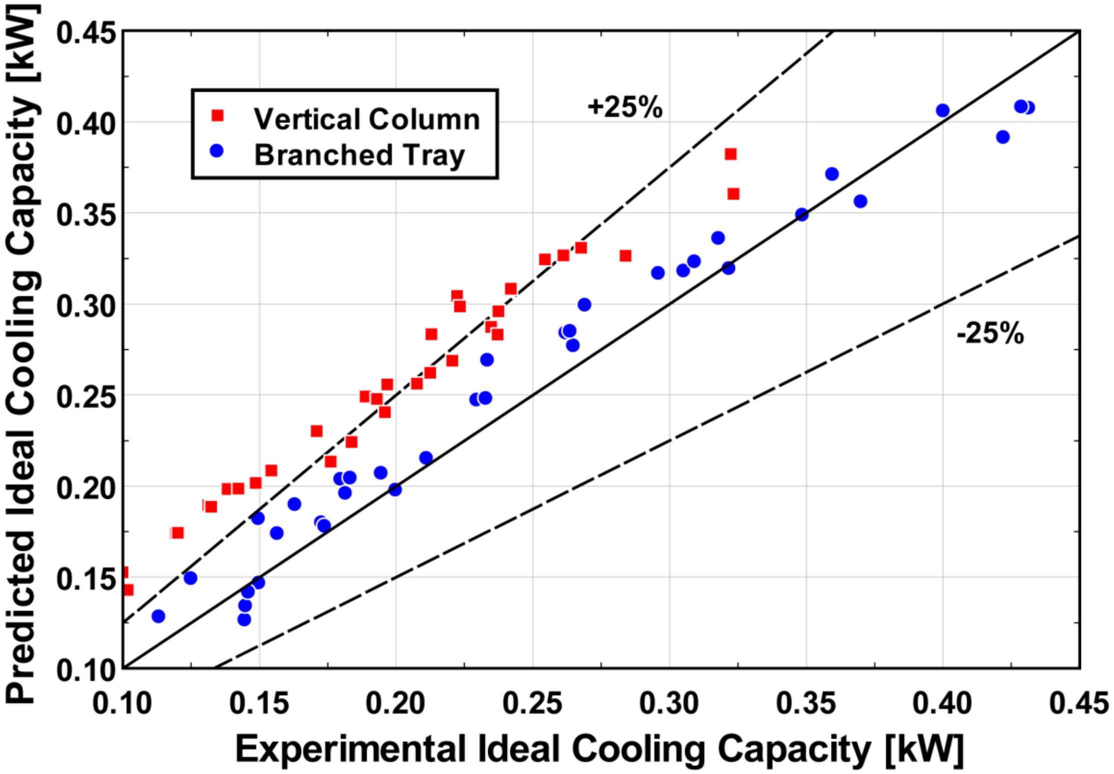

Figure 6.6: Predicted versus experimental ideal cooling capacities

captured by the models and may be due to flow mal-distribution within the vertical column microchannels, which would result in lower desorber duties and lower vapor generation rates. The branched tray average and average absolute deviation were 4.6 and 7.3%, respectively. The vertical column average and average absolute deviation were both 32.5%.

While the refrigerant generation rate, concentration, and ideal cooling capacity are critical component-level parameters, they do not give a complete indication of the performance of the VGUs without consideration of the desorber and rectifier heat duties. The desorber and rectifier heat duties predicted by the heat and mass transfer models are compared with the experimental results in Figures 6.7 and 6.8.

The comparison of the desorber heat duties, shown in Figure 6.7, offers some insight into the lower-than predicted vapor generation rates for the vertical column. The

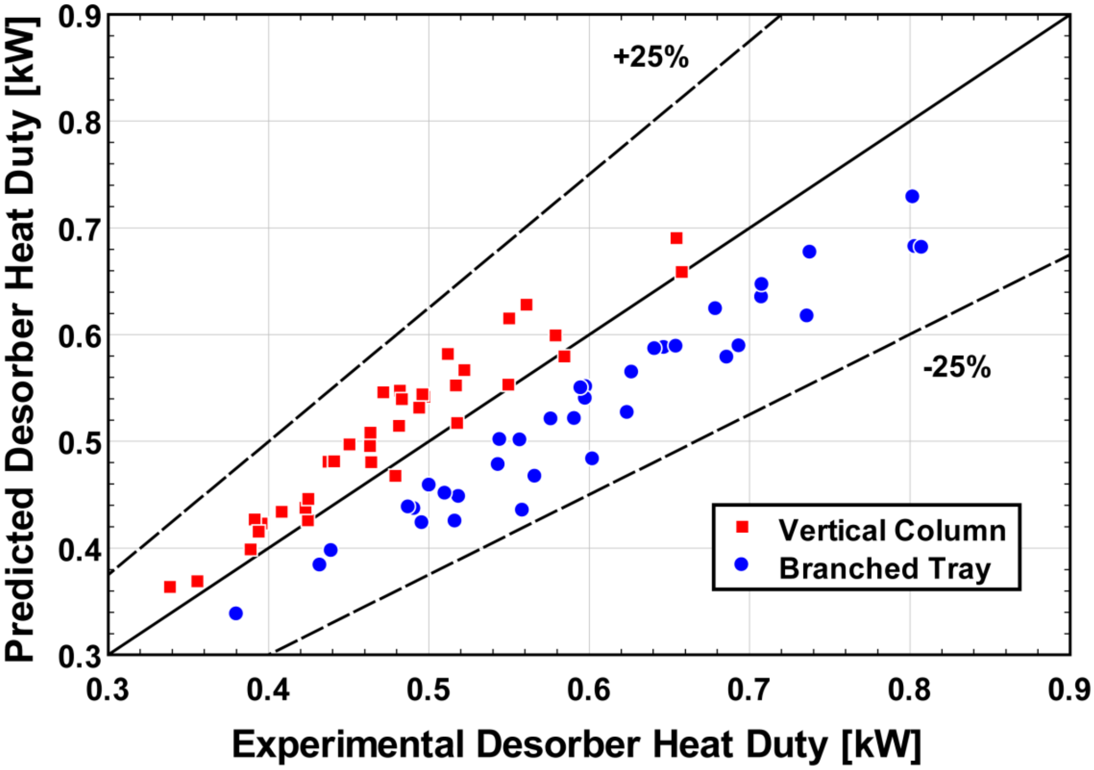

Figure 6.7: Predicted versus experimental desorber heat duties

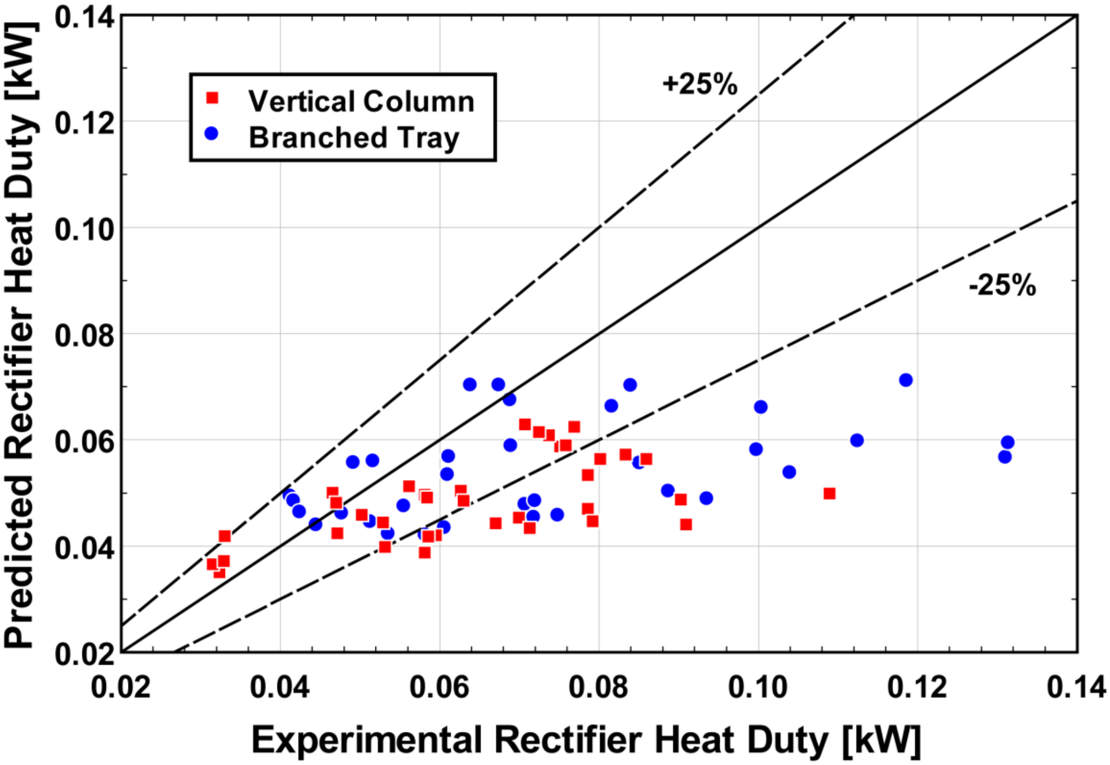

Figure 6.8: Predicted versus experimental rectifier heat duties

experimental heat duty for the vertical column desorber is lower than the predicted values, with average and average absolute deviation of 6.8 and 7.0%, respectively. This indicates that less heat than predicted was transferred to the working fluid from the coupling fluid, ultimately contributing to lower vapor generation rates. The branched tray experimental desorber heat duty, in contrast, is under predicted by the model, with average and average absolute deviation of -11.9 and 11.9%, respectively. While this indicates that the branched tray was capable of transferring more heat than predicted, the refrigerant generation rates were near the predicted values, which indicates good refrigerant generation capacity, but perhaps at a lower than expected efficiency. For most points, the branched tray desorber duty is significantly higher than that of the vertical column. The average experimental heat duties for all points are 602 and 473 W for the branched tray and vertical column, respectively.

Figure 6.8 shows a comparison of the predicted and experimental solution-side rectifier heat duties. Relatively poor agreement is achieved between predictions and experimental results. Values of average and average absolute deviation for the vertical column are -20.4 and 24.6%, respectively, while they are -21.0 and 25.7% for the branched tray. The poor agreement is likely due to the auxiliary heat transfer into the test section from the surrounding gases, as discussed in Section 4.2.4. This is supported by the fact that the models significantly under predict the rectifier heat duty, particularly in cases with high experimental heat duties. The experimental branched tray rectifier duties are generally higher, with an average value of 75.6 W, compared to 64.7 W for the vertical column. This is expected, due to the higher refrigerant generation rates observed for the branched tray design.

Finally, the ideal COP, as defined in Section 4.5, may be compared for the predicted and experimental values. The ideal COP gives one of the most useful indicators of the performance of the VGUs, as it accounts for the ideal cooling capacity, as well as the desorber duty, or driving thermal input required to generate the necessary refrigerant stream. A comparison of the ideal COPs, defined as in Section 4.5, is shown in Figure 6.9. Significant deviation is seen between the model predictions and data, with the models over predicting the ideal COP for all conditions. Values of the average and average absolute deviation are the same, and are 34.2 and 27.9% for the vertical column and branched tray, respectively. The over prediction of the ideal COP is not entirely unexpected, as any auxiliary heat loss from the desorber will decrease the COP significantly. In order to reduce the influence of auxiliary heat loss when comparing the predicted and experimental values, the ideal COP may be calculated using the solution-

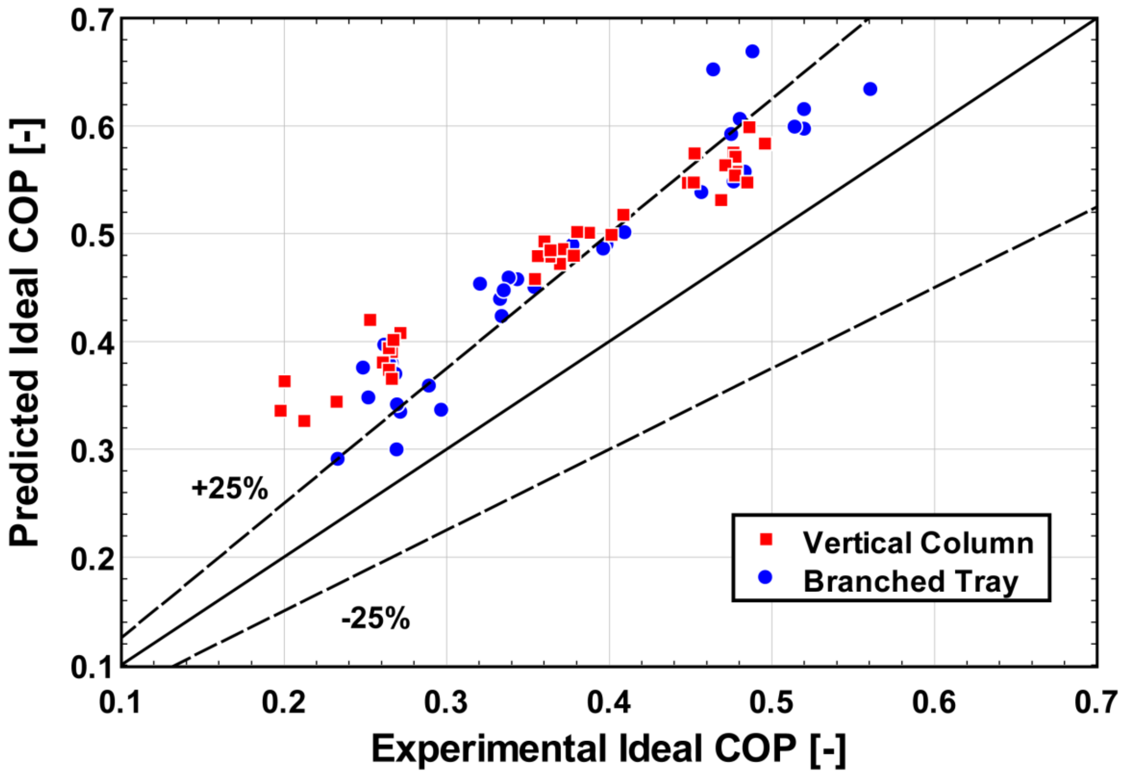

Figure 6.9: Predicted versus experimental ideal COP (calculated using average desorber heat duty)

side desorber heat duty, rather than the average desorber heat duty. Figure 6.10 shows a comparison of predicted and experimental values of the ideal COP calculated using the solution-side desorber heat duty. Agreement is improved significantly, with average and average absolute deviation of -2.9 and 5.1%, respectively, for the vertical column, and -5.4 and 5.4%, respectively, for the branched tray. This indicates that the poor agreement shown in Figure 6.8 is likely due, in large part, to desorber heat loss, and that the ideal COP may be accurately predicted by the models if care is taken to minimize auxiliary heat loss or the heat loss is accounted for in cycle- or component-level modeling.

To provide additional insights on the relative importance of the heat and mass transfer coefficients in determining VGU performance at the component level, a sensitivity study was conducted using the uncertainty propagation tools in *Engineering*

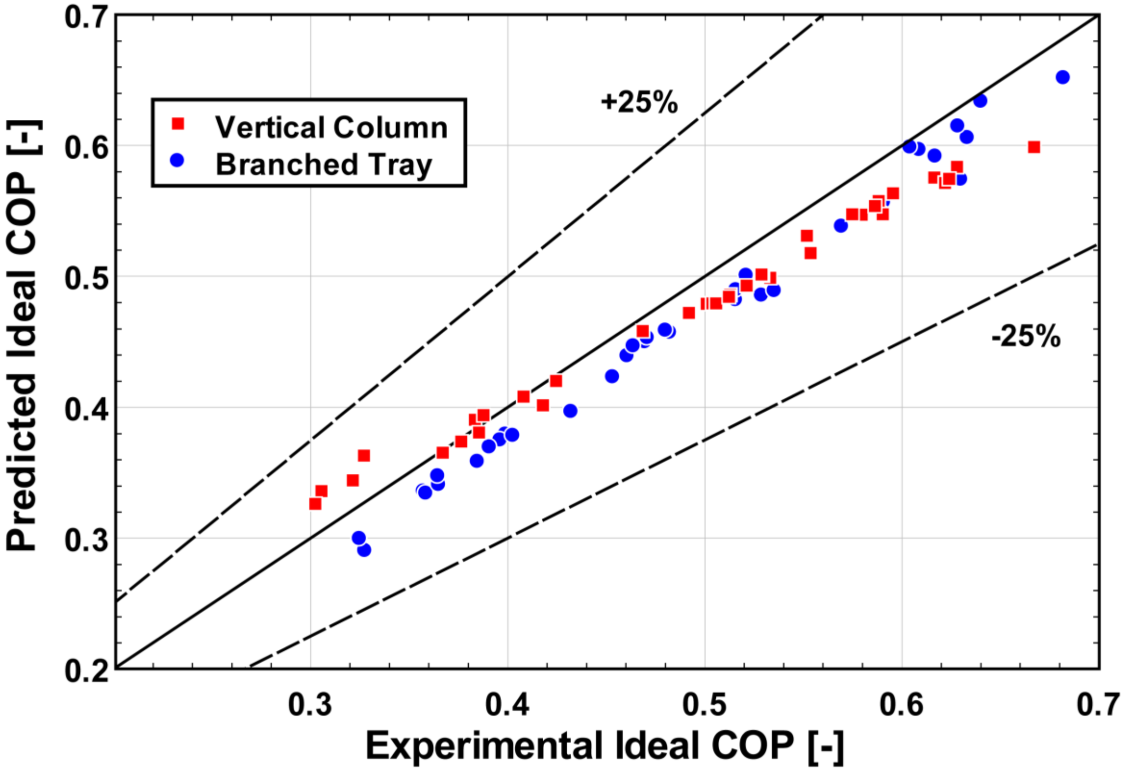

Figure 6.10: Predicted versus experimental ideal COP (calculated using solution-side desorber heat duty)

Equation Solver (Klein, 2011). Using the revised models with the baseline experimental conditions as inputs, the values of the various heat and mass transfer coefficients used in the models (Table 6.3) were varied simultaneously. The resulting changes in the ideal COP and ideal cooling capacity were determined and the contribution to the resulting change attributable to each of the heat and mass transfer coefficients was calculated. The percent of the total resulting change that is attributable to each of the heat and mass transfer coefficients is provided in Table 6.3. From this analysis, it becomes clear that these component-level performance parameters are most sensitive to the desorber heat transfer coefficients. Thus, 91.5% of the change in the ideal COP and 81.2% of the change in the ideal cooling capacity is attributable to the influence of the desorber heat transfer coefficient, which was well-predicted by the correlations used in the revised

Table 6.3: Sensitivity of performance parameters to heat and mass transfer coefficients

		Change in Ideal COP	Change in Ideal Cooling Capacity
Attributed to:	$\alpha_{des,l}$	91.5%	81.2%
	$\beta_{des,v}$	7.1%	16.6%
	$\alpha_{rect,v}$	0.9%	2.2%
	$\alpha_{des,v}$	0.5%	0.1%
	$\alpha_{rect,l}$	0.0%	0.0%
	Total	100.0%	100.0%

models. This explains why component-level parameters predicted by the model can achieve good agreement with the present data, despite relatively poor agreement of the mass transfer and rectifier heat transfer correlations with the data. Additionally, this provides some insight into potential areas of improvement for this modeling approach, with the most appreciable increases in modeling accuracy likely to result from improved desorber heat transfer correlations and desorber vapor mass transfer correlations, the first and second most significant parameters in the sensitivity study, respectively.

Based on the comparison of the modeled and experimental results, the heat and mass transfer models described here should be adequate for most VGU design studies utilizing similar geometries and operating conditions. Additionally, the models can be used in future work to optimize the present VGU designs, by considering changes in the aspect ratio and diameter of fluid passages, thickness of the walls and ribs, and the overall VGU aspect ratio (height versus width), which influence the temperature and concentration profiles within the component.

A summary of the major component-level parameters discussed above is provided in Table 6.4. A summary of the baseline values was provided previously in Table 6.2. Generally, the heat and mass transfer models provide reasonable agreement with the major component-level parameters that would be of primary concern in the design of subsequent VGUs. Very good agreement was achieved with the data for solution-based ideal COPs, perhaps the most important parameter for VGUs. Additionally, predicted desorber heat duties, ideal cooling capacities, refrigerant concentrations, and refrigerant generation rates were all predicted with reasonable accuracy, although improvements could be made to the vertical column model, which tended to over predict the vapor generation rate. Rectifier heat duties were not predicted with satisfactory accuracy, although this is likely due to auxiliary heat gain in the rectifier.

Table 6.4: Component-level experimental results with model deviation

	Branched Tray					Vertical Column				
Parameter	**Average of Data**	**Maximum of Data**	**Minimum of Data**	**Average Deviation [%]**	**Average Absolute Deviation [%]**	**Average of Data**	**Maximum of Data**	**Minimum of Data**	**Average Deviation [%]**	**Average Absolute Deviation [%]**
Vapor outlet flow rate, g s^{-1}	0.248	0.434	0.113	1.4	5.89	0.196	0.342	0.069	28.0	28.0
Vapor outlet concentration, -	0.9907	0.9944	0.9868	0.62	0.62	0.9900	0.9950	0.9835	0.65	0.65
Ideal cooling capacity, W	246	432	113	4.6	7.3	189	323	68	32.5	32.5
Desorber heat duty, W	602	808	380	-11.9	11.9	473	658	289	6.8	7.0
Rectifier heat duty, W	75.6	136.4	41.2	-21.0	25.7	64.7	108.9	31.5	-20.4	24.6
Ideal COP, -	0.372	0.561	0.233	27.9	27.9	0.364	0.496	0.198	34.2	34.2
Ideal COP (solution-side), -	0.497	0.702	0.325	-5.4	5.4	0.494	0.667	0.302	-2.9	5.1

CHAPTER 7

CONCLUSIONS AND RECOMMENDATIONS

7.1 Conclusions

A comprehensive investigation of two novel vapor generation units, for use in small-scale ammonia-water absorption systems, was conducted. Two compact, counter-flow vapor generation units, featuring integrated desorber, analyzer, and rectifier sections, and making use of microscale features, were conceptualized. Segmented heat and mass transfer models were developed based on available correlations and modeling methodologies and were used in the design of branched tray and vertical column VGU test sections. An experimental facility was designed and constructed to conduct flow visualization and heat and mass transfer experiments at conditions that are representative of typical operating ranges of ammonia-water absorption chillers. Using this facility, the performance of the VGU test sections was evaluated across a range of concentrated solution concentrations (0.400 – 0.550), desorber coupling-fluid inlet temperatures (170 – 190°C), and concentrated solution flow rates (0.70 – 1.3 g s^{-1}). Flow rates in this range correspond to desorber liquid Reynolds numbers of approximately 175 to 410 for the branched tray design, and desorber film Reynolds numbers of approximately 90 to 215 for the vertical column. Pressures observed within the VGU test sections ranged from approximately 1620 to 2840 kPa during testing. Additionally, high-speed video and images were used to gain insights into the hydrodynamic phenomena and heat transfer mechanisms in these VGUs during the desorption and rectification processes.

Prior to the present study, the knowledge of the internal operation of the branched tray and vertical column VGU test sections was almost entirely based on unverified assumptions of the flow patterns and heat transfer mechanisms. Use of the high-speed flow visualization images and video was essential in determining the applicable heat transfer mechanisms, degree of mixing and wall-wetting, and flooding limits within the VGUs during operation at realistic conditions. These, mostly qualitative, observations allowed the data to be analyzed using the appropriate idealizations, and for the present data to be compared with results and correlations in the literature that were developed for the same conditions and used to describe the same heat transfer mechanisms and flow phenomena.

Data were analyzed to determine the boiling/evaporation (desorber) and condensation (rectifier) heat transfer coefficients, and to determine values of the desorber liquid and vapor mass transfer coefficients. Results were compared between the two test sections and with results from the limited number of similar studies in the literature. Additionally, existing heat and mass transfer correlations and modeling methods were discussed and compared with experimental values from the present study.

Experimental heat transfer coefficients, determined for the pool-boiling desorption of the branched tray VGU, were found to range from approximately 1860 to 11690 W m^{-2} K^{-1}. No available correlation was capable of capturing the trends in these data across the range of experimental conditions, due to the high influence of inter-phase surface and flow phenomena that are not typically considered in boiling correlations. Therefore, a new correlation was proposed, based on a modified formulation of the binary fluid mixture boiling correlation of Schlunder (1982). The pure component heat transfer coefficients required for the binary correlation were determined using the correlations of Gorenflo (1993). The proposed correlation includes additional terms that account for the vapor-liquid interaction that occurs within the branched tray geometry, and which is not captured in available pool-boiling correlations that focus exclusively on the local boiling process within the liquid bulk and are often developed for simple or ideal geometries with large quiescent pools and little or no bulk fluid motion caused by influences other than buoyancy forces. Therefore, the proposed correlation is limited in applicability to cases in similar geometries at similar conditions and which exhibit the combined vapor flow and pool-boiling phenomenon described in this study. The proposed correlation provides good agreement with the data, achieving average and average absolute deviations of -5.2 and 16.1%, respectively, across the range of conditions tested.

The experimental heat transfer coefficients, determined for the falling-film evaporation/boiling desorption process in the vertical column VGU, were found to range from approximately 1290 to 4310 W m^{-2} K^{-1}. The SBG method (Silver, 1947; Bell and Ghaly, 1972) was used to compare available pure-component correlations with the experimental results. The film evaporation correlation of Damman (1973) and vapor heat transfer correlation of Nellis and Klein (2009), when used with the SBG method, were found to provide good agreement with the data, achieving average and average absolute deviations of -1.3 and 17.5%, respectively, across the range of conditions tested.

Rectifier condensation heat transfer coefficients for both VGU designs were best predicted by the condensation correlation of Rohsenow *et al.* (1956) and vapor heat transfer coefficient of Schmidt and Newell (1967) when applied using the SBG method.

Agreement was poor at low vapor Reynolds numbers. The average and absolute average deviations were 18.2 and 39.3%, respectively, for the branched tray, and were 16.6 and 32.9%, respectively, for the vertical column.

Experimental liquid and vapor mass transfer coefficients, determined for the desorber sections, were also compared with available correlations. In the case of the branched tray VGU, the liquid mass transfer coefficient data were best predicted by a heat transfer analogy applied to the binary fluid mixture boiling correlation developed in the present study. This method results in average and average absolute deviation of -4.7 and 48.2%, respectively, for all data points. Best agreement with the vertical column liquid mass transfer coefficient data was achieved by the correlation of Calderbank and Moo-Young (1961), which resulted in average and average absolute deviations of 8.7 and 36.5%, respectively. The vapor mass transfer coefficients were best predicted by the correlation of Onda *et al.* (1968), for both VGUs. The average and average absolute deviation for the branched tray were -0.3 and 45.7%, respectively, and 10.5 and 62.5%, respectively, for the vertical column.

Of the correlations considered, those with the best agreement with the data were used to revise the preliminary heat and mass transfer models used for the design of the test sections. These revised models were used to predict the component-level experimental results, such as refrigerant generation rates, refrigerant concentration, desorber and rectifier heat duties, ideal cooling capacity, and ideal COP. The novel VGUs were shown to achieve experimental ideal cooling capacities as high as 432 and 323 W for the branched tray and vertical column, respectively. Ideal COPs of 0.561 and 0.496 were achieved for the branched tray and vertical column, respectively. The revised models were found to adequately predict component-level performance and may be used in the design of future compact VGUs with similar geometries and operating conditions.

Considering the modeling methods, the revised models indicate that the use of the Colburn and Drew (1937) method in the modeling of the coupled heat and mass transfer process of the desorber sections provides a good estimate of performance, and that the SBG method may be used to predict rectifier performance with enough accuracy to determine component-level parameters. Using these methods the models were able to predict refrigerant generation rates, refrigerant concentration, desorber heat duties, ideal cooling capacity, and ideal COP to within approximately 25% error or better, with much of the deviation likely due to scatter in the experimental results. The revised model achieved particularly good agreement with the branched tray results, as discussed in Chapter 6. This indicates that the Colburn and Drew (1937) method may be successfully applied to the counter-flow pool-boiling geometry of the branched tray VGU.

Comparing the experimental results, the branched tray appears to offer better performance in most respects (ideal cooling capacity, ideal COP, etc.), relative to the vertical column. This is notable given the relative similarity of performance as predicted by the models. During the investigation, it was observed that the boiling process within the branched tray test section was very vigorous and likely provided a high degree of surface wetting and mixing of both phases. This is in contrast to the vertical column, which typically operated in a stable falling-film regime with smooth film surfaces, and relatively little phase interaction, other than at the film interface. The additional mixing and more dynamic boiling process of the branched tray design may have contributed to the higher performance. This is supported by the observed trends of increasing heat and mass transfer coefficients with increasing Reynolds number or flooding coefficient. In future work, it may be possible to achieve some increase in the heat transfer performance of the vertical column desorber by considering alternate surface treatments that promote boiling in the liquid film. Regions of boiling were observed in the present study, but were typically small relative to the total film area. By using surface treatments that promote nucleation across the entire film area, an increase in the heat transfer coefficient might be observed. Other investigators have reported an increase in heat transfer coefficient of approximately ten percent between falling-film evaporation and combined evaporation/boiling in similar geometries (Fujita and Ueda, 1978a, b).

Considering the flooding investigation, additional data would be useful in determining the exact limits of flooding of the components and the best methods for recovering from a flooded condition. However, the data available from this study indicate excellent agreement with the correlation of Wallis (1969). Operating near the flooding limit appears to result in increased performance, in most cases, as the vapor velocity increases. Therefore, accurate estimation of the flooding limits and development of control methods that can maintain desorber operation near those limits, without causing flooding, would be essential for optimization of full-scale VGUs using similar geometries.

Generally, most performance metrics evaluated here were found to have some, often strong, dependence on vapor velocity. This is notable as the desorption process does not rely heavily on vapor transport mechanisms, unlike absorption or binary fluid condensation processes, where sensible cooling of the vapor and transport of the less-volatile species to the interface may be important, even dominant processes. Whether the dependence of the desorption process on vapor velocity is related to vapor-liquid shear and induced mixing in the liquid phase, increased wall-wetting, or increased heat and mass transfer within the vapor itself, is not entirely clear, and additional investigation would be useful in determining which mechanism or mechanisms contribute to the improved apparent solution heat transfer coefficients.

7.2 Recommendations

The present study provided new concepts and configurations to achieve integrated desorption and rectification of refrigerant vapors from binary fluid mixture solutions in compact geometries. Such countercurrent VGUs may facilitate more advanced small-scale absorption systems in the future. However, based on the results and conclusions of the present study, there are a number of areas that would benefit from additional investigation. These areas are summarized here:

- While good agreement was achieved between heat and mass transfer correlations and experimental results in most cases, the heat and mass transfer coefficient data showed a large degree of dependence on working fluid flow rates or Reynolds numbers. For example, the rectifier condensation coefficients, and branched tray pool-boiling desorption heat transfer coefficient, showed a large dependence on the vapor Reynolds number. This is likely due to the increased interfacial area, mixing, and surface wetting that are expected to occur at higher Reynolds numbers. However, many of the available correlations for heat and mass transfer in similar geometries do not account for the influence of fluid motion in both phases, leading to poor agreement across the wide ranges of vapor and liquid flow rates that may be observed in absorption VGUs. Development of additional correlations that consider these effects could lead to much more accurate predictions of component performance.

- The heat and mass transfer experiments conducted in the present work attempted to quantify the heat and mass transfer coefficients within operating VGUs. However, several difficulties were encountered in the design of the experimental test sections and in collection of the required measurements. Due to the desire to maintain as much similarity between the test sections and full-scale prototype VGUs as possible, the coupling-fluid geometry and fluid specifications were not ideal. This resulted in high uncertainties in some cases. Future investigations would benefit from coupling-fluid operating parameters and geometries that minimize the coupling-fluid-side thermal resistance. Alternately, electrically heating the desorber heat transfer surfaces could be considered, although maintaining realistic temperature profiles while using electric heating elements may prove challenging.
- Another major challenge that was faced in the experimental investigation was the difficulty of obtaining reliable measurements of both the liquid and vapor phases at many locations within small-scale passages. Due to the counter-flow design of the VGUs, most locations within the working-fluid passages are exposed to both liquid and vapor phases at some point during operation. Therefore, it is difficult to take reliable temperature measurements using conventional methods. Additionally, without direct measurement of the ammonia-water concentration, any data analysis methods must rely on saturation assumptions to determine the state of the working fluid. This causes particular difficulty in the mass transfer analysis, which requires values of several concentrations (vapor bulk, liquid bulk, and interface), all of which

must be determined from measurements made in close proximity to one another. Future studies may be able to overcome some of these challenges through the use of more advanced thermal measurement techniques, such as the use of infra-red imaging. Studies focused on accurately determining mass transfer coefficients may consider the use of titrations obtained from local fluid-sampling ports. Additionally, the use of optical or pH sensors may provide alternate methods for determining fluid concentrations.

- While an effort was made to qualitatively observe the surface wetting within the VGUs in the present study, quantitative analysis of interfacial area and wetted areas within the VGUs could lead to more accurate prediction of component capacities and performance. Development of correlations to predict the wetted area and interfacial area could be developed using the experimental facility and flow visualization techniques employed in the present study, with minor modifications.
- In the present study, the geometry and operating conditions of the test section were largely specified to match the full-capacity VGUs designed for specific absorption heat pump applications. As such, the coupling-fluid microchannel geometry and the choice of coupling fluid were fixed. This resulted in high uncertainties in the desorber heat transfer coefficients under some conditions. Future studies seeking to investigate high-flux desorber heat transfer coefficients, particularly using the pool-boiling mechanism of the branched tray desorber, should make use of alternate designs or coupling-fluids to decrease the thermal resistance of the coupling-fluid and reduce uncertainty in the calculated working-fluid heat transfer coefficients.

- Additional studies focusing on the effects of working- and coupling-fluid mal-distribution within the VGU passages would be beneficial, particularly for larger capacity components. While mal-distribution of the working fluid did not appear to be a major factor in the present study, there is some indication that mal-distribution of the coupling fluid within the microchannel array, may have contributed to the decrease in the performance of the vertical column desorber. In larger capacity VGUs that use geometry similar to the present study, additional distribution issues may be faced due to the need for multiple coupling-fluid shims and working-fluid plates. Development of appropriate headers and additional understanding of mal-distribution phenomena under representative conditions in representative geometries may be important in these cases.
- During the experimental investigation, control of the various working- and coupling-fluid flow rates represented a major challenge and required a high degree of manual control of expansion valves, pump speeds, and bypass valve settings by the operator. Future compact absorption systems will need to progress past this level of operator involvement to autonomous control systems. Therefore, the modeling and development of control strategies and automated systems for management of fluid levels and flow rates in compact VGUs will be critical to future commercially-oriented systems employing compact counter-flow VGUs, such as those developed in the present study.

APPENDIX A

HEAT LOSS MODEL

The details of the heat transfer model used to estimate auxiliary thermal losses and gains form the desorber and rectifier, respectively, are given here. Additionally, Figures A.1 and A.2 are presented. These figures show the coupling-fluid, working-fluid, and adjusted heat duty for the vertical column desorber and rectifier sections, respectively. The corresponding figures for the branched tray (Figures 4.6 and 4.7) were shown in Section 4.2.4.

The heat transfer model used for estimation of auxiliary heat duties uses the thermal resistance network approach and considers the rectifier and desorber separately. Each data point was analyzed using this model to estimate thermal losses for that

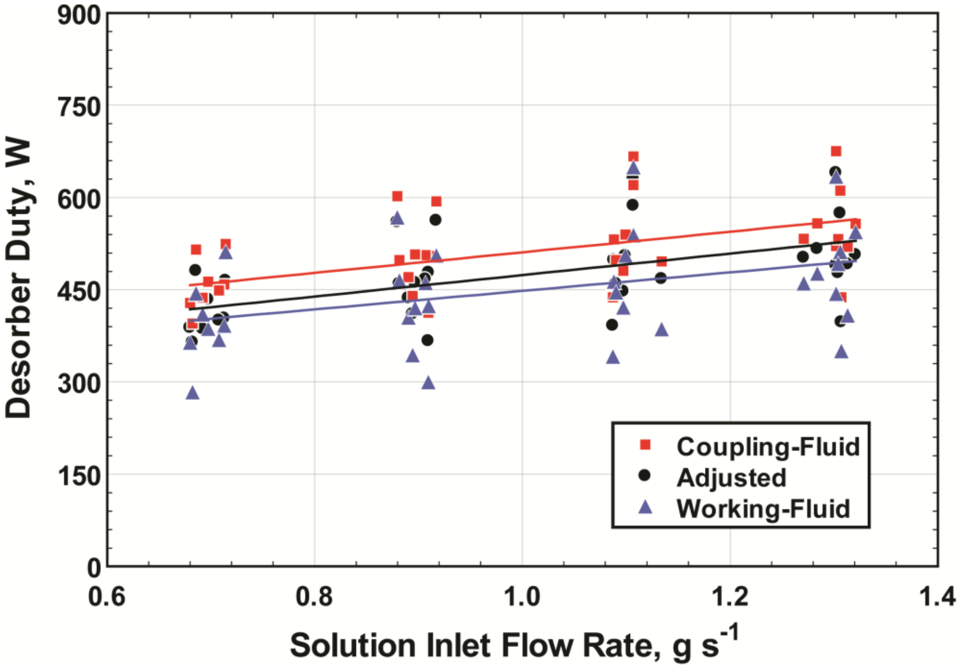

Figure A.1: Experimental and adjusted desorber heat duties

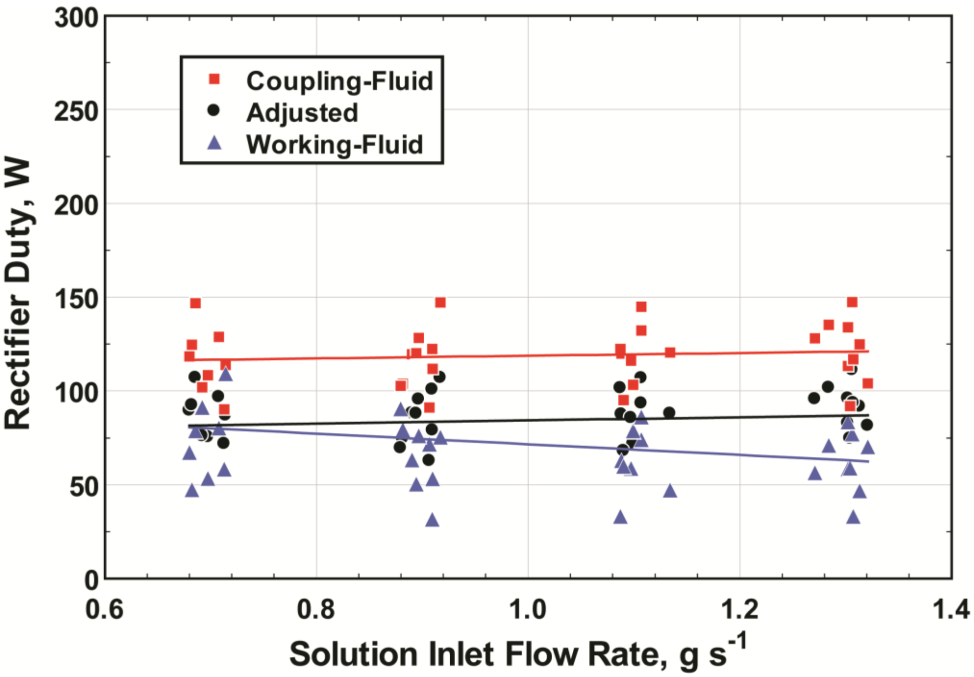

Figure A.2: Experimental and adjusted rectifier heat duties

condition. In the model, a resistance network is constructed for each face of the test section, which is approximated as a rectangular prism. Average coupling-fluid temperatures are calculated for the desorber and the rectifier and represent the source temperature (for the desorber analysis) and sink temperature (for the rectifier), respectively. The ambient vapor temperature was measured directly during experiments and is assumed to be at the same temperature as the heated chamber walls. This temperature is taken to be the sink temperature, for the desorber analysis, and source temperature, for the rectifier analysis.

Sample calculations are shown below for the back face of the branched-tray desorber. All other faces for both the desorber and rectifier are analyzed using the same approach, with appropriate adjustments for the geometry and materials.

The back face of the desorber was insulated to reduce thermal losses. The insulation was constructed of two PTFE plates, each with 12.7 mm thickness. PTFE was selected due to the low thermal conductivity of the material and good chemical stability at high temperatures in an ammonia-water environment. A rendering of the test section, and insulation plates in exploded and collapsed views is given in Figure A.3.

In practice, all equations given in the following analysis are solved simultaneously. However, for purposes of illustration, these calculations are presented in sequential fashion, with some subsequent results used as necessary for demonstrating the approach.

In order to determine the natural convection coefficients at the surface of the test section, and to quantify the radiation heat rate, the back surface temperature must be determined.

$$\dot{Q}_{cond} = \frac{1}{R_{cond,T}} \Delta T_{cond} \tag{A.1}$$

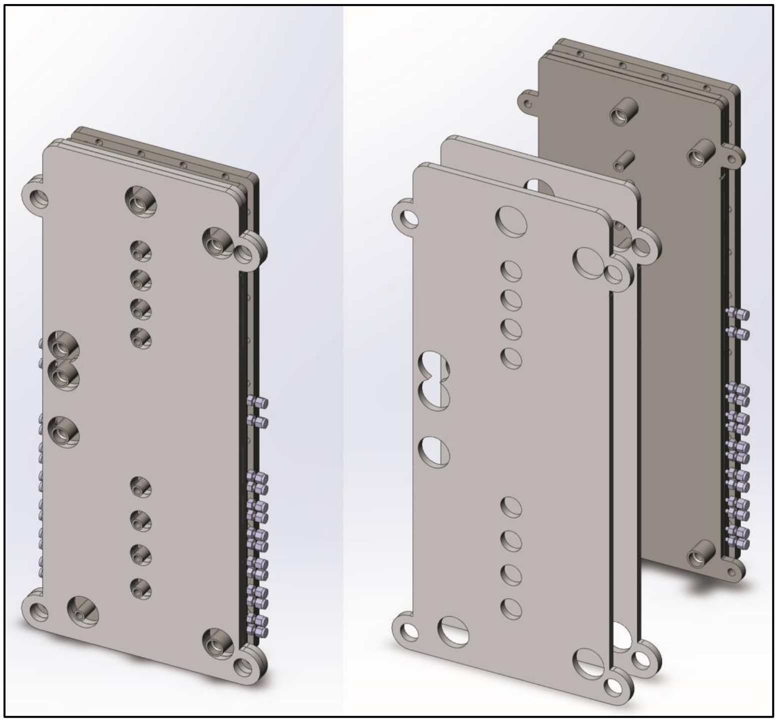

Figure A.3: Back face of test section with insulation plates

The heat rate for the conduction analysis is the sum of the radiation and natural convection heat losses at the back surface of the test section.

$$\dot{Q}_{cond} = \dot{Q}_{rad} + \dot{Q}_{conv} \tag{A.2}$$

This is illustrated in Figure A.4, which shows the conduction resistance network, convection resistance, and radiation heat loss for the desorber. Temperatures and heat rates shown are given for the branched tray sample point.

The conduction temperature difference is defined between an average coupling-fluid temperature, $T_{des,CF,avg}$, and the back surface temperature of the test section, T_s. This assumes that the convection resistance in the coupling-fluid is negligible, which is found to be a valid assumption for this analysis.

$$\Delta T_{cond} = T_{des,CF,avg} - T_s \tag{A.3}$$

The conduction resistance given in Eq. (4.86) is the sum of the resistances through the back of the stainless steel test section, R_{SS}, and through the PTFE insulation, R_{PTFE}.

$$R_{cond,T} = R_{SS} + R_{PTFE} \tag{A.4}$$

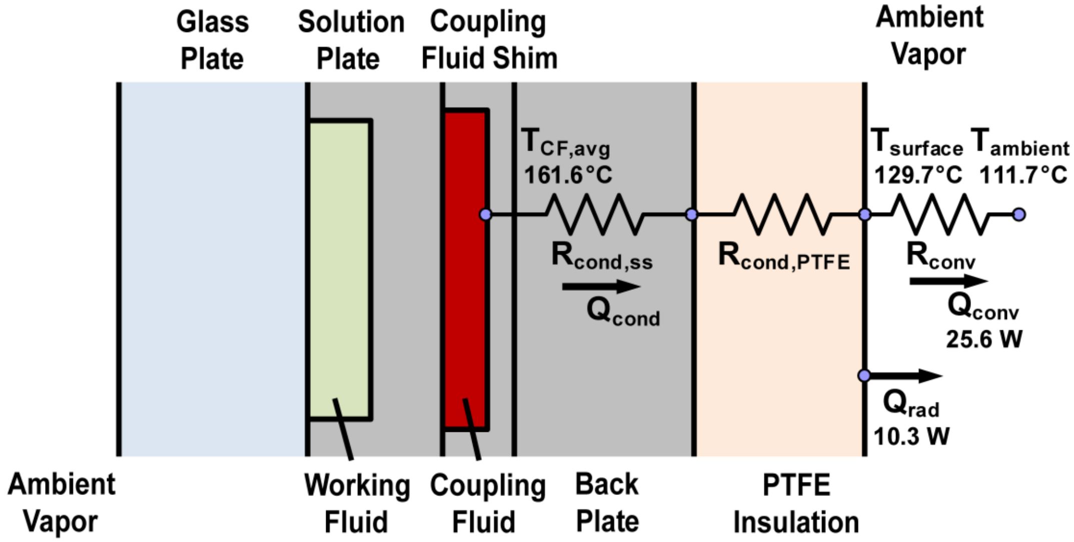

Figure A.4: Desorber resistance network for back face

The conduction resistances are defined in the typical manner, and are functions of the material conductivity, *k*, depth in the direction of conduction, *x*, and cross-sectional area normal to conduction, A_c.

$$R_{cond} = \frac{x}{kA_c} \tag{A.5}$$

Combining Eq. (A.5) and Eq. (A.4):

$$\begin{aligned} R_{cond,T} &= \frac{x_{SS}}{k_{SS} A_{c,SS}} + \frac{x_{PTFE}}{k_{PTFE} A_{c,PTFE}} \\ 1.26\ \text{K W}^{-1} &= \frac{0.00635\ \text{m}}{16.7\ \text{W m}^{-1}\ \text{K}^{-1}\ 0.0405\ \text{m}} + \frac{0.0127\ \text{m}}{0.25\ \text{W m}^{-1}\ \text{K}^{-1}\ 0.0405\ \text{m}} \end{aligned} \tag{A.6}$$

Substituting into Eq. (4.86):

$$\begin{aligned} \dot{Q}_{cond} &= \frac{1}{R_{cond,T}} \Delta T_{cond} \\ 24.4\ \text{W} &= \frac{1}{1.26\ \text{K W}^{-1}} 30.8°\text{C} \end{aligned} \tag{A.7}$$

The back surface temperature is then solved with Eq. (A.3) and the average coupling-fluid temperature, which was found in Eq. (4.10).

$$\begin{aligned} \Delta T_{cond} &= T_{des,CF,avg} - T_s \\ 30.8°\text{C} &= 160.6°\text{C} - 129.7°\text{C} \end{aligned} \tag{A.8}$$

With the surface temperature defined, the natural convection and radiation losses to the surroundings may be quantified.

The natural convection heat transfer coefficient is determined using the numerical method for flat vertical plates developed by (Nellis and Klein, 2009), which applies appropriate laminar or turbulent equations based on the fluid and geometric parameters. For the purpose of computing the heat transfer coefficient, the vapor is assumed to be pure ammonia. The average vapor outlet concentration for all test data (both test sections) was above 0.99, so this approximation is reasonable.

The natural convection coefficient may then be used with the surface and ambient vapor temperatures to determine the convection losses.

$$\begin{aligned}\dot{Q}_{conv} &= \frac{1}{R_{conv}}\Delta T_{conv} = \frac{1}{1/\alpha_{conv}A_c}(T_s - T_{v,amb})\\ 15.8\text{ W} &= \frac{1}{\left(\dfrac{1}{21.7\text{ W m}^{-2}\text{ K}^{-1}\ 0.0405\text{ m}}\right)}(129.7°\text{C} - 111.7°\text{C})\end{aligned} \tag{A.9}$$

Radiation losses are calculated assuming grey body radiation exchange with the surroundings. Temperatures for the surroundings and surface are taken to be uniform. Additionally, the chamber surface area is much larger than the test section face area, so radiation from the chamber can be approximated as that of a black body. If the test section face is taken to be a plane wall, the radiation heat loss may then be approximated.

$$\begin{aligned}\dot{Q}_{rad} &= \varepsilon_{PTFE}\sigma A_c(T_s^4 - T_{v,amb}{}^4)\\ 8.6\text{ W} &= 0.85\cdot 0.0405\text{ m}\left[\left(129.7°\text{C}\right)^4 - \left(111.7°\text{C}\right)^4\right]\end{aligned} \tag{A.10}$$

With the convection and radiation losses quantified, the total heat loss for the back face of the desorber is known. (In practice, the values determined in Eqs. (A.9) and (A.10) are used in Eqs. (A.2) and (A.1), closing the equation set and allowing for a solution to be determined by numerical iteration.)

This method is repeated for all faces of the desorber with appropriate changes to the geometric parameters, material properties, etc. The rectifier analysis also uses this method. Tables A.1 and A.2 provide the results of the analysis for the branched tray and vertical column, respectively. The results for all data points were then compared with the experimental results to generate Figures A.1 and A.2, above, and Figures 4.6 and 4.7, provided in Section 4.2.4. As shown in these figures, and discussed previously, the estimates of auxiliary heat loss or gain account for a significant portion of the difference

Table A.1: Branched tray auxiliary heat transfer rates, shown for sample point

	Desorber Rates, W		**Rectifier Rates, W**	
	Convection	**Radiation**	**Convection**	**Radiation**
Back	15.8	8.6	-9.4	-4.0
Sides	3.9	1.1	-4.8	-0.4
Bottom	1.4	0.6	-6.6	-0.2
Front	4.5	-	-4.1	-
Subtotals	25.6	10.3	-24.9	-4.7
Total	**35.9**		**-29.6**	

between the coupling- and working-fluid heat duties. However, this does not account for the full difference. The remaining portion is likely due to evaporation and condensation of ammonia-water on the exterior surfaces of the test section. To estimate the evaporation or condensation rate that would be required to account for the remaining auxiliary heat transfer, the following analysis is conducted. Calculations are again shown for the branched tray desorber.

The unaccounted heat loss, which is attributed to phase change, $\dot{Q}_{PC}$, is determined from an energy balance.

$$\begin{gathered}\dot{Q}_{PC} = \dot{Q}_{des,CF} - \dot{Q}_{des,WF} - \dot{Q}_{rad,T} - \dot{Q}_{conv,T} \\ 37.8\text{ W} = 744.6\text{ W} - 670.9\text{ W} - 10.3\text{ W} - 25.6\text{ W}\end{gathered} \tag{A.11}$$

The rate of phase change is then determined on a mass basis.

$$\dot{Q}_{PC} = \dot{m}_{PC}(h_{v,amb} - h_{l,amb}) \tag{A.12}$$

It is assumed that any liquid drops that fall onto the desorber walls originated from the rectifier section or coolant plumbing, immediately above the desorber. The ambient liquid concentration is then determined from the measured pressure, temperature of the exterior surface of the rectifier, and assumption of saturation.

$$\begin{gathered}x_{l,amb} = f(T,P,q) \\ 0.445 = f(94.0°\text{C}, 1626\text{ kPa}, 0)\end{gathered} \tag{A.13}$$

Table A.2: Vertical column auxiliary heat transfer rates, shown for sample point

	Desorber Rates, W		Rectifier Rates, W	
	Convection	**Radiation**	**Convection**	**Radiation**
Back	6.1	7.2	-16.5	-6.1
Sides	4.4	1.0	-	-0.5
Bottom	1.3	0.5	-	-0.3
Front	0.3	-	-7.7	-
Subtotals	12.1	8.7	-24.2	-6.9
Total	**20.8**		**-31.1**	

The enthalpies of the ambient liquid and vapor are then determined.

$$\begin{gathered} h_{l,amb} = f(T,P,q) \\ 188\ \text{kJ kg}^{-1}\ \text{K}^{-1} = f(94.0^\circ\text{C}, 1626\ \text{kPa}, 0) \end{gathered} \tag{A.14}$$

$$\begin{gathered} h_{v,amb} = f(P,q,x_{l,amb}) \\ 2257\ \text{kJ kg}^{-1}\ \text{K}^{-1} = f(1626\ \text{kPa}, 0, 0.445) \end{gathered} \tag{A.15}$$

Eq. (A.12) may then be solved to determine the phase change rate.

$$\begin{gathered} \dot{Q}_{PC} = \dot{m}_{PC}(h_{v,amb} - h_{l,amb}) \\ 37.8\ \text{W}\frac{1\ \text{kW}}{1000\ \text{W}} = 0.0183\ \text{g s}^{-1}\ (2257\ \text{kJ kg}^{-1}\ \text{K}^{-1} - 188\ \text{kJ kg}^{-1}\ \text{K}^{-1}) \end{gathered} \tag{A.16}$$

The phase change rate can be compared to the vapor generation rate inside the desorber, or condensation rate inside the rectifier to give an indication of whether this is a reasonable value. For the sample conditions, the branched tray desorption rate was 0.296 g s^{-1}. Therefore, the external evaporation rate is approximately 6.2% of the internal vapor generation rate. This is as expected due to the insulation on the exterior face of the desorber and the fact that relatively little liquid is available to evaporate, since it would rely on droplets condensing at higher locations and falling onto the desorber section. The rectifier analysis is conducted in the same manner. Average results for the phase change rates are provided in Table A.3.

Table A.3: Average external phase change rates

	Branched Tray		Vertical Column	
	Desorber	**Rectifier**	**Desorber**	**Rectifier**
Phase Change Rate, g s^{-1}	0.0284	0.0103	0.0226	0.0114
Percent of Internal Rate	11.8%	38.3%	11.3%	47.0%

APPENDIX B

DATA ANALYSIS AND UNCERTAINTIES, VERTICAL COLUMN GEOMETRY

The following tables provide the details of the data reduction and uncertainty analyses for the representative data point for the vertical column. This discussion supplements the corresponding description of the branched tray test section equations and data analysis presented in Chapter 4. Additional discussion of the uncertainty propagation methods is presented in Section 5.2. The locations of temperatures referenced here that are specific to the vertical column test section are shown in Figure 3.7. Locations of the thermocouples used for several of the average temperatures are highlighted in Figure 4.4. Facility instrumentation was discussed in Section 3.3 and uncertainties and details of the various instruments are provided in Table 3.3.

The vertical column sample data point nominal conditions and measured values for the various instruments are provided in Table B.1. Table B.2 provides the equations, inputs, and outputs, including values and uncertainties, for the desorber heat transfer analysis. This information is provided in Tables B.3, B.4, and B.5 for the rectifier heat transfer, desorber liquid mass transfer, and desorber vapor mass transfer analyses, respectively.

Table B.1: Vertical column sample point data

	Nominal Conditions
$\dot{m}_{l,in}$ (g s^{-1})	0.90
$x_{l,in}$	0.475
$T_{des,CF,in}$ (^{o}C)	180.0
	Measured Value
$\dot{m}_{l,in}$ (g s^{-1})	0.890
$\dot{m}_{l,out}$ (g s^{-1})	0.711
P (kPa)	2459
$T_{l,in}$ (^{o}C)	102.4
$T_{l,out}$ (^{o}C)	137.0
$T_{v,out}$ (^{o}C)	92.4
T_{1L}, T_{1R} (^{o}C)	122.2, 148.2
T_{2L}, T_{2R} (^{o}C)	118.6, 151.8
T_{3L}, T_{3R} (^{o}C)	115.4, 150.1
T_{4L}, T_{4R} (^{o}C)	114.1, 147.5
T_{5L}, T_{5R} (^{o}C)	110.4, 145.7
T_{6L}, T_{6R} (^{o}C)	110.9, 141.8
T_{7L}, T_{7R} (^{o}C)	108.5, 136.3
T_{8R} (^{o}C)	134.0
T_{9L}, T_{9R} (^{o}C)	104.7, 107.8
T_{10L}, T_{10R} (^{o}C)	104.1, 102.0
$\dot{V}_{des,CF}$ (cm^{3} s^{-1})	9.69
$T_{des.CF,in}$ (^{o}C)	180.4
$T_{des,CF,out}$ (^{o}C)	157.2
$\dot{m}_{rect,CF}$ (g s^{-1})	0.938
$T_{rect,CF,in}$ (^{o}C)	63.1
$T_{rect,CF,out}$ (^{o}C)	93.5

Table B.2: Desorber heat transfer and uncertainty analysis

Input	Equations	Output
$U_{des} = 701.4 \pm 7.818\ \text{W m}^{-2}\ \text{K}^{-1}$ $R_{wall,des} = 0.008204 \pm 1.55\times10^{-5}\ \text{K W}^{-1}$ $A_{WF,des} = 0.01601 \pm 0\ \text{m}^{2}$ $\alpha_{des,CF} = 899.1 \pm 89.91\ \text{W m}^{-2}\ \text{K}^{-1}$ $A_{CF,des} = 0.02448 \pm 2\times10^{-5}\ \text{m}^{2}$	$\frac{1}{\alpha_{WF,des}} = \frac{1}{U_{des}} - R_{wall,des}A_{WF,des} - \frac{1}{\alpha_{des,CF}A_{CF,des}}A_{WF,des}$	$\alpha_{WF,des} = 1764 \pm 233.3\ \text{W m}^{-2} K^{-1}$
$\eta_{fin,ch,des} = 0.9914 \pm 0.0008341$ $A_{CF,ch,des} = 0.0002774 \pm 0\ \text{m}^{2}$ $N_{ch,des} = 89 \pm 0$	$A_{CF,des} = A_{CF,ch}N_{ch,des}\eta_{fin,ch,des}$	$A_{CF,des} = 0.02448 \pm 2\times10^{-5}\ \text{m}^{2}$
$\alpha_{des,CF} = 899.1 \pm 89.91\ \text{W m}^{-2}\ \text{K}^{-1}$ $k_{wall,des} = 16.92 \pm 0.0319\ \text{W m}^{-2}\ \text{K}^{-1}$ $L_{fin,CF} = 0.00035 \pm 0\ \text{m}$ $t_{fin,CF} = 0.0005 \pm 0\ \text{m}$	$\eta_{fin} = \frac{\tanh\left(\left(\frac{2\cdot\alpha_{des,CF}}{k_{wall,des}t_{fin,CF}}\right)^{0.5}L_{fin,CF}\right)}{\left(\frac{2\cdot\alpha_{des,CF}}{k_{wall,des}t_{fin,CF}}\right)^{0.5}L_{fin,CF}}$	$\eta_{fin,ch,des} = 0.9914 \pm 0.0008341$
$\text{Re}_{des,CF} = 161.3 \pm 0.92$ $D_{h,CF} = 0.000442 \pm 0\ \text{m}$ $k_{des,CF} = 0.09731 \pm 9\times10^{-6}\ \text{W m}^{-2}\ \text{K}^{-1}$ $\phi = 1.571 \pm 0$ assigned uncertainty = 10%	$\alpha_{des,CF} = f\left(\text{Re}_{des,CF}, D_{h,CF}, k_{des,CF}, \phi\right) \pm \text{assigned uncertainty}$	$\alpha_{des,CF} = 899.1 \pm 89.91\ \text{W m}^{-2}\ \text{K}^{-1}$
$T_{wall,des} = 147.1 \pm 2.00^{\circ}\text{C}$	$k_{wall,des} = f\left(T_{wall,des}\right)$	$k_{wall,des} = 16.92 \pm 0.0319\ \text{W m}^{-2}\ \text{K}^{-1}$
$P_{ch} = 0.0019 \pm 0\ \text{m}$ $L_{ch,des} = 0.1461 \pm 0\ \text{m}$	$A_{CF,ch,des} = P_{ch}L_{ch,des}$	$A_{CF,ch,des} = 0.0002774 \pm 0\ \text{m}^{2}$

Table B.2 Continued

Input	Equations	Output
$R_{ch} = 0.00035 \pm 0\ \text{m}$ $L_{flat} = 5.0\times10^{-5} \pm 0\ \text{m}$	$P_{ch} = \left[2\left(2\pi R_{ch}/4\right)+L_{flat}\right]+\left(2R_{ch}+L_{flat}\right)$	$P_{ch} = 0.0019 \pm 0\ \text{m}$
$T_{CF,avg,des} = 168.8 \pm 0.1768°\text{C}$	$k_{des,CF} = f\left(T_{cf,avg,des}\right)$	$k_{des,CF} = 0.09731 \pm 9\times10^{-6}\ \text{W m}^{-2}\ \text{K}^{-1}$
$T_{des,CF,in} = 180.4 \pm 0.25°\text{C}$ $T_{des,CF,out} = 157.2 \pm 0.25°\text{C}$	$T_{CF,avg,des} = \dfrac{T_{des,CF,in}+T_{des,CF,out}}{2}$	$T_{CF,avg,des} = 168.8 \pm 0.1768°\text{C}$
$P_{ch} = 0.0019 \pm 0\ \text{m}$ $A_{face,ch} = 2.099\times10^{-7} \pm 0\ \text{m}^2$	$D_{h,CF} = 4A_{face,ch}/P_{ch}$	$D_{h,CF} = 0.000442 \pm 0\ \text{m}$
$R_{ch} = 0.00035 \pm 0\ \text{m}$ $L_{flat} = 5.0\times10^{-5} \pm 0\ \text{m}$	$A_{face,ch} = 2\left(\pi R_{ch}^2/4\right)+\left(R_{ch}L_{flat}\right)$	$A_{face,ch} = 2.099\times10^{-7} \pm 0\ \text{m}^2$
$\dot{V}_{des,CF} = 9.689\times10^{-6} \pm 4.845\times10^{-8}\ \text{m}^3\ \text{s}^{-1}$ $D_{h,CF} = 0.000442 \pm 0\ \text{m}$ $A_{face,ch} = 2.099\times10^{-7} \pm 0\ \text{m}^2$ $N_{ch,rect} = 89 \pm 0$ $\rho_{des,CF} = 785.5 \pm 0.12\ \text{kg m}^3$	$\text{Re}_{des,CF} = \rho_{des,CF}\dot{V}_{des,CF}D_{h,CF}/\left(\mu_{des,CF}A_{face,ch}N_{ch,des}\right)$	$\text{Re}_{des,CF} = 161.3 \pm 0.92$
$T_{CF,avg,des} = 168.8 \pm 0.1768°\text{C}$	$\rho_{des,CF} = f\left(T_{CF,avg,des}\right)$	$\rho_{des,CF} = 785.5 \pm 0.12\ \text{kg m}^3$
$T_{CF,avg,des} = 168.8 \pm 0.1768°\text{C}$	$\mu_{des,CF} = f\left(T_{CF,avg,des}\right)$	$\mu_{des,CF} = 0.001137 \pm 3.1\times10^{-6}\ \text{kg m}^{-1}\ \text{s}^{-1}$

Table B.2 Continued

Input	Equations	Output
$n_{col} = 4 \pm 0$ $Depth_{c,des} = 0.00200 \pm 0 \text{ m}$ $Width_c = 0.0254 \pm 0 \text{ m}$ $L_{ch,des} = 0.1461 \pm 0 \text{ m}$	$A_{WF,des} = n_{col}\left(Depth_{c,des} L_{ch,des} + Width_c L_{ch,des}\right)$	$A_{WF,des} = 0.01601 \pm 0 \text{ m}^2$
$x_{wall,des} = 0.00222 \pm 0 \text{ m}$ $A_{wall,des} = 0.01601 \pm 0 \text{ m}^2$ $k_{wall,des} = 16.92 \pm 0.0319 \text{ W m}^{-2} \text{ K}^{-1}$	$R_{wall,des} = x_{wall,des} / \left(k_{wall,des} A_{wall,des}\right)$	$R_{wall,des} = 0.008204 \pm 15 \times 10^{-5} \text{ K W}^{-1}$
$A_{WF,des} = 0.01601 \pm 0 \text{ m}^2$	$A_{wall,des} = A_{WF,des}$	$A_{wall,des} = 0.01601 \pm 0 \text{ m}^2$
$\dot{Q}_{des,avg} = 437.4 \pm 3.936 \text{ W}$ $A_{WF,des} = 0.01601 \pm 0 \text{ m}^2$ $LMTD_{des} = 38.96 \pm 0.223°\text{K}$	$\dot{Q}_{des,avg} = U_{des} A_{WF,des} \cdot LMTD_{des}$	$U_{des} = 701.4 \pm 7.8 \text{ W m}^{-2} \text{ K}^{-1}$
$T_{l,in,des} = 122.4 \pm 0.125°\text{C}$ $T_{l,out} = 137.0 \pm 0.25°\text{C}$ $T_{des,CF,in} = 180.4 \pm 0.25°\text{C}$ $T_{des,CF,out} = 157.2 \pm 0.25°\text{C}$	$LMTD_{des} = \dfrac{\left(T_{des,cf,in} - T_{l,out}\right) - \left(T_{des,cf,out} - T_{l,in,des}\right)}{\ln\left(\dfrac{T_{des,cf,in} - T_{l,out}}{T_{des,cf,out} - T_{l,in,des}}\right)}$	$LMTD_{des} = 38.96 \pm 0.223°\text{K}$
$T_{7L} = 114.14 \pm 0.25°\text{C}$ $T_{7R} = 147.51 \pm 0.25°\text{C}$	$T_{l,in,des} = average(T_{7L}, T_{7R})$	$T_{l,in,des} = 122.4 \pm 0.125°\text{C}$

Table B.2 Continued

Input	Equations	Output
$R_{CF,des} = 0.04543 \pm 0.004517 \text{ K W}^{-1}$ $R_{wall,des} = 0.008204 \pm 1.5\times10^{-5} \text{ K W}^{-1}$ $T_{CF,avg,des} = 168.8 \pm 0.1768°\text{C}$ $T_{wall,des} = 147.1 \pm 2.00°\text{C}$	$\dot{Q}_{des,avg} = \left(R_{CF,des} + \frac{R_{wall,des}}{2}\right)^{-1} \cdot \left(T_{des,CF,avg} - T_{wall,des}\right)$	$\dot{Q}_{des,avg} = 437.4 \pm 3.936 \text{ W}$
$\alpha_{des,CF} = 899.1 \pm 89.91 \text{ W m}^{-2} \text{ K}^{-1}$ $A_{CF,ch,des} = 0.0002774 \pm 0 \text{ m}^2$	$R_{CF,des} = \frac{1}{\alpha_{des,CF} A_{CF,des}}$	$R_{CF,des} = 0.04543 \pm 0.004517 \text{ K W}^{-1}$
$R_{CF,des} = 0.04543 \pm 0.004517 \text{ K W}^{-1}$ $R_{wall,des} = 0.008204 \pm 1.5\times10^{-5} \text{ K W}^{-1}$ $\dot{Q}_{des,avg} = 437.4 \pm 3.936 \text{ W}$	$\dot{Q}_{des,avg} = \left(R_{cf,des} + \frac{R_{wall,des}}{2}\right)^{-1} \Delta T_{wall,des}$	$\Delta T_{wall,des} = 21.67 \pm 1.989°\text{K}$
$T_{CF,avg,des} = 168.8 \pm 0.1768°\text{C}$ $\Delta T_{wall,rect} = 21.67 \pm 1.989°\text{K}$	$\Delta T_{wall,des} = \left(T_{cf,avg,des} - T_{wall,des}\right)$	$T_{wall,des} = 147.1 \pm 2.00°\text{C}$

Table B.3: Rectifier heat transfer and uncertainty analysis

Input	Equations	Output
$U_{rect} = 201.2 \pm 2.3\ \mathrm{W\ m^{-2}\ K^{-1}}$ $R_{wall,rect} = 0.01459 \pm 3\times10^{-6}\ \mathrm{K\ W^{-1}}$ $A_{WF,rect} = 0.01409 \pm 0\ \mathrm{m^2}$ $\alpha_{rect,CF} = 6181.0 \pm 618.1\ \mathrm{W\ m^{-2}\ K^{-1}}$ $A_{CF,rect} = 0.0212 \pm 0.0001\ \mathrm{m^2}$	$\frac{1}{\alpha_{WF,rect}} = \frac{1}{U_{rect}} - R_{wall,rect}A_{WF,rect} - \frac{1}{\alpha_{rect,CF}A_{CF,rect}}A_{WF,rect}$	$\alpha_{WF,rect} = 214.7 \pm 2.7\ \mathrm{W\ m^{-2}}K^{-1}$
$\eta_{fin,ch,rect} = 0.9405 \pm 0.0055$ $A_{CF,ch,rect} = 0.0002533 \pm 0\ \mathrm{m^2}$ $N_{ch,rect} = 103 \pm 0$	$A_{CF,rect} = A_{CF,ch}N_{ch,rect}\eta_{fin,ch,rect}$	$A_{CF,rect} = 0.0212 \pm 0.0001\ \mathrm{m^2}$
$\alpha_{rect,CF} = 6181.0 \pm 618.1\ \mathrm{W\ m^{-2}\ K^{-1}}$ $k_{wall,rect} = 15.75 \pm 0.0032\ \mathrm{W\ m^{-2}\ K^{-1}}$ $L_{fin,CF} = 0.00035 \pm 0\ \mathrm{m}$ $t_{fin,CF} = 0.0005 \pm 0\ \mathrm{m}$	$\eta_{fin} = \frac{\tanh\left(\left(\frac{2\cdot\alpha_{rect,CF}}{k_{wall,rect}t_{fin,CF}}\right)^{0.5}L_{fin,CF}\right)}{\left(\frac{2\cdot\alpha_{rect,CF}}{k_{wall,rect}t_{fin,CF}}\right)^{0.5}L_{fin,CF}}$	$\eta_{fin,ch,rect} = 0.9405 \pm 0.0055$
$\mathrm{Re}_{rect,CF} = 52.96 \pm 0.29$ $D_{h,CF} = 0.000442 \pm 0\ \mathrm{m}$ $k_{rect,CF} = 0.669 \pm 0.0001\ \mathrm{W\ m^{-2}\ K^{-1}}$ $\phi = 1.571 \pm 0$ assigned uncertainty = 10%	$\alpha_{rect,CF} = f\left(\mathrm{Re}_{rect,CF}, D_{h,CF}, k_{rect,CF}, \phi\right) \pm \text{assigned uncertainty}$	$\alpha_{rect,CF} = 6181.0 \pm 618.1\ \mathrm{W\ m^{-2}\ K^{-1}}$
$T_{wall,rect} = 76.96 \pm 0.189^{\circ}\mathrm{C}$	$k_{wall,rect} = f\left(T_{wall,rect}\right)$	$k_{wall,rect} = 15.75 \pm 0.0032\ \mathrm{W\ m^{-2}\ K^{-1}}$
$P_{ch} = 0.0019 \pm 0\ \mathrm{m}$ $L_{ch,rect} = 0.1334 \pm 0\ \mathrm{m}$	$A_{CF,ch,rect} = P_{ch}L_{ch,rect}$	$A_{CF,ch,rect} = 0.0002533 \pm 0\ \mathrm{m^2}$

Table B.3 Continued

Input	Equations	Output
$R_{ch}=0.00035\pm 0\ \text{m}$ $L_{flat}=5.0\times 10^{-5}\pm 0\ \text{m}$	$P_{ch}=\left[2\left(2\pi R_{ch}/4\right)+L_{flat}\right]+\left(2R_{ch}+L_{flat}\right)$	$P_{ch}=0.0019\pm 0\ \text{m}$
$T_{CF,avg,rect}=78.32\pm 0.1768^{\circ}\text{C}$	$k_{rect,CF}=f\left(T_{cf,avg,rect}\right)$	$k_{rect,CF}=0.669\pm 0.0001\ \text{W m}^{-2}\ \text{K}^{-1}$
$T_{rect,CF,in}=63.12\pm 0.25^{\circ}\text{C}$ $T_{rect,CF,out}=93.53\pm 0.25^{\circ}\text{C}$	$T_{CF,avg,rect}=\dfrac{T_{rect,CF,in}+T_{rect,CF,out}}{2}$	$T_{CF,avg,rect}=78.32\pm 0.1768^{\circ}\text{C}$
$P_{ch}=0.0019\pm 0\ \text{m}$ $A_{face,ch}=2.099\times 10^{-7}\pm 0\ \text{m}^2$	$D_{h,CF}=4A_{face,ch}/P_{ch}$	$D_{h,CF}=0.000442\pm 0\ \text{m}$
$R_{ch}=0.00035\pm 0\ \text{m}$ $L_{flat}=5.0\times 10^{-5}\pm 0\ \text{m}$	$A_{face,ch}=2\left(\dfrac{\pi R_{ch}^2}{4}\right)+\left(R_{ch}L_{flat}\right)$	$A_{face,ch}=2.099\times 10^{-7}\pm 0\ \text{m}^2$
$\dot{m}_{rect,CF}=0.000938\pm 4.688\times 10^{-6}\ \text{kg s}^{-1}$ $D_{h,CF}=0.000442\pm 0\ \text{m}$ $A_{face,ch}=2.099\times 10^{-7}\pm 0\ \text{m}^2$ $N_{ch,rect}=103\pm 0$	$\text{Re}_{rect,CF}=\dot{m}_{rect,CF}D_{h,CF}/\left(\mu_{rect,CF}A_{face,ch}N_{ch,rect}\right)$	$\text{Re}_{rect,CF}=52.96\pm 0.29$
$T_{CF,avg,rect}=78.32\pm 0.1768^{\circ}\text{C}$	$\mu_{rect,CF}=f\left(T_{CF,avg,rect}\right)$	$\mu_{rect,CF}=0.000362\pm 8.117\times 10^{-7}\ \text{kg m}^{-1}\ \text{s}^{-1}$
$n_{col}=4\pm 0$ $Depth_{c,rect}=0.001016\pm 0\ \text{m}$ $Width_c=0.0254\pm 0\ \text{m}$ $L_{ch,rect}=0.1334\pm 0\ \text{m}$	$A_{WF,rect}=n_{col}\left(Depth_{c,rect}L_{ch,rect}+Width_cL_{ch,rect}\right)$	$A_{WF,rect}=0.01409\pm 0\ \text{m}^2$
$x_{wall,rect}=0.00324\pm 0\ \text{m}$ $A_{wall,rect}=0.01409\pm 0\ \text{m}^2$ $k_{wall,rect}=15.75\pm 0.0032\ \text{W m}^{-2}\ \text{K}^{-1}$	$R_{wall,rect}=\dfrac{x_{wall,rect}}{k_{wall,rect}A_{wall,rect}}$	$R_{wall,rect}=0.01459\pm 3\times 10^{-6}\ \text{K W}^{-1}$
$A_{WF,rect}=0.01409\pm 0\ \text{m}^2$	$A_{wall,rect}=A_{WF,rect}$	$A_{wall,rect}=0.01409\pm 0\ \text{m}^2$

Table B.3 Continued

Input	Equations	Output
$\dot{Q}_{rect,avg} = 91.28 \pm 0.812\ \mathrm{W}$ $A_{WF,rect} = 0.01409 \pm 0\ \mathrm{m}^2$ $LMTD_{rect} = 32.2 \pm 0.2255°\mathrm{K}$	$\dot{Q}_{rect,avg} = U_{rect} A_{WF,rect} \cdot LMTD_{rect}$	$U_{rect} = 201.2 \pm 2.3\ \mathrm{W\ m^{-2}\ K^{-1}}$
$T_{in,rect} = 128.9 \pm 0.0833°\mathrm{C}$ $T_{v,out} = 92.37 \pm 0.25°\mathrm{C}$ $T_{rect,CF,in} = 63.12 \pm 0.25°\mathrm{C}$ $T_{rect,CF,out} = 93.53 \pm 0.25°\mathrm{C}$	$LMTD_{rect} = \dfrac{\left(T_{in,rect} - T_{rect,CF,out}\right) - \left(T_{v,out} - T_{rect,CF,in}\right)}{\ln\left(\dfrac{T_{in,rect} - T_{rect,CF,out}}{T_{v,out} - T_{rect,CF,in}}\right)}$	$LMTD_{rect} = 32.2 \pm 0.2255°\mathrm{K}$
$T_{v,anlz,out} = 128.9 \pm 0.0833°\mathrm{C}$	$T_{in,rect} = T_{v,anlz,out}$	$T_{in,rect} = 128.9 \pm 0.0833°\mathrm{C}$
$T_{6L} = 110.93 \pm 0.25°\mathrm{C}$ $T_{8R} = 134.02 \pm 0.25°\mathrm{C}$ $T_{6R} = 141.68 \pm 0.25°\mathrm{C}$	$T_{v,anlz,out} = average(T_{6L}, T_{8R}, T_{6R})$	$T_{v,anlz,out} = 128.9 \pm 0.0833°\mathrm{C}$
$R_{CF,rect} = 0.00763 \pm 0.00072\ \mathrm{K\ W^{-1}}$ $R_{wall,rect} = 0.01459 \pm 3\times10^{-6}\ \mathrm{K\ W^{-1}}$ $T_{cf,avg,rect} = 78.32 \pm 0.1768°\mathrm{C}$ $T_{wall,rect} = 76.96 \pm 0.1892°\mathrm{C}$	$\dot{Q}_{rect,avg} = \left(R_{CF,rect} + \dfrac{R_{wall,rect}}{2}\right)^{-1} \cdot \left(T_{rect,CF,avg} - T_{wall,rect}\right)$	$\dot{Q}_{rect,avg} = 91.28 \pm 0.812\ \mathrm{W}$
$\alpha_{rect,CF} = 6181.0 \pm 618.1\ \mathrm{W\ m^{-2}\ K^{-1}}$ $A_{CF,ch,rect} = 0.0002533 \pm 0\ \mathrm{m}^2$	$R_{CF,rect} = \left(\alpha_{rect,CF} A_{CF,rect}\right)^{-1}$	$R_{CF,rect} = 0.00763 \pm 0.00072\ \mathrm{K\ W^{-1}}$
$R_{CF,rect} = 0.00763 \pm 0.00072\ \mathrm{K\ W^{-1}}$ $R_{wall,rect} = 0.01459 \pm 3\times10^{-6}\ \mathrm{K\ W^{-1}}$ $\dot{Q}_{rect,avg} = 91.28 \pm 0.812\ \mathrm{W}$	$\dot{Q}_{rect,avg} = \left(R_{cf,rect} + \dfrac{R_{wall,rect}}{2}\right)^{-1} \Delta T_{wall,rect}$	$\Delta T_{wall,rect} = 1.36 \pm 0.067°\mathrm{K}$
$T_{cf,avg,rect} = 78.32 \pm 0.1768°\mathrm{C}$ $\Delta T_{wall,rect} = 1.36 \pm 0.067°\mathrm{K}$	$\Delta T_{wall,rect} = \left(T_{cf,avg,rect} - T_{wall,rect}\right)$	$T_{wall,rect} = 76.96 \pm 0.189°\mathrm{C}$

Table B.4: Liquid mass transfer and uncertainty analysis

Input	Equations	Output
$A_{WF,des} = 0.01601 \pm 0 \text{ m}^2$ $\dot{m}_{v,out} = 0.000179 \pm 2.04\times10^{-7} \text{ kg s}^{-1}$ $x_{v,out} = 0.9879 \pm 0.000188$ $x_{l,bulk} = 0.4072 \pm 0.00180$ $x_{l,int} = 0.3702 \pm 0.00169$ $\rho_{l,bulk} = 740.1 \pm 0.815 \text{ kg m}^3$ $\rho_{l,int} = 757.0 \pm 0.751 \text{ kg m}^3$	$\dot{m}_{v,out} x_{v,out} = \beta_l A_{WF,des} \left(x_{l,bulk} \cdot \rho_{l,bulk} - x_{l,int} \cdot \rho_{l,int} \right)$	$\beta_{l,des} = 0.000523 \pm 1.179\times10^{-5} \text{ m s}^{-1}$
$\dot{m}_{l,in} = 0.000890 \pm 8.90\times10^{-7} \text{ kg s}^{-1}$ $\dot{m}_{l,out} = 0.000711 \pm 7.110\times10^{-7} \text{ kg s}^{-1}$	$\dot{m}_{v,out} = \dot{m}_{l,in} - \dot{m}_{l,out}$	$\dot{m}_{v,out} = 0.000179 \pm 2.04\times10^{-7} \text{ kg s}^{-1}$
$T_{v,out} = 92.37 \pm 0.25°C$ $P = 2459 \pm 17.24 \text{ kPa}$ $q_{v,out} = 1 \pm 0$	$x_{v,out} = f\left(T_{v,out}, P, q_{v,out}\right)$	$x_{v,out} = 0.9879 \pm 0.00019$
$x_{l,out} = 0.3423 \pm 0.00105$ $x_{l,in} = 0.4721 \pm 0.00111$	$x_{l,bulk} = \dfrac{x_{l,out} + x_{l,in}}{2}$	$x_{l,bulk} = 0.4072 \pm 0.00180$
$T_{l,out} = 137.01 \pm 0.25°\text{C}$ $P = 2459 \pm 17.24 \text{ kPa}$ $q_{l,out} = 0 \pm 0$	$x_{l,out} = f\left(T_{l,out}, P, q_{l,out}\right)$	$x_{l,out} = 0.3423 \pm 0.00105$
$\dot{m}_{l,in} = 0.000890 \pm 8.901\times10^{-7} \text{ kg s}^{-1}$ $\dot{m}_{l,out} = 0.000711 \pm 7.110\times10^{-7} \text{ kg s}^{-1}$ $\dot{m}_{v,out} = 0.000179 \pm 2.04\times10^{-7} \text{ kg s}^{-1}$ $x_{l,out} = 0.3423 \pm 0.00105$ $x_{v,out} = 0.9879 \pm 0.00019$	$\dot{m}_{l,in} \cdot x_{l,in} - \dot{m}_{l,out} \cdot x_{l,out} = \dot{m}_{v,out} \cdot x_{v,out}$	$x_{l,in} = 0.4721 \pm 0.00111$

Table B.4 Continued

Input	Equations	Output
$T_{l,bulk} = 130.4 \pm 0.1°\text{C}$ $x_{l,bulk} = 0.4072 \pm 0.00180$ $q_{l,bulk} = 0 \pm 0$	$\rho_{l,bulk} = f(T_{l,bulk}, x_{l,bulk}, q_{l,bulk})$	$\rho_{l,bulk} = 740.1 \pm 0.815 \text{ kg m}^3$
$T_{l,bulk} = 130.4 \pm 0.1°\text{C}$ $P = 2459 \pm 17.24 \text{ kPa}$ $q_{l,\text{int}} = 0 \pm 0$	$x_{l,int} = f(T_{l,bulk}, P, q_{l,int})$ $\rho_{l,int} = f(T_{l,bulk}, P, q_{l,int})$	$x_{l,int} = 0.3702 \pm 0.00169$ $\rho_{l,int} = 757.0 \pm 0.751 \text{ kg m}^3$
$T_{1L} = 122.19 \pm 0.25°\text{C}$ $T_{3L} = 115.36 \pm 0.25°\text{C}$ $T_{5L} = 110.38 \pm 0.25°\text{C}$ $T_{7L} = 108.47 \pm 0.25°\text{C}$ $T_{1R} = 148.16 \pm 0.25°\text{C}$ $T_{3R} = 150.05 \pm 0.25°\text{C}$ $T_{5R} = 145.71 \pm 0.25°\text{C}$ $T_{7R} = 136.27 \pm 0.25°\text{C}$ $T_{l,out} = 137.0 \pm 0.25°\text{C}$	$T_{l,bulk} = average(T_{1L}, T_{3L}, T_{5L}, T_{7L}, T_{1R}, T_{3R}, T_{5R}, T_{7R}, T_{l,out})$	$T_{l,bulk} = 130.4 \pm 0.1°\text{C}$

Table B.5: Vapor mass transfer and uncertainty analysis

Input	Equations	Output
$\dot{n}''_T = 0.000734 \pm 4.88\times10^{-6}$ kMol m^{-2} s^{-1} $C_T = 0.7315 \pm 0.00513$ kMol m^{-3} $\tilde{z} = 0.748 \pm 0.00060$ $\tilde{x}_{v,int} = 0.9224 \pm 0.00075$ $\tilde{x}_{v,bulk} = 0.9239 \pm 0.00073$	$\dot{n}''_T = \beta_v \cdot C_T \ln\left(\frac{\tilde{z}-\tilde{x}_{v,int}}{\tilde{z}-\tilde{x}_{v,bulk}}\right)$	$\beta_{l,des} = 0.000523 \pm 1.179\times10^{-5}$ m s^{-1}
$\dot{m}_{v,out} = 0.000179 \pm 2.04\times10^{-7}$ kg s^{-1} $A_{WF,des} = 0.01601 \pm 0$ m^2 $\tilde{z} = 0.748 \pm 0.00060$ $M_{NH3} = 17.03 \pm 0$ kg kMol^{-1} $M_{H_2O} = 18.02 \pm 0$ kg kMol^{-1}	$\dot{n}''_T = \frac{\dot{m}_{v,out}}{A_{\text{int},des} \cdot \left(\tilde{z} M_{NH3} + (1-\tilde{z}) M_{H_2O}\right)}$	$\dot{n}''_T = 0.000734 \pm 4.88\times10^{-6}$ kMol m^{-2} s^{-1}
$z = 0.7373 \pm 0.00062$ $M_{NH3} = 17.03 \pm 0$ kg kMol^{-1} $M_{H_2O} = 18.02 \pm 0$ kg kMol^{-1}	$\tilde{z} = \frac{\frac{z}{M_{NH_3}}}{\frac{z}{M_{NH_3}} + \left(\frac{(1-z)}{M_{H_2O}}\right)}$	$\tilde{z} = 0.748 \pm 0.00060$
$h_{des,latent} = 1230 \pm 1.051$ kJ kg^{-1} $h_{fg,NH_3} = 1011 \pm 1.541$ kJ kg^{-1} $h_{fg,H_2O} = 1844 \pm 1.64$ kJ kg^{-1}	$h_{des,latent} = z \cdot h_{fg,NH_3} + (1-z) \cdot h_{fg,H_2O}$	$z = 0.7373 \pm 0.00062$
$h_{v,int} = 1601 \pm 1.348$ kJ kg^{-1} $h_{l,int} = 370.8 \pm 0.4236$ kJ kg^{-1}	$h_{des,latent} = h_{v,\text{int}} - h_{l,\text{int}}$	$h_{des,latent} = 1230 \pm 1.051$ kJ kg^{-1}
$T_{l,bulk} = 130.4 \pm 0.1$°C $P = 2459 \pm 17.24$ kPa $q_{l,\text{int}} = 0 \pm 0$	$h_{l,int} = f(T_{l,bulk}, P, q_{l,int})$	$h_{l,int} = 370.8 \pm 0.4236$ kJ kg^{-1}

Table B.5 Continued

Input	Equations	Output
$T_{l,bulk} = 130.4 \pm 0.1°\text{C}$ $P = 2459 \pm 17.24\ \text{kPa}$ $q_{v,\text{int}} = 1 \pm 0$	$h_{v,int} = f(T_{l,bulk}, P, q_{v,int})$ $x_{v,int} = f(T_{l,bulk}, P, q_{v,int})$	$h_{v,int} = 1601 \pm 1.348\ \text{kJ kg}^{-1}$ $x_{v,int} = 0.9224 \pm 0.0007451$
$P = 2459 \pm 17.24\ \text{kPa}$	$h_{fg,NH_3} = f(P)$	$h_{fg,NH_3} = 1011 \pm 1.541\ \text{kJ kg}^{-1}$
$P = 2459 \pm 17.24\ \text{kPa}$	$h_{fg,H_2O} = f(P)$	$h_{fg,H_2O} = 1844 \pm 1.64\ \text{kJ kg}^{-1}$
$x_{v,int} = 0.9224 \pm 0.00075$ $M_{NH3} = 17.03 \pm 0\ \text{kg kMol}^{-1}$ $M_{H_2O} = 18.02 \pm 0\ \text{kg kMol}^{-1}$	$\tilde{x}_{v,int} = \dfrac{\dfrac{x_{v,int}}{M_{NH_3}}}{\dfrac{x_{v,int}}{M_{NH_3}} + \left(\dfrac{(1 - x_{v,int})}{M_{H_2O}}\right)}$	$\tilde{x}_{v,int} = 0.9224 \pm 0.00075$
$T_{v,bulk} = 131.2 \pm 0.06186°\text{C}$ $P = 2459 \pm 17.24\ \text{kPa}$ $q_{v,\text{int}} = 1 \pm 0$	$x_{v,bulk} = f(T_{v,bulk}, P, q_{v,bulk})$	$x_{v,bulk} = 0.9199 \pm 0.00077$
$T_{2L} = 118.58 \pm 0.25°\text{C}$ $T_{4L} = 114.14 \pm 0.25°\text{C}$ $T_{6L} = 110.93 \pm 0.25°\text{C}$ $T_{2R} = 151.77 \pm 0.25°\text{C}$ $T_{4R} = 147.51 \pm 0.25°\text{C}$ $T_{6R} = 141.68 \pm 0.25°\text{C}$ $T_{8R} = 134.02 \pm 0.25°\text{C}$	$T_{v,bulk} = average(T_{2L}, T_{4L}, T_{6L}, T_{2R}, T_{4R}, T_{6R}, T_{8R})$	$T_{v,bulk} = 131.2 \pm 0.06186°\text{C}$

Table B.5 Continued

Input	Equations	Output
$x_{v,bulk} = 0.9199 \pm 0.00077$ $M_{NH3} = 17.03 \pm 0 \text{ kg kMol}^{-1}$ $M_{H_2O} = 18.02 \pm 0 \text{ kg kMol}^{-1}$	$\tilde{x}_{v,bulk} = \dfrac{\dfrac{x_{v,bulk}}{M_{NH_3}}}{\dfrac{x_{v,bulk}}{M_{NH_3}} + \left(\dfrac{\left(1 - x_{v,bulk}\right)}{M_{H_2O}}\right)}$	$\tilde{x}_{v,bulk} = 0.9239 \pm 0.00073$
$P = 2459 \pm 17.24 \text{ kPa}$ $T_{v,bulk} = 131.2 \pm 0.06186 °\text{C}$ $R = 8.314 \text{ kJ kMol}^{-1} \text{ K}^{-1}$	$C_T = \dfrac{P}{R \cdot \left(T_{v,bulk} + 273.2 °\text{C}\right)}$	$C_T = 0.7315 \pm 0.00513 \text{kMol m}^{-3}$

APPENDIX C

HEAT AND MASS TRANSFER MODEL SAMPLE CALCULATIONS

Sample calculations for the branched tray desorber model are provided here. The nominal experimental conditions are provided in Table C.1 along with the measured values that are used as inputs to the model. Sample calculations are provided specifically for segment 3 of the branched tray desorber model in Table C.2. The model uses 5 desorber segments in total. The equation set provided in Table C.2 is solved iteratively using *Engineering Equation Solver* (Klein, 2011). The desorber segments of the vertical column use the same architecture and similar equation set, but with the appropriate modifications to represent the vertical column geometry and heat and mass transfer mechanisms. The branched tray and vertical column analyzer segments are the same as the respective desorber segments, but have a coolant heat duty of zero. Rectifier segments also use the same general architecture, but make use of the SBG method rather than the explicit mass transfer calculations of the Colburn-Drew method. Additional discussion of the modeling methods of the present study are provided in Section 3.1.1. Details of the revised models, including results and comparisons with experimental values, are provided in Chapter 6.

Table C.1: Vertical column sample point data

Nominal Conditions	
$\dot{m}_{l,in}$ (g s^{-1})	0.90
$x_{l,in}$	0.475
$T_{des,CF,in}$ (^{o}C)	180.0
Measured Value	
$\dot{m}_{l,in}$ (g s^{-1})	0.890
$\dot{m}_{l,out}$ (g s^{-1})	0.595
P (kPa)	1626
$T_{l,in}$ (^{o}C)	82.8
$T_{l,out}$ (^{o}C)	143.8
$T_{v,out}$ (^{o}C)	81.7
$\dot{V}_{des,CF}$ (cm^{3} s^{-1})	9.45
$T_{des.CF,in}$ (^{o}C)	179.5
$\dot{m}_{rect,CF}$ (g s^{-1})	0.790
$T_{rect,CF,in}$ (^{o}C)	56.9

Table C.2: Heat and mass transfer sample calculations

Input	Equations	Output
Segment Inputs, Average Properties, Geometric Parameters, and Dimensionless Parameters		
Input from adjacent segments: $\dot{m}_{l,o,4} = 0.0003841 \text{ kg s}^{-1}$ $h_{l,o,4} = 254.5 \text{ kJ kg}^{-1}$ $x_{l,o,4} = 0.3755$ $\dot{m}_{v,o,2} = 5.706\times10^{-5} \text{ kg s}^{-1}$ $h_{v,o,2} = 1697 \text{ kJ kg}^{-1}$ $x_{v,o,2} = 0.8858$ $T_{cf,o,2} = 166.2°\text{C}$	$\dot{m}_{l,i,3} = \dot{m}_{l,o,4}$ $h_{l,i,3} = h_{l,o,4}$ $x_{l,i,3} = x_{l,o,4}$ $\dot{m}_{v,i,3} = \dot{m}_{v,o,2}$ $h_{v,i,3} = h_{v,o,2}$ $x_{v,i,3} = x_{v,o,2}$ $T_{cf,i,3} = T_{cf,o,2}$ $T_{l,i,3} = f\left(P, h_{l,i,3}, x_{l,i,3}\right)$ $T_{v,i,3} = f\left(P, h_{v,i,3}, x_{v,i,3}\right)$	$\dot{m}_{l,i,3} = 0.0003841 \text{ kg s}^{-1}$ $h_{l,i,3} = 254.5 \text{ kJ kg}^{-1}$ $x_{l,i,3} = 0.3755$ $\dot{m}_{v,i,3} = 5.706\times10^{-5} \text{ kg s}^{-1}$ $h_{v,i,3} = 1697 \text{ kJ kg}^{-1}$ $x_{v,i,3} = 0.8858$ $T_{cf,i,3} = 166.2°\text{C}$ $T_{l,i,3} = 108.4°\text{C}$ $T_{v,i,3} = 154.5°\text{C}$
Component specifications: $\dot{V}_{cf,T} = 9.69\times10^{-6} \text{ m}^3 \text{ s}^{-1}$ $\rho_{cf,3} = 789.5 \text{ kg m}^{-3}$ $n_c = 2$	$\dot{m}_{cf} = \dot{V}_{cf,T} \cdot \rho_{cf,3} / n_c$	$\dot{m}_{cf} = 0.003825 \text{ kg s}^{-1}$

Table C.2: Continued

Input	Equations	Output
Segment Inputs, Average Properties, Geometric Parameters, and Dimensionless Parameters		
$T_{cf,i,3} = 166.2°\text{C}$ $T_{cf,o,3} = 159.3°\text{C}$ $T_{l,i,3} = 108.4°\text{C}$ $T_{l,o,3} = 121.2°\text{C}$ $T_{v,i,3} = 154.5°\text{C}$ $T_{v,o,3} = 152.08°\text{C}$ $x_{l,i,3} = 0.3755$ $x_{l,o,3} = 0.3182$ $x_{v,i,3} = 0.8858$ $x_{v,o,3} = 0.92933$ $\dot{m}_{v,i,3} = 5.706\times10^{-5}\ \text{kg s}^{-1}$ $\dot{m}_{v,o,3} = 9.096\times10^{-5}\ \text{kg s}^{-1}$	$T_{cf,avg,3} = \dfrac{T_{cf,i,3}+T_{cf,o,3}}{2}$ $T_{l,avg,3} = \dfrac{T_{l,i,3}+T_{l,o,3}}{2}$ $T_{v,bulk,3} = \dfrac{T_{v,i,3}+T_{v,o,3}}{2}$ $x_{l,avg,3} = \dfrac{x_{l,i,3}+x_{l,o,3}}{2}$ $x_{v,bulk,3} = \dfrac{x_{v,i,3}+x_{v,o,3}}{2}$ $\dot{m}_{v,avg,3} = \dfrac{\dot{m}_{v,i,3}+\dot{m}_{v,o,3}}{2}$	$T_{cf,avg,3} = 162.7°\text{C}$ $T_{l,avg,3} = 114.8°\text{C}$ $T_{v,bulk,3} = 153.3°\text{C}$ $x_{l,avg,3} = 0.3468°\text{C}$ $x_{v,bulk,3} = 0.9076°\text{C}$ $\dot{m}_{v,avg,3} = 7.523\times10^{-5}\ \text{kg s}^{-1}$
$x_{l,avg,3} = 0.3468°\text{C}$ $P = 1626\ \text{kPa}$	$x_{l,int} = x_{l,avg,3}$ $T_{l,int} = f\left(x_{l,int}, P, q=0\right)$ $x_{v,int} = f\left(T_{L,int}, P, q=1\right)$	$x_{l,int} = 0.3468$ $T_{l,int} = 114.7°\text{C}$ $x_{v,int} = 0.9294$

Table C.2: Continued

Input	**Equations**	**Output**
Segment Inputs, Average Properties, and Dimensionless Parameters		
$T_{cf,avg,3} = 162.7°\text{C}$ $P = 1626\text{ kPa}$ $T_{l,avg,3} = 114.8°\text{C}$ $T_{v,bulk,3} = 153.3°\text{C}$ $x_{l,avg,3} = 0.3468°\text{C}$ $x_{v,bulk,3} = 0.9076°\text{C}$	$\rho_{cf,3} = f\left(T_{cf,avg,3}\right)$ $c_{p,cf,3} = f\left(T_{cf,avg,3}\right)$ $k_{cf,3} = f\left(T_{cf,avg,3}\right)$ $\mu_{cf,3} = f\left(T_{cf,avg,3}\right)$ $T_{sat,NH_3} = f\left(P\right)$ $T_{sat,H_2O} = f\left(P\right)$ $c_{p,NH_3} = f\left(P\right)$ $c_{p,H_2O} = f\left(P\right)$ $P_{r,mix,3} = f\left(x_{l,avg,3}, P\right)$ $\text{vapor bulk properties} = f\left(T_{v,bulk,3}, P, x_{v,bulk,3}\right)$ $\text{liquid average properties} = f\left(T_{l,avg,3}, P, x_{l,avg,3}\right)$ $h_{fg,mix,3} = f\left(x_{l,avg,3}, P\right)$ $k_{wall,3} = f\left(T_{wall,3}\right)$	$\rho_{cf,3} = 789.5\text{ kg m}^{-3}$ $c_{p,cf,3} = 2.58\text{ kJ kg}^{-1}\text{ K}^{-1}$ $k_{cf,3} = 0.09763\text{ W m}^{-1}\text{ K}^{-1}$ $\mu_{v,3} = 0.001248\text{ kg m}^{-1}\text{ s}^{-1}$ $T_{sat,NH_3} = 41.61°\text{C}$ $T_{sat,H_2O} = 202.1°\text{C}$ $c_{p,NH_3} = 1.953\text{ kJ kg}^{-1}\text{ K}^{-1}$ $c_{p,H_2O} = 1.846\text{ kJ kg}^{-1}\text{ K}^{-1}$ $P_{r,mix,3} = 0.08162$ $c_{p,v,3} = 3.242\text{ kJ kg}^{-1}\text{ K}^{-1}$ $\rho_{v,3} = 8.299\text{ kg m}^{-3}$ $\mu_{v,3} = 1.503\times10^{-5}\text{ kg m}^{-1}\text{ s}^{-1}$ $k_{v,3} = 0.04182\text{ W m}^{-1}\text{ K}^{-1}$ $D_{aw,v,3} = 3.369\times10^{-6}\text{ m}^{2}\text{ s}^{-1}$ $\rho_{l,3} = 789.89\text{ kg m}^{-3}$ $h_{fg,mix,3} = 1640\text{ kJ kg}^{-1}$ $k_{wall,3} = 16.52\text{ W m}^{-1}\text{ K}^{-1}$

Table C.2: Continued

Input	Equations	Output (Solved Iteratively)
$x_{v,bulk,3} = 0.9076°\text{C}$ $x_{v,int,3} = 0.9294$ $x_{l,avg,3} = 0.3468°\text{C}$ $M_a = 17.03 \pm 0 \text{ kg kMol}^{-1}$ $M_w = 18.02 \pm 0 \text{ kg kMol}^{-1}$	$\tilde{x} = \dfrac{\dfrac{x}{M_{NH_3}}}{\dfrac{x}{M_{NH_3}} + \left(\dfrac{(1-x)}{M_{H_2O}}\right)}$	$\tilde{x}_{v,bulk,3} = 0.9122$ $\tilde{x}_{v,int,3} = 0.933$ $\tilde{x}_{l,avg,3} = 0.3486$
$R_{ch} = 0.00035 \pm 0 \text{ m}$ $L_{flat} = 0.00005 \pm 0 \text{ m}$ $Width_{c,hor} = 0.009017 \text{ m}$ $Depth_c = 0.005715 \text{ m}$	$D_{h,cf} = 4A_{face,ch} / P_{wet,cf}$ $P_{wet,cf} = \left[2(2\pi R_{ch}/4) + L_{flat}\right] + (2R_{ch} + L_{flat})$ $A_{face,ch} = 2\left(\dfrac{\pi R_{ch}^2}{4}\right) + (R_{ch} L_{flat})$ $D_{h,col} = 4A_{face,col} / P_{col}$ $P_{col} = 2(Depth_c + Width_{c,hor})$ $A_{face,col} = Depth_c \cdot Width_{c,hor}$	$D_{h,cf} = 0.000442 \text{ m}$ $P_{wet,cf} = 0.0019 \text{ m}$ $A_{face,ch} = 2.099 \times 10^{-7} \text{ m}^2$ $D_{h,col} = 0.006996\ m$ $P_{col} = 0.02946 \text{ m}$ $A_{face,col} = 5.153 \times 10^{-5} \text{ m}^2$
$P_{wet,cf} = 0.0019 \text{ m}$ $n_{cf,ch,per,soln,ch} = 51$ $Width_c = 0.01016 \text{ m}$ $pitch_{ch} = 0.00125 \text{ m}$ $Depth_c = 0.005715 \text{ m}$ From iteration: $L_{seg,3} = 0.02585 \text{ m}$	$Area_{cft,3} = P_{wet,cf} \cdot n_{cf,ch,per,soln,ch} \cdot L_{seg,3}$ $Area_{ht,pb,3} = (L_{seg,3} - Width_c)(n_{cf,ch,per,soln,ch}\, pitch_{ch} - Width_c)$ $Area_{ht,vap,3} = \left((n_{cf,ch,per,so\ln,ch})\, pitch_{ch} - Width_c\right) Depth_c + L_{seg,3} Depth_c$	$Area_{cft,3} = 0.002504 \text{ m}^2$ $Area_{ht,pb,3} = 0.0008408 \text{ m}^2$ $Area_{ht,vap,3} = 0.000454 \text{ m}^2$
$L_{T,des} = 0.1524 \text{ m}$	$L_{T,des} = \sum_{i=1}^{n_{seg}} L_{seg,i}$	From iteration: $L_{seg,3} = 0.02585 \text{ m}$

Table C.2: Continued

Input	Equations	Output (Solved Iteratively)
$\mu_{v,3} = 0.001248\ \text{kg m}^{-1}\ \text{s}^{-1}$ $\dot{m}_{cf} = 0.003825\ \text{kg s}^{-1}$ $D_{h,cf} = 0.000442\ \text{m}$ $D_{h,col} = 0.006996\ m$ $\dot{m}_{v,avg,3} = 7.523\times10^{-5}\ \text{kg s}^{-1}$ $\rho_{v,3} = 8.299\ \text{kg m}^{-3}$ $\mu_{v,3} = 1.503\times10^{-5}\ \text{kg m}^{-1}\ \text{s}^{-1}$	$\text{Re}_{des,cf} = \dfrac{\dot{m}_{cf} D_{h,cf}}{\mu_{des,cf} A_{face,ch} n_{cf,ch,per,soln,ch}}$ $\text{Re}_{v,3} = \dfrac{\dot{m}_{v,avg,3} D_{h,col}}{A_{face,col}\mu_{v,3}}$ $Sc_{v,3} = \dfrac{\mu_{v,3}}{\rho_{v,3} D_{aw,v,3}}$	$\text{Re}_{cf} = 63.28$ $\text{Re}_{v,3} = 679.5$ $Sc_{v,3} = 0.5376$
Coupling fluid heat duty and heat transfer		
$n_c = 2$ $n_{seg} = 5$ $T_{cf,i,3} = 166.2°\text{C}$ $c_{p,cf,3} = 2.58\ \text{kJ kg}^{-1}\ \text{K}^{-1}$ $\dot{m}_{cf} = 0.003825\ \text{kg s}^{-1}$ From iteration of all segments: $\dot{Q}_T = 672.4\ \text{W}$	$\dot{Q}_{seg,3} = \dfrac{\dot{Q}_T}{\left(n_c \cdot n_{seg}\right)}$ $\dot{Q}_{seg,3} = \dot{m}_{cf} c_{p,cf,3}\left(T_{cf,i,3} - T_{cf,o,3}\right)$	$\dot{Q}_{seg,3} = 67.2\ \text{W}$ $T_{cf,o,3} = 159.3°\text{C}$
$\dot{Q}_{seg,3} = 67.2\ \text{W}$ $T_{cf,avg,3} = 162.7°\text{C}$ $Area_{cft,3} = 0.002504\ \text{m}^2$ $\alpha_{cf,3} = 902.0\ \text{W m}^{-2}\ \text{K}^{-1}$ $Area_{ht,pb,3} = 0.0008408\ \text{m}^2$ $x_{wall} = 0.00222\ \text{m}$ $k_{wall,3} = 16.52\ \text{W m}^{-1}\ \text{K}^{-1}$	$\dot{Q}_{seg,3} = (R_{wall,3} + R_{cf,3})^{-1}\left(T_{wall,3} - T_{cf,ave,3}\right)$ $R_{cf,3} = \dfrac{1}{Area_{cft,3} \cdot \alpha_{cf,3}}$ $R_{wall,3} = \dfrac{x_{wall}}{Area_{ht,pb,3} \cdot k_{wall,3}}$	$T_{wall,3} = 122.2°\text{C}$ From iteration: $L_{seg,3} = 0.02585\ \text{m}$

Table C.2: Continued

Input	Equations	Output (Solved Iteratively)
$\phi = 1.571$ $D_{h,cf} = 0.000442$ m $k_{cf,3} = 0.09763$ W m^{-1} K^{-1} $\mathrm{Re}_{cf} = 63.28$	$\alpha_{cf,3} = f\left(\phi, D_{h,cf}, k_{cf,3}, \mathrm{Re}_{cf,3}\right)$	$\alpha_{cf,3} = 902.0$ W m^{-2} K^{-1}
	Solution heat and transfer	
$\dot{Q}_{seg,3} = 67.2$ W $\alpha_{boil,3} = 10772$ W m^{-2} K^{-1} $Area_{ht,pb,3} = 0.000841$ m^2 $R_{cf,3} = 0.4427$ K W^{-1} $R_{wall,3} = 0.16$ K W^{-1} $T_{cf,i,3} = 166.2$°C $T_{cf,o,3} = 159.3$°C $T_{l,i,3} = 108.4$°C	$\dot{Q}_{seg,3} = \left(\frac{1}{\alpha_{boil,3} \cdot Area_{ht,pb,3}} + R_{cf,3} + R_{wall,3}\right)^{-1} LMTD_{des}$ $LMTD_{des} = \frac{\left(T_{des,cf,in} - T_{l,o,3}\right) - \left(T_{des,cf,out} - T_{l,i,3}\right)}{\ln\left(\frac{T_{des,cf,in} - T_{l,o,3}}{T_{des,cf,out} - T_{l,i,3}}\right)}$ $q''_{pb,3} = \dot{Q}_{seg,3} / Area_{ht,pb,3}$	$T_{l,o,3} = 121.2$°C $q''_{pb,3} = 79970$ W m^{-2}

Table C.2: Continued

Input	Equations	Output (Solved Iteratively)
$\alpha_{id,Gorenflo,3}$=14851 W m^{-2} K^{-1} $T_{sat,NH_3} = 41.61°\text{C}$ $T_{sat,H_2O} = 202.1°\text{C}$ $q''_{pb,3} = 79970 \text{ W m}^{-2}$ $\rho_{l,3} = 789.89 \text{ kg m}^{-3}$ $h_{fg,mix,3} = 1640 \text{ kJ kg}^{-1}$ $\text{Re}_{v,3} = 679.5$ $P_{r,mix,3} = 0.08162$ $\tilde{x}_{v,bulk,3} = 0.9122$ $\tilde{x}_{l,avg,3} = 0.3486$	$\alpha_{boil,3} = \alpha_{id,Gorenflo,3} \times \left(1+\frac{\alpha_{id,Gorenflo,3}}{q''_{pb,3}}\left(T_{sat,H2O} - T_{sat,NH3}\right)\left(1-\exp\left(-B_{0,prop,3}\frac{q''_{pb,3}}{\rho_{l,3} h_{fg,mix,3} 2\times10^{-4}}\right)\right)\left(\Delta\tilde{x}_3\right)\right)^{-1}$ $B_{0,prop,3} = 11.3 \exp\left(-0.0045\frac{\text{Re}_{v,3}^{0.5}}{P_{r,mix,3}^{1.5}}\right)$ $\Delta\tilde{x}_3 = \tilde{x}_{v,bulk,3} - \tilde{x}_{l,avg,3}$	$\alpha_{boil,3} = 10772 \text{ W m}^{-2}$ K^{-1} $B_{0,prop,3} = 0.0738$
$T_{l,o,3} = 121.2°\text{C}$ $P = 1626 \text{ kPa}$	$x_{l,o,3} = f\left(T_{l,o,3}, P, q=0\right)$	$x_{l,o,3} = 0.3182$

Table C.2: Continued

Input	Equations	Output
$x_{l,avg,3} = 0.3468°\text{C}$ $q''_{pb,3} = 79970\ \text{W m}^{-2}$ $P_{r,mix,3} = 0.08162$ $q''_0 = 20000\ \text{W m}^{-2}\ \text{K}^{-1}$ $\alpha_{0,NH3} = 7000\ \text{W m}^{-2}\ \text{K}^{-1}$ $\alpha_{0,H2O} = 5600\ \text{W m}^{-2}\ \text{K}^{-1}$	$\alpha_{id,Gorenflo,3} = \left(\frac{x_{l,avg,3}}{\alpha_{NH3,Gorenflo,3}} + \frac{1-x_{l,avg,3}}{\alpha_{H2O,Gorenflo,3}}\right)^{-1}$ $\alpha_{NH3,Gorenflo,3} = \alpha_{0,NH3} F_{PR,NH3,3} \left(\frac{q''_{pb,3}}{q''_0}\right)^{n_{Gorenflo,NH_3,3}}$ $n_{Gorenflo,NH_3,3} = 0.9 - \left(0.3 \cdot P_{r,mix,3}^{0.3}\right)$ $F_{PR,NH_3,3} = 1.2 \cdot P_{r,mix,3}^{0.27} + \left(2.5 + \left(\frac{1}{1-P_{r,mix,3}}\right)\right) P_{r,mix,3}$ $\alpha_{H_2O,Gorenflo,3} = \alpha_{0,H2O} F_{PR,H2O,3} \left(\frac{q''_{pb,3}}{q''_0}\right)^{n_{Gorenflo,H_2O,3}}$ $n_{Gorenflo,H_2O,3} = 0.9 - \left(0.3 \cdot P_{r,mix,3}^{0.15}\right)$ $F_{PR,H_2O,3} = 1.73 \cdot P_{r,mix,3}^{0.27} + \left(6.1 + \left(\frac{0.68}{1-P_{r,mix,3}}\right)\right) \cdot P_{r,mix,3}^{2}$	$\alpha_{id,Gorenflo,3} = 14851\ \text{W m}^{-2}\ \text{K}^{-1}$ $\alpha_{NH3,Gorenflo,3} = 18086\ \text{W m}^{-2}\ \text{K}^{-1}$ $\alpha_{H_2O,Gorenflo,3} = 13554\ \text{W m}^{-2}\ \text{K}^{-1}$

Table C.2: Continued

Input	Equations	Output
Vapor heat transfer		
$\dot{Q}_{sen,v,3} = 0.00199\ \text{W}$ $Area_{ht,vap,3} = 0.000454\ \text{m}^2$ $T_{v,i,3} = 154.5°\text{C}$ $T_{l,i,3} = 108.4°\text{C}$ $T_{l,o,3} = 121.2°\text{C}$ $\dot{n}''_{NH_3,3} = 0.004117\ \text{kMol m}^{-2}\ \text{s}^{-1}$ $\dot{n}''_{H_2O,3} = 0.004072\ \text{kMol m}^{-2}\ \text{s}^{-1}$ $c_{p,NH_3} = 1.953\ \text{kJ kg}^{-1}\ \text{K}^{-1}$ $c_{p,H_2O} = 1.846\ \text{kJ kg}^{-1}\ \text{K}^{-1}$ $k_{v,3} = 0.04182\ \text{W m}^{-1}\ \text{K}^{-1}$ $D_{h,col} = 0.006996\ m$ From Schmidt and Newell (1967): $Nu_{v,const} = 3.2$	$\dot{Q}_{sen,vl,3} = \alpha_{v,3}\dfrac{\phi_{T,3}}{\exp\left(\phi_{T,3}\right)-1}Area_{ht,vap,3}LMTD_{v-l}$ $LMTD_{v-l} = \dfrac{\left(T_{v,i,3}-T_{l,o,3}\right)-\left(T_{v,o,3}-T_{l,i,3}\right)}{\ln\left(\dfrac{T_{v,i,3}-T_{l,o,3}}{T_{v,o,3}-T_{l,i,3}}\right)}$ $\phi_{T,3} = \left(\dot{n}_{NH_3,3}c_{p,NH_3}+\dot{n}_{H_2O,3}c_{p,H_2O}\right)\dfrac{1000}{\alpha_{v,3}}$ $\alpha_{v,3} = Nu_{v,const}\dfrac{k_{v,3}}{D_{h,col}}$	$T_{v,o,3} = 152.08°\text{C}$ $\alpha_{v,3} = 19.13\ \text{W m}^{-2}\ \text{K}^{-1}$
$\dot{m}_{v,avg,3} = 7.523\times10^{-5}\ \text{kg s}^{-1}$ $c_{p,v,3} = 3.242\ \text{kJ kg}^{-1}\ \text{K}^{-1}$ $T_{v,i,3} = 154.5°\text{C}$ $T_{v,o,3} = 152.08°\text{C}$	$\dot{Q}_{sen,v,3} = \dot{m}_{v,avg,3}c_{p,v,3}\left(T_{v,i,3}-T_{v,o,3}\right)$	$\dot{Q}_{sen,v,3} = 0.00199\ \text{W}$

Table C.2: Continued

Input	Equations	Output
Mass transfer and vaporizing flux		
$\tilde{x}_{v,int,3} = 0.933$ $\tilde{x}_{v,bulk,3} = 0.9122$ $P = 1626 \text{ kPa}$ $R = 8.314 \text{ kJ kMol}^{-1} \text{ K}^{-1}$ $T_{v,bulk,3} = 153.3°\text{C}$ $D_{aw,v,3} = 3.369\times10^{-6} \text{ m}^2 \text{ s}^{-1}$ $D_{h,col} = 0.006996\ m$ $\mathrm{Re}_{v,3} = 679.5$ $Sc_{v,3} = 0.5376$	$\dot{n}''_{T,3} = -\beta_{v,Onda,3} C_{T,3} \ln\left(\frac{\tilde{z}_3 - \tilde{x}_{v,int,3}}{\tilde{z}_3 - \tilde{x}_{v,bulk,3}}\right)$ $C_{T,3} = \frac{P}{R\left(T_{v,Bulk,3} + 273.15°\text{C}\right)}$ $\frac{\beta_{v,Onda,3}}{D_{aw,v,3}\cdot a_{Onda}} = 2.0\left(a_{Onda}\cdot D_{h,col}\right)^{-2.0} \mathrm{Re}_{v,3}^{0.7} Sc_{v,3}^{1/3}$ $a_{Onda} = \left(\frac{D_{h,col}}{2}\right)^{-1}$ $\dot{n}''_{NH_3,3} = \tilde{z}_3 \cdot \dot{n}''_{t,3}$ $\dot{n}''_{H_2O,3} = \left(1-\tilde{z}_3\right)\cdot \dot{n}''_{t,3}$	$\dot{n}''_{NH_3,3} = 0.004117 \text{ kMol m}^{-2} \text{ s}^{-1}$ $\dot{n}''_{H_2O,3} = 0.004072 \text{ kMol m}^{-2} \text{ s}^{-1}$ $\dot{n}''_{T,3} = 0.004072 \text{ kMol m}^{-2} \text{ s}^{-1}$ $\beta_{v,Onda,3} = 0.0376$
$\dot{n}''_{NH_3,3} = 0.004117 \text{ kMol m}^{-2} \text{ s}^{-1}$ $\dot{n}''_{H_2O,3} = 0.004072 \text{ kMol m}^{-2} \text{ s}^{-1}$ $M_{NH_3} = 17.03 \pm 0 \text{ kg kMol}^{-1}$ $M_{H_2O} = 18.02 \pm 0 \text{ kg kMol}^{-1}$ $Area_{ht,vap,3} = 0.000454 \text{ m}^2$	$\dot{m}_{des,NH_3,3} = M_{NH_3} \cdot \dot{n}''_{NH_3,3} \cdot Area_{ht,vap,3}$ $\dot{m}_{des,H_2O,3} = M_{H_2O} \cdot \dot{n}''_{H_2O,3} \cdot Area_{ht,vap,3}$ $\dot{m}_{des,T,3} = \dot{m}_{des,a,3} + \dot{m}_{des,w,3}$	$\dot{m}_{des,NH_3,3} = 3.183\times10^{-5} \text{ kg s}^{-1}$ $\dot{m}_{des,H_2O,3} = \text{-}3.667\times10^{-7} \text{ kg s}^{-1}$ $\dot{m}_{des,T,3} = 3.146\times10^{-5} \text{ kg s}^{-1}$

Table C.2: Continued

Input	Equations	Output
Segment mass, species and energy balances		
$\dot{m}_{l,i,3} = 0.0003841 \text{ kg s}^{-1}$ $\dot{m}_{v,i,3} = 5.706\times10^{-5} \text{ kg s}^{-1}$ $\dot{m}_{des,T,3} = 3.146\times10^{-5} \text{ kg s}^{-1}$	$\dot{m}_{l,i,3} + \dot{m}_{v,i,3} = \dot{m}_{l,o,3} + \dot{m}_{v,o,3}$ $\dot{m}_{v,o,3} = \dot{m}_{v,i,3} + \dot{m}_{des,tot,3}$	$\dot{m}_{l,o,3} = 0.0003493 \text{ kg s}^{-1}$ $\dot{m}_{v,o,3} = 9.096\times10^{-5} \text{ kg s}^{-1}$
$\dot{m}_{l,i,3} = 0.0003841 \text{ kg s}^{-1}$ $\dot{m}_{v,i,3} = 5.706\times10^{-5} \text{ kg s}^{-1}$ $\dot{m}_{l,o,3} = 0.0003493 \text{ kg s}^{-1}$ $\dot{m}_{v,o,3} = 9.096\times10^{-5} \text{ kg s}^{-1}$ $x_{l,o,4} = 0.3755$ $x_{v,o,2} = 0.8858$ $\dot{m}_{des,NH_3,3} = 3.183\times10^{-5} \text{ kg s}^{-1}$	$\dot{m}_{l,i,3}x_{l,i,3} + \dot{m}_{v,i,3}x_{v,i,3} = \dot{m}_{l,o,3}x_{l,o,3} + \dot{m}_{v,o,3}x_{v,o,3}$ $\dot{m}_{v,o,3}x_{v,o,3} = \dot{m}_{v,i,3}x_{v,i,3} + \dot{m}_{des,NH_3,3}$	$x_{l,o,3} = 0.3182$ $x_{v,o,3} = 0.92933$
$\dot{m}_{l,i,3} = 0.0003841 \text{ kg s}^{-1}$ $\dot{m}_{v,i,3} = 5.706\times10^{-5} \text{ kg s}^{-1}$ $\dot{m}_{l,o,3} = 0.0003493 \text{ kg s}^{-1}$ $\dot{m}_{v,o,3} = 9.096\times10^{-5} \text{ kg s}^{-1}$ $h_{l,o,4} = 254.5 \text{ kJ kg}^{-1}$ $h_{v,o,2} = 1697 \text{ kJ kg}^{-1}$ $P = 1626 \text{ kPa}$ $x_{l,o,3} = 0.3182$	$\dot{Q}_{seg,3} + \dot{m}_{l,i,3}h_{l,i,3} + \dot{m}_{v,i,3}h_{v,i,3} = \dot{m}_{l,o,3}h_{l,o,3} + \dot{m}_{v,o,3}h_{v,o,3}$ $h_{l,o,3} = f\left(x_{l,o,3}, P, q=0\right)$ $h_{l,o,3} = f\left(T_{v,o,3}, P, x_{v,o,3}\right)$	$\dot{Q}_{seg,3} = 67.2 \text{ W}$ $h_{l,o,3} = 337.0 \text{ kJ kg}^{-1}$ $h_{v,o,3} = 1677.4 \text{ kJ kg}^{-1}$

REFERENCES

Akita, K. and F. Yoshida (1974), "Bubble Size, Interfacial Area, and Liquid-Phase Mass Transfer Coefficient in Bubble Columns," *Industrial & Engineering Chemistry Process Design and Development* Vol. 13(1) pp. 84-91.

Arima, H., M. Monde and Y. Mitsutake (2003), "Heat Transfer in Pool Boiling of Ammonia/Water Mixture," *Heat and Mass Transfer* Vol. 39(7) pp. 535-543.

Bell, K. J. and M. A. Ghaly (1972), "Approximate Generalized Design Method for Multicomponent/Partial Condensers," *American Institute of Chemical Engineers, Papers*(24).

Borishanskii, V., A. Kozyrev and L. Svetlova (1964), "Heat Transfer in the Boiling Water in a Wide Range of Saturation Pressure," *High Temperature* Vol. 2(1) pp. 119-121.

Calderbank, P. H. and M. B. Moo-Young (1961), "The Continuous Phase Heat and Mass-Transfer Properties of Dispersions," *Chemical Engineering Science* Vol. 16(1–2) pp. 39-54.

Carey, V. P. (2008). *Liquid-Vapor Phase-Change Phenomena*. 2nd ed. Ed.

Chun, K. R. and R. A. Seban (1971), "Heat Transfer to Evaporating Liquid Films," *Journal of Heat Transfer* Vol. 93 Ser C(4) pp. 391-396.

Colburn, A. P. and T. B. Drew (1937), "The Condensation of Mixed Vapours," *AIChE Transactions* Vol. 33 pp. 197-212.

Damman, J. (1973). Technical University of Braunschweig

Davis, K. R., J. M. Schmitt and D. V. Pence (2010), "Control of an Oil-Heated, Fractal-Like Branching Microchannel Desorber," *Applied Thermal Engineering* Vol. 30(5) pp. 510-519.

Delahanty, J. C., S. Garimella and M. A. Garrabrant (2015), "Design of Compact Microscale Geometries for Ammonia–Water Desorption," *Science and Technology for the Built Environment* Vol. 21(3) pp. 365-374.

Determan, M. D. (2008). *Thermally Activated Miniaturized Cooling System*. Mechanical Engineering. Atlanta, Georgia Institute of Technology, Vol. Ph.D. p. 230.

Determan, M. D. and S. Garimella (2011), "Ammonia–Water Desorption Heat and Mass Transfer in Microchannel Devices," *International Journal of Refrigeration* Vol. 34(5) pp. 1197-1208.

Determan, M. D. and S. Garimella (2012), "Design, Fabrication, and Experimental Demonstration of a Microscale Monolithic Modular Absorption Heat Pump," *Applied Thermal Engineering* Vol. 47(0) pp. 119-125.

Determan, M. D., S. Garimella and S. Lee (2004), "Experimental Demonstration of a Microchannel Desorber for Ammonia-Water Heat Pumps," *Seventeenth National Heat and Mass Transfer Conference and Sixth ISHMT/ASME Heat and Mass Transfer Conference*, Kalpakkam, India, pp. 453-458.

Fernández-Seara, J. and J. Sieres (2006), "The Importance of the Ammonia Purification Process in Ammonia-Water Absorption Systems," *Energy Conversion and Management* Vol. 47(13-14) pp. 1975-1987.

Fernández-Seara, J., J. Sieres and M. Vázquez (2003), "Distillation Column Configurations in Ammonia-Water Absorption Refrigeration Systems," *International Journal of Refrigeration* Vol. 26(1) pp. 28-34.

Fernández-Seara, J., A. Vales and M. Vázquez (1998), "Heat Recovery System to Power an Onboard Nh3-H2o Absorption Refrigeration Plant in Trawler Chiller Fishing Vessels," *Applied Thermal Engineering* Vol. 18(12) pp. 1189-1205.

Fritz, W. (1935), "Maximum Volume of Vapor Bubbles," *Phys. Z* Vol. 36(11) pp. 379-384.

Fronk, B. M. (2014). *Coupled Heat and Mass Transfer During Condensation of High-Temperature-Glide Zeotropic Mixtures in Small Diameter Channels*. Mechanical Engineering. Atlanta, GA, Georgia Institute of Technology, Vol. Ph.D. p. 282.

Fronk, B. M. and S. Garimella (2013), "Analysis of Coupled Heat and Mass Transfer During Condensation of High Temperature Glide Zeotropic Mixtures in Small Channels," *ASME 2013 International Mechanical Engineering Congress and Exposition*, American Society of Mechanical Engineers, pp. V08BT09A067-V008BT009A067.

Fujita, T. (1993), "Falling Liquid Films in Absorption Machines," *International Journal of Refrigeration* Vol. 16(4) pp. 282-294.

Fujita, T. and T. Ueda (1978a), "Heat Transfer to Falling Liquid Films and Film Breakdown—I: Subcooled Liquid Films," *International Journal of Heat and Mass Transfer* Vol. 21(2) pp. 97-108.

Fujita, T. and T. Ueda (1978b), "Heat Transfer to Falling Liquid Films and Film Breakdown—Ii: Saturated Liquid Films with Nucleate Boiling," *International Journal of Heat and Mass Transfer* Vol. 21(2) pp. 109-118.

Fujita, Y. and M. Tsutsui (1997), "Heat Transfer in Nucleate Boiling of Binary Mixtures : Development of a Heat Transfer Correlation," *JSME International Journal Series B* Vol. 40(1) pp. 134-141.

Garimella, S. (1999), "Miniaturized Heat and Mass Transfer Technology for Absorption Heat Pumps," *Proceedings of the International Sorption Heat Pump Conference*, Munich, Germany, pp. 661-670.

Garimella, S. (2000), "Microchannel Components for Absorption Space-Conditioning Systems," *2000 ASHRAE Winter Meeting, Feb 5-Feb 9 2000*, Dallas, TX, USA, Amer. Soc. Heating, Ref. Air-Conditoning Eng. Inc., Atlanta, GA, USA, pp. 453-462.

Garimella, S. (2004). *Method and Means for Miniaturization of Binary-Fluid Heat and Mass Exchangers*. USA, Iowa State University Research Foundation, Inc. (Ames, IA).

Garimella, S., J. C. Delahanty and A. K. Nagavarapu (2011). *Vapor-Liquid Heat and/or Mass Exchange Device,* Google Patents.

Garrabrant, M., R. Stout, P. Glanville, J. Fitzgerald and C. Keinath (2013a). Development and Validation of a Gas-Fired Residential Heat Pump Water Heater-Final Report. Stone Mountain Technologies, Inc.p.

Garrabrant, M., R. Stout, P. Glanville, C. Keinath and S. Garimella (2013b), "Development of Ammonia-Water Absorption Heat Pump Water Heater for Residential and Commercial Applications," *ASME 2013 7th International Conference on Energy Sustainability collocated with the ASME 2013 Heat Transfer Summer Conference and the ASME 2013 11th International Conference on Fuel Cell Science, Engineering and Technology,* American Society of Mechanical Engineers, pp. V001T004A002-V001T004A002.

Garrabrant, M. A. and R. N. Christensen (1997), "Modeling and Experimental Verification of a Perforated Plate-Fin Absorber for Aqua-Ammonia Absorption Systems," *Proceedings of the 1997 ASME International Mechanical Engineering Congress and Exposition, Nov 16-21 1997,* Dallas, TX, USA, ASME, Fairfield, NJ, USA, pp. 337-347.

Golden, J. H. (2012). *Ammonia-Water Desorption in Flooded Columns*. Mechanical Engineering. Atlanta, Georgia Institute of Technology, Vol. M.S.

Gorenflo, D. (1993). Pool Boiling. *Vdi-Heat Atlas*. E. U. Schlunder. Dusseldorf, Germany, VDI-Verlag GmbH pp. Ha 1-13.

Ibrahim, O. M. and S. A. Klein (1993), "Thermodynamic Properties of Ammonia-Water Mixtures," *ASHRAE Transactions* Vol. 99(1) pp. 1495-1502.

Inoue, T., N. Kawae and M. Monde (1998), "Characteristics of Heat Transfer During Nucleate Pool Boiling of Binary Mixtures," *Nippon Kikai Gakkai Ronbunshu, B Hen/Transactions of the Japan Society of Mechanical Engineers, Part B* Vol. 63(608) pp. 1312-1319.

Inoue, T. and M. Monde (1994), "Nucleate Pool Boiling Heat Transfer in Binary Mixtures," *Wärme - und Stoffübertragung* Vol. 29(3) pp. 171-180.

Inoue, T., M. Monde and Y. Teruya (2002a), "Pool Boiling Heat Transfer in Binary Mixtures of Ammonia/Water," *International Journal of Heat and Mass Transfer* Vol. 45 pp. 4409-4415.

Inoue, T., M. Monde, Y. Teruya and H. Ikeda (2002b), "Pool Boiling Heat Transfer in Binary Mixtures of Ammonia/Water: Effect of Heat of Dilution and Dissolution on Heat Transfer Coefficient," *Heat Transfer—Asian Research* Vol. 31(4) pp. 272-283.

Kang, M.-G. (2000), "Effect of Surface Roughness on Pool Boiling Heat Transfer," *International Journal of Heat and Mass Transfer* Vol. 43(22) pp. 4073-4085.

Kang, Y. T., W. Chen and R. N. Christensen (1997), "Generalized Component Design Model by Combined Heat and Mass Transfer Analysis in Nh_3/H_2o Absorption Heat Pump Systems," *Proceedings of the 1997 ASHRAE Winter Meeting, Jan 26-29 1997*, Philadelphia, PA, USA, ASHRAE, Atlanta, GA, USA, pp. 444-453.

Kang, Y. T. and R. N. Christensen (1994), "Development of a Counter-Current Model for a Vertical Fluted Tube Gax Absorber, New Orleans, LA, USA, Publ by ASME, pp. 7-16.

Kang, Y. T. and R. N. Christensen (1995), "Combined Heat and Mass Transfer Analysis for Absorption in a Fluted Tube with a Porous Medium in Confined Cross Flow," *Proceedings of the 1995 ASME/JSME Thermal Engineering Joint Conference. Part 1 (of 4), Mar 19-24 1995*, Maui, HI, USA, ASME, New York, NY, USA, pp. 251-260.

Kang, Y. T., T. Kashiwagi and R. N. Christensen (1998), "Ammonia-Water Bubble Absorber with a Plate Heat Exchanger," *Proceedings of the 1998 ASHRAE Winter Meeting. Part 2 (of 2), Jan 18-21 1998*, San Francisco, CA, USA, ASHRAE, Atlanta, GA, USA, pp. 1565-1575.

Kays, W. M., M. E. Crawford and B. Weigand (2005). *Convective Heat and Mass Transfer*. Fourth Edition Ed. New York, McGraw-Hill.

Keinath, C. M., J. C. Delahanty, S. Garimella and M. A. Garrabrant (2012), "Diesel Engine Waste-Heat Driven Ammonia-Water Absorption System for Space-Conditioning Applications

Keinath, C. M., D. Hoysall, J. C. Delahanty, M. D. Determan and S. Garimella (2015), "Experimental Assessment of a Compact Branched Tray Ggenerator for Ammonia–Water Desorption," *Science and Technology for the Built Environment* Vol. 21(3) pp. 348-356.

Killion, J. D. and S. Garimella (2001), "A Critical Review of Models of Coupled Heat and Mass Transfer in Falling-Film Absorption," *International Journal of Refrigeration* Vol. 24(8) pp. 755-797.

Killion, J. D. and S. Garimella (2003), "A Review of Experimental Investigations of Absorption of Water Vapor in Liquid Films Falling over Horizontal Tubes," *HVAC&R Research* Vol. 9(2) pp. 111-136.

Klein, S. A. (2011). *Engineering Equation Solver*. Madison, WI, F-Chart Software.

Kutateladze, S. S. (1982), "Semi-Empirical Theory of Film Condensation of Pure Vapours," *International Journal of Heat and Mass Transfer* Vol. 25(5) pp. 653-660.

Kwon, K. and S. Jeong (2004), "Effect of Vapor Flow on the Falling-Film Heat and Mass Transfer of the Ammonia/Water Absorber," *International Journal of Refrigeration* Vol. 27(8) pp. 955-964.

Meacham, J. M. (2002). *An Integrated Experimental and Analytical Study of Ammonia-Water Absorption in Microchannel Geometries*. Mechanical Engineering. Ames, Iowa State University p. 140.

Meacham, J. M. and S. Garimella (2002a), "Experimental Demonstration of a Prototype Microchannel Absorber for Space-Conditioning Systems," *International Sorption Heat Pump Conference*, Shanghai, China, pp. 270-276.

Meacham, J. M. and S. Garimella (2002b), "Miniaturized Shell-and-Tube Heat and Mass Exchangers for Absorption Heat Pumps," *12th International Heat Transfer Conference*, Grenoble, France

Meacham, J. M. and S. Garimella (2003), "Modeling of Local Measured Heat and Mass Transfer Variations in a Microchannel Ammonia-Water Absorber," *Technical and Symposium Papers Presented At the 2003 Winter Meeting of The ASHRAE, Jan 26-29 2003*, Chicago, IL, United States, Amer. Soc. Heating, Ref. Air-Conditioning Eng. Inc., pp. 412-422.

Meacham, J. M. and S. Garimella (2004), "Ammonia-Water Absorption Heat and Mass Transfer in Microchannel Absorbers with Visual Confirmation," *ASHRAE Transactions* Vol. 110(1) pp. 525-532.

Nagavarapu, A. K. (2012). *Binary Fluid Heat and Mass Exchange at the Microscale in Internal and External Ammonia-Water Absorption*. Mechanical Engineering. Atlanta, GA, Georgia Institute of Technology, Vol. Ph.D. p. 448.

Nagavarapu, A. K. and S. Garimella (2011), "Design of Microscale Heat and Mass Exchangers for Absorption Space Conditioning Applications," *Journal of Thermal Science and Engineering Applications* Vol. 3(2) pp. 021005-021005.

Nellis, G. and S. A. Klein (2009). *Heat Transfer*. New York, Cambridge University Press.

Nishikawa, K. and Y. Fujita (1977), "On the Pressure Factor in Nucleate Boiling Heat Transfer," *Memoirs of the Kyushu University, Faculty of Engineering* Vol. 36(4) pp. 303-341.

Nusselt, W. (1916), "Die Oberflachenkondesation Des Wasserdamffes," *Zetrschr. Ver. Deutch. Ing.* Vol. 60 pp. 541-546, 569-575.

Onda, K., H. Takeuchi and Y. Okumoto (1968), "Mass Transfer Coefficients between Gas and Liquid Phases in Packed Columns," *Journal of Chemical Engineering of Japan* Vol. 1(1) pp. 56-62.

Ortega, N., O. García-Valladares, R. Best and V. H. Gómez (2008), "Two-Phase Flow Modelling of a Solar Concentrator Applied as Ammonia Vapor Generator in an Absorption Refrigerator," *Renewable Energy* Vol. 33(9) pp. 2064-2076.

Price, B. C. and K. J. Bell (1974), "Design of Binary Vapor Condensers Using the Colburn-Drew Equations," *AIChE Symposium Series - Heat Transfer - Research and Design* Vol. 70(138) pp. 163-171.

Rattner, A. S. and S. Garimella (2011), "Energy Harvesting, Reuse and Upgrade to Reduce Primary Energy Usage in the USA," *Energy* Vol. 36(10) pp. 6172-6183.

Rohsenow, W. M. (1952), "Method of Correlating Heat-Transfer Data for Surface Boiling of Liquids," *American Society of Mechanical Engineers -- Transactions* Vol. 74(6) pp. 969-975.

Rohsenow, W. M. (1985). Thin-Film Heat Transfer. *Handbook of Heat Transfer Fundamentals* W. M. Rohsenow, J. P. Hartnett and E. N. Ganic. New York, NY, McGraw-Hill Book Co. pp. 12.75-12.82

Rohsenow, W. M., J. P. Hartnett and E. N. Ganic (1985). *Handbook of Heat Transfer Fundamentals (2nd Edition)*. New York, NY, McGraw-Hill Book Co.

Rohsenow, W. M., J. H. Webber and A. T. Ling (1956), "Effect of Vapor Velocity on Laminar and Turbulent Film Condensation," *Trans. Asme* Vol. 78(8) pp. 1637-1643.

Rose, J., Y. Utaka and I. Tanasawa (1999). Dropwise Condensation. *Handbook of Phase Change: Boiling and Condensation*. M. S. S. G. Kandlikar, V. K. Dhir. Philadelphia, PA, Taylor and Francis pp. 581-594.

Sauceda, D., N. Velázquez, O. García-Valladares and R. Beltrán (2011), "Numerical Simulation and Design of a Parabolic Trough Solar Collector Used as a Direct Generator in a Solar-Gax Cooling Cycle?," *Journal of Mechanical Science and Technology* Vol. 25(6) pp. 1399-1408.

Schlunder, E. U. (1982), "Heat Transfer in Nucleate Pool Boiling of Mixtures," *Proc. 7th Int. Heat Transfer Conf*, pp. 2073-2079.

Schmidt, F. W. and M. E. Newell (1967), "Heat Transfer in Fully Developed Laminar Flow through Rectangular and Isosceles Triangular Ducts," *International Journal of Heat and Mass Transfer* Vol. 10(8) pp. 1121-1123.

Shah, R. K. and M. S. Bhatti (1987). Laminar Convective Heat Transfer in Ducts. *Handbook of Single-Phase Convective Heat Transfer*. S. Kakaç, R. K. Shah and W. Aung. New York, NY, Wiley New York et al.

Shi, C., Q. Chen, T.-C. Jen and W. Yang (2010), "Heat Transfer Performance of Lithium Bromide Solution in Falling Film Generator," *International Journal of Heat and Mass Transfer* Vol. 53(15–16) pp. 3372-3376.

Sieres, J. and J. Fernández-Seara (2007), "Modeling of Simultaneous Heat and Mass Transfer Processes in Ammonia–Water Absorption Systems from General Correlations," *Heat and Mass Transfer* Vol. 44(1) pp. 113-123.

Sieres, J., J. Fernández-Seara and F. J. Uhía (2008), "Experimental Analysis of Ammonia-Water Rectification in Absorption Systems with the 10 mm Metal Pall Ring Packing," *International Journal of Refrigeration* Vol. 31(2) pp. 270-278.

Silver, L. (1947), "Gas Cooling with Aqueous Condensation," *Industrial Chemist and Chemical Manufacturer* Vol. 23(269) pp. 380-386.

Sparrow, E. M. and A. Haji-Sheikh (1965), "Laminar Heat Transfer and Pressure Drop in Isosceles Triangular, Right Triangular, and Circular Sector Ducts," *Journal of Heat Transfer* Vol. 87 pp. 426-427.

Spindler, K. (2010), "Overview and Discussion on Pool Boiling Heat Transfer Data and Correlations of Ammonia," *International Journal of Refrigeration* Vol. 33(7) pp. 1292-1306.

Stephan, K. and M. Abdelsalam (1980), "Heat-Transfer Correlations for Natural Convection Boiling," *International Journal of Heat and Mass Transfer* Vol. 23(1) pp. 73-87.

Stephan, K. and M. Körner (1969), "Berechnung Des Wärmeübergangs Verdampfender Binärer Flüssigkeitsgemische," *Chemie Ingenieur Technik* Vol. 41(7) pp. 409-417.

Táboas, F., M. Vallès, M. Bourouis and A. Coronas (2007), "Pool Boiling of Ammonia/Water and Its Pure Components: Comparison of Experimental Data in the Literature with the Predictions of Standard Correlations," *International Journal of Refrigeration* Vol. 30(5) pp. 778-788.

Táboas, F., M. Vallès, M. Bourouis and A. Coronas (2010), "Flow Boiling Heat Transfer of Ammonia/Water Mixture in a Plate Heat Exchanger," *International Journal of Refrigeration* Vol. 33(4) pp. 695-705.

Táboas, F., M. Vallès, M. Bourouis and A. Coronas (2012), "Assessment of Boiling Heat Transfer and Pressure Drop Correlations of Ammonia/Water Mixture in a Plate Heat Exchanger," *International Journal of Refrigeration* Vol. 35(3) pp. 633-644.

Thome, J. R. (1981), "Nucleate Pool Boiling of Binary Liquids - an Analytical Equation," *AIChE Symposium Series* Vol. 77(208) pp. 238-250.

Thome, J. R. (1983), "Prediction of Binary Mixture Boiling Heat Transfer Coefficients Using Only Phase Equilibrium Data," *International Journal of Heat and Mass Transfer* Vol. 26(7) pp. 965-974.

Thome, J. R. and S. Shakir (1987), "A New Correlation for Nucleate Pool Boiling of Aqueous Mixtures," *Heat Transfer - Pittsburgh 1987.*, Pittsburgh, PA, USA, AIChE, pp. 46-51.

Tillner-Roth, R. and D. G. Friend (1998), "A Helmholtz Free Energy Formulation of the Thermodynamic Properties of the Mixture {Water + Ammonia}," *Journal of Physical and Chemical Reference Data* Vol. 27(1) pp. 63-96.

Venegas, M., A. Zacarías, C. Vereda, A. Lecuona and R. Ventas (2012), "Subcooled and Saturated Boiling of Ammonia–Lithium Nitrate Solution in a Plate-Type Generator for Absorption Machines," *International Journal of Heat and Mass Transfer* Vol. 55(17–18) pp. 4914-4922.

Wagner, W. and A. Pruß (2002), "The Iapws Formulation 1995 for the Thermodynamic Properties of Ordinary Water Substance for General and Scientific Use," *Journal of Physical and Chemical Reference Data* Vol. 31(2) pp. 387-535.

Wallis, G. B. (1969). *One-Dimensional Two-Phase Flow*. New York, McGraw-Hill.

Wilke, W. (1962), "Warmeubertragung an Rieselfilme," *VDI-Forschungsheft* Vol. 490 p. B28.

Zacarías, A., R. Ventas, M. Venegas and A. Lecuona (2010), "Boiling Heat Transfer and Pressure Drop of Ammonia-Lithium Nitrate Solution in a Plate Generator," *International Journal of Heat and Mass Transfer* Vol. 53(21–22) pp. 4768-4779.